Searching for Short Range Correlations Using (e,e'NN) Reactions

by

Bin Zhang

B.S., University of Science and Technology of China (1997)

Submitted to the Department of Physics
in partial fulfillment of the requirements for the degree of

Doctor of Philosophy

at the

MASSACHUSETTS INSTITUTE OF TECHNOLOGY

February 2003

Author . . . .
Department of Physics
September 28, 2002

Certified by . . . .
William Bertozzi
Professor of Physics
Thesis Supervisor

Accepted by . . . .
Thomas J. Greytak
Professor of Physics
Associate Department Head for Education

Searching for Short Range Correlations Using (e,e'NN) Reactions

by

Bin Zhang

Submitted to the Department of Physics
on September 28, 2002, in partial fulfillment of the
requirements for the degree of
Doctor of Philosophy

Abstract

Electron induced two nucleon knockout reactions (e,e'pp) and (e,e'np) were performed for ^{3}He, ^{4}He and ^{12}C nuclei with incident energies of 2.261 GeV and 4.461 GeV using the CLAS detector at Jefferson Lab. Events with missing momenta lower than the Fermi level and missing energies smaller than the pion threshold were studied. The residual system was assumed to be a spectator and the process was considered as a quasi-free knockout of an NN pair. The cross sections for 15 different reactions were presented as functions of the initial relative momentom per nucleon of the NN pair. The data showed that the inital momentum extends up to 800 MeV/c with considerable strength. The cross sections for ^{3}He(e,e'pp)n were compared to the calculations of J.M. Laget. It was found that the final state interactions (FSI) and the meson exchange currents (MEC) dominate the cross sections and the short range properties of the NN pair were substantially undermined. However, the node of the S state wave function of the pp pair at around 400 MeV/c inital momentum starts to be recognizable in the 4.461 GeV data. The data and the theory suggest that with higher momentum transfers, especially in the region of $x_{Bj} > 1$, the competing processes such as FSI and MEC will be less important and the detailed study of the short-range properties of nucleons inside nuclei will be more desirable.

Thesis Supervisor: William Bertozzi
Title: Professor of Physics

Contents

List of Figures

List of Tables

Chapter 1

Physics Motivations

1.1 Introduction

At the femtometre length scale, atomic nuclei can be described as a system of protons and neutrons. The phenomenological independent particle model (IPM) assumes that the mutual attraction of the nucleons averages to a mean nuclear field in which point-like nucleons move independently. As early as in the 1940's, Fermi already realized that this conception is too naive [40]. Without repulsive short-range forces between the nucleons any nuclei would just collapse to a size corresponding to the range of the attractive nuclear force (about 2 fm), even when Pauli blocking is taken into account. The strong repulsive nucleon-nucleon interaction in many-body systems, which is needed to explain the quantum-gas like behavior of nucleons, is related to the repulsive core seen in nucleon-nucleon (NN) scattering experiments. The effects of this repulsion are usually referred to as short-range correlations (SRC) [26].

The Hartree-Fock method adopted the single particle potential model. It assumed the single particle potential is generated by the mutual two-body interactions between the nucleons. The Hamiltonian can be written as

$$H = \sum_i T_i + \sum_{i<j} V_{ij} = \sum_i (T_i + U_i) + (\sum_{i<j} V_{ij} - \sum_i U_i), \tag{1.1}$$

where T represents the kinetic energy, V represents NN interactions, U represents the single particle potential and the subscription stands for each nucleon in the system. In order to find a single particle approximation so that the residual interaction $\sum_{i<j} V_{ij} - \sum_i U_i$ is small, a variational method was usually used to satisfy the condition $\delta(\langle\Psi|H|\Psi\rangle/\langle\Psi|\Psi\rangle) = 0$. The method can also achieve self-consistency, i.e. U is dependent on the states of the nucleons and at the same time the states of the nucleons are the solution of the Schrödinger equation with U in the Hamiltonian. Hartree-Fork calculations making use of the NN potentials including the repulsive core still do not describe nuclear properties correctly (the calculations sometimes yield unbound nuclei) [27].

One important drawback of mean field theory is its assumption that each nucleon moves in a single particle orbit and, therefore, the wave function of the nucleon is independent of whether or not another nucleon is close to it. Since there is a strong short range nucleon-nucleon force, this assumption would seem to be unreasonable. The random phase approximation (RPA) solves this problem by concentrating on certain types of important correlations. It can account for the strong one-particle-one-hole excitations (promoting one nucleon from an occupied single-particle state below Fermi level to an unoccupied state above) observed in many nuclei with a relatively simple calculation [41]. The Bethe-Goldstone equation [2, 44] used a so-called G matrix to account for the repulsive part of the NN potential. Because the G matrix is smoother than the actual potential, the independent particle wave function is a useful starting point to solve the equation.

The work of Müther and Polls [23] followed the Bethe-Goldstone approach to derive the correlation functions from several modern NN potentials: the charge dependent Bonn potential (CD-Bonn) [34], the Argonne V_{18} potential (AV_{18}) [35] and the Nijmegen potential [39]. Although all the potentials produce very accurate fits of the proton-proton and proton-neutron scattering data, they exhibit significant differences in calculating correlation functions in nuclear matter. The reason is obvious:

the accurate fits of NN scattering data only mean that the on-shell elements of the transition matrix are essentially identical for all the potentials. This, however, does not imply that the effective interactions between the off-shell nucleons moving inside a nucleus are the same. In fact, these phase-shift equivalent potentials have different descriptions of the short-range part of the interaction. The Nijmegen potential uses the local form of the short-range interaction. The same is true for the AV_{18} potential. The CD-Bonn potential is derived in the framework of the relativistic meson field theory in momentum space and contains non-local terms in the short-range part of the interaction.

Recently, Wiringa et al. developed the Quantum Monte Carlo (QMC) method by combining both the Variational Monte Carlo (VMC) method and the Green's Function Monte Carlo (GFMC) method [36]. The VMC method is used to construct a variational wave function as a product of two-body and three-body correlation operators acting on an independent particle wave function. Monte Carlo evaluation of the energy expectation value is used to optimize the trial wave function. The GFMC method starts from the trial wave function obtained from the VMC method and makes a Euclidean propagation that converges to the lowest energy for the state of given quantum numbers. This technique can be used to calculate many-body problems. Calculations for $A = 3$ up to $A = 10$ nuclei have been reported.

Most of the modern NN potentials (some were mentioned before) normally generate the short-range part of the NN interaction by assuming a specific dynamical model based on heavy meson exchanges, combined with phenomenological treatments at very small distances. The effective field theory (EFT) and the renomalization group method (RG) used by D.E. Brown et al. [13] eliminates the model dependence by keeping only nucleons and pions as explicit degrees of freedom. All other heavy mesons and nucleon resonances are considered to be integrated out of the theory. Their effects are contained inside the renormalized pion exchange and no underlying dynamics are assumed for the heavy mesons and nucleon resonances.

There are different ways to account for ground state correlations. Instead of introducing correlation functions in the many-body wave function in the real coordinate space, Heisenberg et al. [21] used the approach of adding correlated multi-particle multi-hole configurations to the uncorrelated ground state multi-particle multi-hole configurations. This is accomplished by using the so-called coupled cluster expansion method to solve the many-body Schrödinger equation in the configuration space.

The investigation of ground state correlations in nuclei, particularly those which originate from the most peculiar features of the NN interactions, i.e. the strong short range repulsion and the complex state dependencies (spin, isospin, tensor etc.), has become one of the most challenging aspects of modern experimental and theoretical nuclear physics. The experimental probe of the nuclear wave function or various density matrices is necessary to ascertain whether the prediction of the standard model of nuclei (structureless non-relativistic nucleons interacting via the know NN forces) is indeed justified in practice, or other phenomena such as relativistic effects, many-body forces, medium modification and explicit sub-nucleonic degrees of freedom (quarks and gluons) etc. have to be advocated in order to describe ground state properties of nuclei at normal density and temperature [4].

Several experiments were performed using hadron beams with the attempt to probe the short range properties of the NN interaction inside nucleus. One of them is pion absorption by various nuclei (^{3}He, ^{4}He, N, Xe, Ar) [58, 7]. Pion absorption by nuclei usually yields multi-nucleon emissions. The data in [7] indicate at the pion energy of 70 MeV the two-nucleon emission is the major process. If we ignore the binding energies of the two nucleons and the excitation energy of the residual nuclei, the two nucleons share a kinetic energy of about 210 MeV (the sum of 70 MeV and the pion mass which is about 140 MeV). As a result, each nucleon on the average has a final momentum of about 450 MeV/c. The momentum transfered by the pion is about 150 MeV/c. This indicates the initial momentum of the nucleons are quite large (300 to 600 MeV/c) compared to typical Fermi momentum (200 - 250 MeV/c).

It is a suggestion for the existence of short range correlations (SRC).

Another hadron beam experiment is the ^{12}C(p,2p+n) measurement performed at Brookhaven National Laboratory [6]. Proton beams with high momenta (5.9, 8.0 and 9.0 GeV/c) were used to study the quasi-elastic (p,2p) reaction on ^{12}C. In addition, neutrons were detected coincidentally in the backward hemisphere with respect to the beam direction. The range of the neutron momentum is from 50 to 550 MeV/c. The initial momentum of the knockout proton was reconstructed by the momentum conservation. It is found that when the neutron momentum is above 220 MeV/c, which is the typical Fermi momentum of ^{12}C, the directions of the initial proton momentum and the neutron momentum are preferentially back-to-back. The same is not true if the neutron momentum is below 220 MeV/c (see Fig. 1-1). This strong directional correlation is indicative of the short-range n-p correlations.

Electron induced reactions are a very good tool for investigations of ground state properties of nuclei. First the electromagnetic part of the interaction is well known. Second, it is sensitive to the off-shell behavior of the NN interaction, i.e. the total energy of the nucleons involved in the reaction is not the same in the final state and the initial state, something that cannot be probed by on-shell NN scattering experiments. In addition, the use of virtual photons offers the possibility to vary independently the energy and the momentum transfered to the system.

It has been notoriously difficult to obtain a clear experimental signature of short range correlations (SRC) in nuclei. Inclusive electron scattering off nuclei of $A > 1$ in quasi-elastic kinematics shows a large widening of the quasi-elastic peak with respect to the elastic peak on proton, which is the strong evidence for the momentum distribution of constituent nucleons. The large strength at $x_{Bj} > 1$ for inclusive (e,e') reactions compared to the independent particle model predictions has been considered as the evidence for short range correlations [28]. Semi-exclusive (e,e'p) experiments were performed [24, 33, 53] and gave indirect evidence for the presence of SRC. It was found that the occupation probabilities for the valence shells are considerably

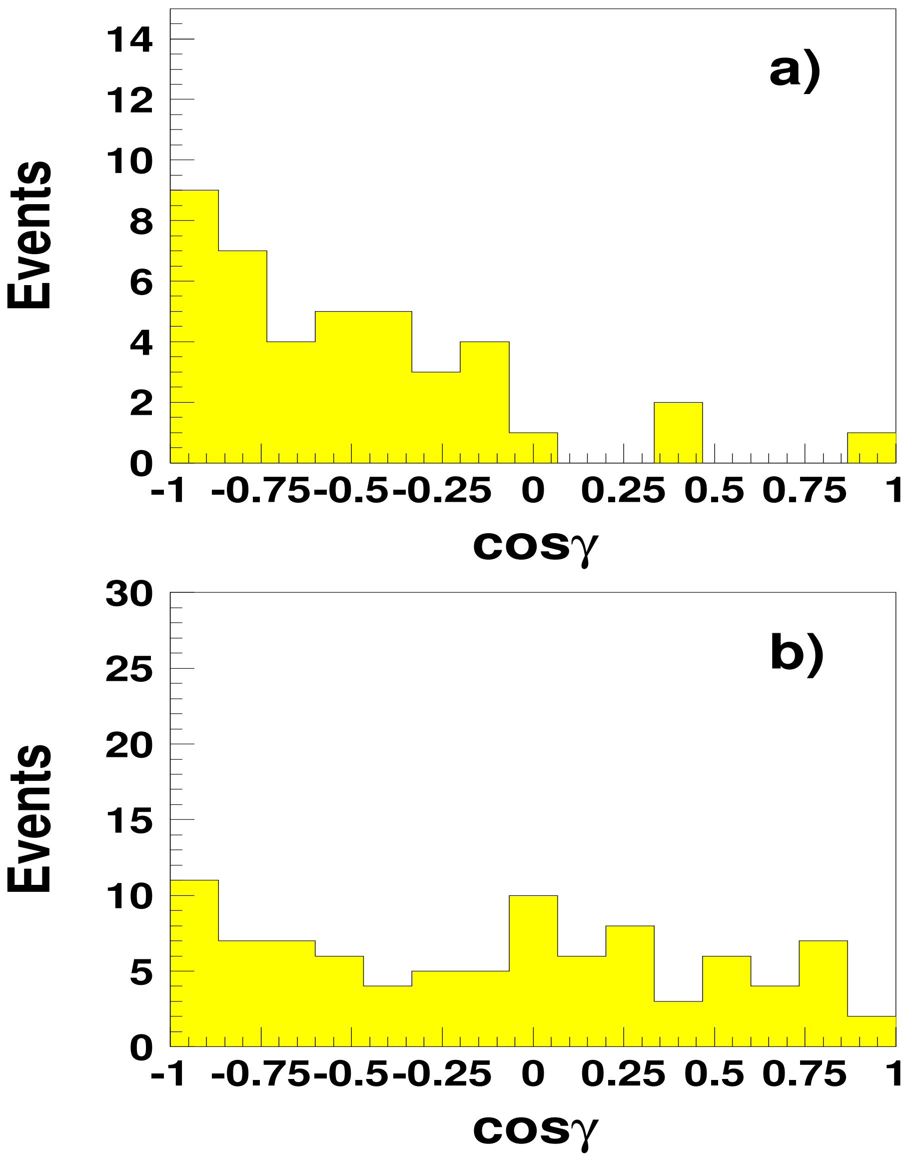

Figure 1-1: Distributions of cosγ for Brookhaven ^{12}C(p,2p+n) data, where γ is the angle between the reconstructed inital momentum of the knockout proton and the momentum of the neutron [6]. (a) is for events with neutron momentum above the Fermi momentum 220 MeV/c. (b) is for events with neutron momentum below 220 MeV/c.

smaller than predicted by the IPM [54]. According to references [10, 22], part of the quasi-hole strength is shifted to high (missing) momenta, which are well above the Fermi momentum, and high missing energies. However, the cross sections at large missing momenta are highly influenced by meson exchange currents (MEC) and final state interactions (FSI), adding complexity and limiting simple interpretions. A clear signature of SRC is normally expected to be the observation of an enhancement, with respect to mean field theory predictions, in the cross sections which has to be explained by SRC. The difficulty in obtaining the signature is directly due to the big influences by other effects such as MEC and FSI. These effects, at most times, are dominant parts of the cross sections, which makes it very difficult to single out the underlying SRC effects.

Because of the enhancement of orders of magnitude at large missing momenta and missing energies with respect to mean field calculations, the SRC effects are more likely to be associated with the emission of another nucleon. It is more promising to go beyond (e,e'p) experiments and also observe the second nucleon in two-nuleon knockout (e,e'NN) reactions, as first proposed by Gottfried [45]. By detecting both emitted nucleons of the correlated pair, we can get much richer information on the initial properties of the pair compared to just detecting one of them. The CLAS detector at Jefferson Lab (see Chapter 2) provides a good device to do this kind of experiments.

1.2 (e,e'NN) reactions

1.2.1 Kinematics

In this thesis, natural units are used, i.e. $\hbar = c = 1$. Using this convention, the four-momentum of a particle is expressed as $p^\mu = (\vec{p}, E)$, where E is the total energy of the particle and $\vec{p}$ is the three-momentum of the particle. For light and medium nuclei where $Z\alpha \ll 1$ (Z is the number of protons inside the nuclei and α is the fine

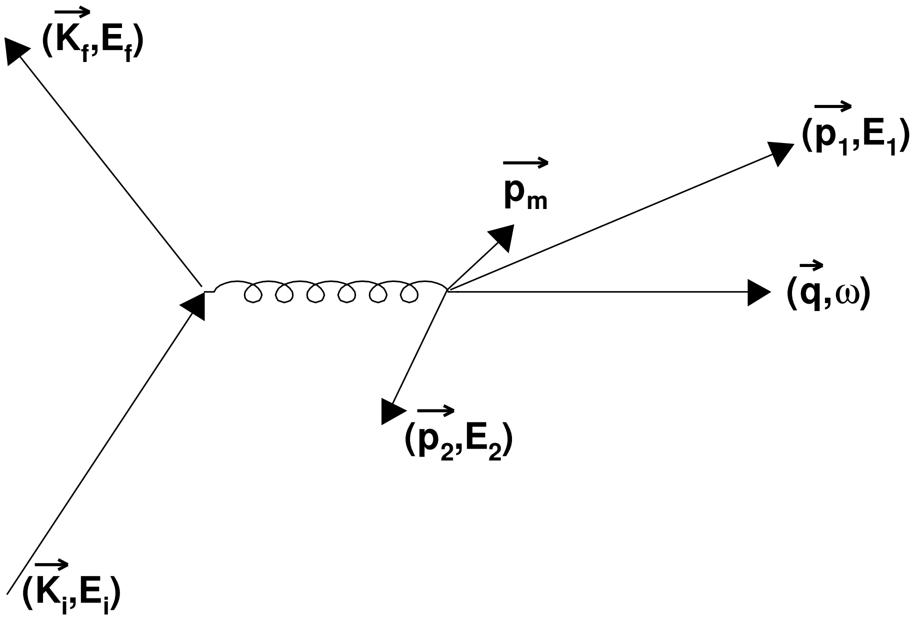

Figure 1-2: Diagram of (e,e'NN) reaction

structure constant), the distortion of the electron wave is not very big in the process of electron scattering and it is a good approximation to assume only one photon is exchanged. In (e,e'NN) experiments, the three-momenta of the two emitted nucleons are measured in coincidence with that of the scattered electron as shown in Fig. 1-2, where $k_i^\mu = (\vec{k}_i, E_i)$ and $k_f^\mu = (\vec{k}_f, E_f)$ are four-momenta of the initial and final electrons respectively, $p_1^\mu = (\vec{p}_1, E_1)$ and $p_2^\mu = (\vec{p}_2, E_2)$ are four-momenta of the two emitted nucleons and $q^\mu = (\vec{q}, \omega) = k_i^\mu - k_f^\mu$ is the four-momentum transfer carried by the virtual photon.

The missing momentum, missing energy and missing mass are defined as

$$\vec{p}_m = \vec{q} - \vec{p}_1 - \vec{p}_2 \tag{1.2}$$

$$E_m = \omega - T_1 - T_2 \tag{1.3}$$

$$M_m = \sqrt{E_m^2 - p_m^2} \tag{1.4}$$

where T_1 and T_2 are kinetic energies of the two emitted nucleons. Note p_m is also the momentum of the residual A-2 system. Missing mass determines how excited the residual A-2 system is. In this experiment, we always require the missing momentum to be smaller than Fermi momentum and missing energy to be smaller than the pion threshold m_π in order to enhance the probability that the residual system is a spectator and that we are measuring the direct knockout of a correlated NN pair (See Section 3.7 for our selection of kinematics).

Short Range Correlations are directly related to the relative momentum per nucleon of the NN pair in the initial state

$$\vec{p}_{rel} = \frac{\vec{p_1}^i - \vec{p_2}^i}{2}, \tag{1.5}$$

where $\vec{p_1}^i$ and $\vec{p_2}^i$ denote the initial momenta of the two emitted nucleons. Within the plane wave impulse approximation (PWIA), assuming nucleon 1 was hit by the virtual photon, then $\vec{p_1}^i = \vec{p}_1 - \vec{q}$, $\vec{p_2}^i = \vec{p}_2$ and

$$\vec{p}_{rel} = \frac{\vec{p_1}^i - \vec{p_2}^i}{2} = \frac{\vec{p}_1 - \vec{q} - \vec{p}_2}{2} \tag{1.6}$$

Our chosen observable is $\vec{p}_{rel}$.

1.2.2 Cross Sections Formalism

In the one photon exchange approximation, the 9-fold differential cross section for the exclusive two-nucleon knockout by unpolarized electrons can be expressed as the contraction of a lepton tensor $L_{\mu\nu}$ and a hadron tensor $H^{\mu\nu}$ [8]:

$$\begin{aligned} \frac{d^9\sigma}{dE_{e'}d\Omega_{e'}dE_1 d\Omega_1 dE_2 d\Omega_2} &= E_1 E_2 p_1 p_2 \frac{\alpha^2 E_{e'}}{Q^4 E_e} L_{\mu\nu} H^{\mu\nu} \\ &= E_1 E_2 p_1 p_2 \sigma_{eNN}(\vec{p}_{rel}, \vec{q}) S_{h_1,h_2}(E_m, P_m) \end{aligned} \tag{1.7}$$

$Q^2 = -q^\mu q_\mu = q^2 - \omega^2$ and $S_{h_1,h_2}(E_m, P_m)$ is the joint probability to find a pair of nucleons with momentum p_m in the single-particle states (h_1, h_2) at an energy corresponding to the missing energy. The elementary cross section σ_{eNN} describes the physics of absorption of a virtual photon on a NN pair in the target nucleus which depends on the photoabsorption mechanism and the relative motion of the two nucleons. σ_{eNN} can be expressed as a sum of terms containing longitudinal, transverse and transverse-transverse structure functions which depend on scalar (Jastrow), spin-spin and tensor correlation operators [60].

Particularly, for the ^{3}He target, the only target for which we have calculations available for this experiment, the differential cross section of breaking up the tri-nucleon system, in the absence of spin observables, can be written as

$$d\sigma = \frac{1}{(2\pi)^2}\frac{E'}{E} m_e^2 |M_{fi}^{3N}|^2 \delta(M_{^3He} + \omega - E_1 - E_2 - E_3)\delta^3(\vec{q} - \vec{p}_1 - \vec{p}_2 - \vec{p}_3) dE' d\Omega_{e'} d^3\vec{p}_1 d^3\vec{p}_2 d^3\vec{p}_3 \tag{1.8}$$

where $m_e^2 |M_{fi}^{3N}|^2$ is the contraction of the leptonic and hadronic tensor [43]. After integration over the three momentum of the third (unobserved) nucleon $\vec{p}_3$ and the momentum of the second nucleon p_2, the cross section can be written as

$$\frac{d^8\sigma}{dE' d\Omega_{e'} dp_1 d\Omega_1 d\Omega_2} = \Gamma_\nu \frac{E_3 p_2^3 p_1^2}{E_1 |E_3 p_2^2 - E_2 \vec{p}_3 \cdot \vec{p}_2|} \left(\frac{E_{12}}{p}\right)_{cm} \frac{d^5\sigma}{(d\Omega_1)_{cm} d^3\vec{p}_3} \tag{1.9}$$

where Γ_ν is the virtual photon flux, p and E_{12} are the momentum of each nucleon and the total energy measured in the center of mass (c.m.) frame of the two detected nucleons respectively [52].

The last factor in Equation 1.9 is the "reduced cross section" defined by J.M. Laget. As usual it can be expanded in terms of its transverse, longitudinal parts and the interferences as

$$\frac{d^5\sigma}{(d\Omega_1)_{cm} d^3\vec{p}_3} = \frac{d^5}{(d\Omega_1)_{cm} d^3\vec{p}_3}(\sigma_T + \epsilon\sigma_L + inteferences) \tag{1.10}$$

where ϵ is the virtual photon polarization and four inteferences cross sections should be taken into account [5].

There are various ways for the virtual photon to couple to ^{3}He nuclei, some of which are showed in Fig. 1-3. The virtual photon can couple to one nucleon only via a one-body hadronic current which leads to a full breakup of the 3-nucleon system. The full breakup can also occur via two-body currents, i.e. sharing energies and momenta of two nucleons. The two-body currents include meson exchange currents (MEC) where the virtual photon couples to the mesons exchanged between the two nucleons and isobar currents (IC) which involves excitation of Δ in the intermediate state. The importance of the two-body mechanisms is strongly dependent on the state of isospin of the NN pair. For example, for pp pairs, the MEC effects are suppressed because the virtual photon does not couple to neutral mesons to first order. The IC effects are also suppressed, because the dominant M1 transition is forbidden (angular momentum and parity conservation) and Δ excitation is only possible via much weaker C2 and E2 transitions. In addition, the virtual photon can also couple to all three nucleons via the three-body mechanism, e.g. couple to simultaneous exchange of two mesons. In this experiment, we always assume that the third nucleon is a spectator, so the three-body mechanism is ignored.

Final state interactions (FSI) are also a very important source of contribution to the cross sections. There are two primary types of FSI in ^{3}He(e,e'NN) as showed in Fig. 1-4: the rescattering of the NN pair in the final state and the rescattering between the pair and the third nucleon. In the case where the third nucleon is assumed to be a spectator, the second kind of rescattering is very small, as pointed out in [52] and confirmed in [4]. However, the rescattering between the NN pair is extreamly large and fully distorts the direct link between the ground state wave function and the cross section. At high momentum transfer, the FSI effects are expected to be reduced.

For this experiment, we used the calculations by J.M. Laget [52]. The antisym-

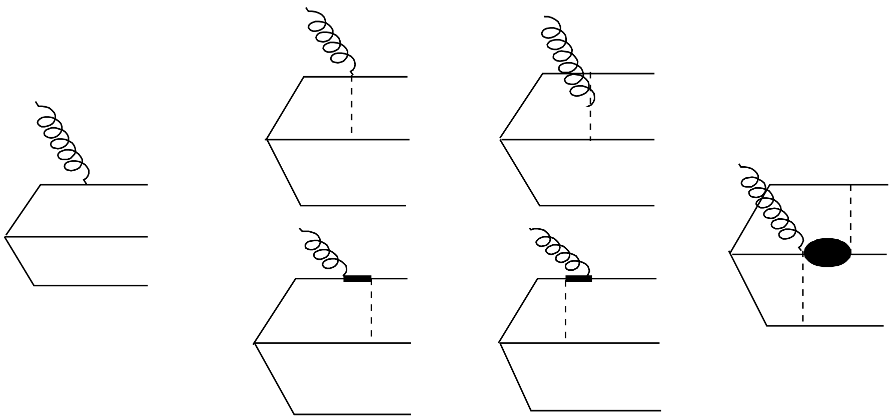

Figure 1-3: Photo-absorption mechanisms for ^{3}He(e,e'NN). The left graph shows interaction via a one-body hadronic current. The four graphs in the middle show some two-body mechanisms: meson exchange current and intermediate Δ excitation then de-excitation. The right graph is an example of three-body mechanism.

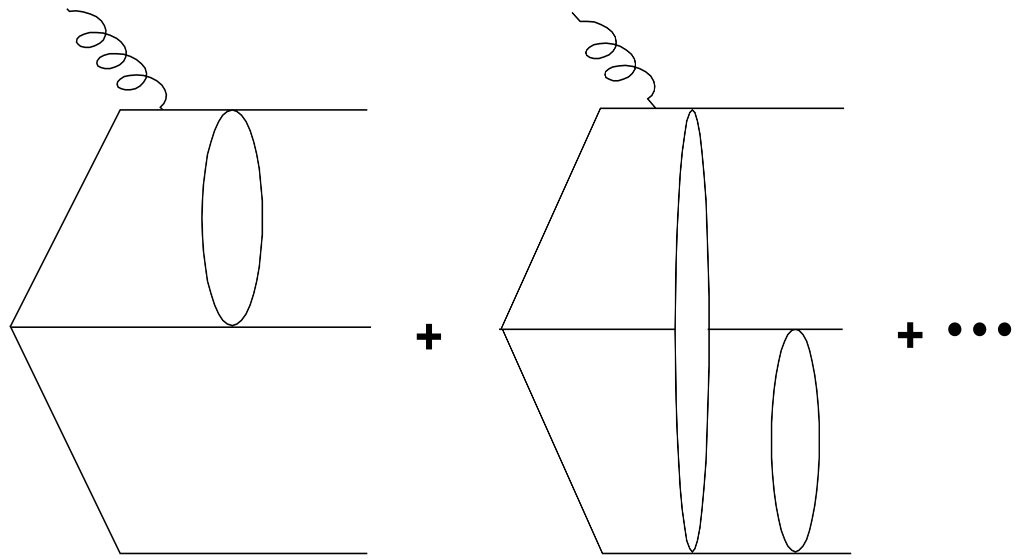

Figure 1-4: Final state rescattering between the nucleons for ^{3}He(e,e'NN), following the reaction via a one-body hadronic current. The left graph shows the rescattering between the NN pair. The right graph shows the rescattering between the pair and the third nucleon. The blobs represent the NN scattering operator.

metric bound state wave function was taken as the solution to the Faddeev equations [47] with the Paris potential [32] and the continuum was approximated by the sum of a plane wave and half-off-shell scattering amplitudes, where two nucleons scatter and the third is a spectator. The antisymmetry of the continuum final state was achieved by exchanging the roles of the three nucleons. In addition, effects of meson exchange current (MEC) were considered. What we are looking for is the influence of short range correlations (SRC) embeded in the ground state wave function while other effects such as FSI and MEC are also present in the reaction. The comparison of the calculation and the data as well as the relative importance of various mechanisms revealed by the calculation will be discussed in detail in the last chapter.

1.2.3 Existing Data

There is a small number of data sets existing for three arm coincident experiments. Particularly, there are a few (e,e'pp) experiments done at NIKHEF and MAMI.

NIKHEF Data

A ^{3}He(e,e'pp)n [11] measurement was performed at NIKHEF with beam energy 564 MeV, $\omega = 220$ MeV, $q = 305$, 375 and 445 MeV/c. Fig. 1-5 shows the average cross sections measured at $q = 305$ MeV/c as a function of the neutron momentum in the final state. Three panels represent three different ranges for γ_1, the angle between the more forward (with respect to $\vec{q}$ direction) proton and $\vec{q}$. The curves show the results of continuum Faddeev calculations, where both the three-nucleon bound state and final state wave functions are exact solutions of the 3N Faddeev equations solved in a partial-wave decomposition using the Bonn-B NN interaction [25]. The solid curve represents results obtained with a one-body hadronic current only, while the dashed curve also includes MEC contributions. One can clearly see that for $p_m < 100$ MeV/c, it is a fair description of data by the solid curve and the MEC contribution is very small. At higher missing momenta, calculations including only one-body current fall short by a factor of 5. The discrepancy is likely due to two-body effects such as MEC and Δ resonance.

Fig. 1-6 shows the dependence of the cross section on the three-momentum transfer q. Again, at higher missing momentum range ($120 < p_m < 220$ MeV/c), two-body effects and FSI play an important role. For smaller missing momentum range ($20 < p_m < 120$ MeV/c), the reaction can be considered as a direct process, leaving the spectator neutron "at rest" in the final state. The agreement in size and slope between the data and the Faddeev calculations performed with a one-body current suggests that in this domain the cross section is dominated by knockout of correlated proton pairs, and the correlation functions of the model have some validity in fact.

MAMI Data

A ^{12}C(e,e'pp)^{10}Be experiment [19] was performed at MAMI with beam energy 705 MeV, $\omega = 225 \pm 55$ MeV, $q = 412 \pm 58$ MeV/c. The protons were detected in a BGO crystal ball with close to 4π acceptance. Fig. 1-7 shows the average cross section as a function of missing energy and the calculations using 0.6 fm hard-core correlation functions [38] and those using the Argonne AV$_{14}$ potential applying cluster variational Monte-Carlo (VMC) methods [37]. The data clearly rejected hard-core calculations and soft-core ones reproduced data reasonably well in low missing energy region ($E_m < 70$ MeV). The rise of the cross section at larger missing energies ($E_m > 70$ MeV) suggests other effects such as meson exchange current (MEC) and Δ production-reabsorption might have played an important role.

In missing momentum distributions shown in Fig. 1-8, VMC calculations agree with data reasonably especially in the low missing momentum region. At large missing momenta, the enhancement of data indicates the break-down of the single-pair approximation. It is likely that the missing system was actively involved in the reaction.

Fig. 1-9 shows the relative momentum ($p_{rel} = |\vec{p}_1 - \vec{p}_2|$) distribution which is

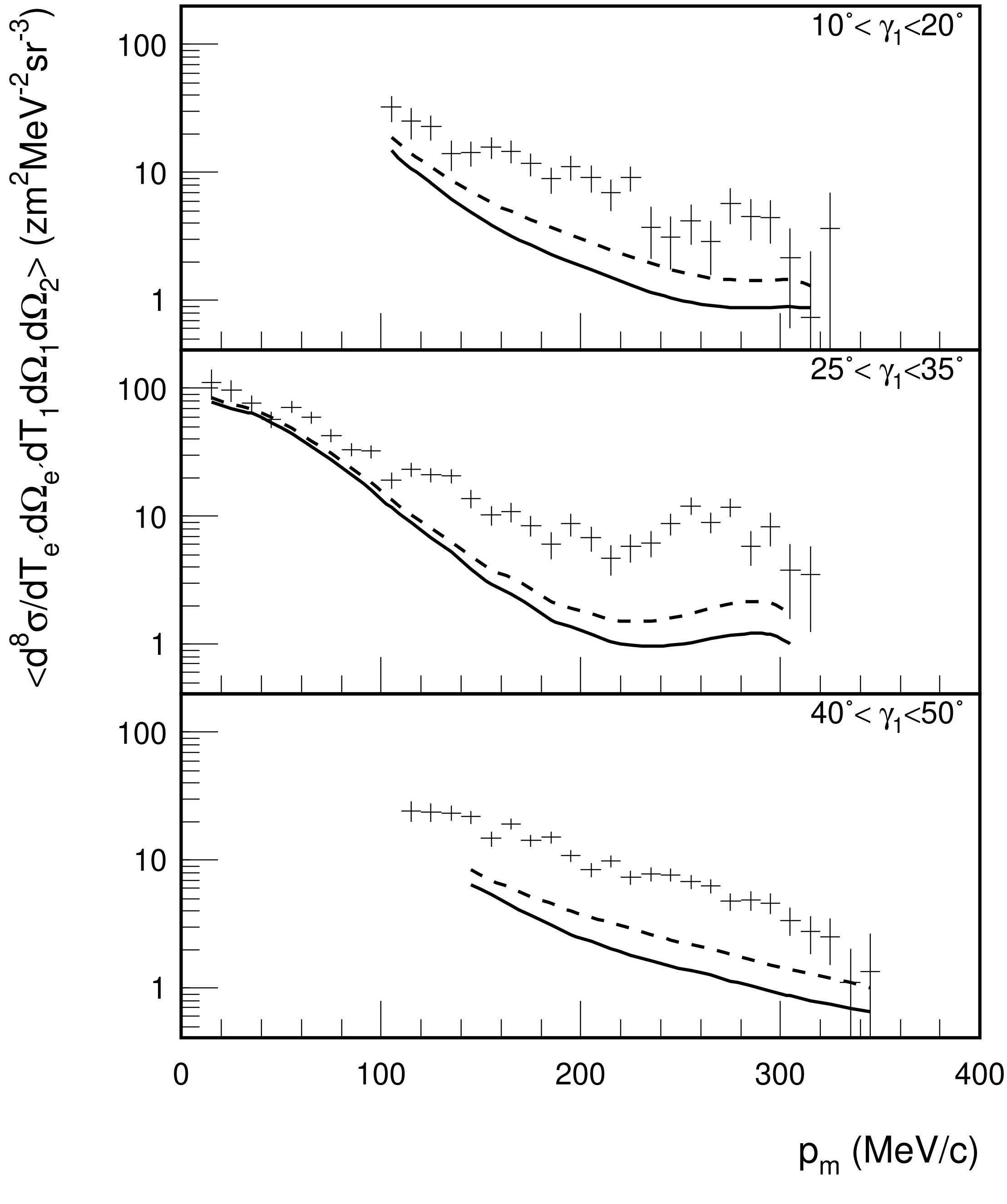

Figure 1-5: Average 8-fold differential cross sections for NIKHEF's ^{3}He(e,e'pp)n data with (q, ω) = (305 MeV/c, 220 MeV) as a function of missing momentum. The unit zm is 10^{-21}m. γ_1 is the angle between the first proton and the momentum transfer. The solid(dash) curves are continuum Faddeev calculations without(including) MEC effects [11, 25].

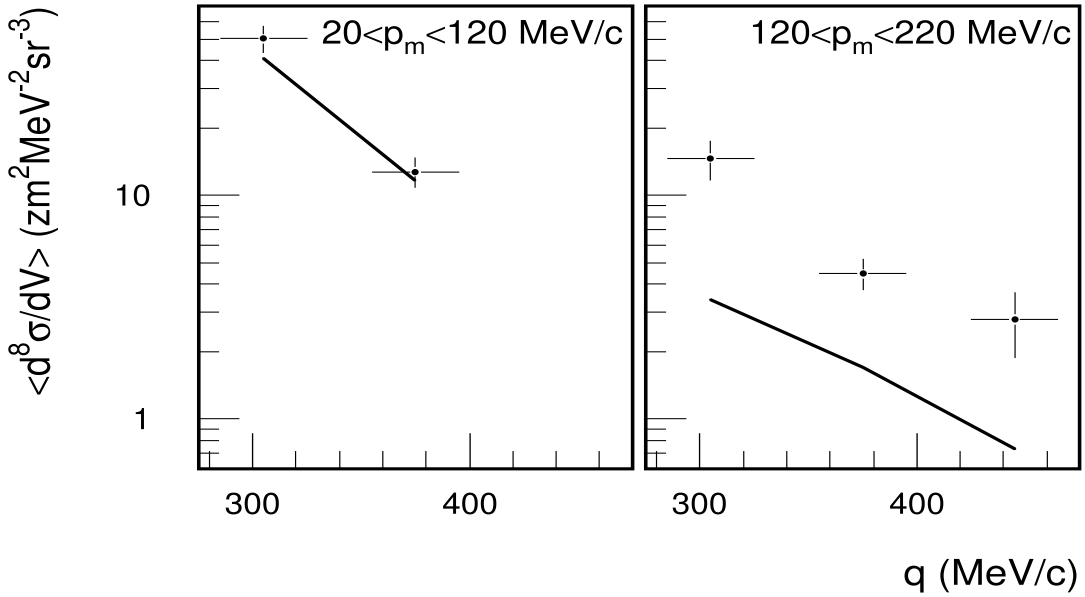

Figure 1-6: Average differential cross sections of NIKHEF's ^{3}He(e,e'pp)n data for different values of q with $\omega = 220$ MeV. The unit of zm is 10^{-21}m. The curves are continuum Faddeev calculations with a one-body hadronic current [11, 25].

believed to be most sensitive to short-range correlations. Although the VMC calculation using the AV_{14} potential [37] is closer to the data than is the calculation using the 0.6 fm hard-core [38], it turns out calculations without short range correlation functions, but with Δ effects instead [37] also agree with data at the same level. It means that in these kinematics, Δ resonance contributions are very large. Other calculations indicate at so-called "super-parallel" kinematics, where one proton is along $\vec{q}$ direction and the other proton is in the direction opposite to $\vec{q}$, the $\Delta^+ p \to pp$ process will be suppressed because the dominant M_{1+} multipole does not contribute in these kinematics if one disregards Fermi motion [64].

A high-resolution ^{16}O(e,e'pp)^{14}C measurement was also performed at MAMI at "super-parallel" kinematics, with beam energy 855 MeV, $\omega = 215$ MeV, $q = 316$ MeV/c [19]. The resolution is high enough to separate different excited states of the residual nucleus. It is the $^1S_0$ proton pair configuration that is expected to be

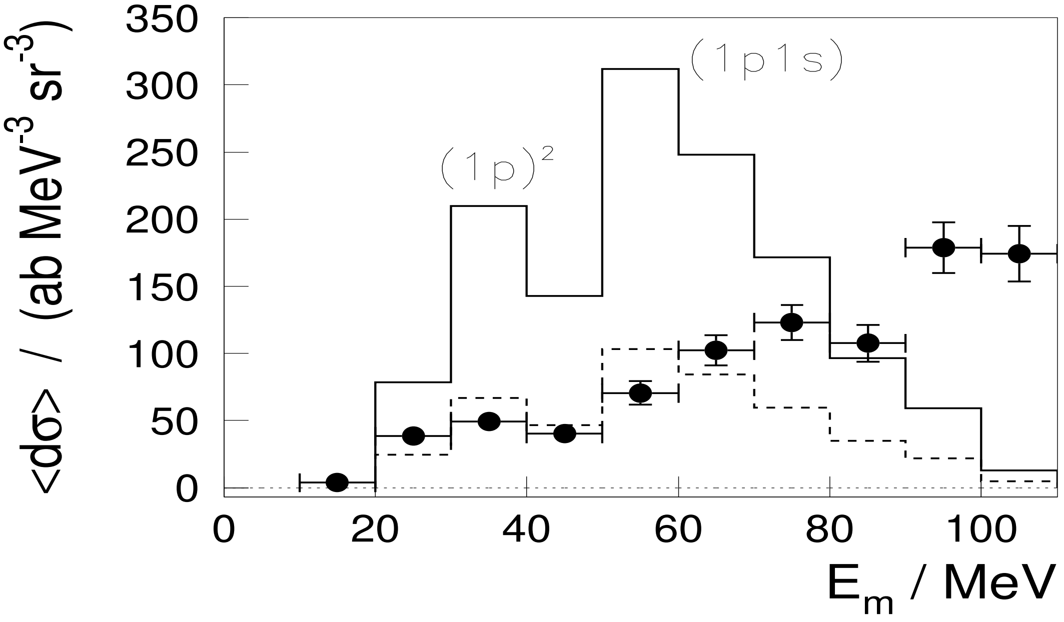

Figure 1-7: Average 9-fold differential cross section for MAMI's ^{12}C(e,e'pp) data as a function of missing energy [19]. The unit ab is 10^{-18}b. Dots denote data, solid line is 0.6 fm hard-core calculation [38] and dash line is soft-core (VMC) calculation using the AV_{14} potential [37].

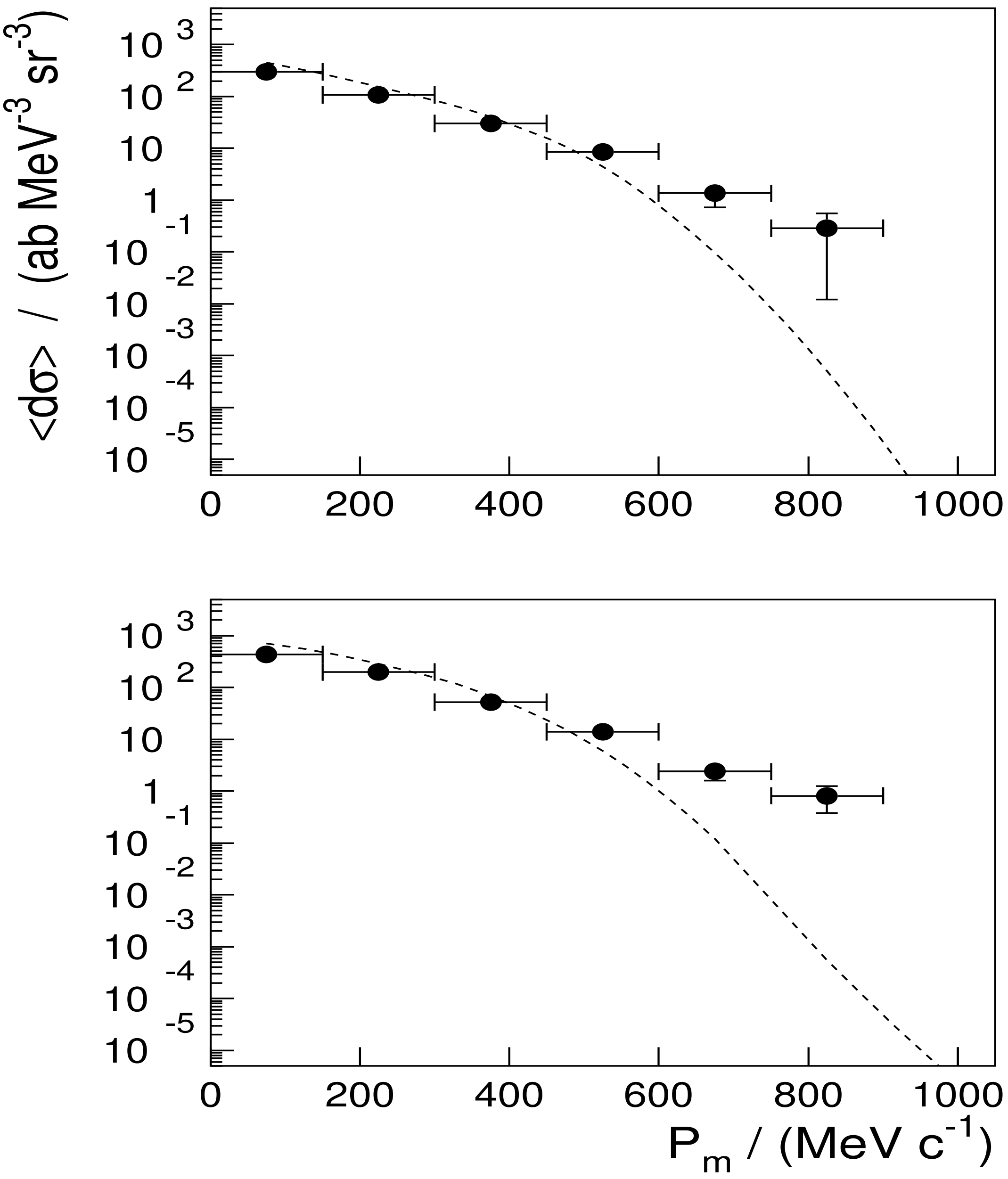

Figure 1-8: Average 9-fold differential cross section for MAMI's ^{12}C(e,e'pp) data as a function of missing momentum for $E_m < 50$ MeV (upper) and $E_m < 70$ MeV (lower) respectively [19]. The unit ab is 10^{-18}b. Dots denote data and dash line is soft-core (VMC) calculation using the AV_{14} potential [37].

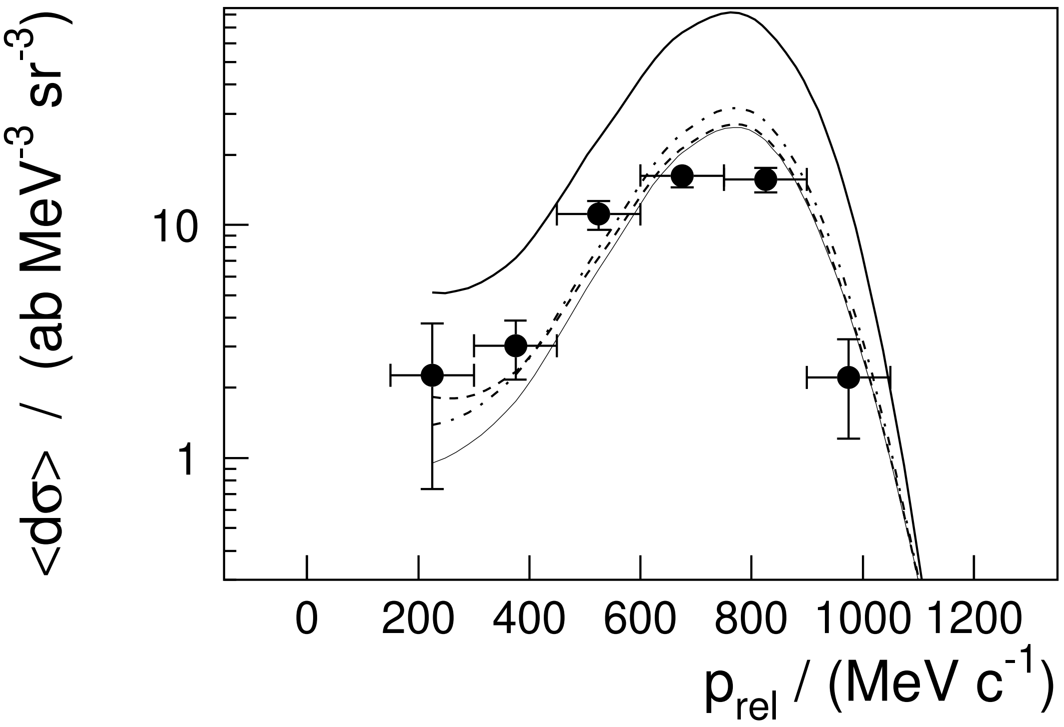

Figure 1-9: Average 9-fold differential cross section for MAMI's ^{12}C(e,e'pp) data as a function of relative momentum for $E_m < 70$ MeV [19]. The unit ab is 10^{-18}b. The dots denote data, the thick solid line is 0.6 fm hard-core calculation [38], the dashed line is soft-core (VMC) calculation using AV_{14} potential [37], the dash-dotted line is another soft-core (G-matrix) calculation [42] and the thin solid line is turning off SRC and including Δ resonance [37].

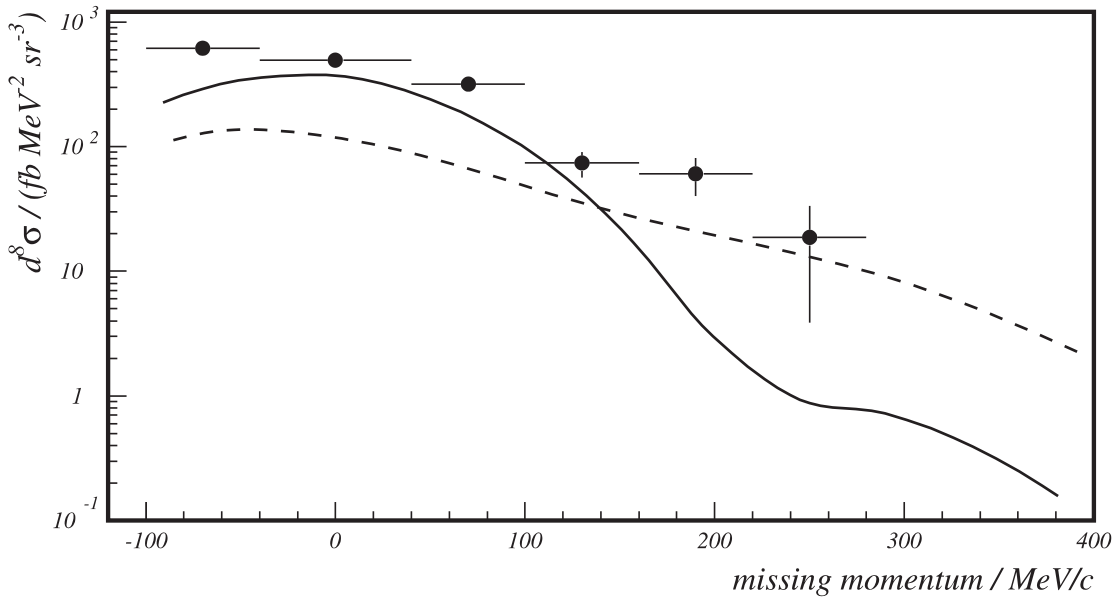

Figure 1-10: The missing momentum distribution for MAMI's measurement of ^{16}O(e,e'pp)^{14}C [19]. The unit fb is 10^{-15}b. Dots denote data, solid line is Pavia's unfactorized calculation [9] and dash line is Gent's calculation using G-matrix to account for SRC [61].

most sensitive to SRC. According to unfactorized calculations for ^{16}O(e,e'pp) [9], the ground state of ^{14}C is mainly populated via the emission of a $^1S_0$ proton pair for low missing momentum. Fig. 1-10 shows the missing momentum distribution for ^{16}O(e,e'pp)^{14}C. One can see reasonable agreement between the data and the theory with the ground state missing momentum smaller than 150 MeV/c, the region of predominant $^1S_0$ proton pair emission. The calculations fall short at higher momenta, where emission of $^3P_1$ proton pairs should become important, which is dominated by two-body currents such as MEC and Δ resonance.

Generally speaking, MAMI data are in favor of the VMC soft-core calculation using AV_{14} potential compared to the calculations using 0.6 fm hard-core correlation functions. This indicates the short range correlation (SRC) functions are more likely "softer" than the 0.6 fm hard-core. However, because of the big influences of two-body mechanisms such as meson exchange currents (MEC), isobar currents (IC) and final state interactions (FSI), one's confidence in SRC effects is significantly undermined, especially in regions of large missing momentum and high missing energy. This makes it very difficult to test different NN potentials with different approaches of accounting for the correlation functions. In fact, NIKHEF data was compared to calculations using different potentials such as Bonn-B, CD-Bonn, Nijemegen-93 and Argonne AV_{18}; MAMI data was compared with soft-core calculations using the Argonne AV_{14} potential as well as the G-matrix approach (the results can be found in [46], [19]). It turns out that all those potentials are close to the data and their differences cannot be distinguished with the considerable presence of other competing processes. Both NIKHEF and MAMI data showed that it is more promising to access "cleaner" reactions in the region of small missing momentum and low missing energy where the residual system is believed to be not so actively involved in the reaction.

1.3 About This Experiment

In summary, the (e,e'NN) reaction is a good tool to investigate the short range behavior of nucleons inside nuclei. However, there are many other effects besides SRC which can contribute considerably such as FSI, MEC, Δ resonance, etc. In most circumstances, these "contamination" effects are quite big and almost obscure the SRC effects. As a result, it is very difficult to single out the SRC sensitive part in the data and study it in detail to see what kind of theoretical approach can best account for the SRC. One important question is under which kinematic conditions other effects are relatively small and the process is sensitive to SRC. We also try to answer this question in this experiment. NIKHEF and MAMI data indicate that the region of small missing momentum and low missing energy is a good place to start. In addition, large momentum transfer may decrease FSI and MEC contributions.

This experiment was performed in spring of 1999 at Jefferson Lab using the CLAS detector with close-to-4π geometrical acceptance. We focused on studying the two-nucleon knockout (e,e'pp) and (e,e'pn) reactions on ^{3}He, ^{4}He and ^{12}C with incident electron energies of 2.261 and 4.461 GeV. With larger momentum transfers compared with previous NIKHEF and MAMI data, we hoped the MEC and FSI effects might be smaller. Fig. 1-11 shows one example of the kinematical coverage of our data (four momentum transfer Q^2 vs energy transfer ω). Besides searching for signatures of short range correlations, we also tried to explore potential differences in different nuclei and at different Q^2. This is a survey experiment. With our data, we hoped we could be able to provide a testing ground for theoretical calculations, as well as a guideline for further experimental and theoretical efforts.

In chapter 2, I will describe the experimental setup including Jefferson Lab and the CLAS detector. Chapter 3 is devoted to the description of the procedure and the techniques used to analyze the data. Finally, in chapter 4, the results of the measurements will be presented, discussions and conclusions will be provided.

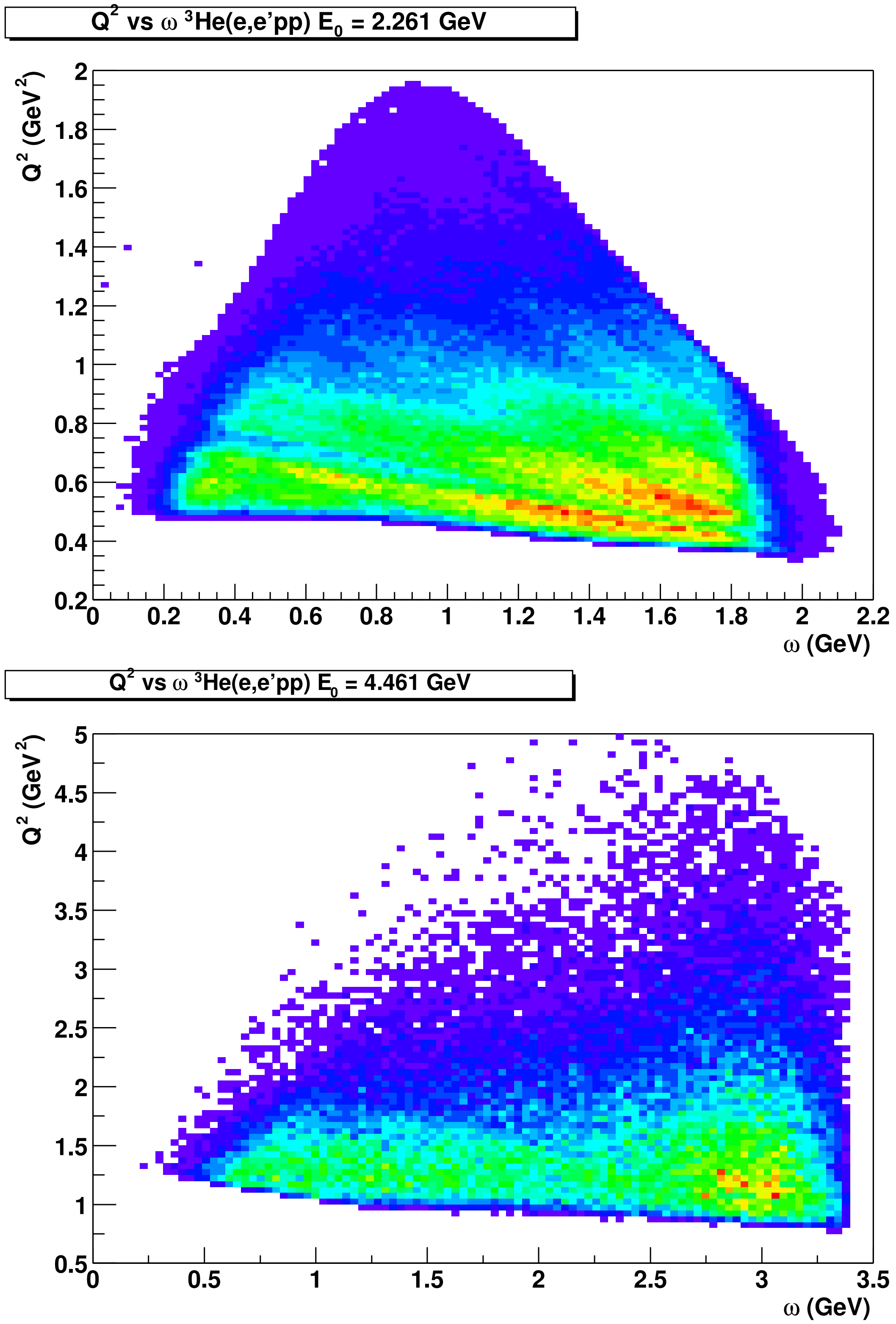

Figure 1-11: Four momentum transfer Q^2 vs energy transfer ω for ^{3}He(e,e'pp) with the incident electron energies of 2.261 and 4.461 GeV.

Chapter 2

Experimental Setup

2.1 Thomas Jefferson National Accelerator Facility

Thomas Jefferson National Accelerator Facility (TJNAF or JLab) is a U.S. Department of Energy's national laboratory for nuclear physics research. The laboratory is located in Newport News, Virginia, United States. As a user facility for university scientists worldwide, its primary mission is to conduct basic research of the atom's nucleus. With industry and university patterns, it has a derivative mission as well: applied research for using Free Electron Lasers. As a center for both basic and applied research, Jefferson Lab also reaches out to help educate the next generation in science and technology.

JLab has an electron accelerator which is capable of delivering high quality continous wave electron beams of up to 5.5 GeV. Currently an upgrade to 12 GeV project [50] is anticipated and the machine is eventually upgradable to 25 GeV. In the injector a photocathode gun and an RF chopping system operating at 499 MHz are used to develop a 3-beam 1497 MHz electron bunch train. Every third bunch is for one of the three experimental halls (Hall A, Hall B and Hall C). The beam from the injector is accelerated through a recirculating beamline in a "racetrack" configuration, with two linacs, each of about 550 MeV, joined by two 180^o arcs with a radius of 80 meters. Twenty cryomodules, each containing eight superconducting niobium cavities and cooled by liquid helium at 2 degrees Kelvin, comprise each of the two linacs. The acceleration by the cavities can be up to 5 MeV per meter. Subsequent passes through the accelerator are phased to maximum energy gain by adjusting the length of travel in the dogleg section of the preceding arc. Five passes of acceleration can reach to the energy of about 5.5 GeV. The energy spread of the beam is $\Delta E/E < 10^{-4}$. Beam is directed into three experimental halls (Hall A, Hall B and Hall C) by magnetic or RF extraction. The accelerator can deliver beams of high polarization and high current to Hall A and Hall C, while maintaining high polarization low current beam delivery to Hall B. Fig. 2-1 shows a schematic of the machine.

The three experimental halls are equipped with spectrometers for complementary physics programs. Hall A houses two High Resolution Spectrometers (HRS) with $\Delta p/p \simeq 3 \times 10^{-4}$, and a momentum range from 0.3 to 4.0 GeV/c. The system covers a solid angle of about 6 msr with a 0.3 mrad of angular resolution. Hall A was designed for programs requiring high precision measurements. Hall C, on the other hand, is dedicated to high final momentum programs. It has two magnetic spectrometers of medium resolution of $\Delta p/p \leq 10^{-3}$, but different maximum momentum: the High Momentum Spectrometer (HMS) has a maximum momentum of 7 GeV/c while the Short Orbit Spectrometer (SOS) has maximum momentum of 1.8 GeV/c. The angular acceptance is about 6 msr for HMS and 9 msr for SOS. The angular resolution is in the range of 0.4 to 0.9 mr.

Hall B is the home of CEBAF Large Acceptance Spectrometer (CLAS). Its almost 4π acceptance makes it an ideal device to study exclusive multi-particle final states. It also allows simultaneous measurements of different channels over a broad kinematic range. The CLAS detector is described in more detail in the next section.

Besides the current three experimental halls, a new hall, Hall D, is planned to be

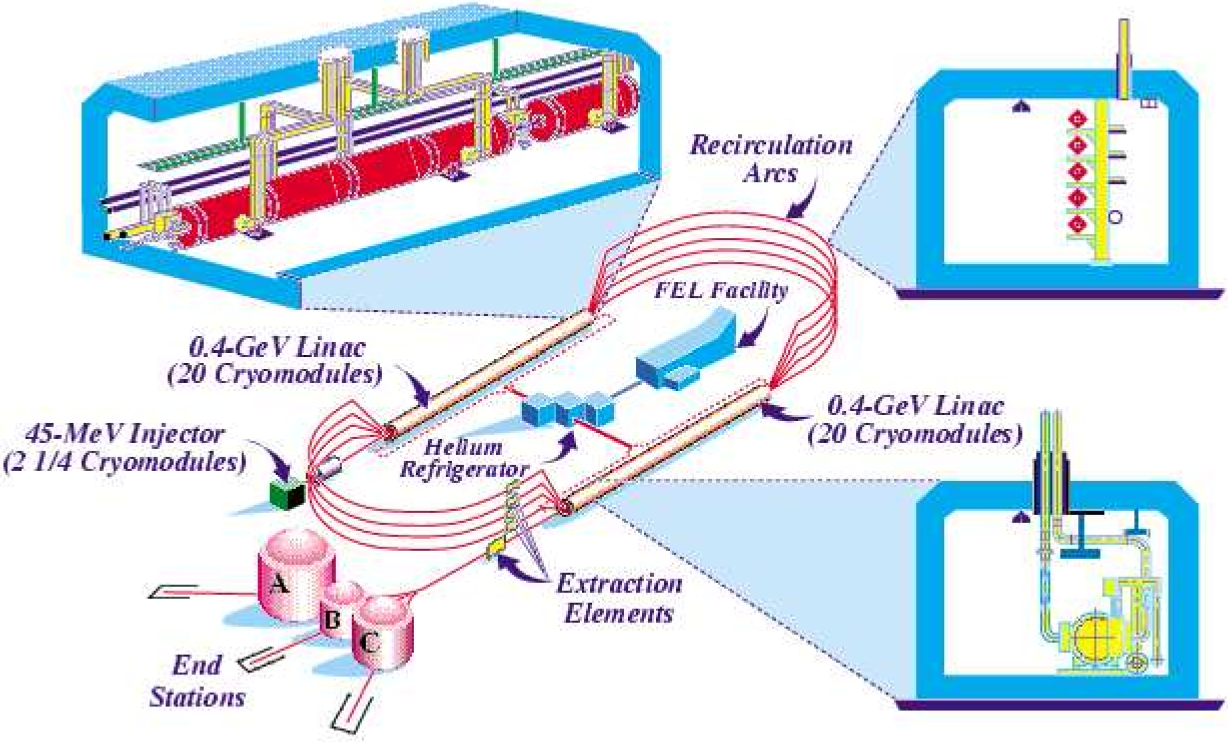

Figure 2-1: Jefferson Lab Machine Configuration. The linacs have been designed as 0.4 GeV, but the energy actually reached about 0.55 GeV at the time of this experiment.

added to Jefferson Lab. It will host a state-of-the-art 4π solenoidal spectrometer to detect the production and decays of mesons produced in photon-induced reactions. The designed photon energy is from 8 to 9 GeV to access the desired meson mass range.

2.2 CEBAF Large Acceptance Spectrometer and Experimental Hall B

2.2.1 General Description

Hall B of Jefferson Lab is equipped with a near 4π acceptance detector, the CEBAF Large Acceptance Spectrometer (CLAS), as shown in Fig. 2-2. Its main advantage is the ability to do exclusive measurements that requires simultaneous detection of several particles in the hadronic final state at limited luminosity ($\sim 10^{34} cm^{-2} sec^{-1}$).

The detector is divided into six sectors forming an orange-like shape with the beamline as its symmetrical axis shown as Fig. 2-3. The sectors are separated by six iron-free superconducting coils producing an approximate toroidal magnetic field with a maximum intensity of 2 Tesla. The size (about 5 meters long and 2.5 meters wide) and the shape of the coils were chosen to optimize them based on the physics programs for fixed target operation using up to 4 GeV electron beams.

The detector components are placed as different layers around a fixed target in the middle of CLAS. The detector has three layers of Drift Chambers (DC). The coils only produce magnetic fields inside the middle layer of Drift Chamber, Region 2. The DC system is used to determine the trajectories of charged particles and measure their momenta. A threshold Čerenkov Counter (CC) and an Electromagnetic Calorimeter (EC) are located in the forward direction and are used to identify electrons. The Scintillation Counters (SC) are used for Time-of-Flight (TOF) measurements for charged particles. Electromagnetic Calorimeters (EC), with a polar angle extension by Large

Angle Calorimeters (LAC) in two sectors, can also do TOF measurements for neutral particles (neutrons and photons). In this experiment, due to calibration problems, we only use EC to detect neutrons in the forward region. The polar angle coverage is $8^o - 140^o$ for DC, $9^o - 140^o$ for SC and $8^o - 45^o$ for EC. The azimuthal coverage of the detector is almost complete except for the gaps between sectors occupied by the magnetic coils.

2.2.2 Drift Chambers

The measurements of the trajectories and the momenta of charged particles are made by using the Drift Chambers [31]. When a charged particle flies through the chambers, it will cause ionization of the gas (90%/10% mixure of Argon and CO_2) in the chambers. With the presence of the electric field created by the wires in the chambers, the electrons and the ions drift in opposite directions and are collected by the anode and the cathode wires. When the electrons drift close to the anode wires where the electric fields become very strong, the electrons can collide with the gas atoms, cause secondary ionization and create an amplification effect. Argon provides a gain of $\sim 10^4$ while CO_2 can prevent uncontrolled avalanches from occuring. When the electrons and the ions reach the anode and cathode wires, the wires produce the electrical signals, from which we can determine the drift time or the shortest distances from the trajectory to the wires (See Fig. 2-4).

The Drift Chambers are located in three radial regions. Region One chambers surround the target in a small volume. Region Two chambers are larger and located in high magnetic fields. Region Three chambers are the largest and out of the magnetic fields (see Fig. 2-5). The wires are located in layers of concentric circles. In each region layers of wires are grouped into two superlayers, one axial to the magnetic field and the other tilted at a 6^o angle to provide stereo information. Each superlayer has six layers (with the exception of superlayer one which is the most inside superlayer and only has four layers) of hexagonal drift cells forming a “brick-wall” configuration.

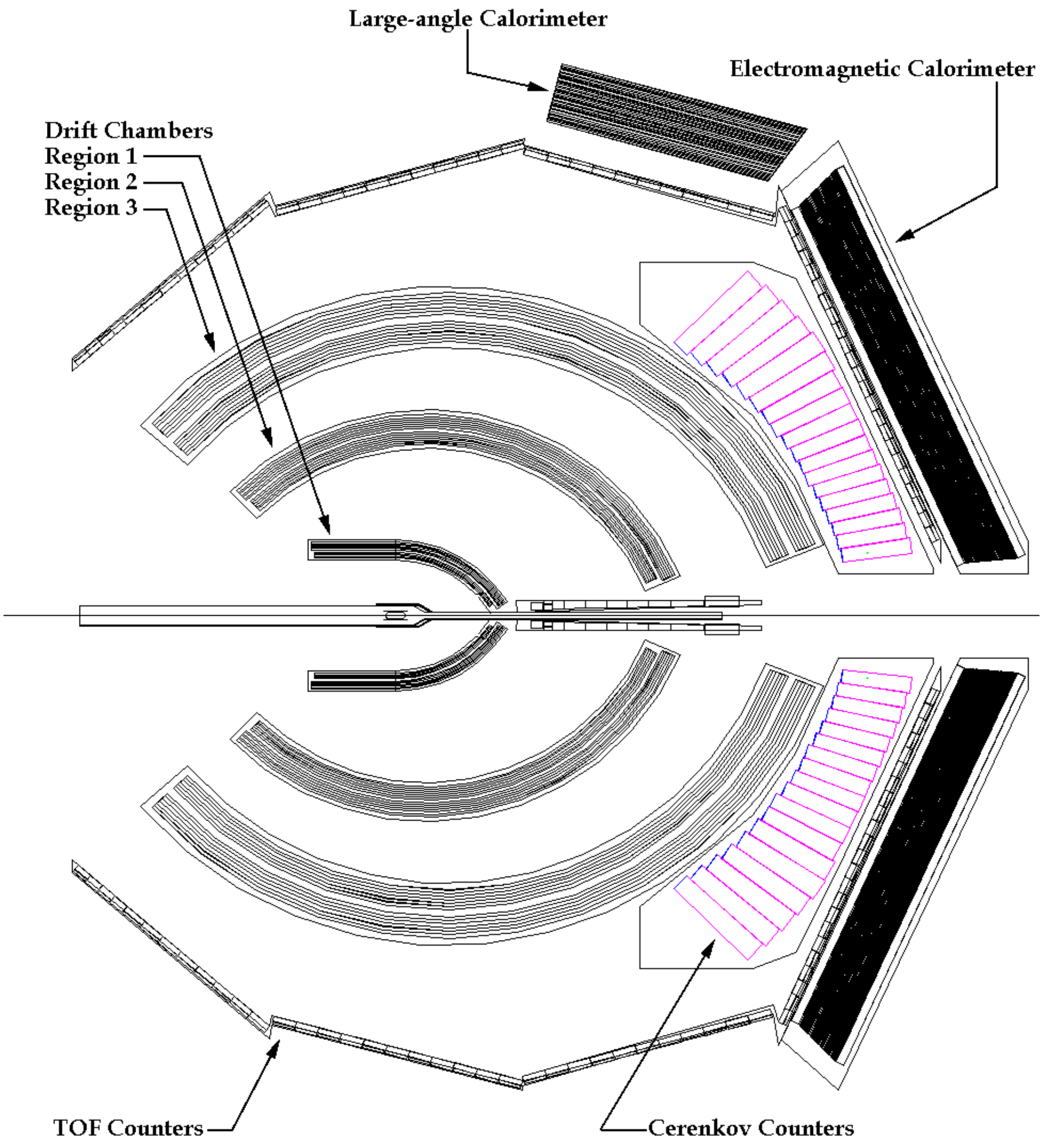

Figure 2-2: CLAS Detector Layout (sliced along the beamline)

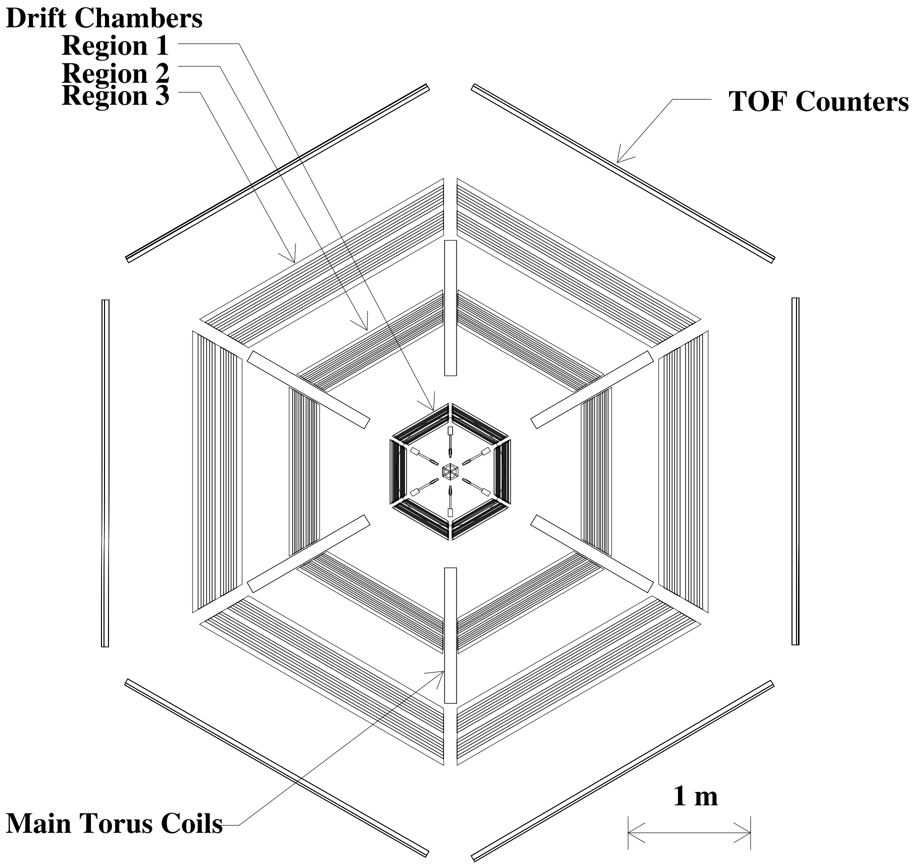

Figure 2-3: CLAS Detector Layout (sliced perpendicular to the beamline)

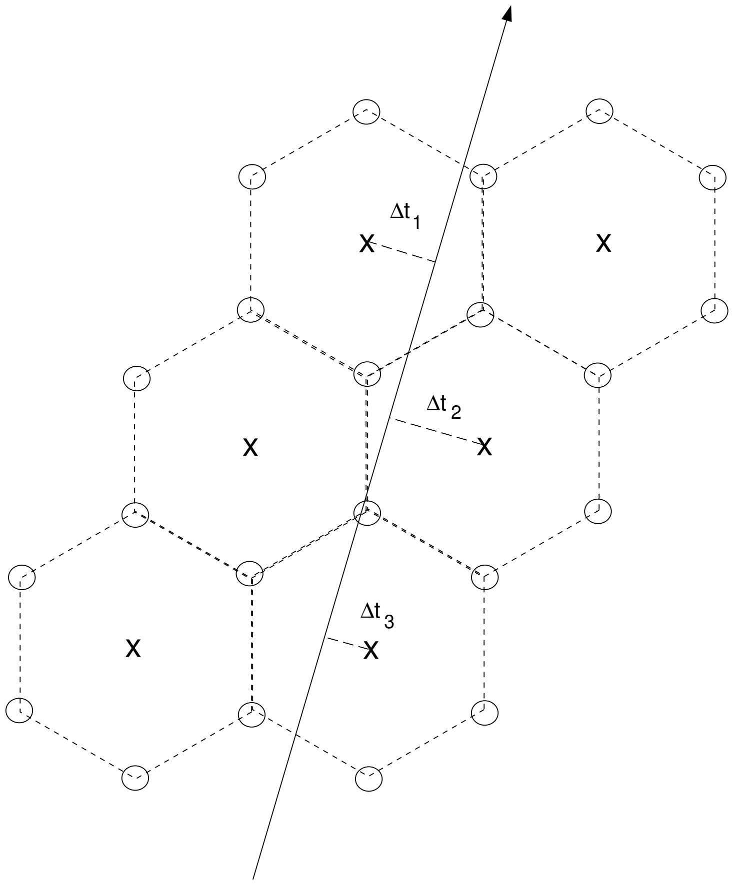

Figure 2-4: A schematic diagram showing a charged particle passing through some portion of the Drift Chambers. The circles represent the field wires and the crosses represent the sense wires. The dashed lines are showed as the boundary of neighboring drift cells. The time for the electrons to drift from the track to the sense wires gives the shortest distances from the track to the sense wires. Only a straight track is shown. If magnetic fields are present, the actual track should not be a straight line.

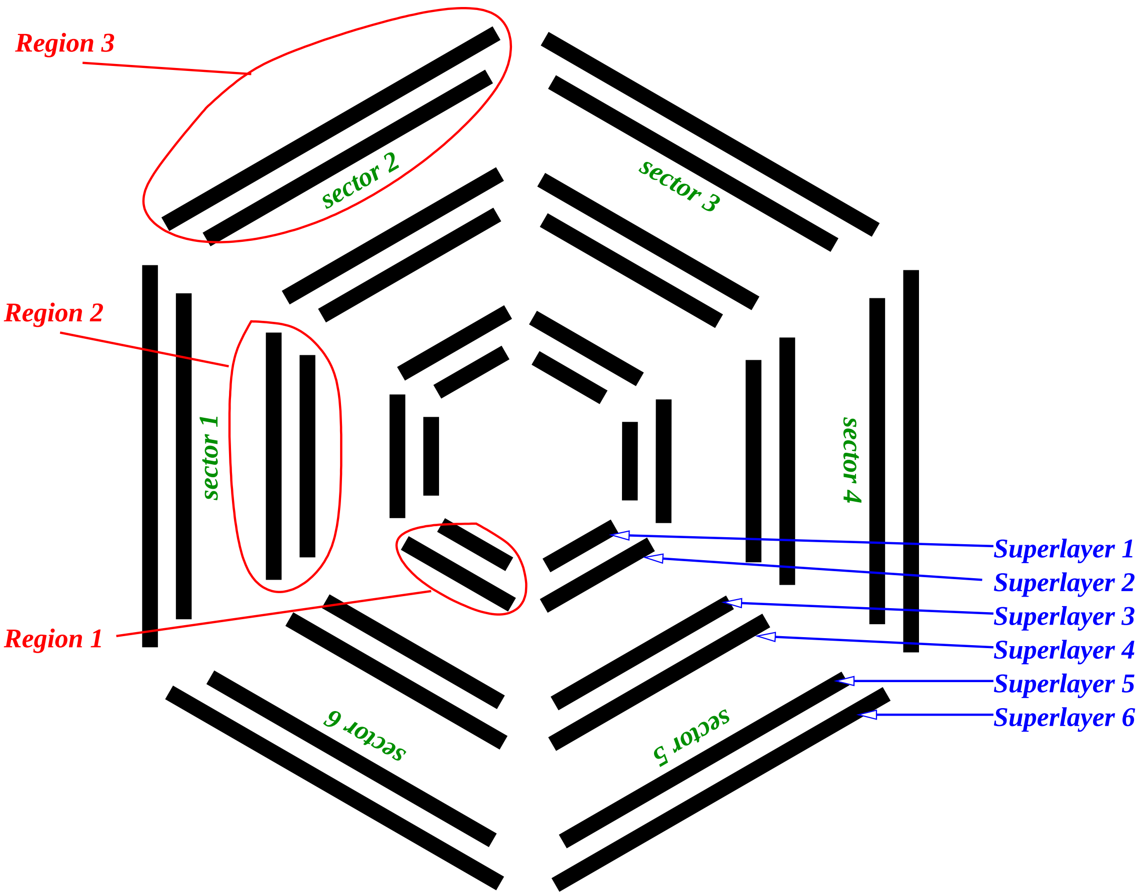

Figure 2-5: A schematic of the drift chambers showing how the regions and the superlayers are named. The beam line is perpendicular to the paper plane and in the direction of coming out.

(See Fig. 2-6) With this wire arrangement and the magnetic field, the resolution is about 400 μm for the trajectory positions, $\leq 1\%$ for the reconstructed momentum and a few mrad for the angles. The tracking efficiency is above 99%.

2.2.3 Čerenkov Counters

The main source of contamination in identifying scattered electrons are negative pions produced in the reaction. To distinguish electrons from pions, CLAS uses threshold Čerenkov Counters [18]. When a particle travels in some medium at a speed greater than the speed of light in that medium, it can emit electromagnetic radiation known

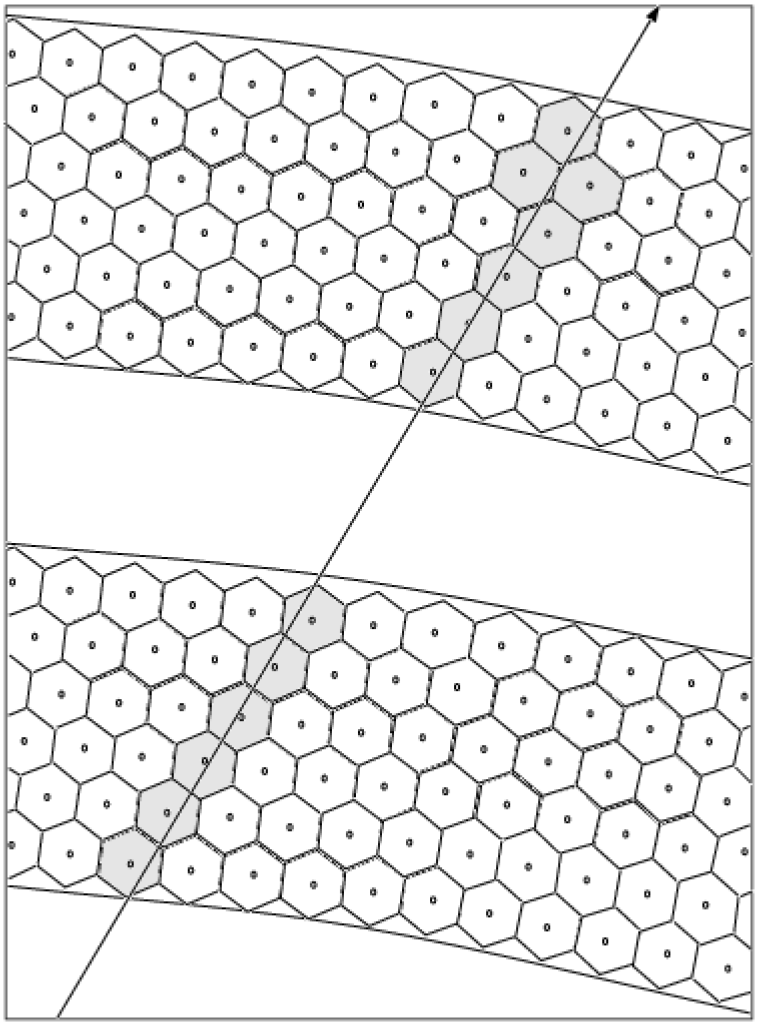

Figure 2-6: A schematic of a part of drift chamber showing two superlayers each consisting of six hexagonal layers. The cells are electrostatic boundaries determined by field wires located at each corner of the hexagon. A charged particle is shown crossing the drift chamber, with the shadowed area indicating the hit cells.

as Čerenkov light. The threshold for producing Čerenkov light is $\beta = 1/n$, where n is the index of refraction for the medium. CLAS Čerenkov Counters use perflurobutane gas, C_4F_{10}, as the medium. This gas is easily purified, ten times heavier than air, non-flammable and ultra-violet light transparent. Its refraction index $n = 1.00153$, which corresponds to the energy threshold

$$E = m\gamma = \frac{m}{\sqrt{1-\beta^2}} = \sqrt{\frac{n}{n-1}}m = 18.09m \tag{2.1}$$

where m is the mass of the particle. So the energy threshold is 9.24 MeV for electrons and 2.51 GeV for pions. The requirement of Čerenkov signals in electron identification can get rid of contaminating pions with energies smaller than 2.51 GeV. For pions with energies larger than the threshold, other techniques are used to minimize the contamination (See Section 3.3.1).

CLAS Čerenkov Counters have six identical counters, one for each sector. Each counter has two side walls mounted in the planes of CLAS main magnetic coils and a partial cylindrical piece at the vertex near the beamline. The entrance window is made of 10 μm mylar with 2 μm Tedlar (a trademark of DuPont Corporation) on either side. The whole system is gas sealed with C_4F_{10} at 0.2% above atmosphere pressure.

Because of CLAS toroidal magnetic fields, particles almost do not change their azimuthal angles. The optical system in the Čerenkov Counters can focus the light produced by the particles with different azimuthal angles and the same polar angle to a point. The focal area is equipped with an array of photomultiplier tubes (PMTs) positioned in the shadow of the coils. In the optical system, there are three types of mirrors: elliptical, hyperbolic and cylindrical. The Čerenkov light is reflected by those three types of mirrors in order then collected by the PMTs (See Fig. 2-7). The average number of photo-electrons collected is about seven and the inefficiency is in the order of 10^{-3}.

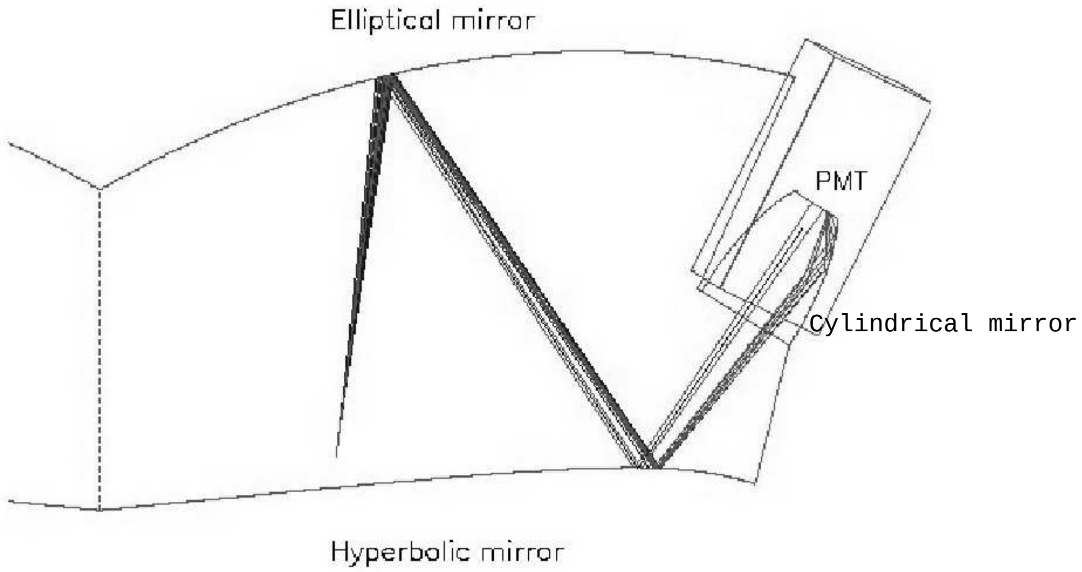

Figure 2-7: A Čerenkov Counter segment. Čerenkov light is reflected by elliptical, hyperbolic and cylindrical mirrors in order then collected by the PMTs.

2.2.4 Time of Flight System (Scintillation Counters)

The time of flight (TOF) system [16] measures the time during which a particle flies from the reaction vertex in the target through the drift chambers and hits the scintillation counters (SC). The velocities of the particles are then determined as

$$\beta = \frac{L}{ct} \tag{2.2}$$

where L is the path length from the target to SC and determined by the trajectory in Drift Chambers, c is the speed of light and t is the time of flight. The time of flight t is determined by t_{sc}, the time when the particle hits the SC and t_{tr}, the trigger time or the vertex time.

$$t = t_{sc} - t_{tr} \tag{2.3}$$

We have electrons as triggers, so the trigger time can be calculated as

$$t_{tr} = t^e_{sc} - \frac{L^e}{\beta^e c} \tag{2.4}$$

where β^e is 1 because the mass of the electron is very small and the energy of the electron is very large. Once the velocities of the particles are known, combined with the momenta information measured by the drift chambers, we can easily get the masses of the particles as

$$m = \frac{p}{\beta\gamma} = \frac{p\sqrt{1-\beta^2}}{\beta} \tag{2.5}$$

The scintillation counters are located between the Čerenkov counters and the forward electromagnetic calorimeters. They are Bicron BC-408 scintillation bars oriented in the azimuthal direction. The bars are 5 cm thick, 15 or 22 cm wide which can cover about 1.5^o of the polar angle and their lengths vary from 32 cm at small polar angles to 4.5 m at large polar angles. In each sector, 57 bars are grouped and mounted on four panels perpendicular to the sector's mid-plane as shown in Fig. 2-8. Each of the first 39 bars has one PMT at either end while the last 18 bars share 9

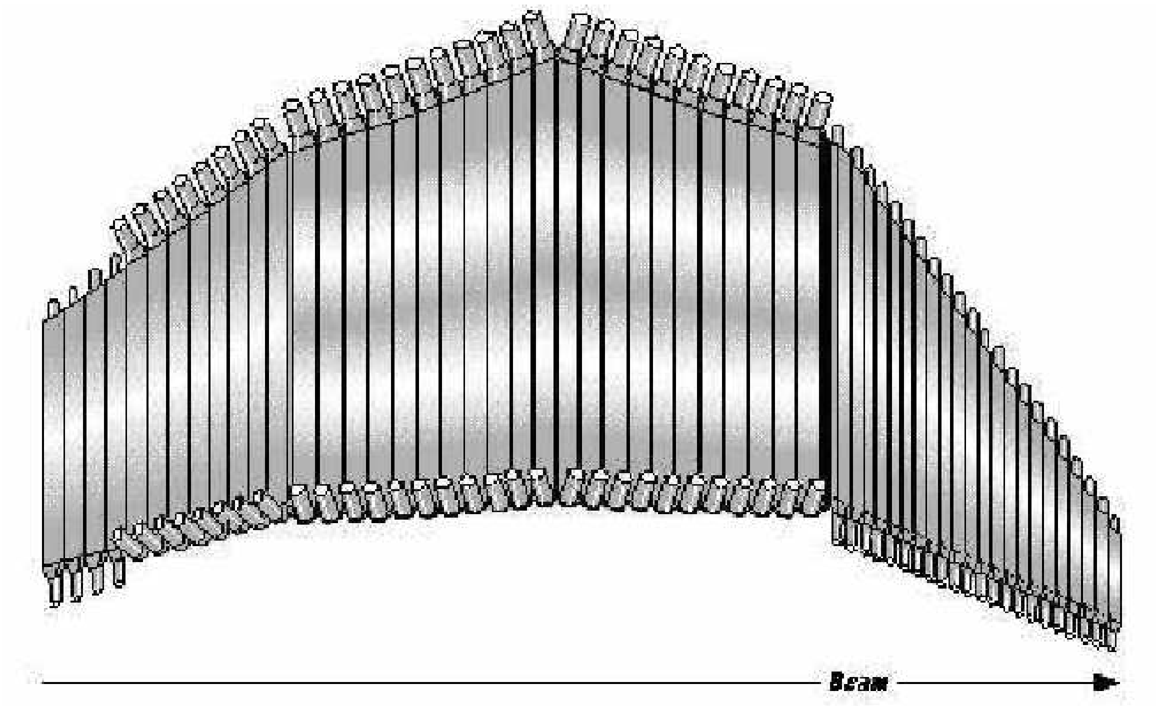

Figure 2-8: TOF bars in one sector

pairs of PMTs. The overall time resolution is about 150 ps.

Besides measuring the time, Scintillation Counters can also measure the energy deposited in the scintillation bars by particles. This helps to identify the particle types. A typical example is the energy deposit for positive hadrons as shown in Fig. 2-9. One can clearly see the proton band on the top and the pion band at the bottom.

2.2.5 Electromagnetic Calorimeter

The electromagnetic calorimeter (EC) [30] is made of alternating layers of 10 mm thick scintillator sheet and 2.2 mm thick lead sheet as shown in Fig. 2-10. In each sector, there are 39 layers stacked to top of each other, with the shape of the equilateral triangle. Each scintillation layer is made of 36 strips of BC-412 scintillators alligned parallel to one side of the triangle. The bars orientation rotates by 120^o in each

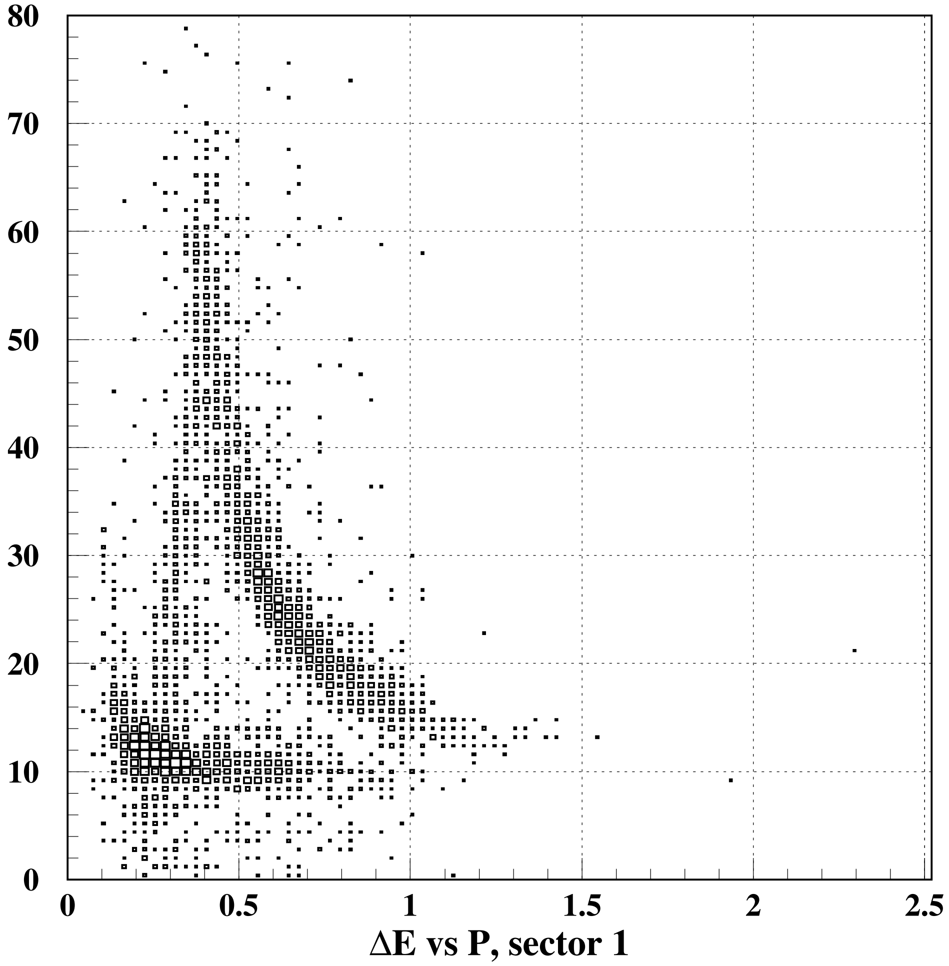

Figure 2-9: SC Energy Loss vs Momentum for positive hadrons. The top band is protons and the bottom band is pions.

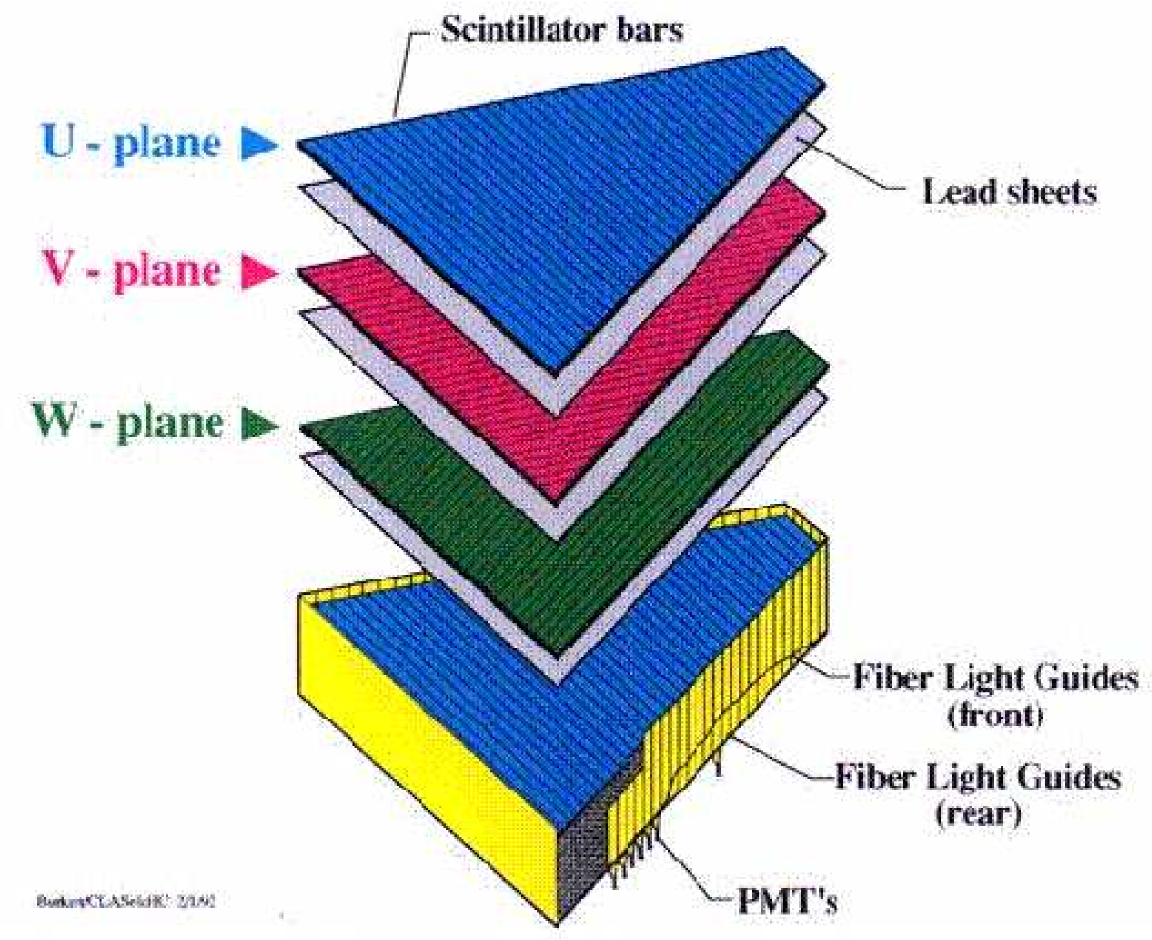

Figure 2-10: Electromagnetic Calorimeter layers. U, V, W label three orientation of the scintillator bars. Only 3 layers are shown here and there are actually 39 such layers stacked to top of each other.

consecutive layer. Therefore, there are 13 stacks of “sandwiches”, each consisting of 3 layers of scintillators with lead sheet between them. Furthermore, they are divided into an inner group (5 stacks) and an outer group (8 stacks), to provide longitudinal sampling.

Light guides and fibers are attached to one end of each scintillator bar and the fibers run into photomultiplier tubes (PMTs) (See Fig. 2-11). A particle hitting the EC produces a shower in the lead, which creats light in the scintillators. The light is guided through fibers and collected by the PMTs. Then the signals produced by

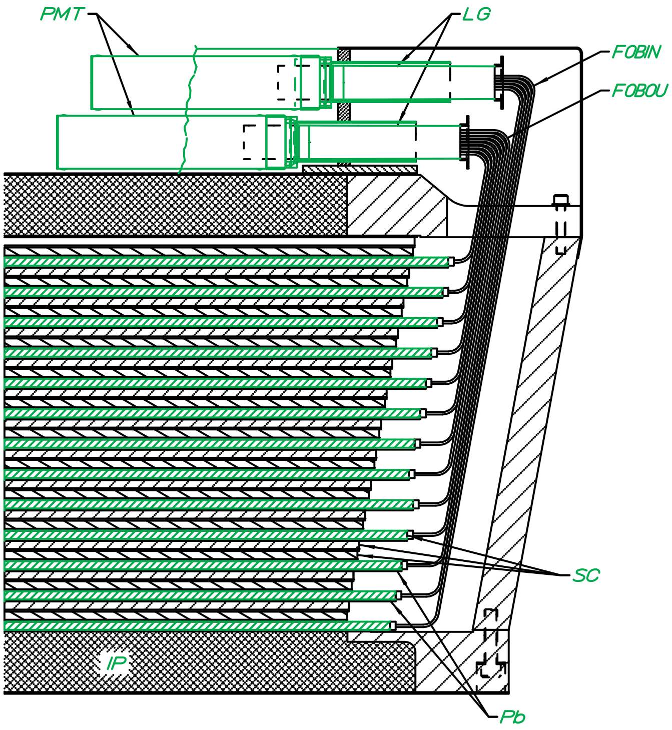

Figure 2-11: Electromagnetic Calorimeter readout. Scintillators with the same orietation and strip number within inner or outer layer are sharing one read out channel.

the PMTs are sent to the ADC (analog-digital converter) and TDC (time-digital converter) boards. The sampling fraction, or the fraction of the shower energy collected by the EC, is about 0.3.

EC's overall position resolution is about 2.3 cm. The energy resolution is

$$\frac{\Delta E}{E} = 0.003 + \frac{0.093}{\sqrt{E(GeV)}} \tag{2.6}$$

The time resolution for electrons is about 200 ps, while that for neutral particles is about 600 ps [30]. Neutral hits are identified by absence of matching DC tracks and SC hits. The separation of the neutrons and the photons is merely based on their velocities up to the momentum of 2 GeV/c.

2.2.6 Targets

In this experiment, we used cryogenic ^{3}He and ^{4}He targets and solid CH_2, ^{12}C and ^{56}Fe targets. The cryogenic targets were cooled to liquid by liquid helium. The targets consisted of a cylindrical target cell, 4 to 5 cm long, with entrance and exit windows made of aluminium and a heat shield. (See Fig. 2-12 and Fig. 2-13.)We used four different target cells during the experiment. Due to the difficulty of keeping the helium cold enough as liquid, we experienced several target cell explosions. The first cell was made from a single piece of aluminium, while the other cells had a cylindrical part made of kapton. The target cells were not removable and stayed in the beam during the run. The solid targets were thin square plates with dimensions of $0.9 \times 0.9(cm^2)$ and thickness varying from 0.15 mm to 1 mm. A mechanical handler was used to flip the solid targets into and out of the beam.

2.2.7 Data Acquisition and Monitoring

The Data Acquisition System (DAQ) of CLAS is a very complex system consisting of read-out electronics for each detector component, central computers and the associated softwares. The scheme of the DAQ is shown in Fig. 2-14. The DAQ system was designed by the CODA group of Jefferson Lab and the DAQ group of CLAS.

The signals from the CLAS detectors, forming an event pretrigger, pass through the pretrigger discriminator, whose thresholds are programmed according to each experiment's requirments. If the conditions of the pretrigger are satisfied, a signal is passed to the Level-1 trigger, which has the final configuration of the event trigger. The Level-2 trigger, which selects events with at least one track (a electron candidate) in the drift chambers, was not implemented at the time of this experiment. If the Level-1 trigger requirements are satisfied, the signal is passed to the Trigger Supervisor, which communicates with 17 FASTBUS crates. Then Data signals are read

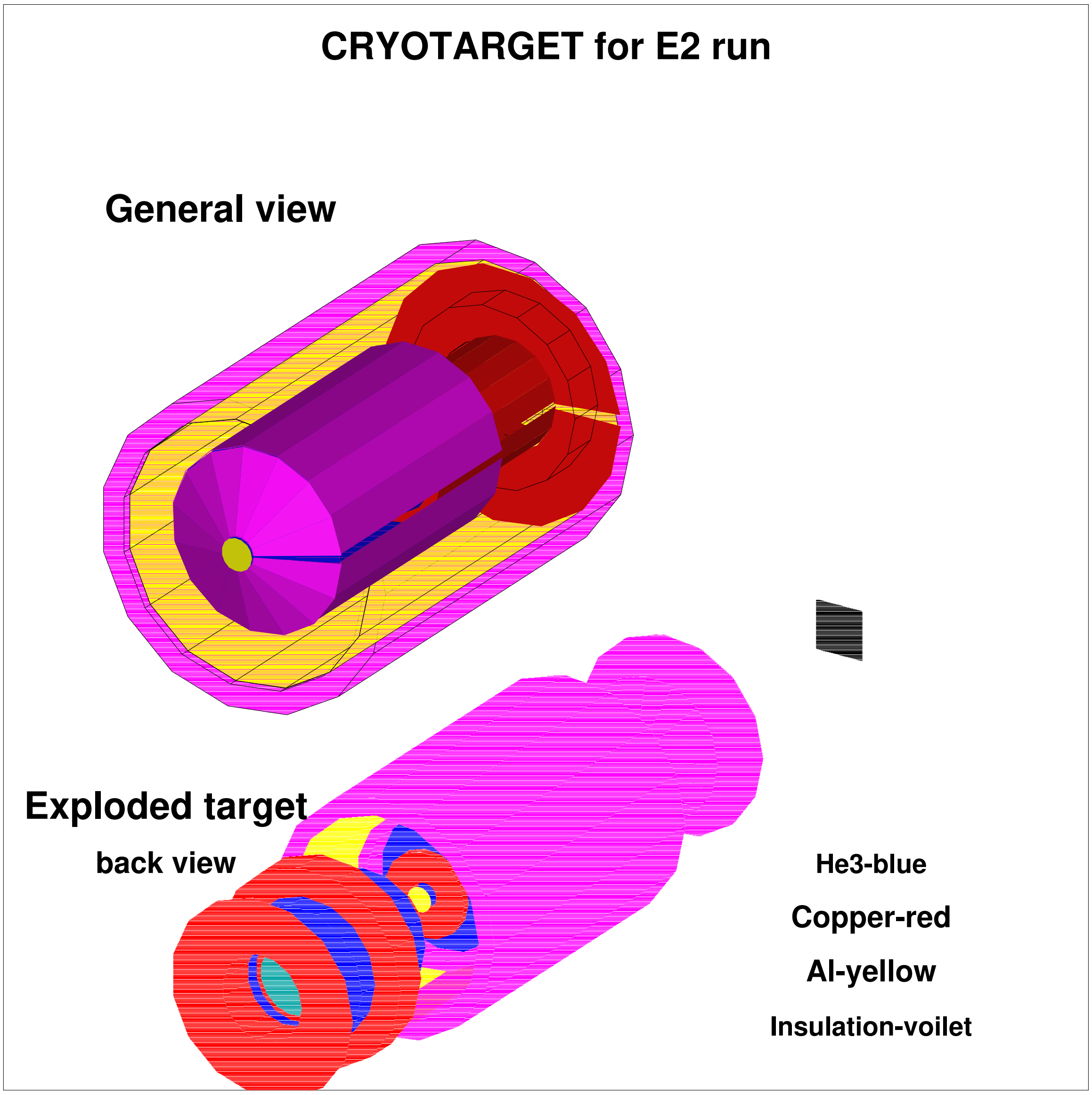

Figure 2-12: E2 cryogenic target

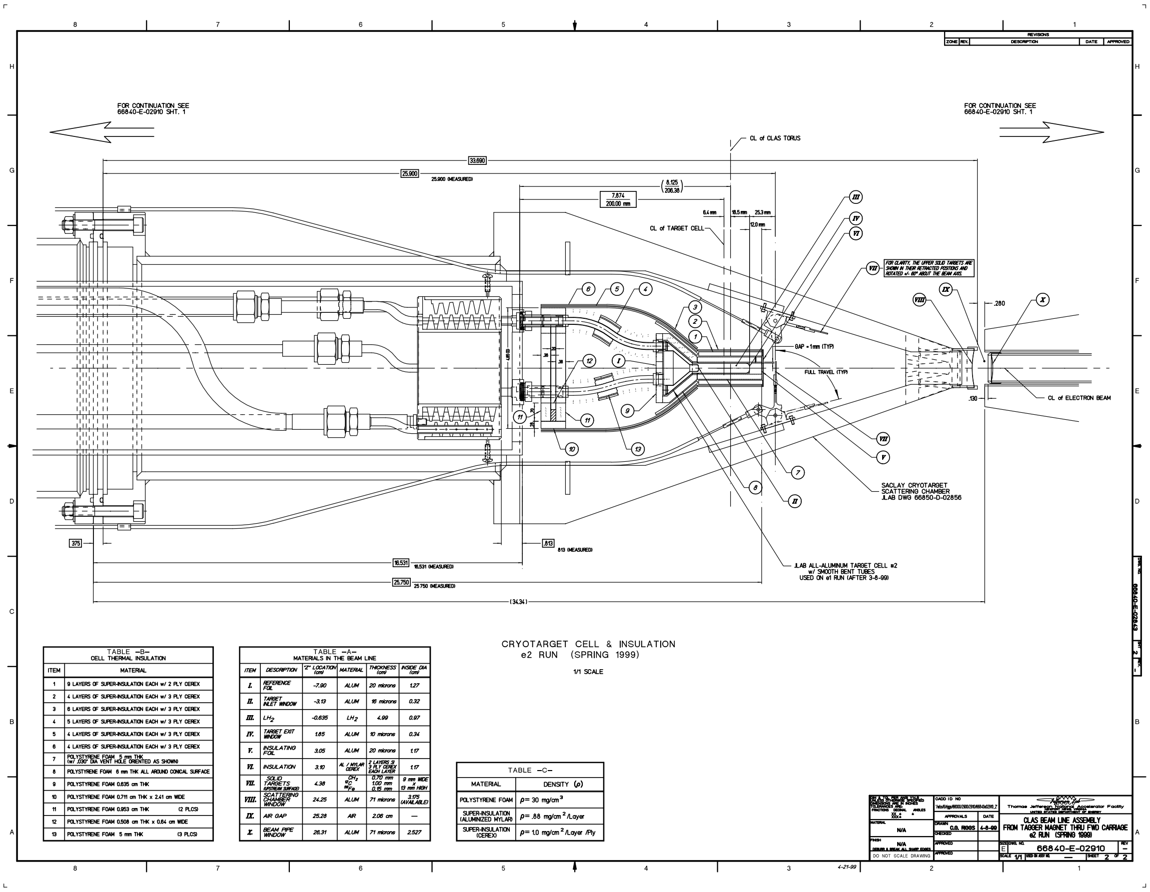

Figure 2-13: E2 cryotarget tech drawing

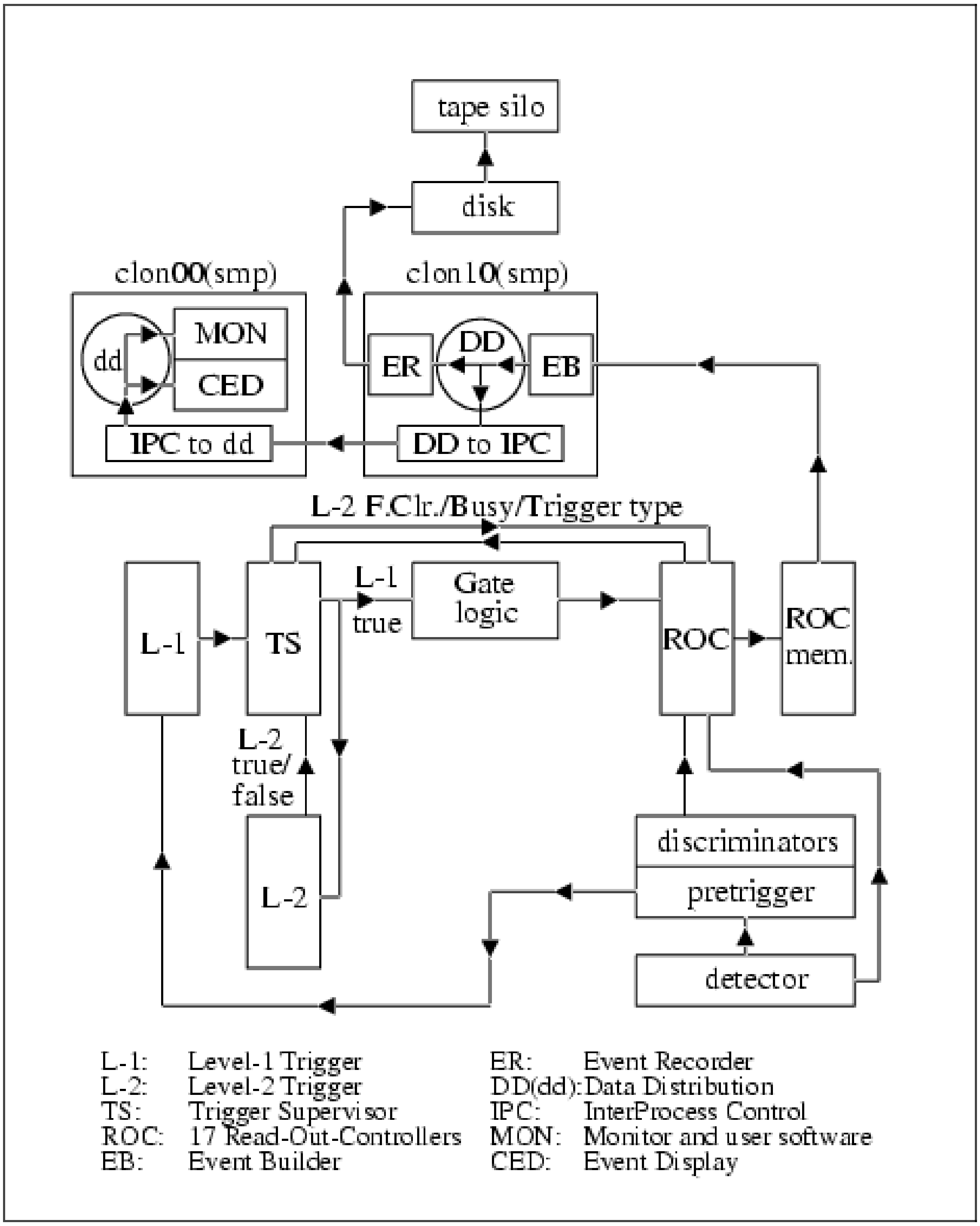

Figure 2-14: Data Acquisition System of CLAS

out, digitized and transferred through the Read-Out-Control (ROC) memories and the network to the Event Builder, then through the main Data Distribution shared memory to the Event Recorder and finally written to the local disks and the tape silo [55]. During this experiment, the luminosity was $\sim 10^{34} cm^{-2} s^{-1}$ and the DAQ system was able to record data at a frequency of 2000 Hz with a live time of about 95%.

For online monitoring purposes, the main Data Distribution system picks up events from the data stream at a frequency of 20 Hz and transfers them to a satellite computer on which the monitoring programs are running. The detector status, beam and data quality were continuously monitored in real time during the data taking. The most important run conditions were stored in the online database and available for inquiry during the data analysis.

Chapter 3

Data Analysis

3.1 Data Processing Overview

CLAS reconstruction software (RECSIS) has several packages whose functions are to analyze the information for single detector components and combine them to get the complete determination of each physics event. Due to the complexity of the CLAS detectors, the reconstruction process is subdivided into several steps.

The raw detector information (ADC, TDC values) needs to be converted into the corresponding physical quantities (energy, time, etc.). For this purpose, a sample (about 10%) of the total data was selected throughout the whole run period. Our selection criteria were that we selected one run from each day's data and we also selected the runs immediatly following each change of run conditions. For these selected runs, both the energy and time calibrations of each detector component were checked. The corresponding calibration constants were adjusted to give the best performances (I will select some detector components to discuss the detailed procedure in the next section). When the reconstruction of the partial data had reached the satisfactory level of accuracy the calibration constants were "frozen", and the values were used for the primary data reconstruction.

During the full data processing, it takes a computer with a 600 MHz CPU approximately 50 ms to reconstruct one event, which is about 100 times slower than taking the data. This is directly due to the complexity of CLAS. For instance, because CLAS drift chambers have a very large geometrical coverage, each track could involve thousands of wires that are hit. As a result, 90% of the CPU time is used for reconstruction of tracks using the least square fit method (minimizing the sum of the squares of the closest distance from each hit wire to the track candidate). It took us about four months to process the whole data set for this experiment on the computer farm of Jefferson Lab. In the meantime, we paid particular attention and dedicated considerable effort to monitoring the process in order to identify problems that include failures of the reconstructing software, bad data files that were affected by hardware faults and not seen at the time of data taking. The results of the monitoring process were summarized in a database and could be used to choose good runs.

3.2 Detector Calibrations

Precise calibration of detectors is a crucial first step to measure any physical observables. Before the primary data processing, all components of CLAS detectors were calibrated for each day's run condition during the data taking period. In the following, I will make brief descriptions about calibrations for some of the components, which are most important to the data analysis.

3.2.1 Time of Flight Calibration

The system of Scintillation Counters (SC) is used to measure the Time of Flight (TOF) of particles. Because the masses of the charged particles are obtained by combining results of TOF and momentum measurements, the SC system is essential to making charged particle identifications. Furthermore, a precise TOF measurement is also a prerequisite for some other calibrations such as the drift chamber and calorimeter time calibrations which I will discuss later. Calibration of the TOF system involves not only calibration for timing measurements but also calibration for energy deposited in the scintillation counters. The precedure for TOF calibration consists of several steps (See [57, 17] for details). I will choose two of them as an example for more detailed discussion (one for time measurement and the other for energy measurement).

Left-Right Alignment

Each TOF scintillation counter has one PMT attached to each of the two ends. Each end actually measures the arrival time of the leading edge of the pulse generated by the PMT. The difference between the time measured by the left end and that by the right end indicates the position along the length of the scintillation bar where the particle hits. If we choose the x coordinate so that 0 sits at the middle point of the bar, the hit position x is

$$x = \frac{v(t_r - t_l)}{2} \tag{3.1}$$

where $t_{r(l)}$ is time measured by the right(left) TDC and v is the velocity of light in the scintillator which is approximately 16 cm/ns.

If the particle hits the middle point of the scintillator bar, the time measured by the left end and the right end should be the same. But in reality, cable length delays and PMT delays for the left and the right ends are different and we must adjust the offset. If we look at the distribution of hit positions calculated by the time difference for each bar (as in Fig. 3-1(a)), we can see they are not centered at 0. We have to find the center point offset with respect to 0 for each bar. To bring the center point back to 0, we have to adjust the relative time offset of the two readout ends by the corresponding length offset in the reconstruction. Fig. 3-1(b) shows the result of left-right alignment.

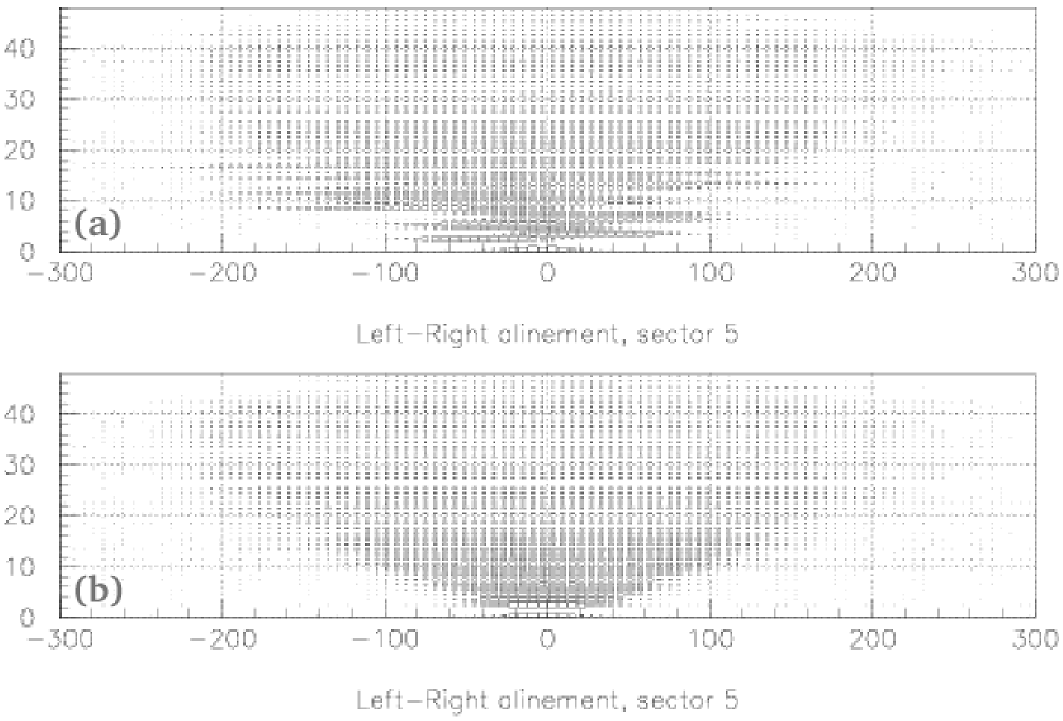

Figure 3-1: Hit positions (x axis in cm) vs scintillation bar number (y axis) for sector 5. (a) is before left-right alignment and (b) is after left-right alignment.

Attenuation Length

Calibration of the attenuation length for each scintillation bar is important to the measurement of the deposited energy. If a particle hits the scintillation bar at some position and causes an energy deposit, it is reasonable to assume the same amount of energy (let it be A) starts to propagate towards the left and right end in the form of scintillation light. The energy measured by the ADC of each end is after attenuation.

$$A_l = A \times e^{-(x+\frac{l}{2})/\lambda} \tag{3.2}$$

$$A_r = A \times e^{-(\frac{l}{2}-x)/\lambda} \tag{3.3}$$

where $A_{l(r)}$ is energy measured by left(right) ADC, x is the hit position, l is the length of the bar and λ is the attenuation length.

To determine the initial deposited energy A by the measurements of A_l and A_r, we can use Equation 3.2 or 3.3 directly. We can also avoid using the hit position x by multiply the two equations as

$$A_l A_r = A^2 \times e^{-l/\lambda} \tag{3.4}$$

However, we still have to know the attenuation length λ for each scintillation counter in order to get the correct measurement of the deposited energy. If we divide equation 3.2 by equation 3.3, we can get

$$ln\left(\frac{A_l}{A_r}\right) = -\frac{2}{\lambda}x \tag{3.5}$$

If we plot $ln\left(\frac{A_l}{A_r}\right)$ against x, it should be a straight line through the origin and with the slope $-\frac{2}{\lambda}$. Fig. 3-2 shows the plot for one scintillation bar. Through a straight line fit, we can get the attenuation length for that scintillation bar is 199.82 cm.

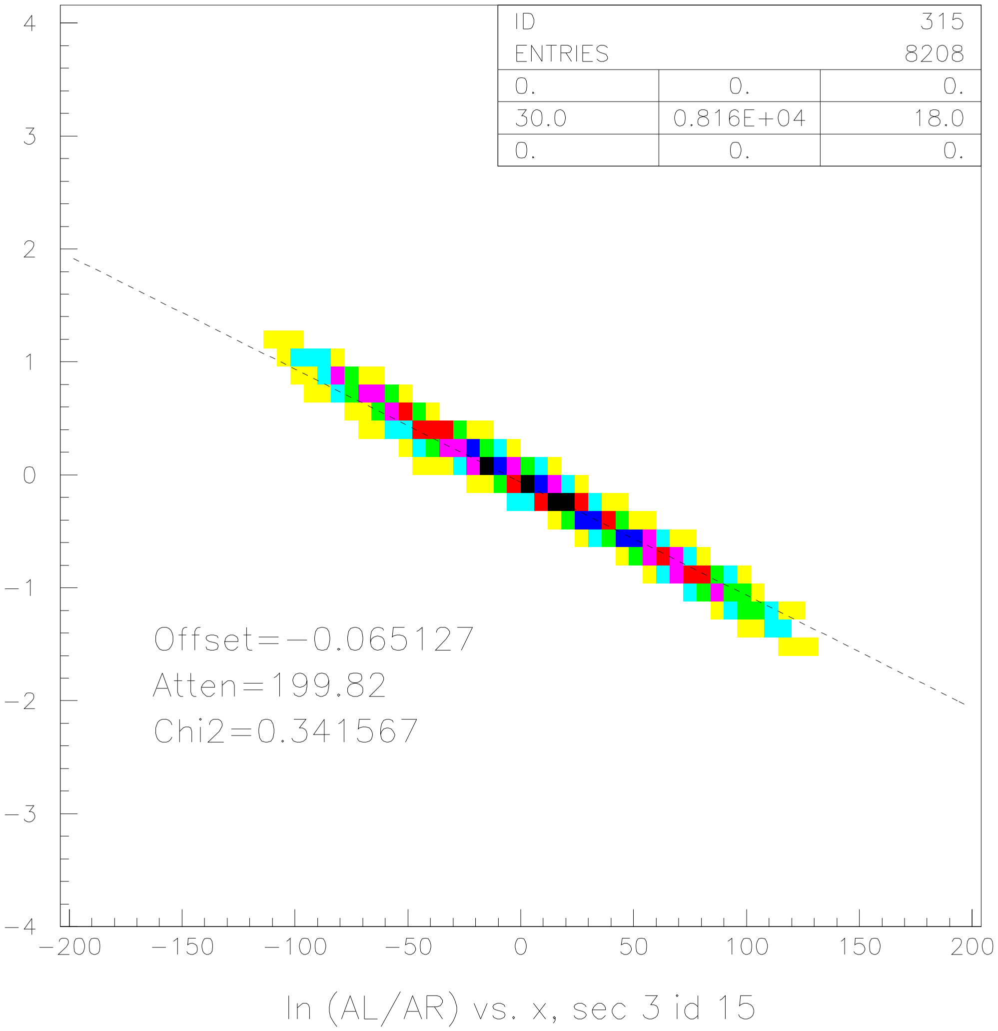

Figure 3-2: Scattering plot of $ln\left(\frac{A_l}{A_r}\right)$ vs x(cm) for sector 3 and paddle 15. The slope of the line is $-\frac{2}{\lambda}$, where λ is the attenuation length. By the straight line fitting, λ is found to be 199.82 cm.

3.2.2 Drift Chamber Calibration

In CLAS, the Drift Chambers (DC) are the primary devices used to measure any charged particle's momentum. A charged particle's momentum is determined by its trajectory in the DC together with the information of the magnetic field.

As described in section 2.2.2, when a charged particle goes through the drift chambers, each of the 34 layers is supposed to be hit. Actually, due to inefficiencies or holes in the chambers, we find an average of 30 hits per track. Each hit detected in the chambers is used to determine the particle's track via a least square fit (minimizing the sum of the squares of the closest distance from each hit wire to the track candidate).

The drift chambers are calibrated by parameterizing the drift velocity function for each superlayer in each sector [12, 56]. The drift velocity function is the relationship between the closest distance from the track to the sense wire and the time it takes the ions created by the particle to drift from the track to the sense wire. The drift time is measured by the TDCs attached to each wire. To parameterize the drift velocity function, a trial function based on the calibration of earlier data was used to reconstruct the tracks using the least square fit method. With the reconstructed tracks we can geometrically calculate the closest distances, which can be fitted against the drift time to improve the trial function. Then the improved function was used to reconstruct the tracks again, and so on. After several iterations, the drift velocity function converged to the best parameterization. Fig. 3-3 shows an example of the fitting of the drift velocity function for one super layer in the final iteration.

We can calculate the closest distance from the track to the sense wire using the final drift velocity function (we denote this distance as $DIST$). The reconstruction is essentially to choose a track so that the sum of $DIST^2$ for all hit wires is minimum. After the track is reconstructed, we can geometrically determine the closest distance from the reconstructed track to the sense wire (we denote this distance as distance of closest approach $DOCA$). $DOCA$ should be close to $DIST$ but not equal. In fact the difference between them, which we denote as the residual $RESI = |DOCA - DIST|$,

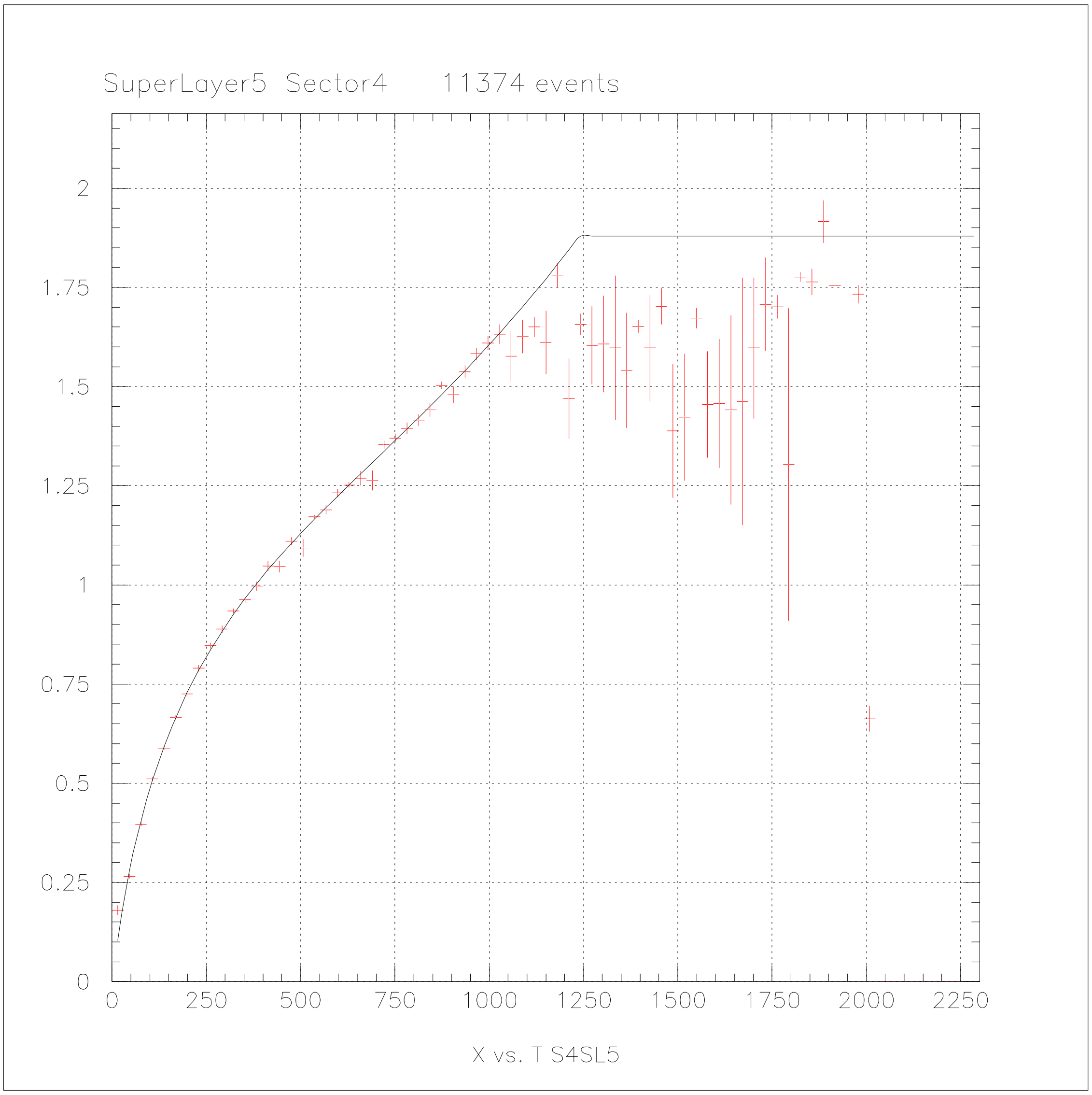

Figure 3-3: Drift velocity function for superlayer 5 sector 4. Vertical axis is defined by the distance from the track to the sense wire [cm], horizontal axis is defined by drift time [ns]. The plot shows the fitting for the last iteration. The points are data reconstructed using the parameterization of the previous iteration. The line is the fitting and the parameters are used for the actual reconstruction.

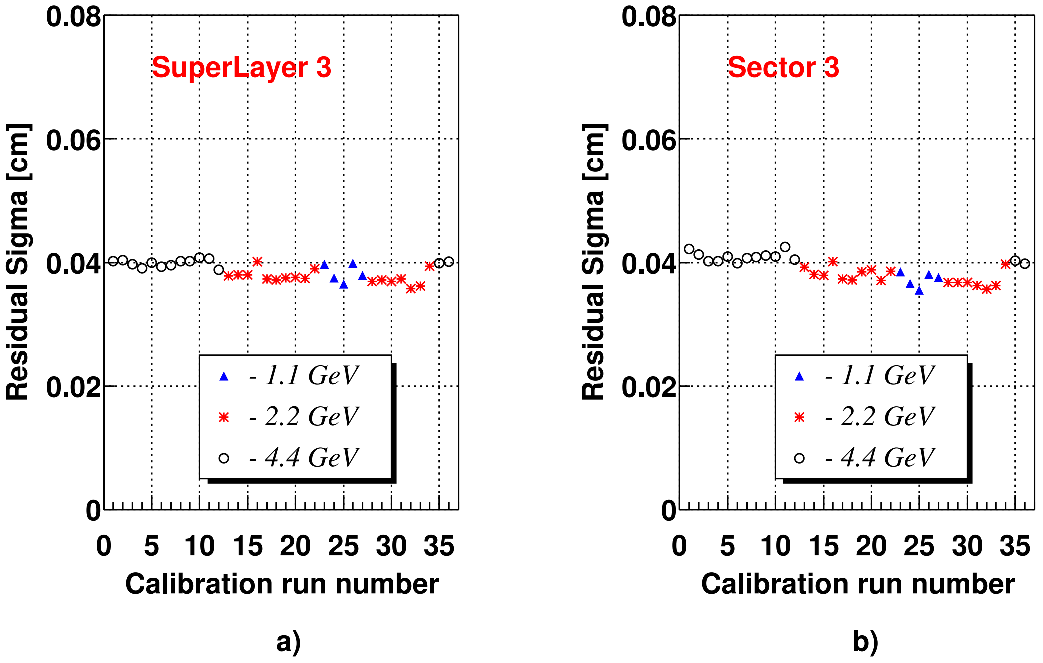

Figure 3-4: Residual sigmas versus calibration run number *a*) Superlayer 3 averaged for 6 sectors *b*) Sector 3 averaged for 6 superlayers. Different markers correspond to different beam energies of the runs. Calibration run number corresponds to the time of data taking (covers every day of running period). The resolution of position determination is about 0.4 mm and it is very stable during the run period with small changes between different run conditions.

is the primary measurement of the drift chamber's resolution, or the accuracy of the position determination. The resolution is obtained as the sigma of a Gaussian fit of the residuals. Fig. 3-4 shows the typical residual sigmas during the whole run period. One can see the resolution was about 0.4mm and very stable during the run time.

3.2.3 Electromagnetic Calorimeter Time Calibration

In CLAS the Electromagnetic Calorimeter (EC) is used to detect neutral particles (photons and neutrons). As a result, the EC time measurement is crucial to neutral particle identification because we can only distinguish neutrons from photons by their velocities. Moreover, unlike charged particles, a neutron can start interacting with materials anywhere on its path in the EC. It does not necessarily deposit all of it energy in the EC. As a result, the velocities of neutrons become the only measurement of their energies. This fact also makes EC time calibration more important.

The hardware design of the EC causes some difficulties in making a simple calibration of the particle arrival time. As discussed in Sector 2.2.5, the scintillation bars have PMTs attached to only one end. Moreover, the calorimeter is subdivided into inner and outer layers and in each layer five or eight scintillation bars share one PMT for readout. All those facts makes hit position determination very difficult and consequently makes the determination of the time it takes the scintillation light to travel from the hit position to the readout end very difficult.

We use the following formula to reconstruct particle arrival time measured by the EC:

$$t_{ec} = a \times tdc + b + \frac{c}{\sqrt{adc}} + d \times l^2 + e \times l^3 - \frac{l}{v_l}, \tag{3.6}$$

where a,b,c,d,e are five parameters to be calibrated, $tdc(adc)$ is the TDC(ADC) value, l is the length from the hit point to the readout edge, v_l is the velocity of the scintillation light travelling inside the material. The first two terms $(a \times tdc + b)$ represent the simple linear TDC response. The third term $(c/\sqrt{adc})$ is the correction to the time-walk effect of the signal pulse. The fourth and the fifth term $(d \times l^2 + e \times l^3)$ are small corrections for the fact that signals arrive at the readout edge at slightly different times for scintillation bars connected to the same PMT. The last term (l/v_l) is obviously the compensation to the time for the scintillation light to travel from the hit position to the readout edge.

Because we measure the arrival time for electrons by both the EC and the Scintillation Counters (SC), the calibration can be done by matching the two measurements of the electron arrival time, with the assumption that the SC measures the time accurately. After the calibration, the calibration constants are only used for neutral particle arrival time reconstruction. For electrons, we still use the time measurements by the SC, which is believed to be more accurate.

In order to obtain the calibration constants by fitting the formula 3.6, we must know the electron arrival time that should be reported by the EC. This can be done by extrapolating the arrival time in the SC to the EC. Because there is no magnetic field outside the SC, the electron track from the SC to the EC should be a straight line. If we denote the electron arrival time measured by the SC as t_{sc}^{el}, the distance between the EC layer (inner or outer) and the SC layer as d_{ecsc}, the electron velocity as v which is close to speed of light, and the electron's impacting angle to the EC plane as α, we can predict the time measured by the EC as

$$t_{ec}^{el} = t_{sc}^{el} + \frac{d_{ecsc}/cos\alpha}{v} \tag{3.7}$$

(See Fig. 3-5).

Then we are ready to fit t_{ec}^{el} using the formula 3.6 to get the best parameterizations of the five constants (a,b,c,d,e) for each of the scinllation bar in the EC. These constants are finally used to measure the neutral particle arrival time. To check the quality of the EC time measurement, we can compare the electron arrival time reconstructed by formula 3.6 with the final calibration constants to the time extrapolated from the SC time by formula 3.7. These two numbers should be close to each other. The difference between them represents the quality or the resolution of the time measurement. Fig. 3-6 shows the distribution of the time difference in one EC sector. The overall σ is $\sim$ 250 ps, which is combined with the SC resolution. The SC time resolution obtained by separate measurements is $\sim$ 150 ps [16]. So the EC time resolution for electrons is $\sim \sqrt{250^2 - 150^2} = 200$ ps. For neutral particles, the resolution is about 600 ps. We will discuss more detail about neutral particles in Neutron Detection (Section 3.5).

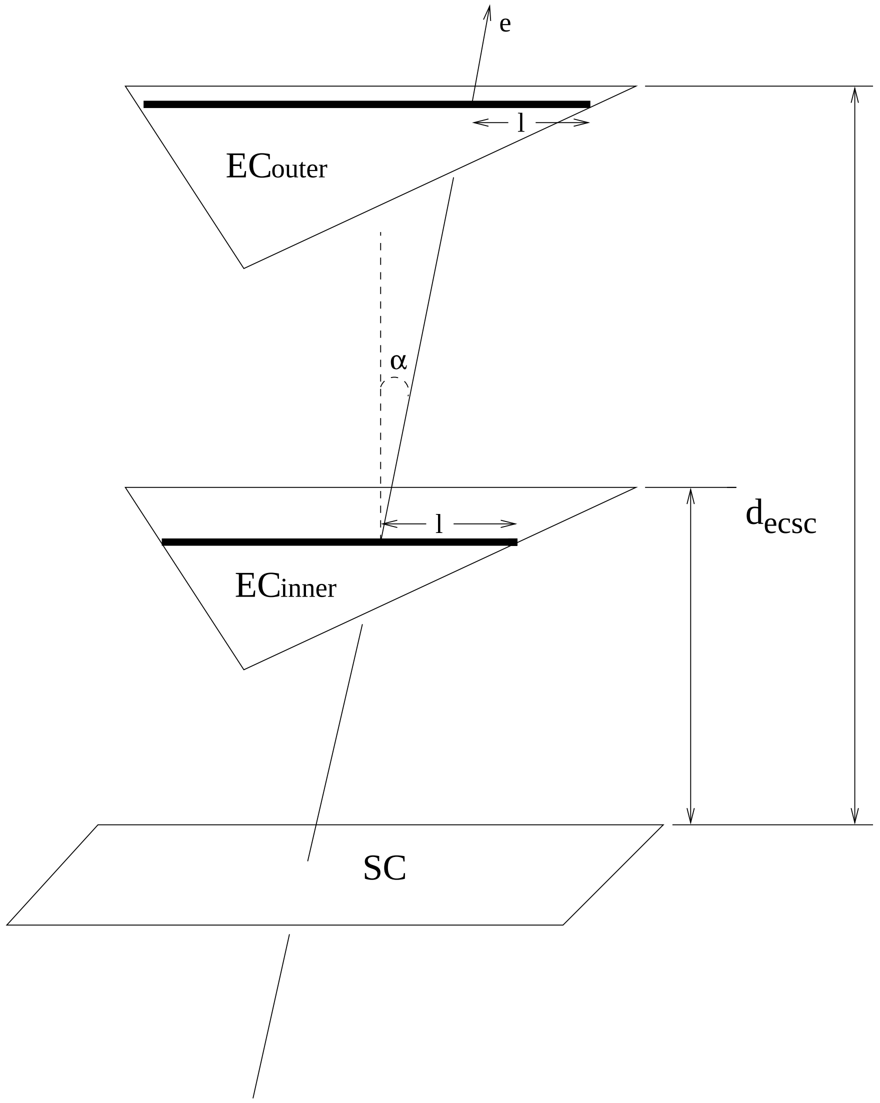

Figure 3-5: EC time extrapolation from SC time. d_{ecsc} is the distance between the EC layer (inner or outer) and the SC layer, α is the electron's impacting angle to the EC plane and l is the length from the hit point to readout edge along the scintillation bar.

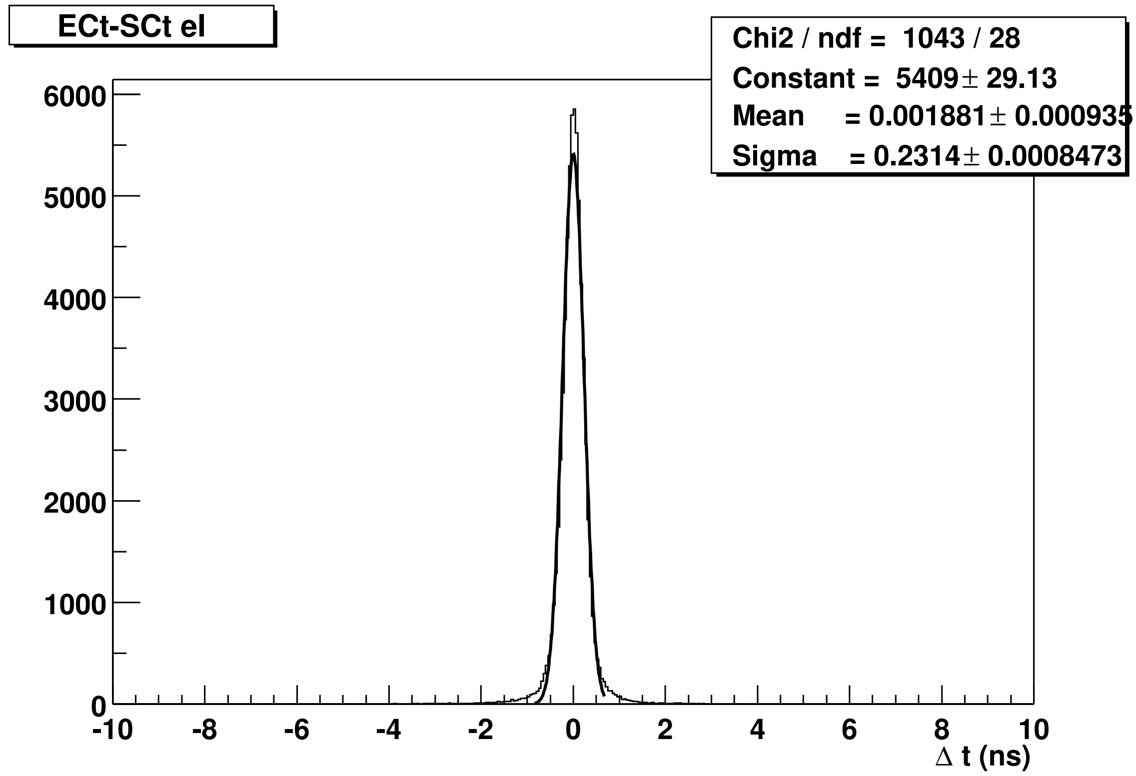

Figure 3-6: The distribution of the difference between the electron arrival time measured by the EC and that extrapolated from the SC measurement for the EC sector one.

3.3 Electron Detection

3.3.1 Electron Identification

Electron identification is crucial to CLAS electro-production data analysis, because electrons are the trigger particles and the identification of other particles is strongly dependent on identifying electrons correctly and obtaining precise time information. The main source of contamination for electrons is the presence of relativistic negative pions. A series of data cuts were developed to minimize pion contamination. We will take advantage of the different behaviors of electrons and pions in the CLAS detectors.

Initial Indentification

During initial primary data processing ("cooking") the following criteria have been applied to select electron candidates [65]:

1. An event was recorded only if there was at least one negative track which had geometrically matched hits in the Electromagnetic Calorimeter (EC) and the Scintillation Counters (SC).

2. If an event had only one negative track then it was considered as the scattered electron. If it had several negative tracks, the one which matched the electron characteristics best, i.e. had matching hits in the EC, the SC, the Čerenkov Counters (CC) etc., was taken as the electron candidate.

3. After the electron was identified, time of flight and momentum analysis was used to identify other particles.

However, the above criteria are very loose for electron selection in the sense of rejecting pions. In order to make more precise identification for electron, we need to apply more cuts.

Z Vertex Cut

The vertex of the particles is the point where the reaction occurs. From a particle's track inside the Drift Chambers (DC) and the knowledge of the magnetic field, we can extrapolate its trajectory. Because in this experiment, we always had at least two charged particles (electron and proton), we were able to use the crossing point of two or more tracks as the event vertex.

Fig. 3-7 shows a typical distribution of the z component (the z axis is along the beam line) of the electron vertice for the ^{3}He target. The central plateau is the main target material and the peak to the right is the heat shield. We apply a cut which requires $-3\ cm < VertexZ < 0\ cm$. The wall of the target cell was fitted an exponential tail (I). The heat shield was fitted by a Gaussian distribution (II). The remaining downstream material was fitted by another exponential tail (III). As one can see the Gaussian shape of the heat shield has practically no contamination in our cut target region. The worst case is that the exponential tail III is all from the heat shield and there should be a symmetrical tail (IV) on the lefthand side. We can make this assumption because all these distributions are produced by electrons and the target length, compared to the scale of CLAS, is not long enough to make a difference in detection efficiencies. In the worst case, tail IV has a contamination of 0.5% inside our cut target region. Thus a conservative estimate of error introduced by the vertex cut is

$$Error_{vertexHe3} = 0.5\% \tag{3.8}$$

We obtained z vertex cuts for different targets as shown in Fig. 3-8. Note that there are two cases for ^{12}C target: one is running with the target alone and the other is running together with an empty cryotarget cell placed upstream. The reason is that we first run with the solid target, then we installed the cryotarget and took the cryotarget data, at last we run the solid target again without pulling out the cryotarget cell. The actual vertex cuts and associated errors for all targets are shown

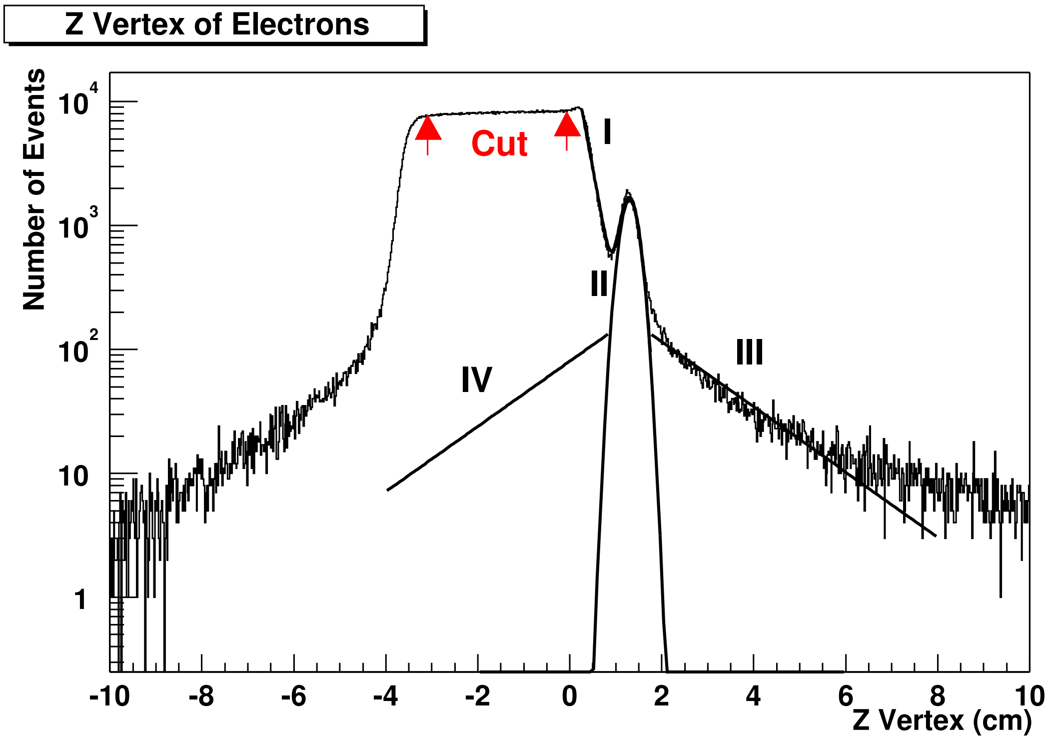

Figure 3-7: Distribution of the Z component of electron verteice along the beam line for the ^{3}He target. The central plateau is the main target material and the peak to the right is the heat shield.

Target	^{3}He	^{4}He Cell 1	^{4}He Cell 2	^{12}C	^{12}C + cell
Z Cut (cm)	-3 < Z < 0	-2.5 < Z < 1.7	-2.1 < Z < 0.7	3.6 < Z < 6.6	4.2 < Z < 6.6
$Error_{vertex}$ (%)	0.5	0.3	0.2	0.5	0.6

Table 3.1: Z vertex cuts for all targets.

in Table 3.1.

Cut on Total Energy Deposited in the Calorimeter

Pions can only deposit a small amount of energy in the Electromagnetic Calorimeter (EC) compared to electrons. During data taking, we set a hardware threshold for the calorimeter to minimize pion contamination. However, some pions could still pass the hardware threshold and produce a trigger. Therefore after reconstruction, we need to put an additional software threshold to reject pions which typically deposit a small amount of energies. Fig. 3-9 shows the distribution of the total energy deposited in the calorimeter for electron candidates in 2.2 GeV data. We put the threshold at 0.08 GeV (for 4.4 GeV data, the threshold is 0.33 GeV [49]). There are 1.2% of events below the threshold. So a conservative estimation of the error is

$$Error_{etotcut} = 1.2\% \tag{3.9}$$

Cut on Energy Deposited in the Inner Layer of Calorimeter

The amount of energy a minimum ionizing pion deposits in the inner layer of the calorimeter depends only on the material and the thickness of the calorimeter layer. It is independent of the pion's momentum and it is small compared to electron case. Fig. 3-10 shows the distribution of energy deposited in the inner layer of the calorimeter for electron candidates. The small peak corresponds to pions. We put a cut at 0.055 GeV. The pion contamination above the cut value is about 0.1%. The estimated

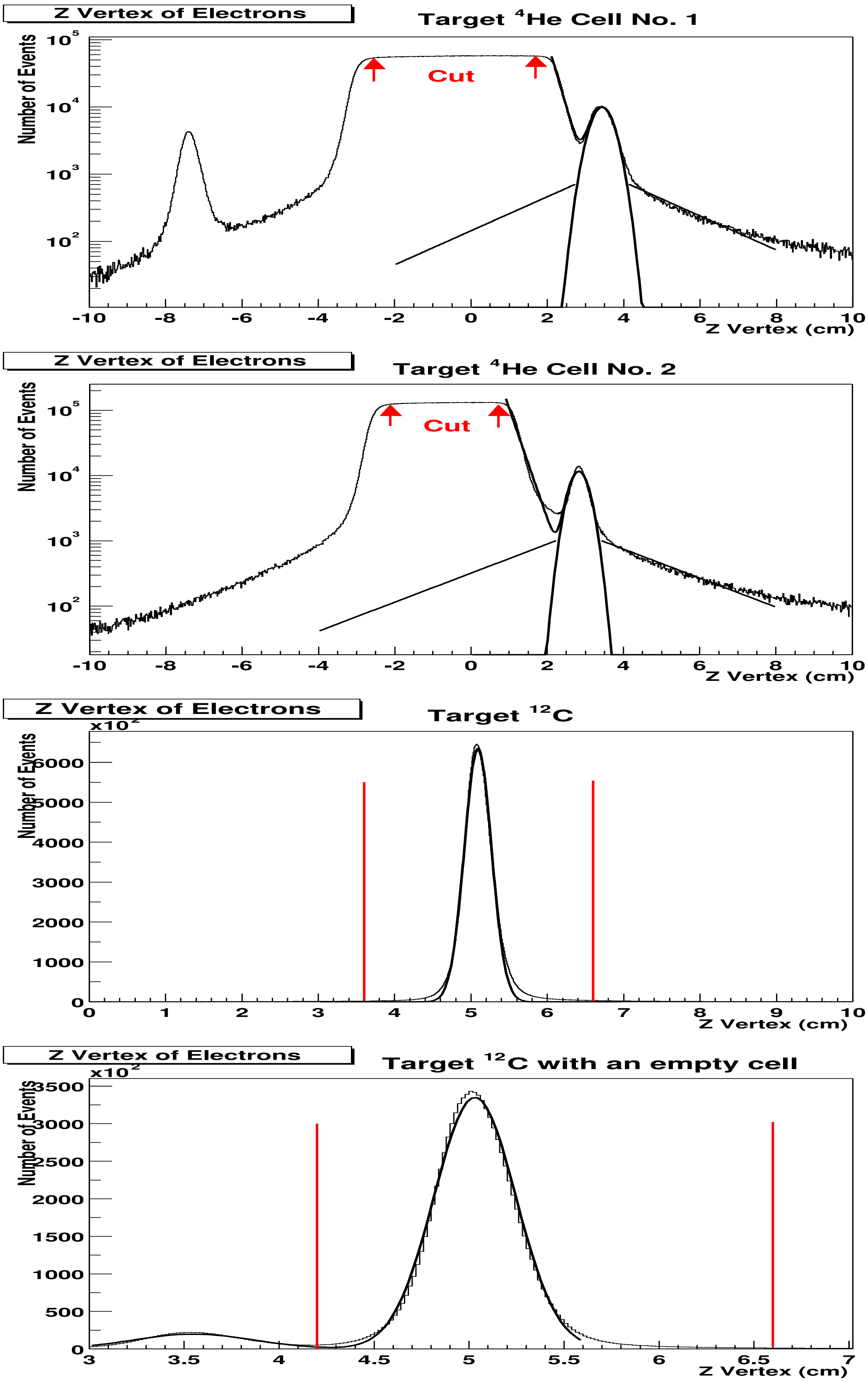

Figure 3-8: Distributions of the electron Z vertice for the ^{4}He (two cells) and the ^{12}C targets. The red lines and arrows show the vertex cut positions. The small peak in the bottom figure is the empty cryotarget cell.

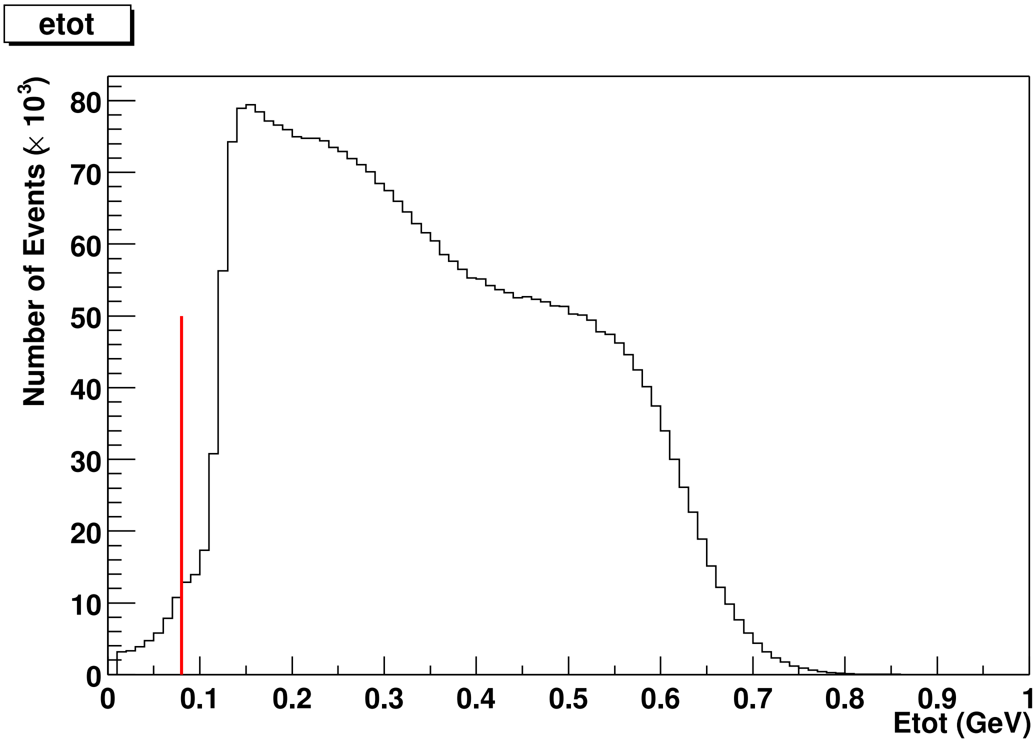

Figure 3-9: Total energy deposited in electromagnetic calorimeter for electron candidates. A software threshold is put at 0.08 GeV for incident energy of 2.261 GeV.

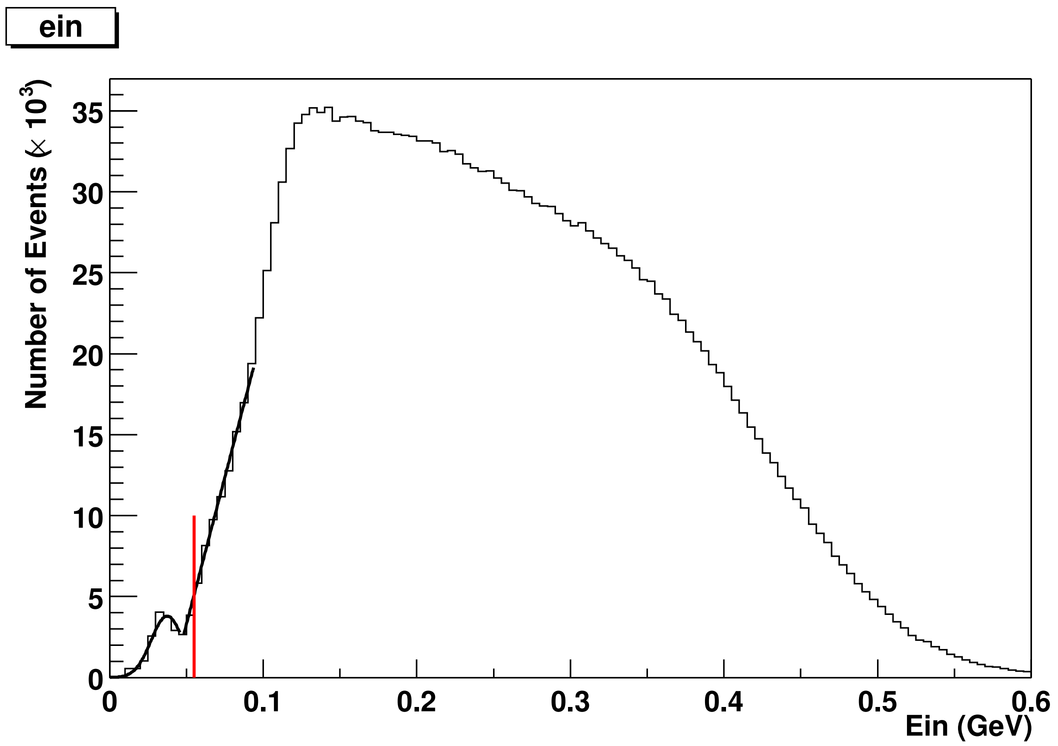

Figure 3-10: Energy deposited in the inner layer of the electromagnetic calorimeter for electron candidates. A small peak on the left corresponds to minimum ionizing pions. A software cut was put at 0.055 GeV.

loss of electrons is 0.5%. So a conservative estimation of the error is

$$Error_{eincut} = \sqrt{0.5^2 + 0.1^2} = 5\% \tag{3.10}$$

Cut on the EC Sampling Fraction

The total energy deposited in the scintillators is measured as a fraction of the incident particle's energy. This fraction, which is called the EC sampling fraction, is about 0.3 [30]. Fig. 3-11 shows the scatter plot of the total deposited energies vs the momenta (numerically equal to the energies because the velocities of the electrons are very close to the speed of light) of electron candidates. One can clearly see the "good" electron band with the sampling fraction centering about 0.3. The plot then was sliced along

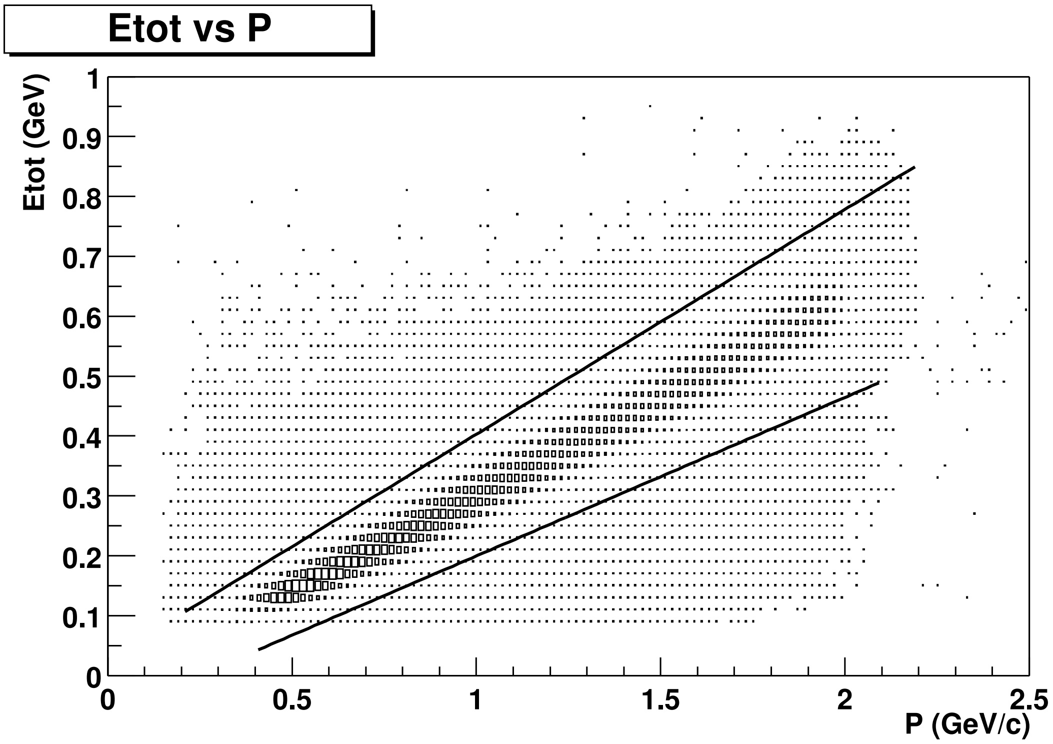

Figure 3-11: Total energy deposited in calorimeter vs the momentum for electron candidates. The two lines indicate the 3σ cut around the center of the electron band.

y axis direction and a Gaussian fit of each slice was used to determine the center and width of that slice of the band [49]. Cuts are put at 3 times the standard deviation above and below the center of the band. The estimated loss of electrons is 1.3%. So a conservative estimation of the error is

$$Error_{splfr} = 1.3\% \tag{3.11}$$

In Summary, the total error associated with electron identification is the quadratic sum of the errors for all cuts.

$$\begin{aligned} Error_{electronID} &= \sqrt{Error^2_{vertex} + Error^2_{etotcut} + Error^2_{eincut} + Error^2_{splfr}} \\ &= \sqrt{0.5^2 + 1.2^2 + 0.5^2 + 1.3^2} = 2\% \end{aligned} \tag{3.12}$$

3.3.2 Electron Momentum Correction

Due to a lack of exact knowledge of the CLAS magnetic field, the geometrical misalignments of the Drift Chambers and possibly some other unknown reasons, the electron momentum reconstructed from its track in the Drift Chambers has a small error. From the invariant mass (W) distribution for Hydrogen data (upper plot of Fig. 3-12), one can see that the elastic peak is shifted roughly by 24 MeV/c^2. This corresponds to the electron momentum being off by about 1%.

To correct the electron momentum, we used elastic hydrogen data taken one month before our experiment. In a $H(e, e'p)$ measurement, by cutting the invariant mass W around the elastic peak and requiring the azimuthal angles of the electron and the proton be opposite to each other, we can be sure the reaction is elastic scattering. If we assume the angles are correctly measured, we can determine the magnitude of the scattered electron's momentum precisely from the kinematics. Then the electron momentum correction function is derived by comparing the predicted value to the measured value. The correction is a function of the magnetic field (coil current), the measured momentum and the scattering angle. An empirical expression was used to fit the data. After the momentum correction, the elastic peak of the W distribution for hydrogen data has been brought back to the correct position and the σ of the peak has been improved from 21 MeV to 14 MeV, which is the energy resolution of CLAS (see lower plot of Fig. 3-12). The correction is usually less than 1% of the electron momentum. Separated momentum corrections were derived for different incident beam energies and magnetic field settings.

There are two concerns about the electron momentum correction. The first is that we apply a correction derived from an earlier data set to our data set. The second is that we apply a correction derived from the elastic region to other regions (this data analysis involves the region extending up to the Δ peak).

To clarify the first question, we checked the effect of the correction on our data. Fortunately beside lots of ^{12}C data, we had collected a small amount of CH_2 data.

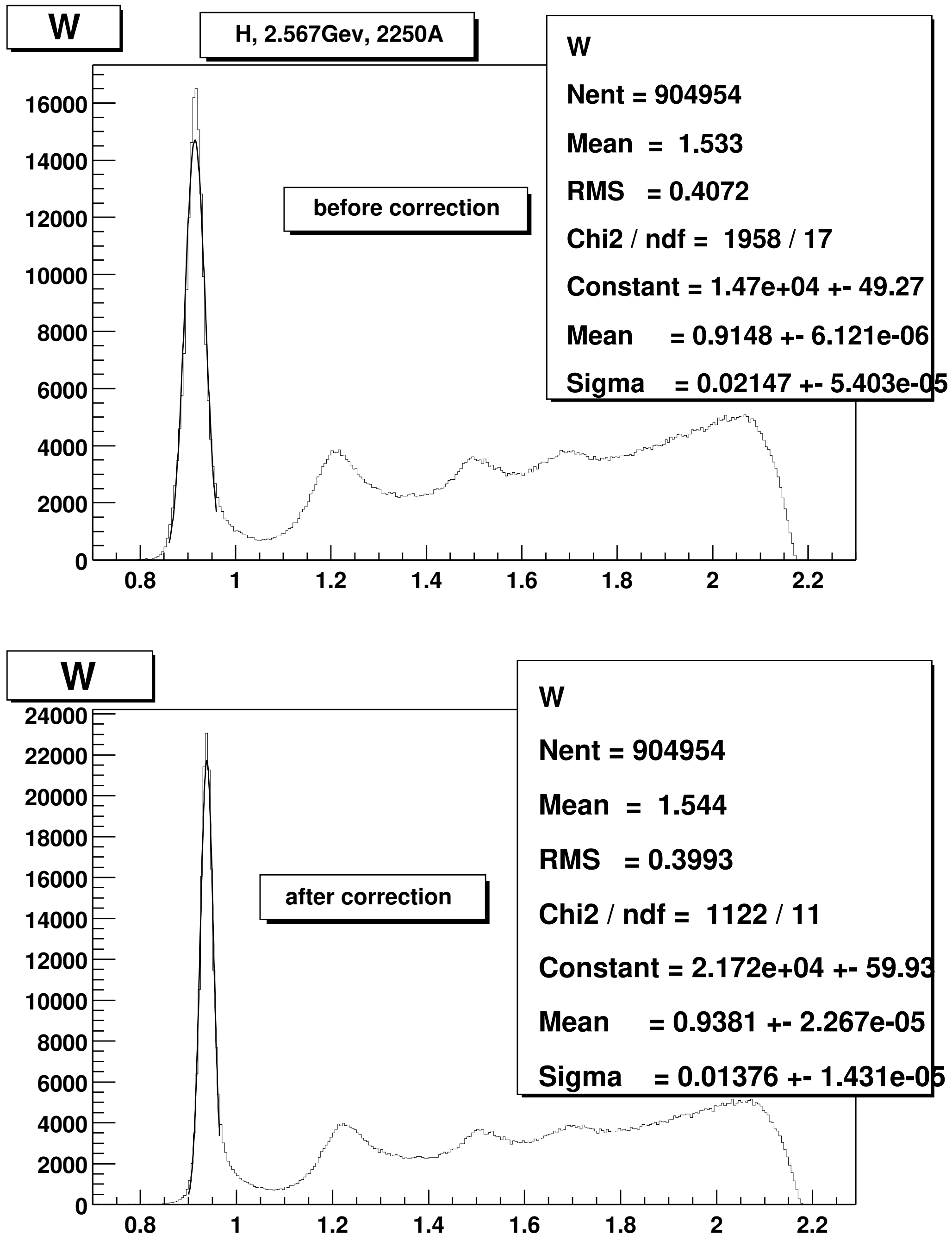

Figure 3-12: W distribution (in the unit of GeV/c^2) for Hydrogen data before and after the electron momentum correction.

By subtracting ^{12}C contribution from CH_2, we can get the results for scattering off Hydrogen during our run. Fig. 3-13 shows the effect of the correction on the elastic peak. The peak has been brought back to the right position and the width has been improved.

To clarify the second question, we checked the effect of the electron momentum correction in the Δ region by looking at the missing mass of $H(e, e'\pi^+)X$ reaction (See Fig. 3-14). The correction brought the neutron peak to the right position and improved the width.

3.3.3 Electron Fiducial Cuts

CLAS efficiency is a complicated function of the particle momentum vector. Most of the inefficiencies come from the edges of the detector sectors, while the middle part of each sector is almost 100% efficient. The purpose of the fiducial cuts is to cut off the inefficient regions such as edges, malfunctioning TOF scintillators and other holes in the detectors so that we can use events only from the efficient part of the detectors. Fiducial cuts are different for different particle types and different magnetic field settings.

To derive the fiducial cuts for electrons, the data have been binned by small segments in momentum. For each detector sector and momentum bin, the angular distribution of the electrons is plotted as upper plot of Fig. 3-15. One can clearly see the efficiency changes rapidly at the edges. The distribution is further sliced at different θ angles (See Fig. 3-16). It clearly shows that the efficiency is flat in the middle part and falls at the edges. A cut is made to locate the two ends of the plateau and use electrons only inside that region. All parameters are fitted against the momenta and the scattering angles of the electrons so that the final fiducial cuts are smooth functions throughout the kinematic range. The lower plot of Fig. 3-15 shows the angular distribution of the electrons after the fiducial cuts.

To determine the uncertainty of restricting CLAS electron acceptance within its

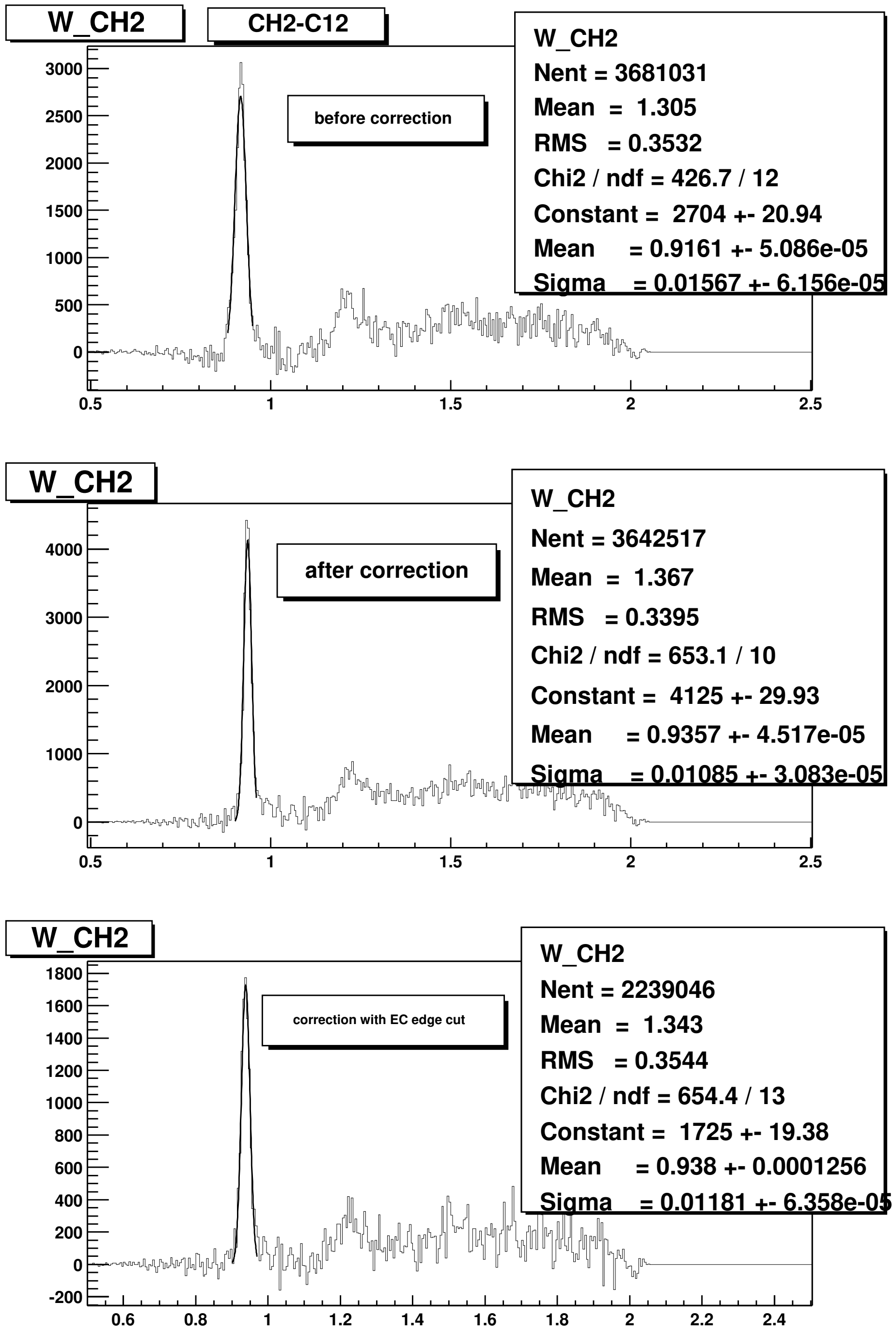

Figure 3-13: W distribution (in unit of GeV/c^2) for $CH_2 -^{12} C$. Top is before correction, middle is after correction and bottom is after further fiducial cuts (see next section).

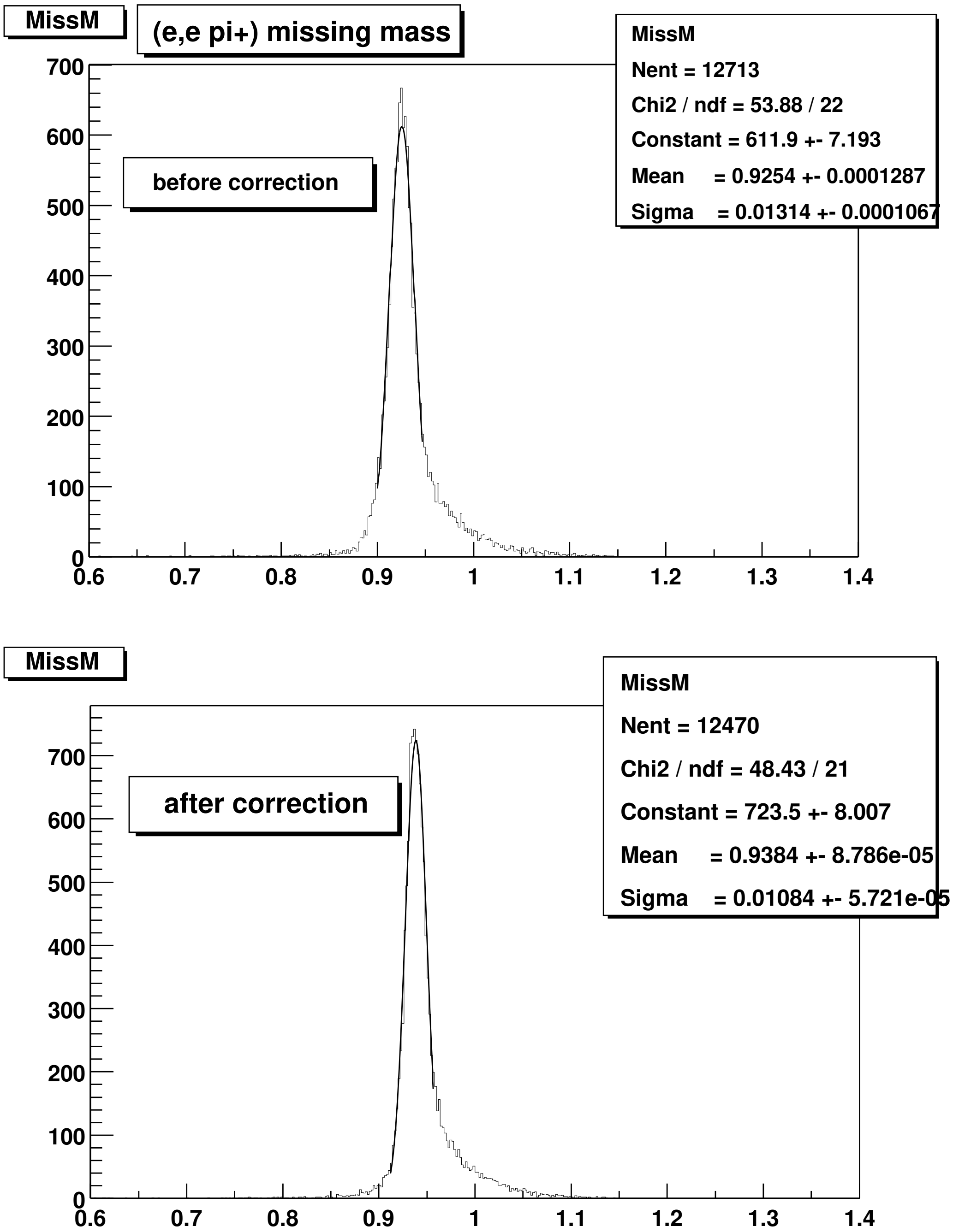

Figure 3-14: Missing Mass (in unit of GeV/c^2) for $H(e, e'\pi^+)X$ before (upper) and after (lower) the electron momentum correction.

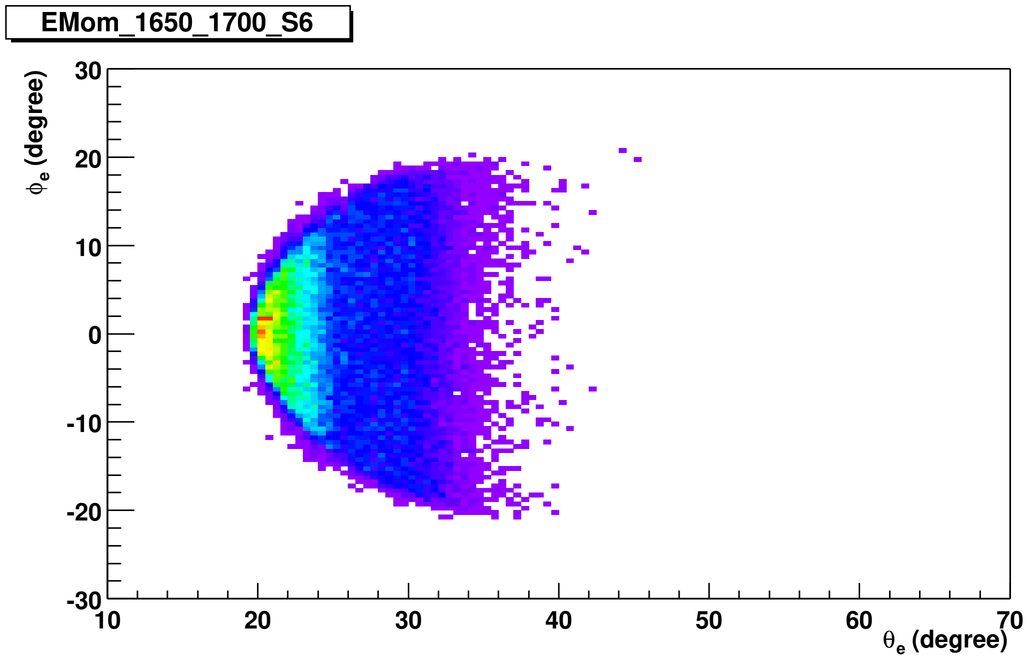

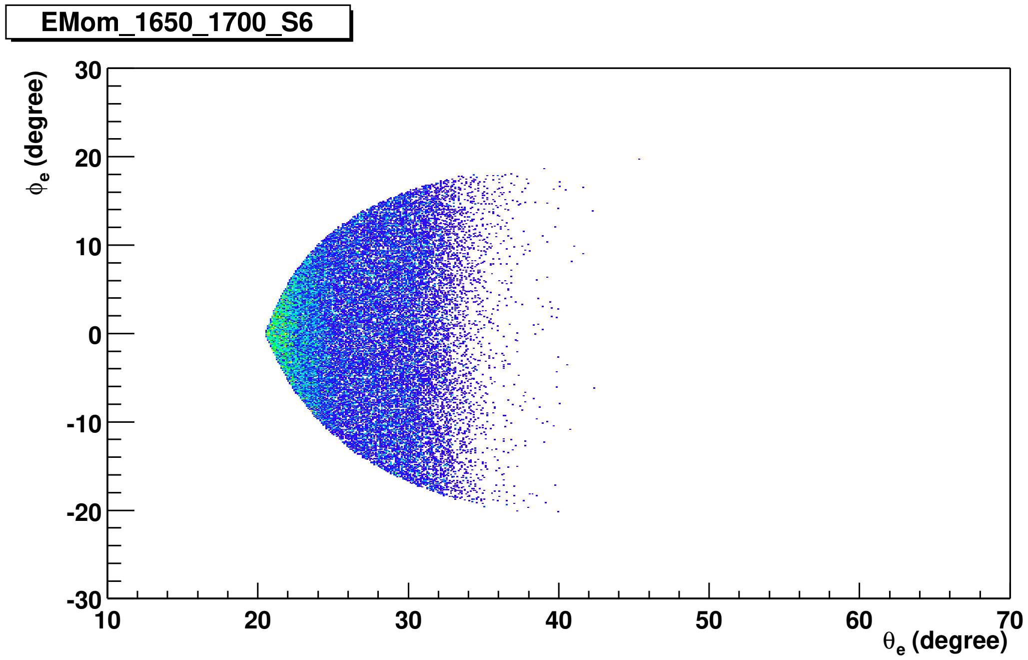

Figure 3-15: Electron angular distribution for momentum bin 1.65 - 1.70 GeV/c and sector 6. Upper plot is before the fiducial cuts and lower plot is after the fiducial cuts.

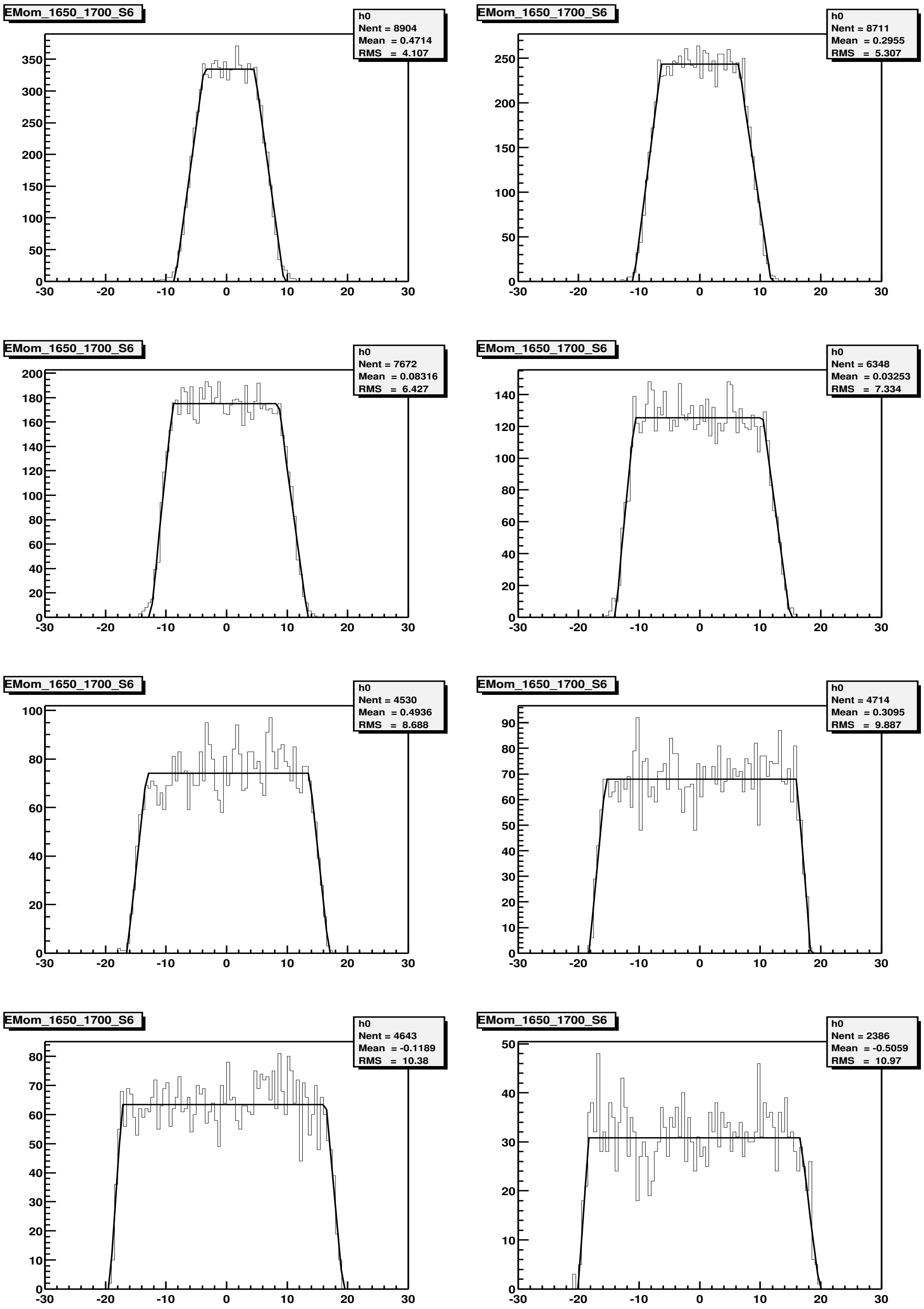

Figure 3-16: Electron ϕ distribution (in unit of degree) for sector 6, momentum bin 1.65-1.70 GeV/c and 8 different θ bins. The width of each θ bin is 1^o.

fiducial region or to measure how "flat" the plateau regions are, we used the following method. First we measured the differential cross section for the inclusive reaction by restricting electrons within the derived fiducial region; let us call it $d\sigma_1$. Then we measured the same cross section by restricting the azimuthal (ϕ) angles of the electrons within 5 degrees around the center point of each sector where the electron acceptance is believed to be very flat; let us call it $d\sigma_2$. By comparing the two cross sections we can get an idea of the quality of our fiducial cuts.

We examined several scattering angles and the results are almost the same. We can take ^{3}He 2.2 GeV $\theta_{e'} = 22^o$ data as an example. The top plot of Fig. 3-17 shows the two differential cross sections and the bottom plot shows the relative deviation of the two cross sections $\frac{d\sigma_1 - d\sigma_2}{(d\sigma_1 + d\sigma_2)/2}$. Then uncertainty was estimated by the average deviation in all bins

$$Error_{electron\,Acpt} = \sqrt{\frac{1}{N}\sum_{i=1}^{N}\left(\frac{d\sigma_1^i - d\sigma_2^i}{(d\sigma_1^i + d\sigma_2^i)/2}\right)^2} = 4\% \tag{3.13}$$

In earlier experiments, people have investigated the acceptance uncertainty by comparing cross sections measured in different magnetic fields and using different sectors of CLAS [63]. Our uncertainty is consistent with their results (their uncertainty was estimated to be 5%).

3.4 Proton Detection

3.4.1 Proton Identification

In CLAS, hadrons are identified by combining the momentum measurement with the time of flight measurement. This is essentially the mass measurement. Fig. 3-18 shows β measured by the time of flight vs momentum measured by the drift chambers for particles of positive charge. From the plot one can see positrons, pions, kaons, protons, deuterons and tritons.

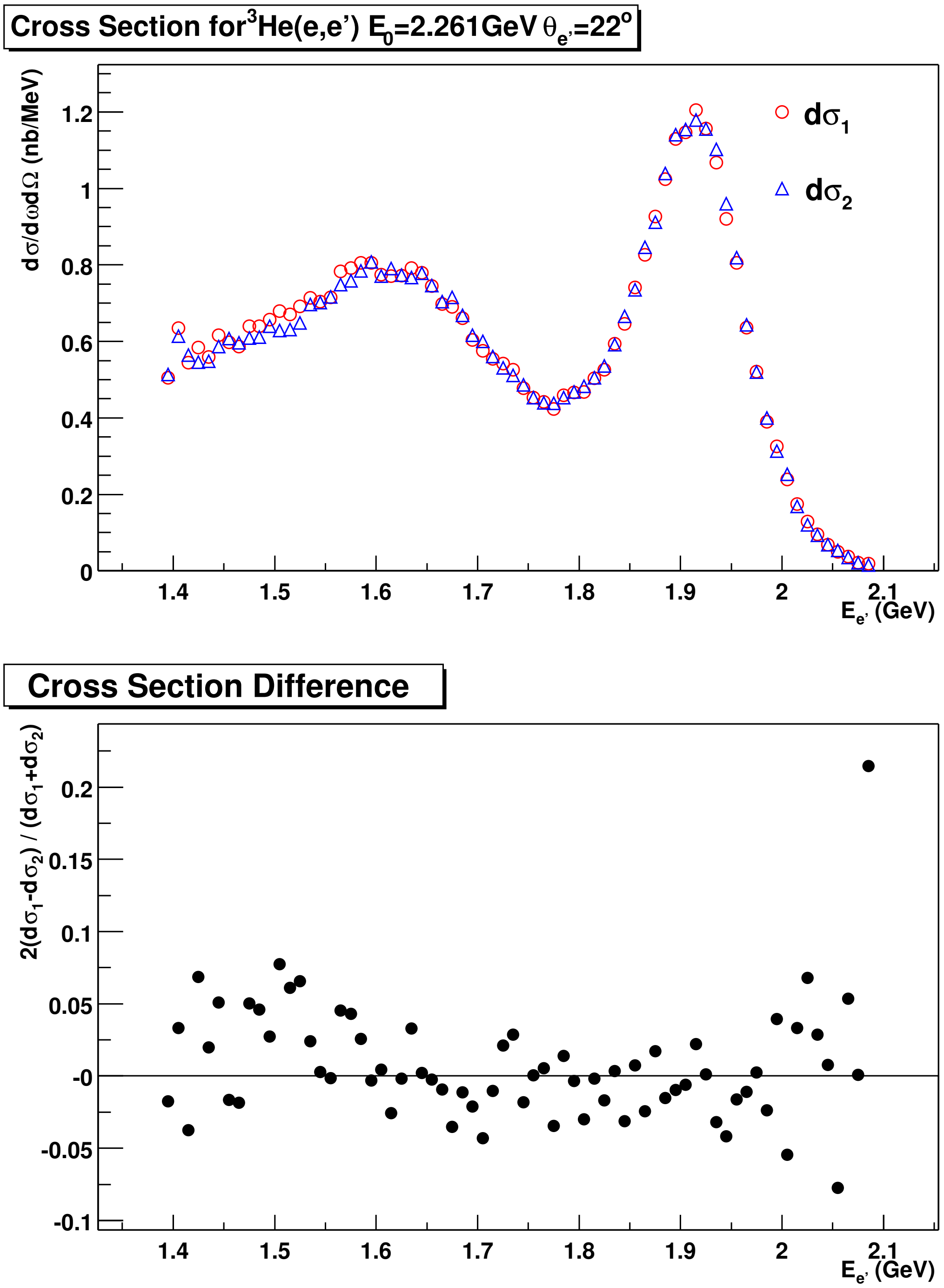

Figure 3-17: ^{3}He inclusive cross section was measured (1) within fiducial cuts and (2) within more strict fiducial region where the electron's ϕ angle is within 5 degrees around the center point of each sector. We denote the cross section as $d\sigma_1$ and $d\sigma_2$ respectively. The bottom plot is the relative deviation of the two cross sections $\frac{d\sigma_1 - d\sigma_2}{(d\sigma_1+d\sigma_2)/2}$. The incident energy is 2.261 GeV and the electron scattering angle is 22 degrees.

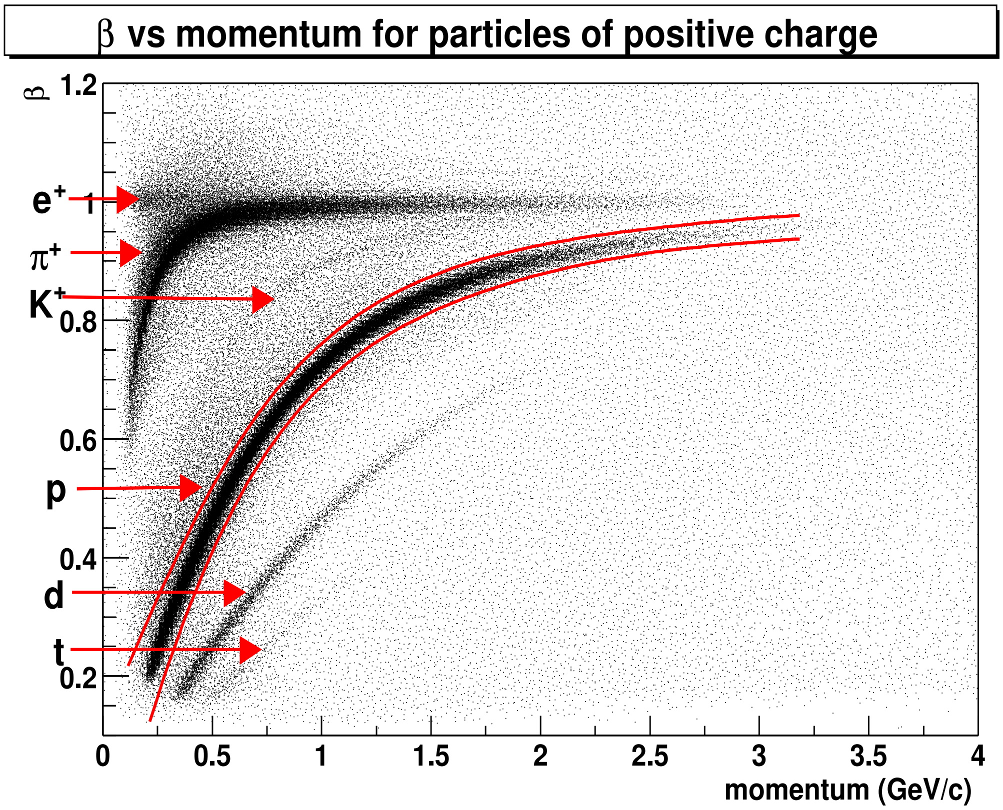

Figure 3-18: β measured by the time of flight vs momentum measured by the drift chambers for particles of positive charge. From the plot one can see positrons, pions, kaons, protons, deuterons and tritons. A 3-σ cut around the central line of proton band is used to identify protons.

Particles were preliminarily identified by the maximum likelihood approach [66], i.e. a particle was assigned an ID so that $|\beta_{measured} - \beta_{calculated}|$ is minimum, where $\beta_{measured}$ is its velocity measured by the time of flight and $\beta_{calculated}$ is its velocity calculated by its momentum using the mass of the particle of the assigned type. Furthermore we applied a 3-σ cut around the central line of the proton band to identify protons. The estimated loss of protons by this cut is about 3% while the background contribution is negligible. We can take the error of proton identification to be

$$Error_{protonID} = 3\% \tag{3.14}$$

The energy deposited in the Scintillation Counters (SC) is another piece of information we can use to identify protons. This is especially helpful to eliminate pion contaminations. The energy deposited by a minimum ionizing pion is independent of its momentum while the deposited energy is momentum dependent for protons. Fig. 3-19 shows the energy deposited by proton candidates in SC vs β after the time of flight cut discussed above. One can see there is no minimum ionizing pion band (the pion band, if existing, should be at the level of $dE \sim 10$ MeV) and the proton band is very clean. Therefore it is not necessary to apply an additional cut.

3.4.2 Proton Fiducial Cuts

Just as with electrons (see section 3.3.3), we need to define the regions of flat efficiencies for protons. We use the same technique as in the electron case to derive the proton fiducial cuts for different incident energies and magnetic field settings. Fig. 3-20 shows the angular distribution for protons before and after the fiducial cuts for one sector and one momentum bin. The gaps in θ indicate the cut on malfuctioning scintillation counters.

Because we can not detect an independent proton (each of the events always includes a triggering electron), to estimate the uncertainty of proton acceptance, we

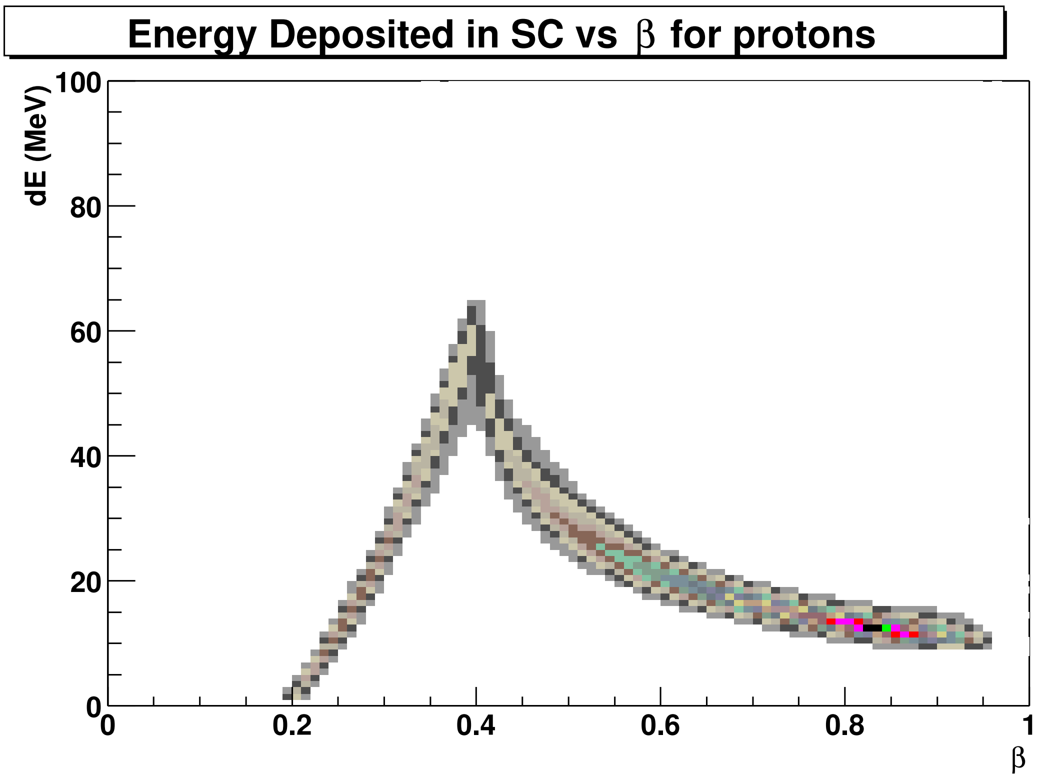

Figure 3-19: Energy deposited by proton candidates in SC vs β after the time of flight cut. One can see there is no minimum ionizing pion band and the proton band is very clean.

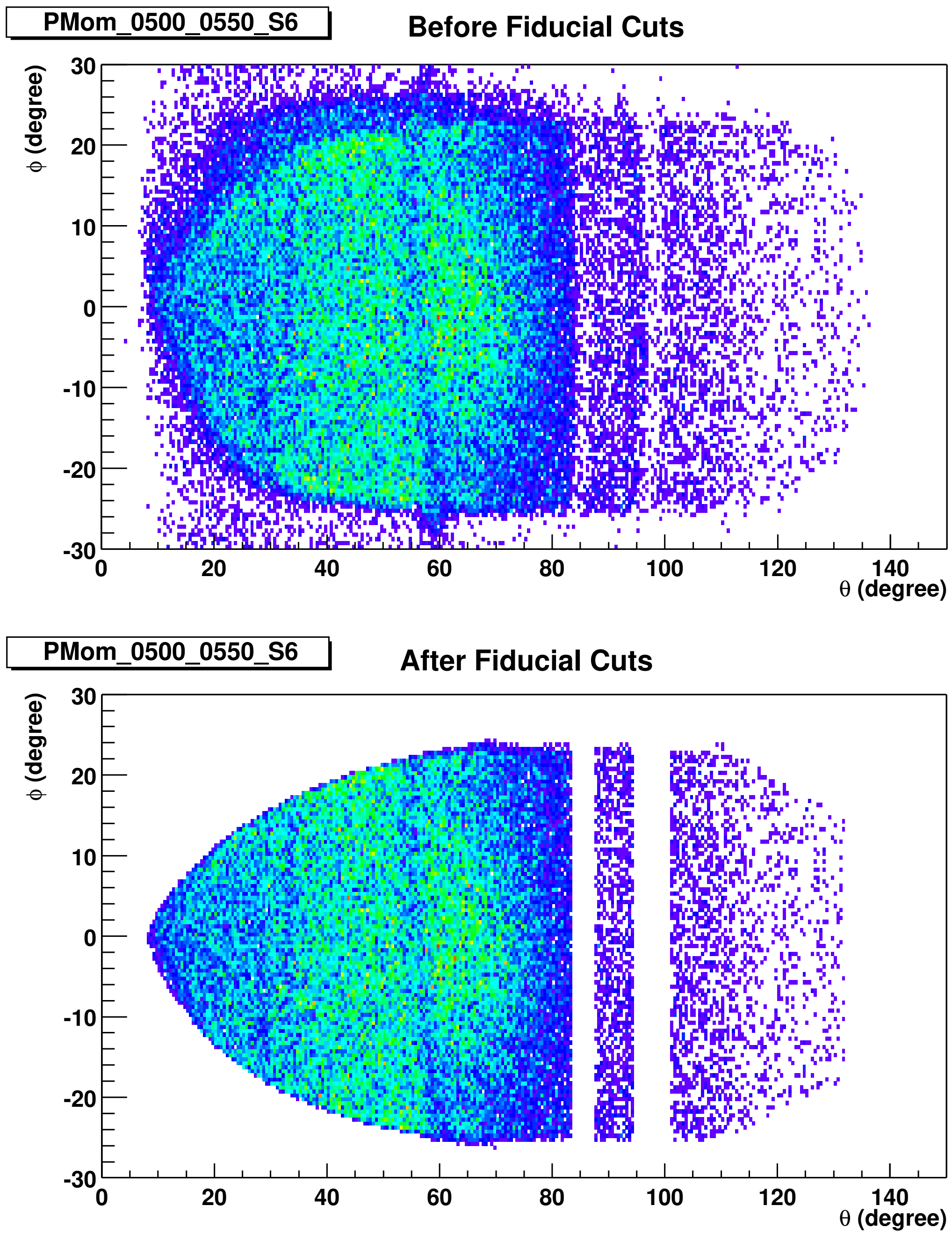

Figure 3-20: Proton angular distribution for momentum bin 0.50 - 0.55 GeV/c and sector 6. Upper plot is before the fiducial cuts and lower plot is after the fiducial cuts.

must use the (e,e'p) reaction. We made two measurements in the quasi-elastic region. In the first measurement, we only used sectors 1, 2 and 3 of CLAS to detect protons while in the second measurement we used the other 3 sectors. Ideally we should get the same cross sections using different parts of CLAS. So by comparing the two measurements we can get an idea of the quality of our knowledge of the proton acceptance.

We examined several kinematic points and a typical result is shown in Fig. 3-21. The figures shows two measured cross sections of ^{3}He(e,e'p) using different halves of CLAS ($\theta_{e'} = 30^o$, $E_0 = 2.261$ GeV and $E_{e'} = 1.7$ GeV) as functions of the proton momentum. The uncertainty of half of CLAS was estimated by the average deviation of the two measurements.

$$Error_{\frac{1}{2}CLAS} = \sqrt{\frac{1}{N}\sum_{i=1}^{N}\left(\frac{d\sigma_1^i - d\sigma_2^i}{(d\sigma_1^i + d\sigma_2^i)/2}\right)^2} = 7\% \tag{3.15}$$

Because the acceptances of the two halves of CLAS are independent, when we make the measurement using the whole CLAS, the total relative uncertainty should be

$$Error_{proton\,Acpt} = \frac{1}{\sqrt{2}} Error_{\frac{1}{2}CLAS} = \frac{7}{\sqrt{2}} = 5\% \tag{3.16}$$

3.4.3 Energy Loss Correction

Protons lose a small amount of energy when passing through the target material and the detectors. Especially for a low momentum proton, a considerable fraction of its energy can be lost before we detect it. In this data analysis, we are very interested in protons with low momenta and we have to correct the data for the lost energies. The best way to make the correction is using real data. If we could tag a missing proton in some reaction such as $H(e,e')p$ elastic or $^3He(e,e'pn)p$, we might be able to make the correction by comparing the proton energy calculated kinematically with the measured energy. We actually use this technique for neutron momentum corrections

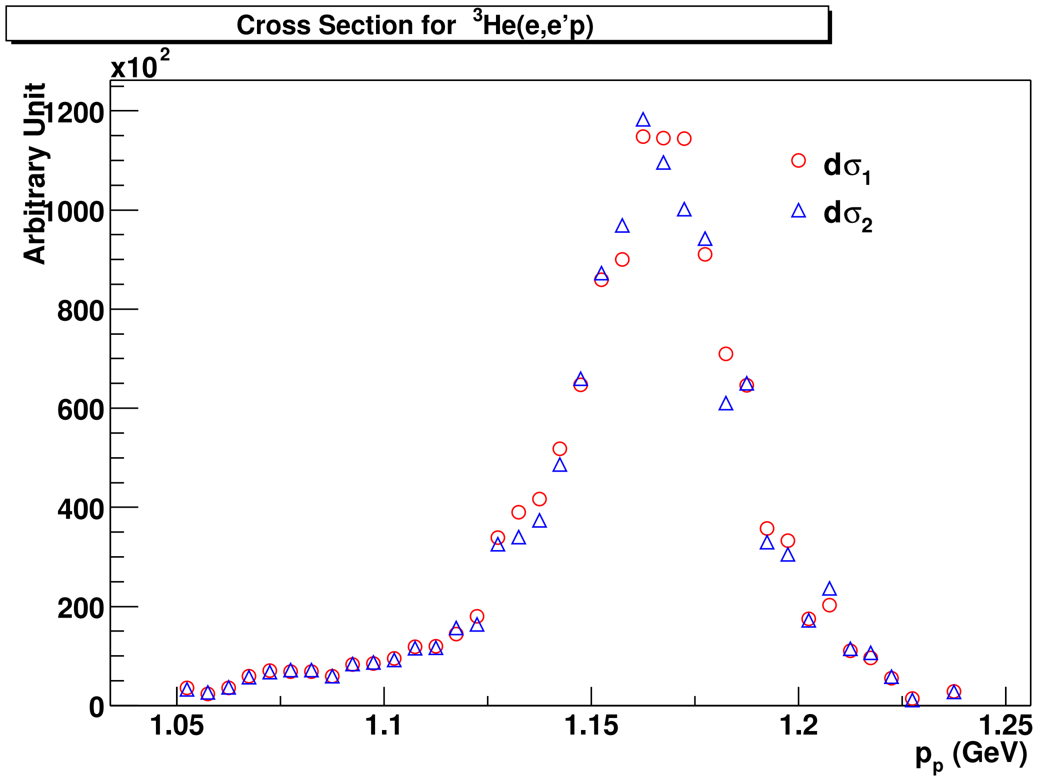

Figure 3-21: ^{3}He(e,e'p) cross section as a function of proton momentum was measured (1) using sector 1, 2, 3 and (2) using sector 4, 5, 6. We denote the cross section as $d\sigma_1$ and $d\sigma_2$ respectively. The incident energy is 2.261 GeV, the electron scattering angle is 30^o and the momentum of the scattered electron is 1.7 GeV/c.

and efficiency determinations later in section 3.5.3. Unfortunately, the available data lack statistics to tag protons in the momentum range in which we are interested. Therefore we made the energy loss correction by GSIM, a GEANT based simulation for CLAS [20].

First we generated protons with a flat distribution in the momentum range of interest, which is from 200 MeV/c to 1 GeV/c. Then we passed the generated protons to GSIM, which simulated the behavior of the protons and the responses of the detectors. The output of GSIM is a set of “pseudo” data with exactly the same structure of the real data. This data was analyzed in the same way as we analyze the real data. By comparing the reconstructed protons to the generated protons, we were able to determine how much energy was lost. Fig. 3-22 shows the difference between the generated momentum and the reconstructed momentum as a function of the reconstructed momentum for the ^3He target and 2250A torus current setting. The correction function was then determined using a polynomial fit. It has a strong dependency on the momentum and only protons with very low momenta (less than 500 MeV/c) lose sizable amounts of energies. Also note the resolution of the proton momentum measurement is taken as the width of the band (about 15 MeV/c).

3.4.4 Proton Detection Efficiency

With the same GSIM simulation discussed in the previous section 3.4.3, we can also get the efficiencies of the proton detection. Fig. 3-23 shows the number of the generated protons and the number of the reconstructed protons as functions of the momentum (energy loss corrected) for the ^3He target and 2250A torus current setting. The detection efficiency was obtained by fitting the ratio of the two numbers. One can see the proton detection efficiency is close to 1 in CLAS with slight inefficiencies for very low momentum protons. To avoid the error associated with using very small efficiencies, we required the momenta of all protons to be greater than 250 MeV/c in this data analysis. The uncertainty of the efficiency was estimated by investigating

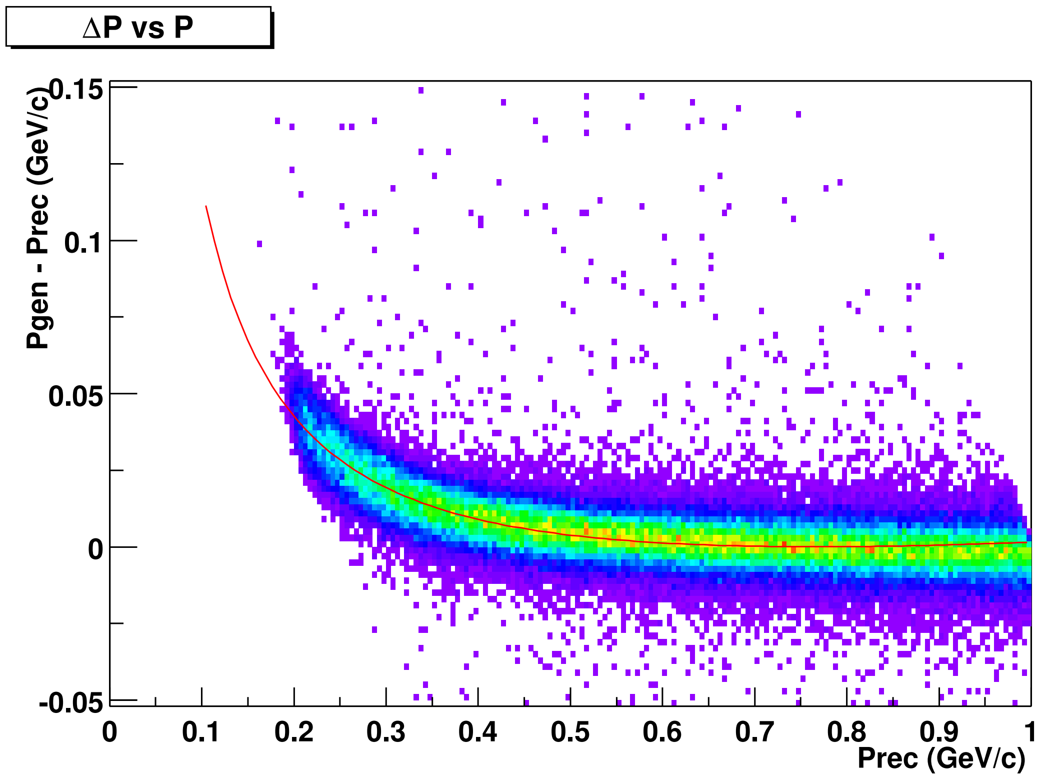

Figure 3-22: The momentum difference of generated and reconstructed protons as a function of the reconstructed momentum for the ^3He target and 2250A torus current setting.

the average deviation of the data curve from the fitting curve in all bins of the bottom plot of Fig. 3-23.

$$Error_{protonEff} = \sqrt{\frac{1}{N}\sum_{i=1}^{N}\left(\frac{\epsilon_i^{data}}{\epsilon_i^{fit}} - 1\right)^2} = 2\% \tag{3.17}$$

Because the energy loss correction and the detection efficiencies are dependent on the target materials and the magnetic fields, we did the same study for all target types and torus current settings and then applied the corrections separately. The errors are all about 2%.

3.4.5 Close Tracks Efficiency

When two charged particles have the same charge and their momenta are close to each other, they will hit the same or neighboring detector cells. This makes the reconstruction of both particles very difficult. Sometimes the reconstruction software considers them as one particle and in some cases it may be so confused that neither of the particles is reconstructed. Fig. 3-24 shows examples of two close proton tracks in the detectors.

Close tracks efficiency is directly related to how close the two tracks are from each other. The closer the two tracks are from each other, the smaller the efficiency is. As the result, the efficiency depends on the relative momentum and the average momentum of the two particles. Either decreasing the relative momentum or increasing the average momentum of the two particles will bring the two tracks closer to each other in a fixed magnetic field. We define the close tracks efficiency $\epsilon(q,p)$ as

$$\frac{d\sigma_{measured}}{d\omega dQ^2 d\vec{p_1} d\vec{p_2}} = \epsilon(q,p)\cdot\epsilon_1(p_1)\cdot\epsilon_2(p_2)\cdot\frac{d\sigma}{d\omega dQ^2 d\vec{p_1} d\vec{p_2}} \tag{3.18}$$

where $\vec{p_1}$, $\vec{p_2}$ are momenta of particles in the lab frame, $\vec{p} = (\vec{p_1} + \vec{p_2})/2$, $\vec{q} = \vec{p_1} - \vec{p_2}$ and ϵ_1, ϵ_2 are single particle reconstruction efficiencies.

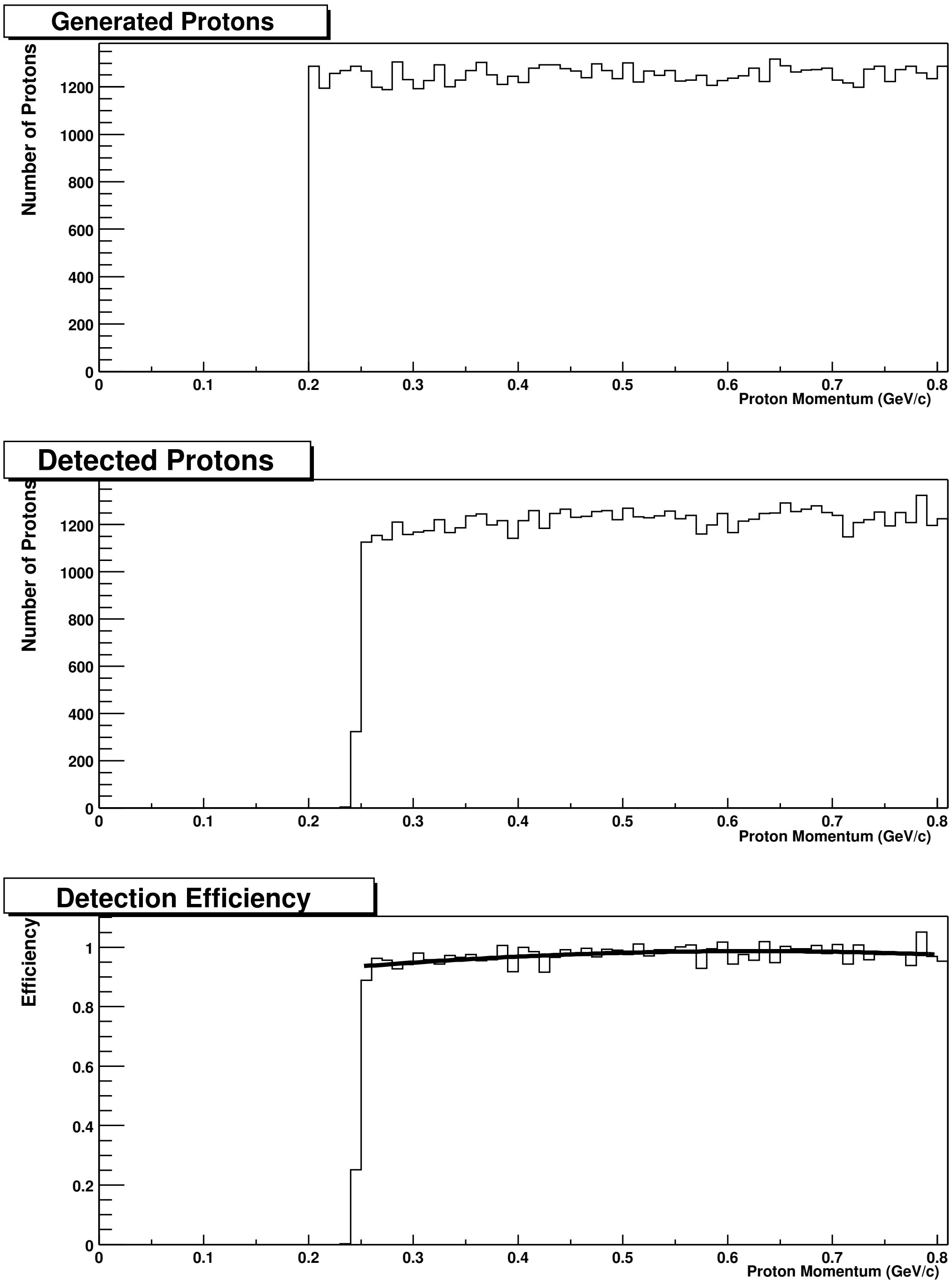

Figure 3-23: Proton detection efficiency as a function of energy loss corrected momentum for the ^3He target and 2250A torus current setting.

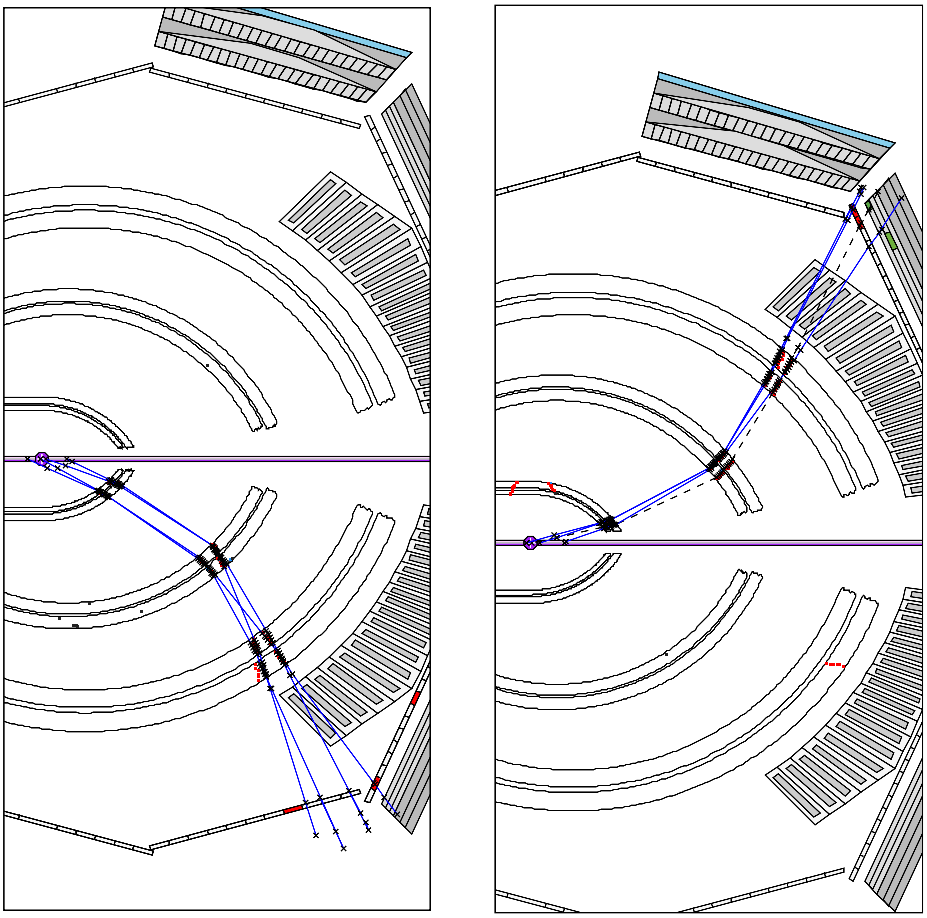

Figure 3-24: Examples of two close proton tracks in the detector

For this data analysis purpose, we are only interested in close tracks efficiency for protons in some kinematic settings (where the two protons are both close to the momentum transfer direction). We used two different methods to study the close tracks efficiency. One uses GEANT based simulations to generate close tracks and checks how often we can detect both of them. The other is more complicated, which involves selecting two real proton tracks from different events to form a "pseudo" event then checking how often we can reconstruct both of the protons (see detailed procedures in [29]). The results from the different methods agree with each other very well. Fig.3-25 shows a typical efficiency curve as a function of the relative momentum of the two protons when the average momentum of the two protons is 700 MeV/c.

The close-track-efficiency correction only affects data that the relative final momentum of the two protons is below 300 MeV/c (only 10% of the selected events). The systematic error of the efficiency itself was estimated by the fitting procedure to be smaller than 5% [29]. So it is reasonable to make a conservative estimation of the error as

$$Error_{closetrack} = 1\% \tag{3.19}$$

3.4.6 Comparison with Hall A (e,e'p) Data

To get confidence about our measurements, we want to compare our cross sections with those measured somewhere else and probably of better precision. A measurement of ^{3}He(e,e'p)d was recently performed in Hall A at Jefferson Lab at perpendicular kinematics. The incident beam energy of Hall A data is 4803 MeV, q is 1500 MeV, ω is 837 MeV and the electron scattering angle is 16.4 degrees. We have a set of data with the beam energy of 4.461 GeV. With the advantage of the large kinematics coverage of CLAS, we are able to select events to match Hall A's q and ω, resulting in a small difference of the electron scattering angle (ours is 17.8 degrees). We can cover the missing momentum up to 300 MeV/c with reasonable statistics.

Fig. 3-26 shows the missing mass and the missing energy of our ^{3}He(e,e'p) data.

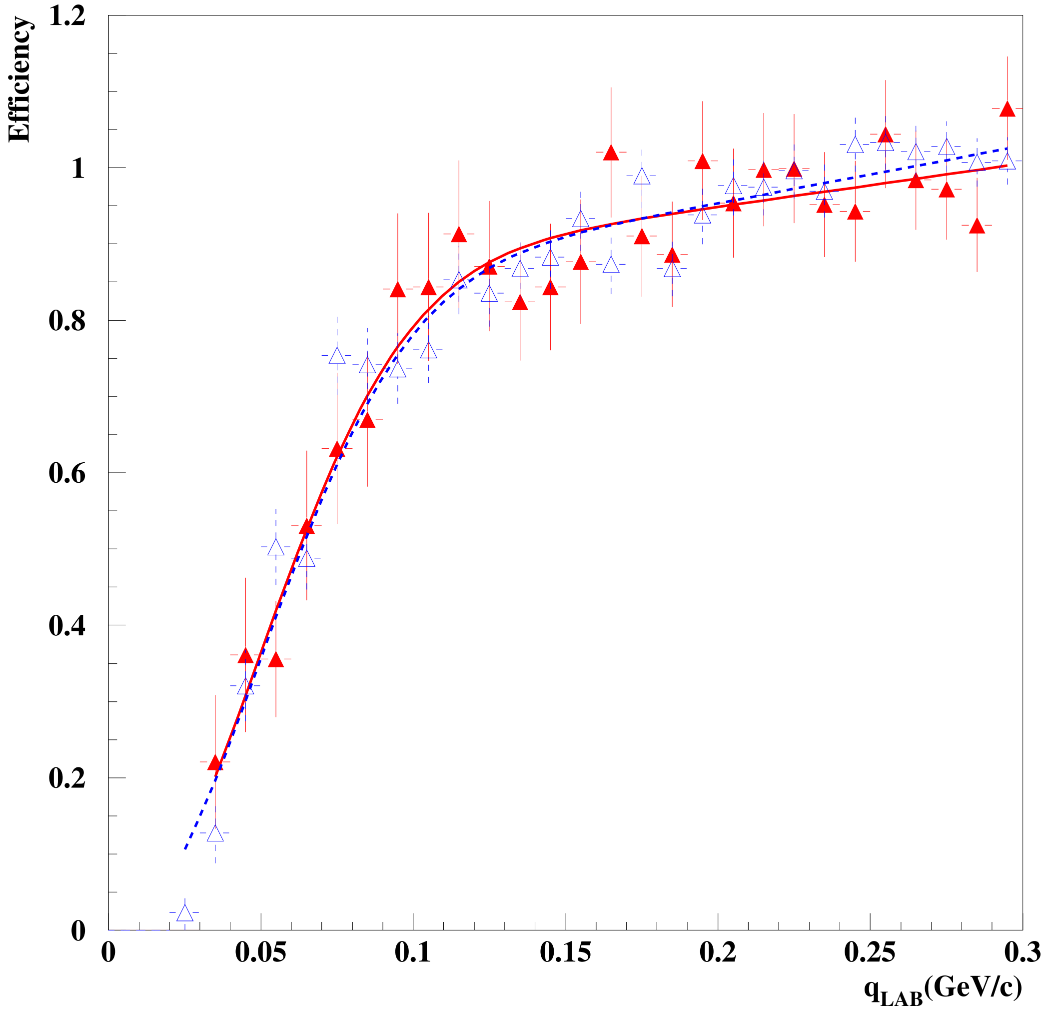

Figure 3-25: Close tracks efficiency for two protons as a function of their relative momentum when their average momentum is 700 MeV/c. The closed triangles and solid line are from simulations; the open triangles and dashed line are from real protons.

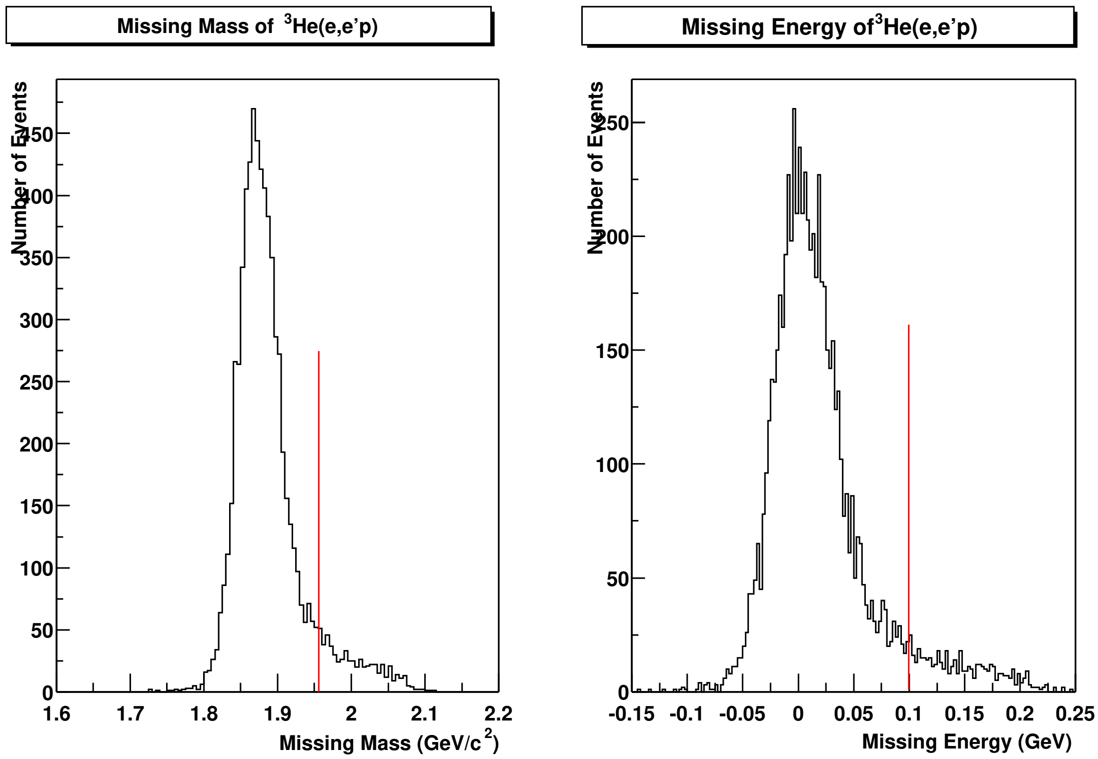

Figure 3-26: Missing mass and energy of ^{3}He(e,e'p). The red lines indicates the cuts below the pion threshold.

We cut them below pion threshold (because of this cut, a radiative correction was performed on the data with the same precedure discussed in Section 3.9). We don't have the resolution to separate 2-body breakup from 3-body breakup. However, Hall A preliminary data (both 2-body and 3-body breakups) agree well with theoretical calculations using Salme's spectral functions and CC1 off-shell elementary cross sections with missing momentum up to 300 MeV [59]. So it is reasonable for us to use the same theoretical model to estimate the relative strength of 2-body and 3-body breakups and subtract the 3-body contribution (15% to 50%) from our data.

To make a fair comparison, we have to take out terms which are different between the two measurements, as much as possible from the cross sections. The differential cross section of (e,e'p) reads:

$$\frac{d^5\sigma}{d\omega d\Omega_{e'} d\Omega_p} = R\frac{E_p p_p}{(2\pi)^3}\sigma_{Mott}(V_L R_L + V_T R_T + V_{LT} R_{LT}\cos\phi + V_{TT} R_{TT}\cos 2\phi) \quad (3.20)$$

where R is the recoil factor, σ_{Mott} is the Mott cross section, ϕ is the proton out-of-plane angle, V represents kinematic factors, R represents response functions, the subscriptions L, T, LT and TT indicate the longitudinal, transverse and interference terms. Our measured cross sections are actually averaged over ϕ, which include only the $V_L R_L + V_T R_T$ term. The Hall A data do not have complete ϕ coverage, so we use the average values as $d\sigma = (d\sigma(\phi = 0^o) + d\sigma(\phi = 180^o))/2$, which results to be $V_L R_L + V_T R_T + V_{TT} R_{TT}$. In fact, comparing $d\sigma/\sigma_{Mott}$ is appropriate for the following reasons:

1. the recoil factors are the same because we have the same hadron kinematics,

2. the response functions are the same because we have the same q and ω,

3. V_L is the same and the difference in the electron scattering angle (16.4^o vs 17.8^o) only causes a difference smaller than 1% in V_T,

4. $V_{TT} R_{TT}$ contribution to the cross section is estimated by the theoretical calculation mensioned above to be smaller than 2%.

Fig. 3-27 shows the comparison of the cross sections divided by σ_{Mott} between our data and Hall A preliminary data (their analysis has not been finalized at this time, however the final results will not differ by more than a few percent), as well as the ratio of the two. The systematic uncertainty for our (e,e'p) measurements is estimated to be about 13% (see Section 3.10 for individual contributors). One can see our data agree with Hall A data very well within this error range.

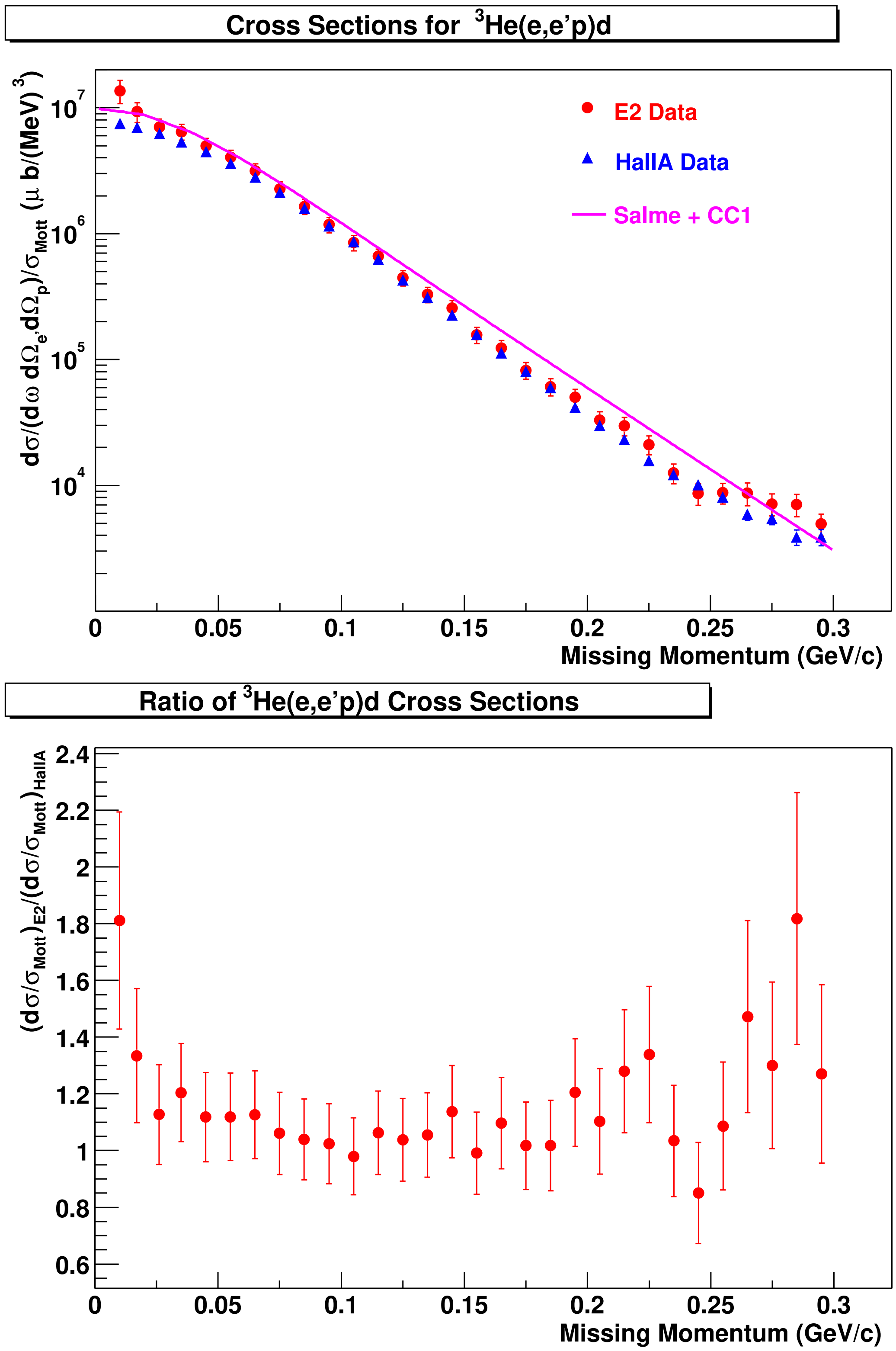

Figure 3-27: Comparison of $d\sigma/\sigma_{Mott}$ for ^{3}He(e,e'p)d with Hall A preliminary data. The bottom plot is the ratio of the two.

3.5 Neutron Detection

3.5.1 Neutron Indentification and Fiducial Cuts

Neutron Identification is determined by the fact that there is a clear neutral hit in the Electromagnetic Calorimeter (EC) without a matching track in the Drift Chambers (DC) or a matching hit in the Scintillation Counters (SC). Moreover, the velocity of the neutral particle should be less than the speed of light. Fig. 3-28 is the typical β distribution for neutral particles measured by the EC. The peak around 1 indicates photons while particles to the left are neutrons. A Gaussian fit of the photon peak shows that its left tail ends above $\beta = 0.9$. We then put the neutron ID cut at this point, i.e. we assign the neutron ID to a neutral particle if its $\beta < 0.9$ which corresponds to the momentum of 1.94 GeV/c (In fact, the neutrons we actually selected in the data analysis turned out to be slower than 1.7 GeV/c or $\beta < 0.875$). Clearly, there is no sizable contamination from photons. The only error could come from resolution effect. Relating the resolution in β, $\Delta\beta$, to the resolution in time, Δt, we have

$$\Delta\beta = \Delta\left(\frac{l}{tc}\right) = \frac{\beta^2 c}{l}\Delta t \tag{3.21}$$

where l is the path length (5 to 6 meters), t is the time of flight and c is the speed of light. The β distribution of neutrons showed in Fig. 3-28 is actually convolved with the resolution that is proportional to β^2. By a de-convolution, we estimate that the cut at $\beta = 0.9$ causes a loss of about 2% for neutrons with $\beta = 0.875$, where the biggest loss occurs. Therefore, a conservative estimation of error is

$$Error_{neutronID} = 2\% \tag{3.22}$$

Because close to EC edges there is a lot of energy leakage, which can significantly affect the time measurement and furthermore can change the efficiencies unpredictably, we have to make a cut to get rid of this edge effect and use events only

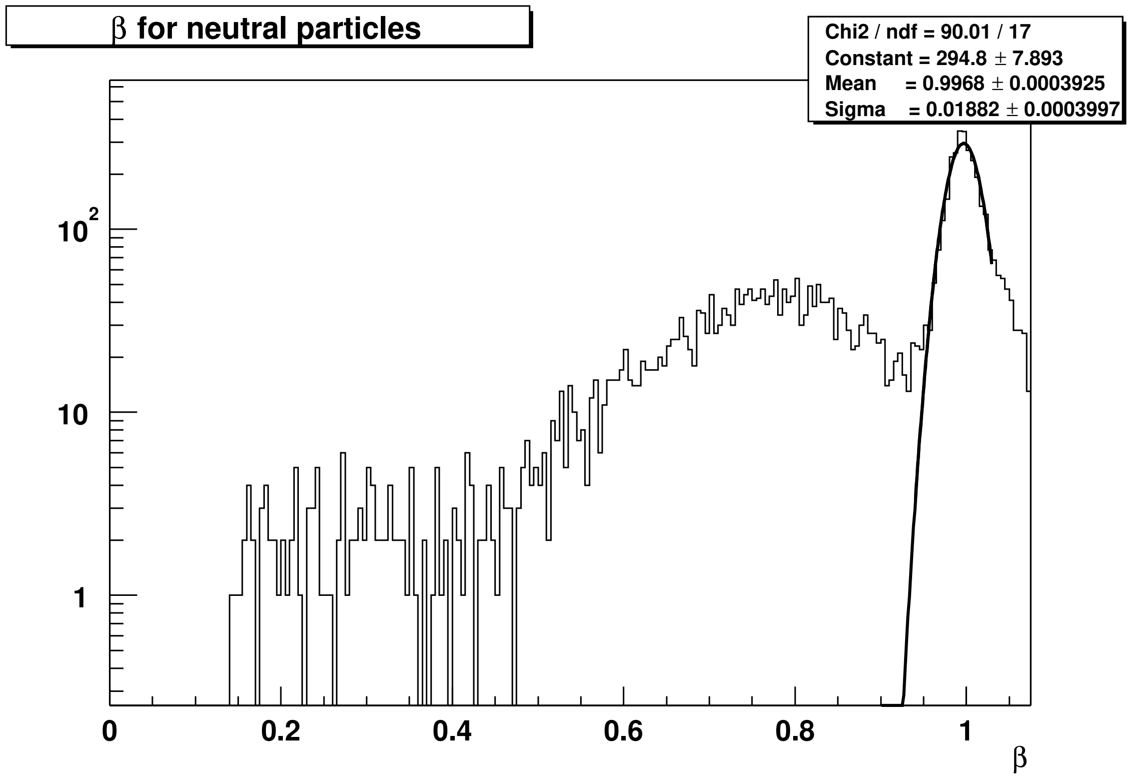

Figure 3-28: β distribution for neutral particles. The peak centering at 1 is from photons while particles to the left are neutrons.

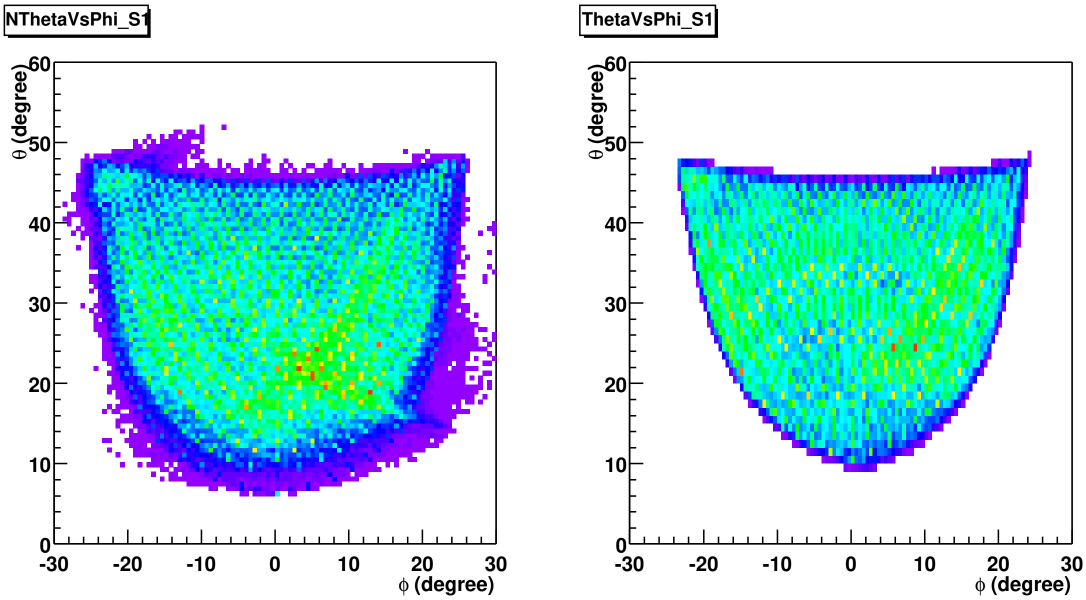

Figure 3-29: θ vs ϕ for neutrons in sector 1. The left figure is before the fiducial cut while the right figure is after the cut.

within the so-called fiducial region where the detection efficiencies can be trusted. Because the track of a neutral is just a straight line from the vertex to the hit spot in EC, and the target's length (4 cm) is negligible compared to the path length ($\sim$ 5.5 m), a simple geometrical cut on the particle's direction is sufficient and the cut is not dependent on the momentum of the particle. Fig. 3-29 shows the effect of this fiducial cut for one EC sector. One can see the fiducial cuts get rid of the inefficient regions around the edge of the EC.

Then we applied the similar procedure as we used in the proton case (see section 3.4.2) to estimate the uncertainty of the neutron acceptance. We measured ^{3}He(e,e'n) cross sections in the quasi-elastic regions using two halves of CLAS (the determination of the detection efficiency for neutrons is discussed in Section 3.5.3). Fig. 3-30 shows the two measured cross sections. The uncertainty of half of CLAS was estimated by the average deviation of the two measurements.

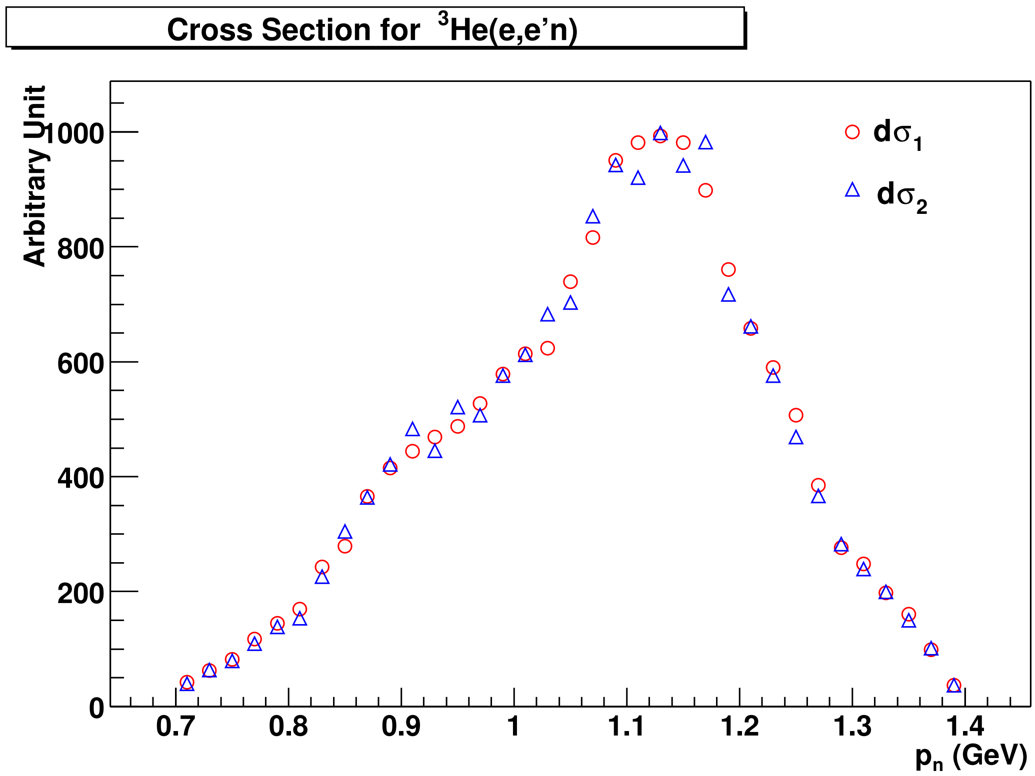

Figure 3-30: ^{3}He(e,e'n) cross sections as functions of the neutron momentum was measured (1) using sector 1, 2, 3 and (2) using sector 4, 5, 6. We denote the cross sections as $d\sigma_1$ and $d\sigma_2$ respectively. The incident energy is 2.261 GeV, the electron scattering angle is 30 degrees, the scattered electron momentum is 1.7 GeV/c and θ_{nq} is integrated from 0^o to 10^o to get enough statistics.

$$Error_{\frac{1}{2}CLAS} = \sqrt{\frac{1}{N}\sum_{i=1}^{N}\left(\frac{d\sigma_1^i - d\sigma_2^i}{(d\sigma_1^i + d\sigma_2^i)/2}\right)^2} = 8\% \tag{3.23}$$

Because the acceptances of the two halves of CLAS are independent, when we make the measurement using the whole CLAS, the total relative uncertainty should be

$$Error_{neutronAcpt} = \frac{1}{\sqrt{2}} Error_{\frac{1}{2}CLAS} = \frac{8}{\sqrt{2}} = 6\% \tag{3.24}$$

3.5.2 Neutron Momentum Correction and Resolution

Due to the difficulty of the EC time calibration (See 3.2.3), after reconstruction of the data we found the EC time measurement for high momentum neutrons, was not correct somehow. This can be seen in the upper plot of Fig. 3-32, which is the missing mass spectra for $^3He(e,e'np)$. We can see the proton peak is centered at 0.921 GeV/c^2, which is not the right proton mass. Therefore we need to correct the momentum of the neutron. To make the correction, we used $H(e,e'\pi^+)n$ reaction from Hydrogen data which was taken one month before this experiment.

First, we select events in the Δ resonance region by cutting the invariant mass around the Δ region, then identify the neutron with the missing mass technique. We can calculate the neutron momentum vector from kinematics. Once we detect a neutron within a small angle around the predicted direction, we can determine how much the magnitude of the detected momentum differs from the expected value. The top plot of Fig. 3-31 shows the ratio of the momenta of the detected and expected neutrons as a function of the detected momentum (this ratio should be 1 if the momentum is correctly measured). The two bands correspond to the errors in time measurements by the inner and the outer layers of the EC. The correction function was determined by two quadratic fittings. After applying the correction function, we brought the ratio back to 1 as shown in the middle plot of Fig. 3-31. From the lower plot of Fig. 3-32, we can also see the neutron momentum correction brings the proton peak of the missing mass spectra for $^3He(e,e'np)$ back to the right position.

The momentum correction does not improve the momentum resolution. The momentum resolution of neutrons is dependent on the resolution of EC time. From

$$p = m\beta\gamma = \frac{m\beta}{\sqrt{1-\beta^2}} \tag{3.25}$$

where p is the neutron momentum and m is the stationary mass of a neutron, we can get

$$\frac{\Delta p}{p} = \frac{\Delta\beta}{\beta(1-\beta^2)} \tag{3.26}$$

And from

$$\beta = \frac{l}{tc} = \frac{p}{\sqrt{m^2+p^2}} \tag{3.27}$$

where t is the time of flight, l is the path length and c is the speed of light, we can get

$$\frac{\Delta\beta}{\beta} = \frac{\Delta t}{t} = \frac{\beta c \Delta t}{l} \tag{3.28}$$

After plugging 3.27 and 3.28 into 3.26, we can get

$$\frac{\Delta p}{p} = \frac{pc\sqrt{m^2+p^2}}{lm^2}\Delta t \tag{3.29}$$

We can see the momentum resolution of neutrons increases with the momentum. In the bottom plot of Fig. 3-31, the resolution is shown as a function of the momentum (we sliced the middle plot of Fig. 3-31 along the y axis at different momenta, performed a Gaussian fit for each slice and took the σ as the resolution). It ranges from below 10% for low momentum neutrons to above 15% for high momentum neutrons and the values are consistent with Equation 3.29 given the typical value for l is from 5 to 6 meters and the EC time resolution is about 0.6 ns.

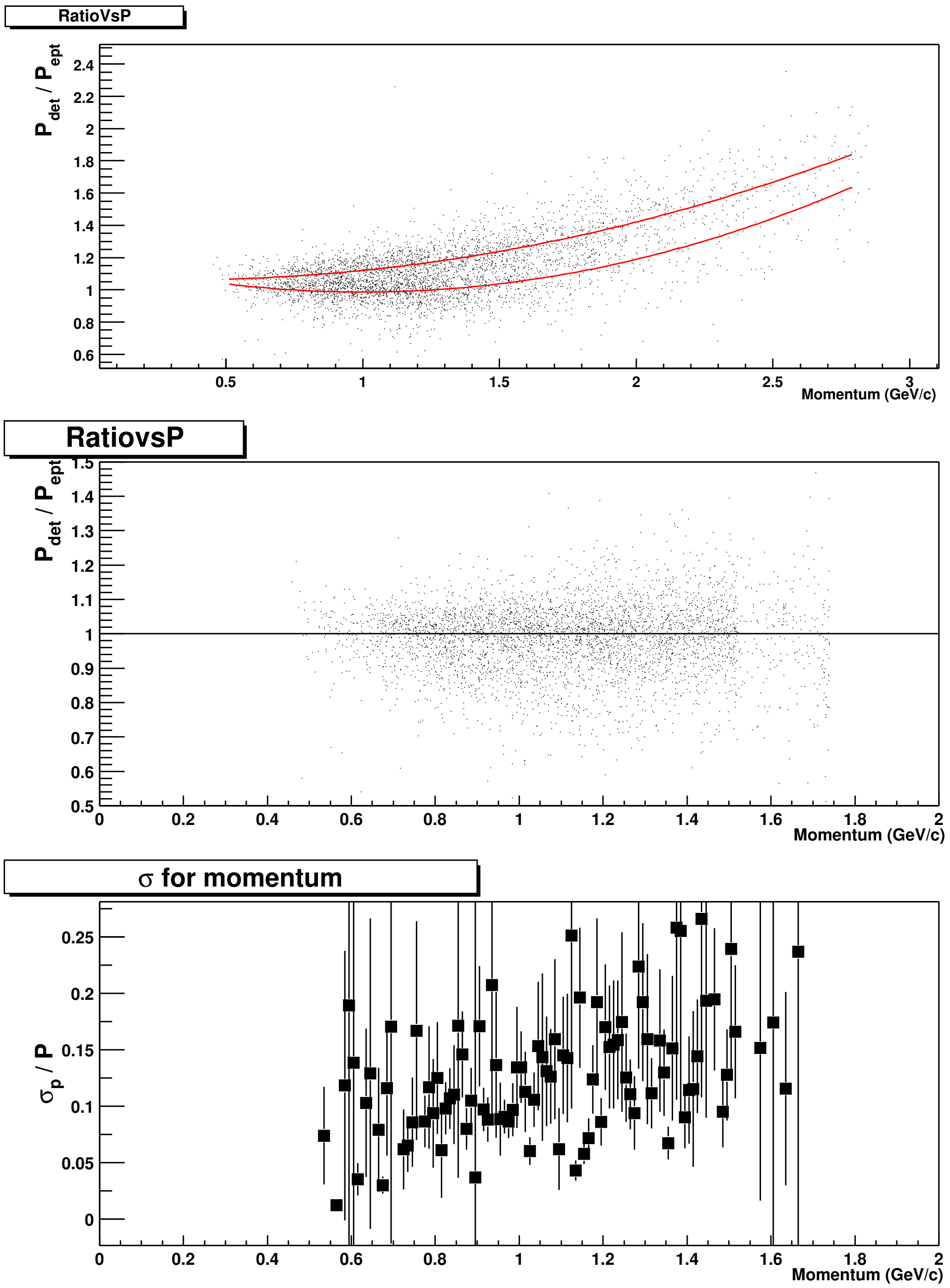

Figure 3-31: Neutron momentum correction using the $H(e, e'\pi^+)n$ reaction. The top plot is the ratio of the momenta of the detected and expected neutrons before the momentum correction. The middle plot is the same after the momentum correction. The bottom plot is the neutron's momentum resolution (σ obtained by a Gaussian fit of the ratio in the middle plot) vs the momentum.

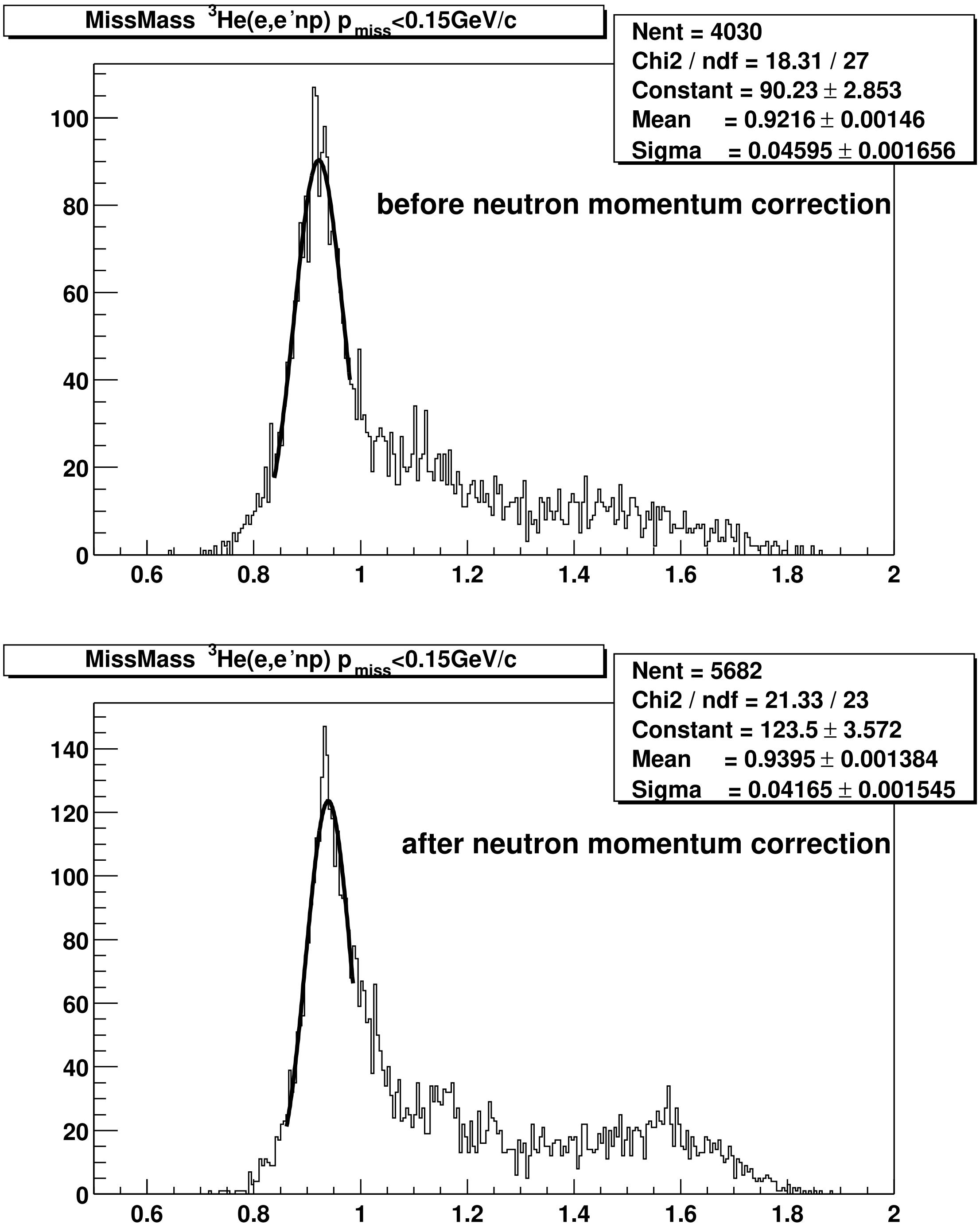

Figure 3-32: Missing mass of $^3He(e, e'np)$ in the unit of GeV/c^2 before (top) and after (bottom) neutron momentum correction.

3.5.3 Neutron Detection Efficiency

The CLAS Electromagnetic Calorimeter is fairly efficient to the detection of neutrons. Because neutrons are mostly detected by (n,p) scattering and the showers produced by the protons scattered from the materials, the neutron detection efficiencies strongly depend on the neutron momentum. The neutron detection efficiencies in CLAS have been stydied using several methods and the results agreed with each other very well [15],[30],[14] up to the momentum of 1.7 GeV/c, which is about the fastest neutrons detected in this experiment.

Generally speaking, there are two kinds of methods. One is using a GEANT based simulation, which of course requires a good description of device responses. The other, which is considered as a better approach, is using real data. Just as described in section 3.5.2, if we are able to tag a missing neutron in some reaction channels, we can look for neutrons in a small region around the predicted direction and get the detection efficiencies as the ratio of the number of detected neutrons and that of expected ones. Fig. 3-33 shows the neutron detection efficiencies as a function of the neutron momentum measured by $H(e,e'\pi^+)n$ [15],[30] and $D(\gamma,p\pi^+\pi^-)n$ [14]reactions.

For this experiment, we used Hydrogen data taken one month earlier. We analyzed the $H(e,e'\pi^+)n$ reaction and were able to re-produce the previous results measured by the same method [15],[30] as in Fig. 3-33. Most of the error came from the background we included in our data analysis. The upper plot of Fig. 3-34 shows the missing mass of $H(e,e'\pi^+)X$ in the Δ region. We made the cuts on the neutron mass peak with a width of 3σ which included 3.3% as background and the loss is negligible. The lower plot of Fig. 3-34 shows the distribution of the *cos* values of the angles between the expected and the detected neutrons. We made the cut to require the angles be smaller than 0.1 rad, which included 1.7% as background and the loss is negligible. So the error estimation is

$$Error_{neutronEff} = \sqrt{(3.3\%)^2 + (1.7\%)^2} = 4\% \tag{3.30}$$

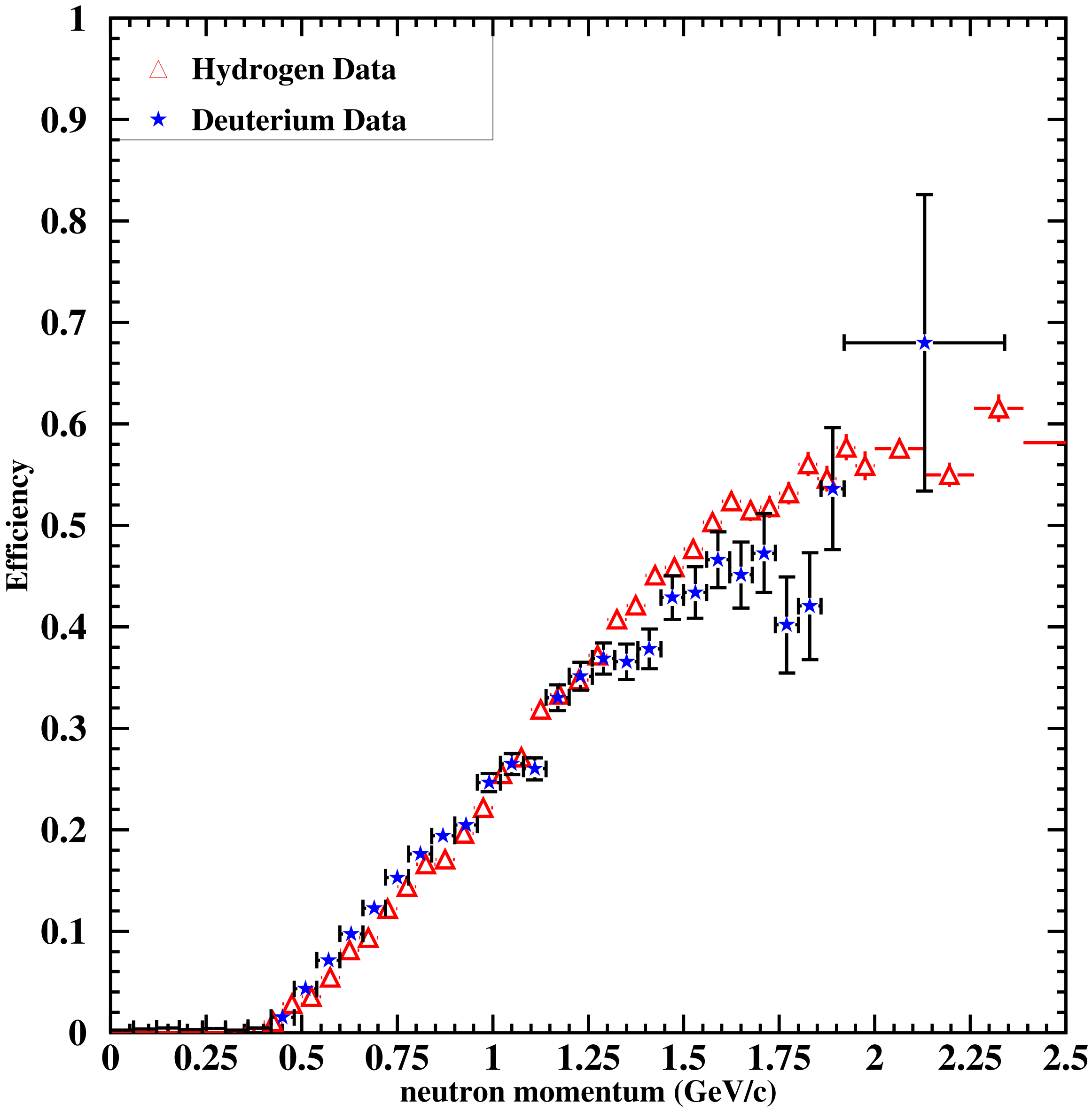

Figure 3-33: Neutron detection efficiencies as a function of the neutron momentum measured by $H(e, e'\pi^+)n$ and $D(\gamma, p\pi^+\pi^-)n$.

3.5.4 Comparison of (e,e'n) and (e,e'p)

As in the proton case (Section 3.4.6), to get confidence for the neutron detection, we compared ^{4}He(e,e'n) and ^{4}He(e,e'p) at the quasi-elastic regions. If we believe in the charge symmetry in NN interactions, the spectral functions for neutrons and protons in ^{4}He should be the same. The Final State Interactions for quasi-elastic reactions, at least in an impulsive picture, should also be the same. Although there are Coulomb effects in the (e,e'p) reaction, the effects should be very small at energies of this experiment. The only difference has to be the elementary cross sections. If we divide the ^{4}He(e,e'N) cross sections by the elementary off-shell cross sections (we chose to use the CC1 model [3] with recent nucleon dipole form factors), the results should be the same for neutron and proton cases.

Fig. 3-35 shows the comparison of the reduced cross sections (divided by CC1) for ^{4}He(e,e'n) and ^{4}He(e,e'p) at the quasi-elastic regions. The incident electron energy is 2.261 GeV, the electron scattering angle is 30 degrees, the momentum and the energy transfers are 1.15 GeV/c and 561 MeV respectively. One can see the neutron peak is much wider compared to the proton peak, which is due to the fact that the momentum resolution of neutrons (about 100 MeV/c in this case, see Section 3.5.2) is much worse than that of protons (about 15 MeV/c, see Section 3.4.3). To make a fair comparison, we smeared the proton peak with the same resolution function of neutrons. The smeared proton peak agrees with the neutron peak very well within the errors of our experiment. The overall integrated cross sections have a difference of about 10%, which could be caused by a slight charge "asymmetry" in meson currents and the Coulomb effects, etc.

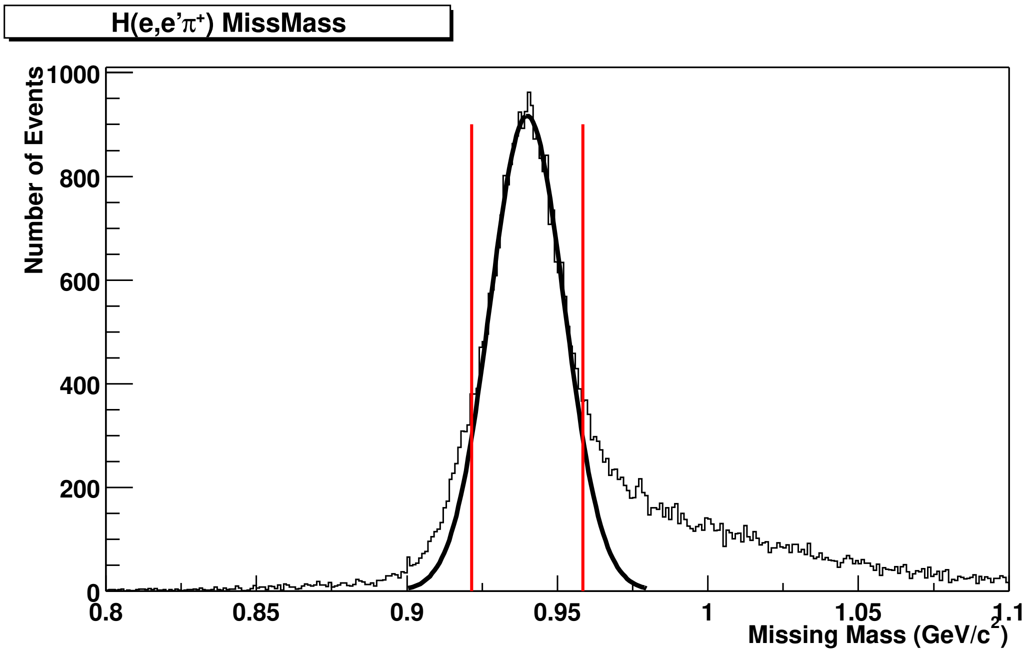

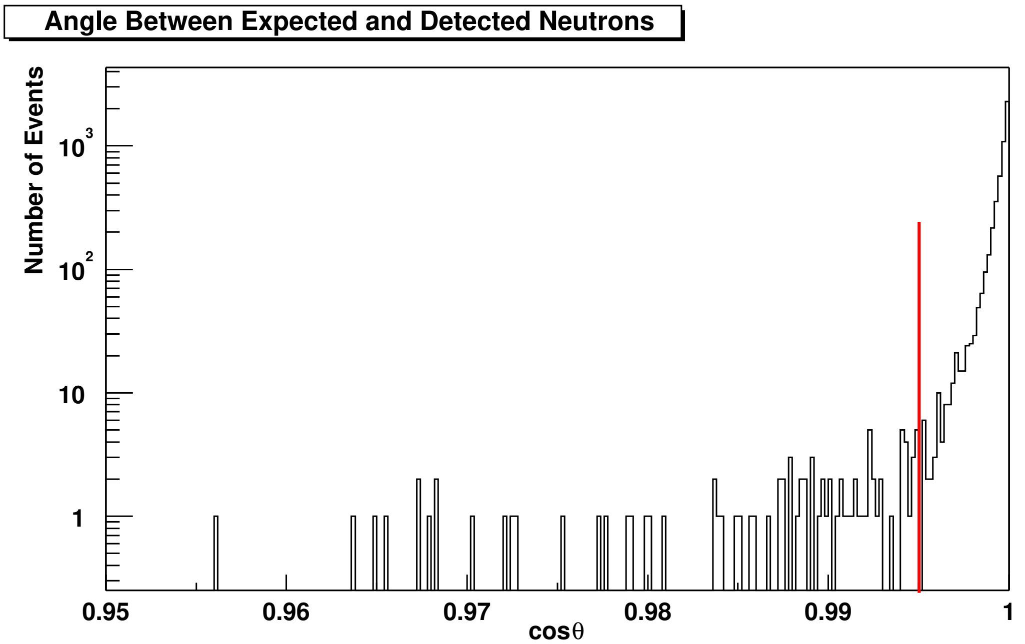

Figure 3-34: Upper plot is the missing mass of $H(e, e'\pi^+)X$ in Δ region. Lower plot is the distribution of *cos* value of the angle between the expected and detected neutrons. The vertical lines are showing the cut points.

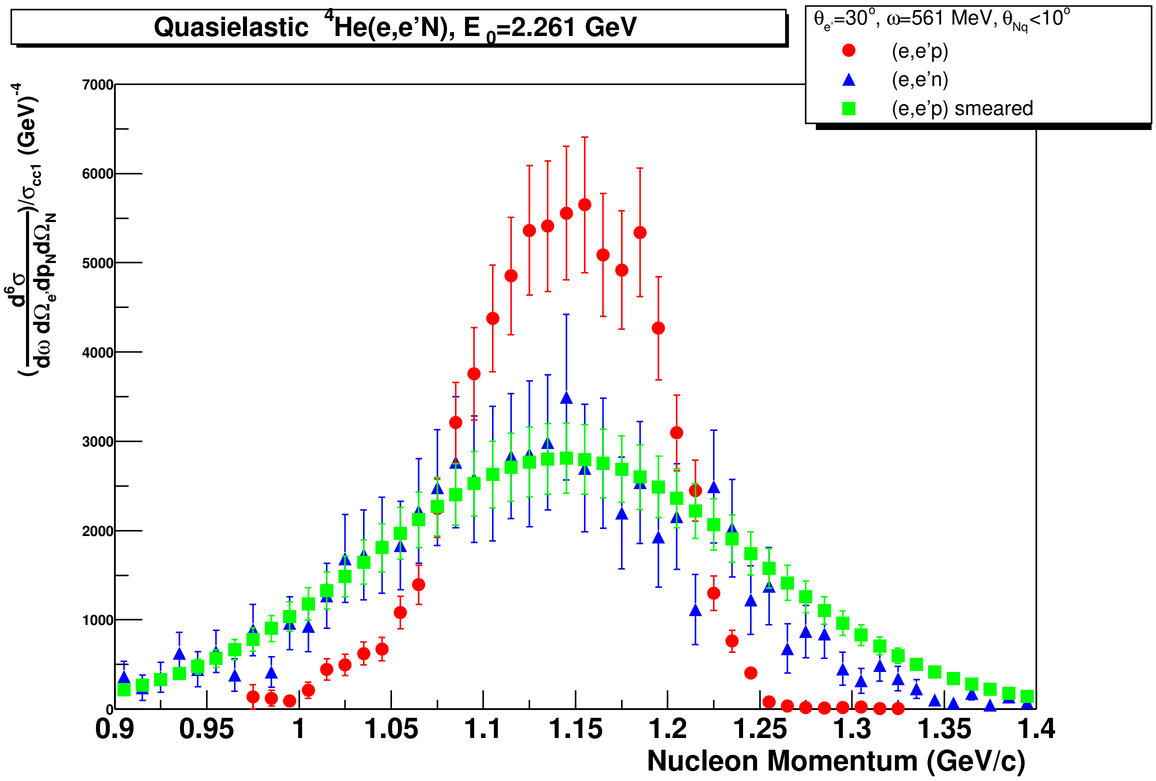

Figure 3-35: Comparison of cross sections of quasi-elastic ^{4}He(e,e'n) and ^{4}He(e,e'p) divided by CC1. The incident electron energy is 2.261 GeV, the electron scattering angle is 30 degrees, the momentum and the energy transfers are 1.15 GeV/c and 561 MeV respectively.

3.6 Absolute Normalizations

3.6.1 Beam Charge

The accumulated charge of the incident electrons is tracked by a Faraday Cup. A scaler-counter keeps counting the electron charge accumulated by the Faraday Cup. Note the counter is live-gated, i.e. it counts only when the data acquisition system is "alive". So it automatically corrects for the computer and electronics deadtimes. Each count of the scaler represents $10^{-4}\mu C$ of charge. The scaler is recorded into the data stream every 10 seconds while the physics data recording rate is about 2 KHz. Duplicated scalers indicate that the beam was off for at least 10 seconds. To synchronize with the physics data, we also record the event number for the most recent physics event into each scaler event.

Although the charge scaler is recording the acumulative charge from the beginning of each run, it is still not appropriate just to take the scaler value in the end of the run as the total charge for several reasons. One reason is that during the data reconstruction some files could be corrupted and useless whthin one run (each run is broken into 10 to 40 files dependding on how long it lasted), but the charge scaler is still accumulating without interruptions. So in our data analysis, we broke the physics data stream into intervals, each with one immediately preceding scaler event and one immediately succeeding scaler event. Therefore the data taking was "continuous" within the intervals. We only analyzed the data within the intervals. We took the sum of the accumulated charges for all the intervals as the total charge.

The error associated with the total charge is very small. Our typical beam current was about 5 nA, so each scaler interval or each 10 seconds has

$$\frac{5nA \times 10sec}{10^{-4}\mu C/count} = 500 \quad counts \tag{3.31}$$

Because the counting is discrete, the error is 1 count out of 500, which is 0.2%. Even if we disregard the total number of scaler intervals in the data, which will significantly lower the error, we can conservatively estimate the error associated with the beam charge as

$$Error_{charge} = 0.2\%. \tag{3.32}$$

3.6.2 Target Thickness

We had three types of targets: liquid ^{3}He, ^{4}He and solid ^{12}C. The thickness of ^{12}C is the easiest one to determine, because it was labeled by the manufacturor. We also checked it by measuring the weight and surface area. The error of the measurement is less than 1%.

The best way to check our target thickness is comparing our data to reliable existing data. Fig. 3-36 shows the comparison of our inclusive cross section with that measured in Hall C of Jefferson Lab. Because there are no data available whose kinematics are exactly the same as ours to make a fair comparison, we have to approximately match the kinematics in the two cases. And the error bars of Hall C data actually represent the errors from this kind of kinematic approximation. One can see within the errors, our data reasonably agree with Hall C data.

The cryogenic ^{3}He and ^{4}He targets are very stable once they are liquidified. We recorded of their temperature and pressure during the whole run period. Their densities taken from temperature and pressure measurements had only a 1% fluctuation. The only problem is that we measured the temperature outside the target cells (the sensors were not inside the cells). So the densities measured by temperature and pressure might have errors as big as 10%. To get more precise values of the densities, we want to compare our inclusive cross sections to reliable data. As discussed above, it is almost impossible to match all kinematics exactly with other data. If we make an approximation, then we have to introduce a sizable error.

One solution to this is to use a theoretical calculation that is parameterized to fit other reliable data. We used Sargsian's code for inclusive cross section calculations

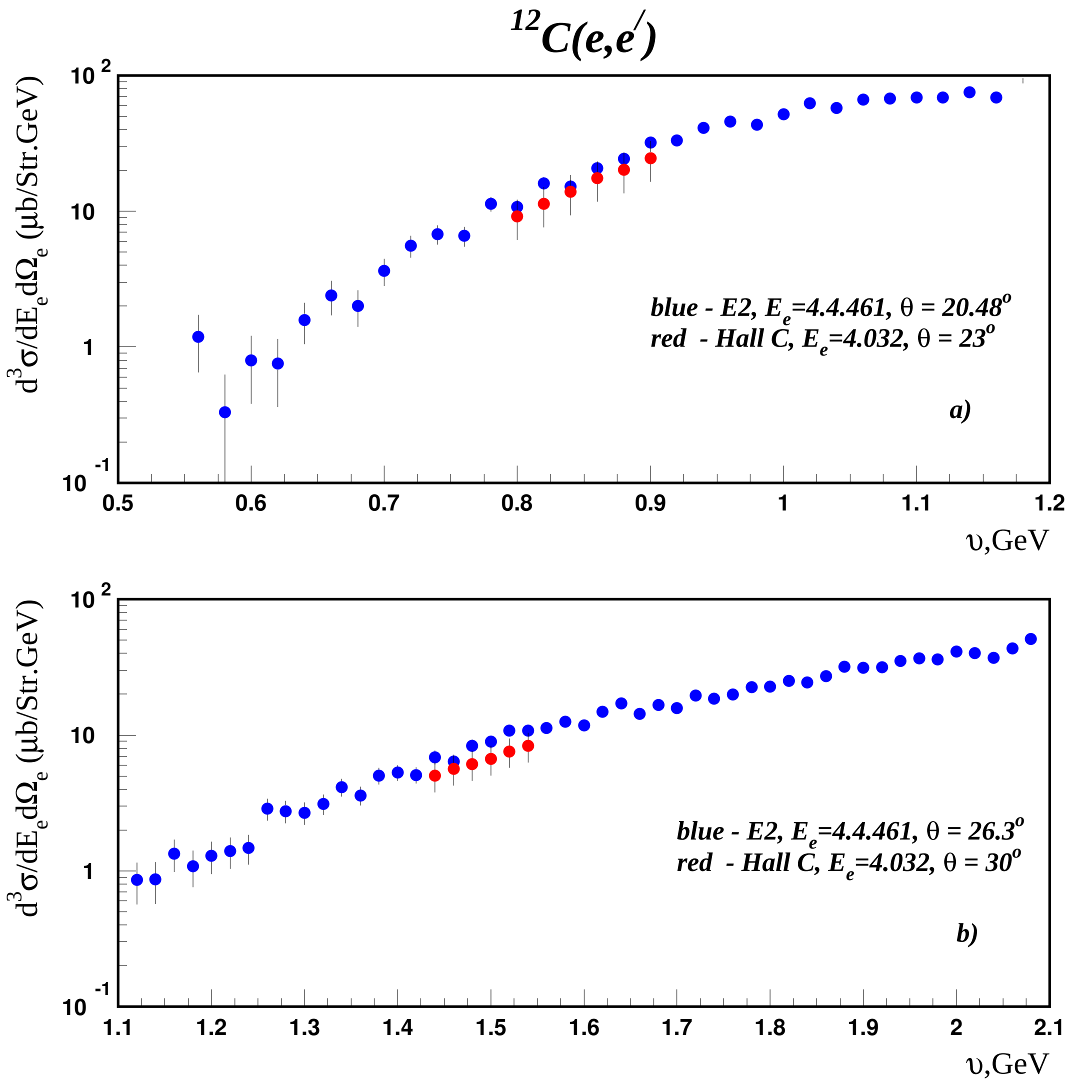

Figure 3-36: Comparison of our ^{12}C inclusive cross section (labeled as E2) as a function of energy transfer with Hall C data at two different electron scattering angles. The error bars of Hall C data represent the errors we have to consider when we approximately match the kinematics in the two cases.

Target	Density (g/cm^3)	Length (cm)	Thickness (g/cm^2)
^{3}He	0.0643	3.0	0.193
^{4}He Cell 1	0.1377	4.2	0.578
^{4}He Cell 2	0.1365	2.8	0.382
^{12}C	1.7860	0.1	0.179

Table 3.2: The density and thickness for all targets.

with radiative effects built in [62]. The code was based on two theoretical approaches: the Virtual Nucleon Impulse Approximation and the Impulse Approximation based on Light Cone Dynamics. It was parameterized to fit various SLAC data. It worked very well especially in the quasi-elastic regions (because we do not have enough elastic data, we have to use the quasi-elastic peak to normalize) with an error of less than 10%. Fig. 3-37 shows out ^{12}C inclusive cross sections compared with the calculations at two electron scattering angles. The calculation agrees very well with data to the accuracy of 3%.

Once we understand the accuracy of the theoretical calculation, we can use it to estimate the densities of our ^{3}He and ^{4}He targets. We used the quasi-elastic peaks of the inclusive cross sections. Because we are using the very efficient region of CLAS, we can assume the efficiency for electrons is 100% in the normalization. In fact, after the normalization the actual electron detection efficiency, which is a constant number very close to 1, is compensated by the overall normalization factors for target densities.

Fig. 3-38 shows our inclusive cross sections of ^{3}He, ^{4}He and the comparisons to calculations. We normalize the data to the theory in the quasi-elastic regions (to the right of the red lines) by equalling the integrated cross sections of the data and the theory. The normalization factors are about 0.98 in both cases. It means our nominal target densities measured by temperature and pressure agree with the theoretical calculations. The final target thickness values we use are in Table 3.2.

In the normalization, the statistical error is less than 1%, so the systematic uncer-

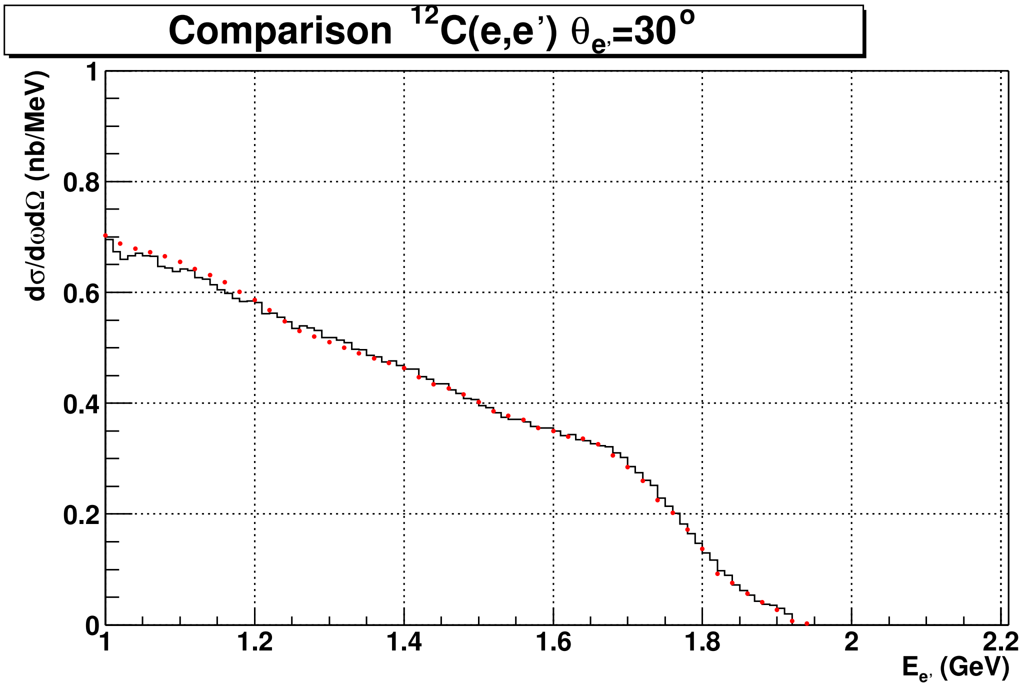

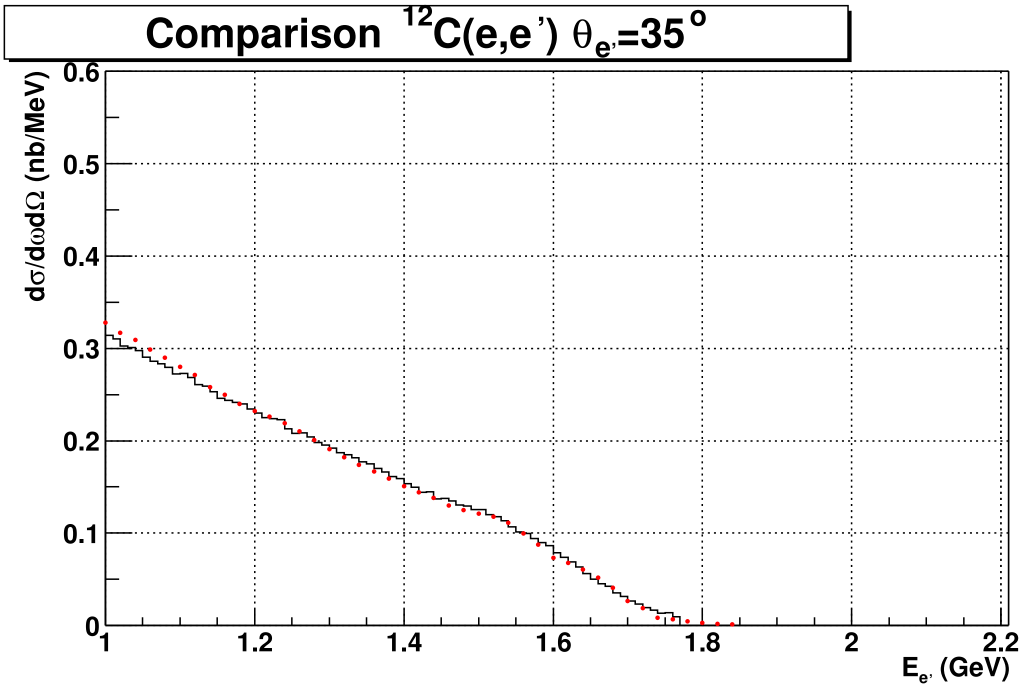

Figure 3-37: Comparison of our ^{12}C inclusive cross sections (histograms) as a function of scatterred electron energy with Sargsian's calculations (points) at two different electron scattering angles.

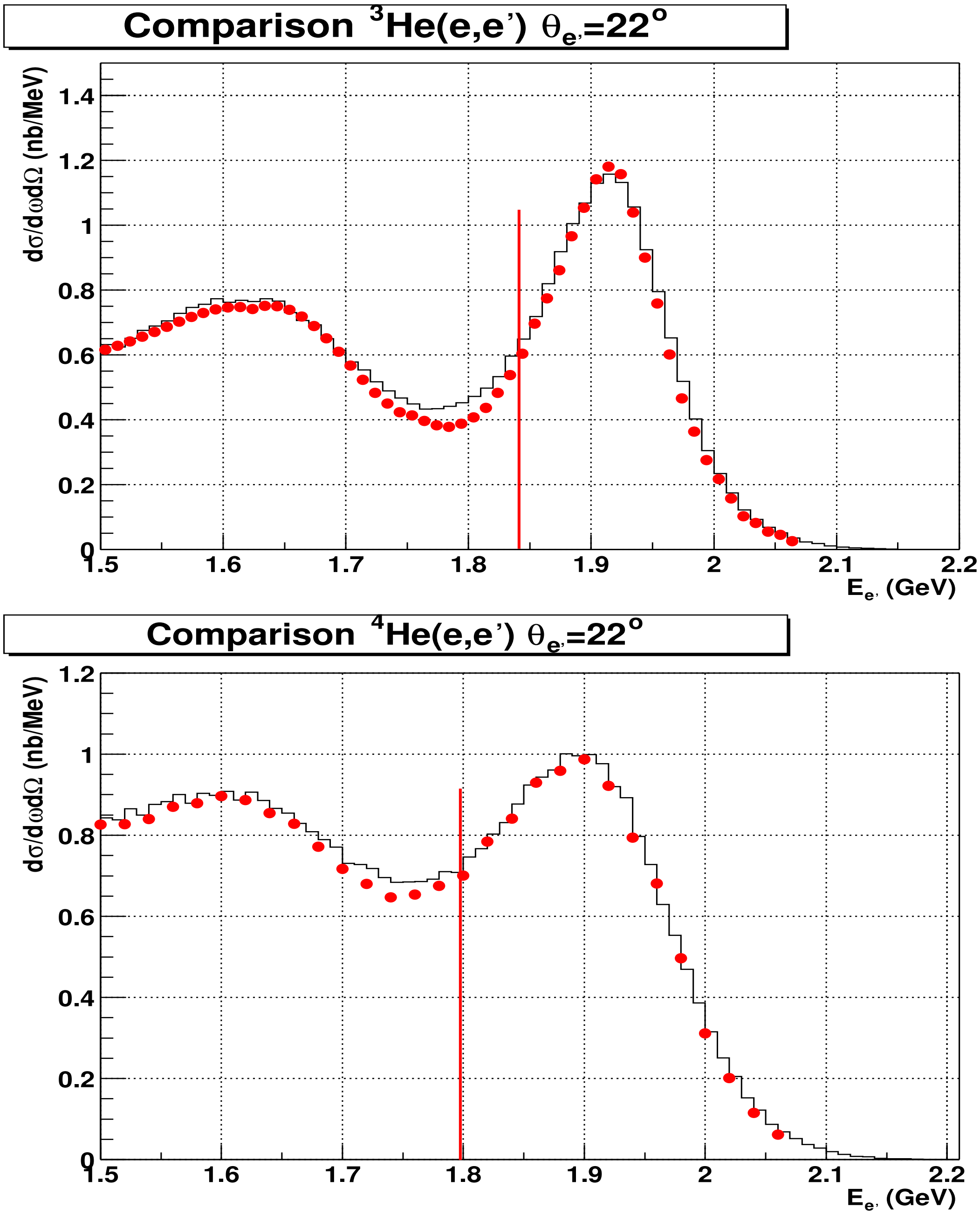

Figure 3-38: Our ^{3}He and ^{4}He inclusive cross sections (histograms) as functions of the enery of the scatterred electrons and the comparisons with Sargsian's calculations (points). The quasi-elastic peaks we used to normalize the data to theory are indicated as the region to the right of the the red lines.

tainty of target thickness is mainly determined by the error of theoretical calculation. A very conservative estimation is

$$Error_{target} = \sqrt{Error_{theory}^2 + Error_{stat}^2} = \sqrt{10^2 + 1^2} = 10\%. \qquad (3.33)$$

3.7 Event Selection and Kinematic Cuts

Because we have very exclusive final states in our data, we have to select parts of the data to study. Our event selection was guided by the ideas about the kinematic regions where Short Range Correlations (SRC) might have a strong influence..

To study the initial properties of a correlated nucleon-nucleon pair, we have to enhance the possibility that the remaining system is not involved in the reaction and does not interact with the pair. For this purpose, we have to make cuts on both missing momentum and missing energy

$$\vec{p}_{miss} = \vec{q} - \vec{p}_1 - \vec{p}_2 \qquad (3.34)$$

$$E_{miss} = \omega - K_1 - K_2 \qquad (3.35)$$

where $\vec{q}$ and ω are the momentum and the energy transfers respectively, $\vec{p}$ and K are the momentum and kinetic energy of the detected nucleons. By cutting the missing momentum to be below a fixed value (for ^{4}He and ^{12}C we take their typical Fermi momenta 200 MeV/c and 220 MeV/c respectively, for ^{3}He, which has a smaller Fermi momentum, to get enough statistics, we take 150 MeV/c), we restrict the total momentum of NN pair to be small, i.e. we integrate over the region where the NN pair is not strongly interactive with the other nucleons. Together with the missing momentum cut, by cutting the missing energy below a fixed value (typically the pion threshold), we restrict the remaining system from being energetic or excited, i.e. it is not strongly involved in the reaction.

Fig. 3-39 shows the missing energy distributions for different reactions we are interested in. The width of the lowest energy peak results from the energy resolutions of the electron and the two detected nucleons. The distributions are fitted with the fitting code ALLFIT [48]. The code takes the missing energy spectrum as input and performs the least χ^2 fits to each peak using a predefined function. The shape of each peak takes the form of an asymmetric hypergaussian function with 10 parameters. A resolution function of the spectrometer convoluted with a theoretical radiation tail is also built into the fitting routine. To be consistent and for the purpose of radiative corrections (see section 3.9), we put the cut 100 MeV above the center position of the lowest missing energy peak and approximately below pion threshold. The contaminations from above the cut is negligible for most cases with the exceptions of ^{4}He(e,e'np) and ^{12}C(e,e'np) where the errors are 4% and 2% respectively. The losses of the lowest energy peaks due to the tails extending above the cuts will be corrected by the radiative correction (see Section 3.9 for details).

In the following, we take ^{3}He(e,e'pp) as an example and the results of other reactions are very similar. After the missing momentum and missing energy cuts, Fig. 3-40 shows the isotropic distribution of the missing momentum (the average value of the missing momentum is about 80 MeV/c). This indicate that in this region the neutrons are mostly in an S state and they are not strongly involved in the reaction. The angular distributions of the two detected protons are shown in Fig. 3-41 and Fig. 3-42. For most of the events, the opening angle of the two protons is around 90^0. This is a typical angle for final-state rescattering. However, when the angle of the backward proton relative to $\vec{q}$ is selected to be larger than 100^0 (we denote it as backward kinematics), as illustrated in Fig. 3-42, the forward proton is detected almost along the $\vec{q}$ direction. Moreover the forward-going proton carries most of the energy transfer as illustrated in Fig. 3-43. So the momenta of the two protons are not close to each other and we hope in this kinematics, FSI effect would be small.

At the above kinematics, the selected events are above the quasi-elastic peak and

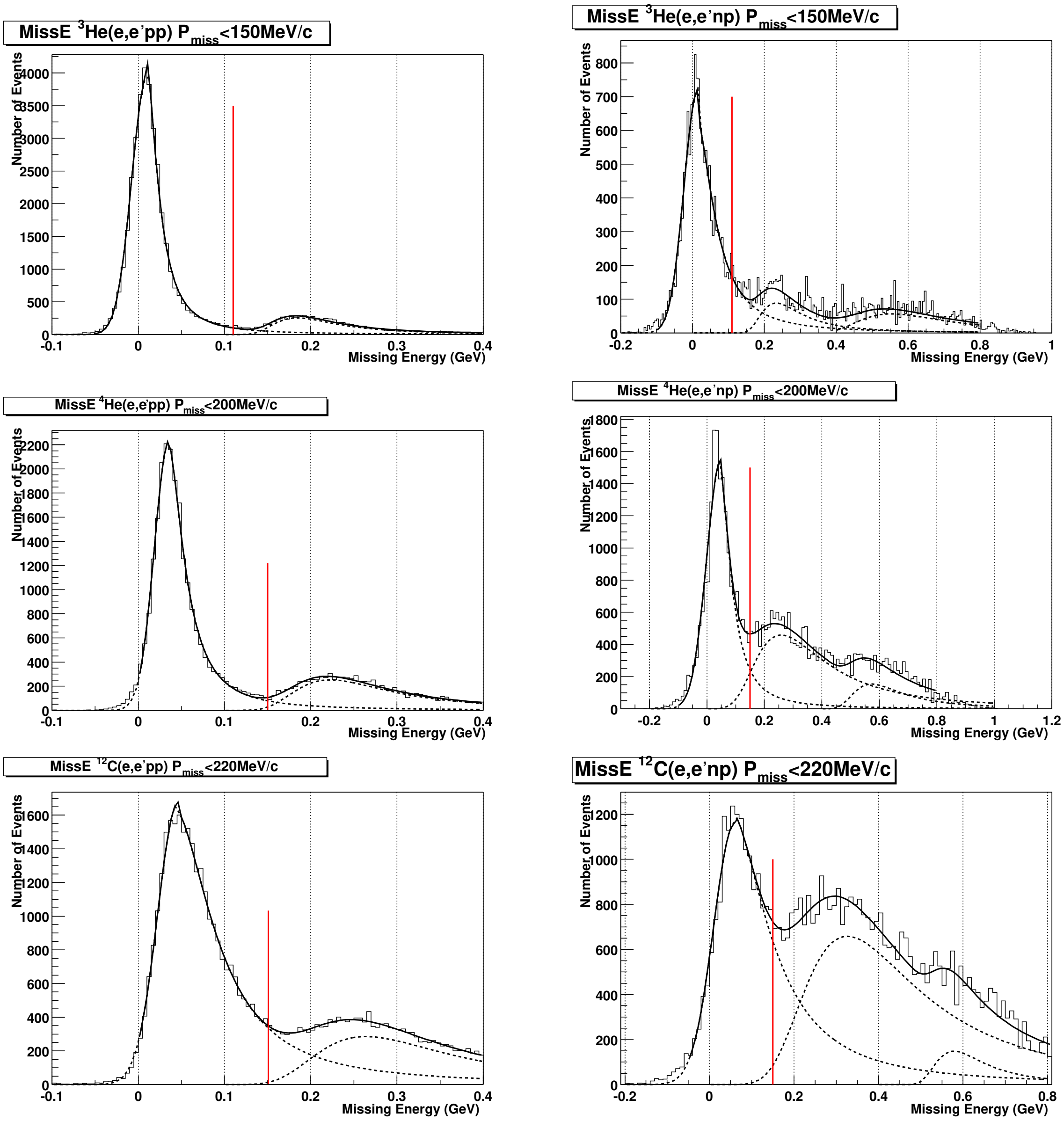

Figure 3-39: Missing energy distributions for different reactions. We made the cuts to restrict missing energy below pion threshold.

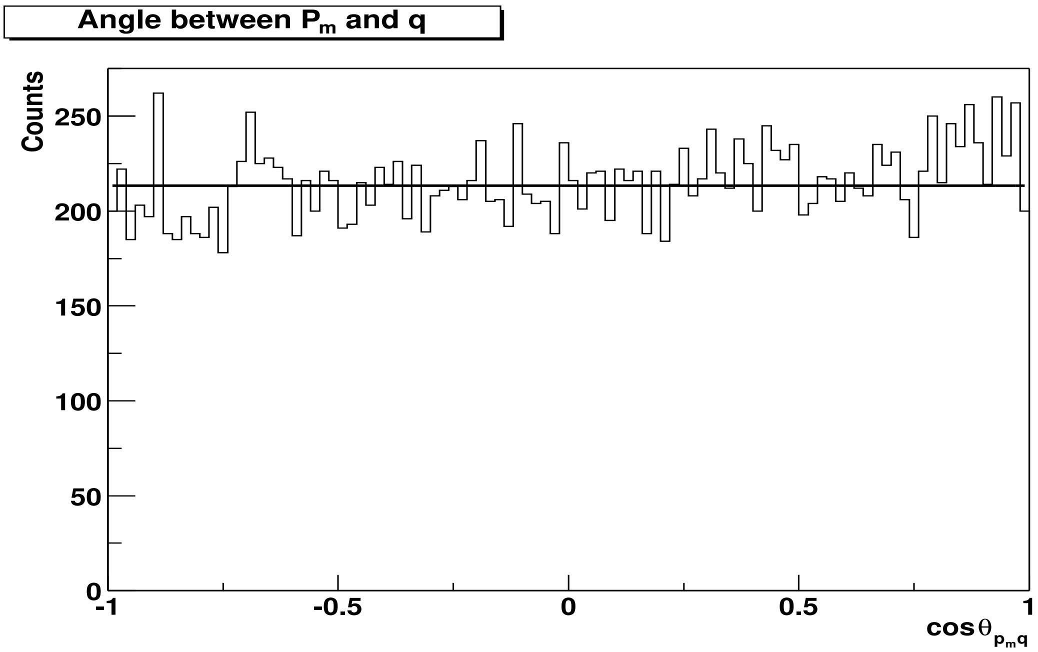

Figure 3-40: Angle between missing momentum and momentum transfer after missing momentum and missing energy cuts. The horizontal line indicates the isotropic distrubtion of the angle.

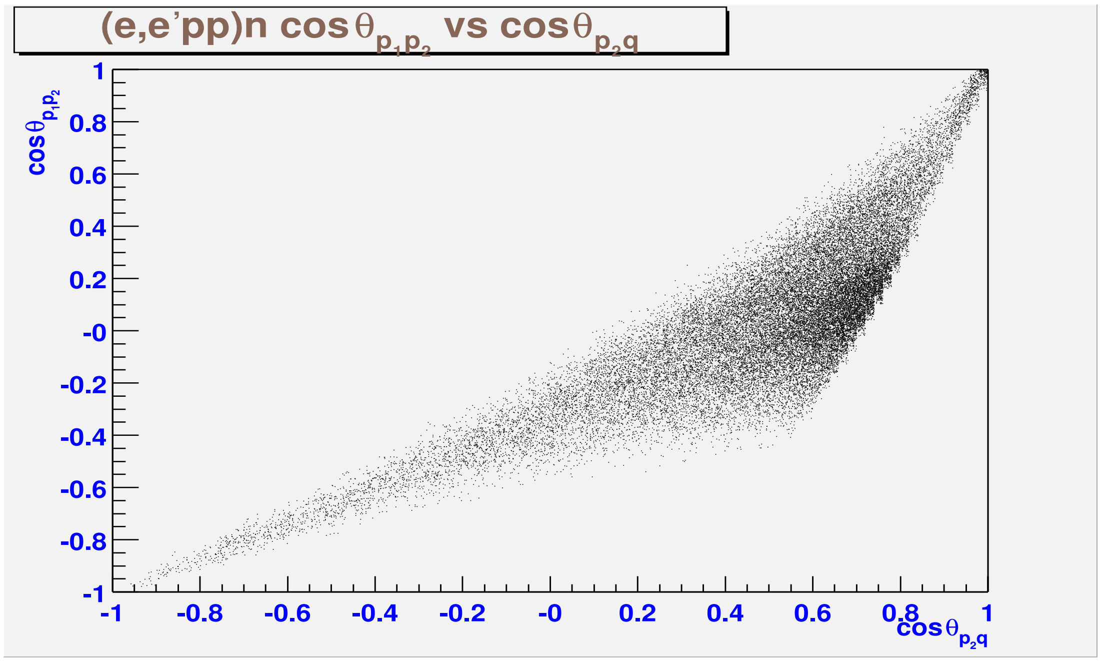

Figure 3-41: Angle between the two detected protons vs. angle between the more backward-going proton and the momentum transfer $\vec{q}$. There is an intense yield in the region of $\theta_{pp} \sim 90^o$ which is the typical angle for final state rescattering.

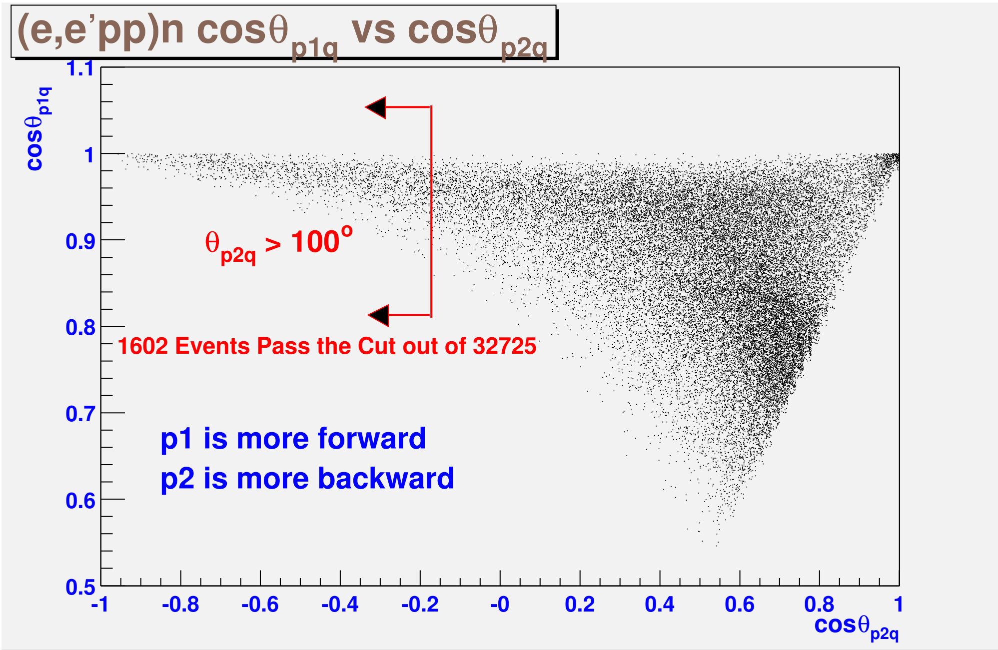

Figure 3-42: Angle between the more forward-going proton and $\vec{q}$ vs. angle between the more backward-going proton and $\vec{q}$. The cut for the backward kinematics is shown.

the average value of $x_{Bj} = \frac{Q^2}{2m_N\omega}$ is 0.6. To compare the effects of two body currents such as MEC and Δ production, we also select events where two protons are both within 30^o of the $\vec{q}$ direction (we denote it as forward kinematics). In this case, the virtual photon hits one proton coming toward and turns it around. The events are below the quasi-elastic peak and the average x_{Bj} is 1.5. We hope in this case the effects from MEC and Δ production are small. However, the final momenta of the two protons are very close to each other and the FSI effect might be large.

When we look at an np pair, due to the neutron detection range in CLAS and the limited statistics, the only case we can study is backward kinematics with the incident electron energy of 2.261 GeV, where the virtual photon hits a forward-going neutron and leaves its partner proton going backward.

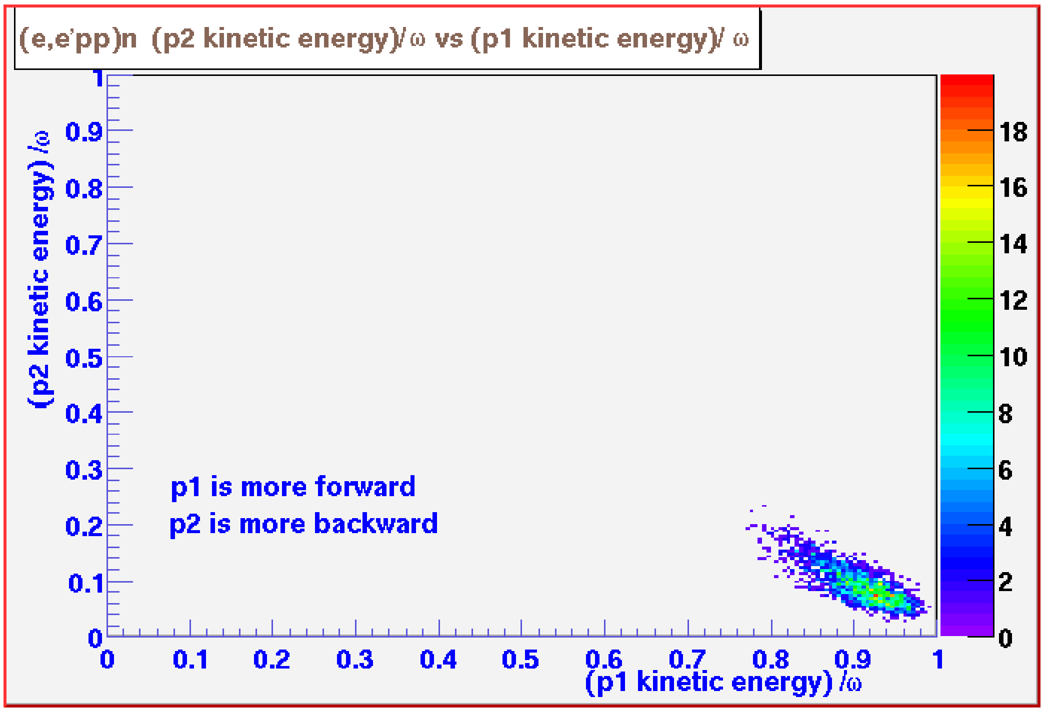

Figure 3-43: Fraction of energy transfer carried by the backward proton vs that carried by the forward proton for the backward kinematics.

3.8 Cross Sections Calculation

The number of events in the kinematic bin dK (for $(e, e'p_1p_2)$ reactions, $dK = dE_{e'}d\Omega_{e'}dp_1d\Omega_1dp_2d\Omega_2$) is

$$N_{dK} = \frac{\int Idt}{e}\frac{\rho}{A}N_A l\frac{d\sigma}{dK}dK \tag{3.36}$$

where ρ, A, l are the density, the atomic number and the length of the target respectively. The electron charge is $e = 1.602 \times 10^{-19}$ Coulomb and the Avogadro's number is $N_A = 6.02 \times 10^{23}$ per mol. The accumulated charge is $\int Idt = N_{FCup} \times 10^{-10}$ Coulomb, where N_{FCup} is the accumulated Faraday Cup counts and each count corresponds to 10^{-10} Coulomb. So the cross section is

$$\frac{d\sigma}{dK} = \frac{N_{dK}}{dK} \times \frac{e}{\int Idt} \times \frac{A}{\rho N_A l}$$

$$
\begin{aligned}
&= \frac{N_{dK}}{dK} \times \frac{1.602 \times 10^{-19}}{N_{FCup} \times 10^{-10}} \times \frac{A}{6.02 \times 10^{23} \rho l} \\
&= \frac{N_{dK}}{dK[MeV/c]} \times \frac{2.661A}{N_{FCup}\rho[g/cm^3]l[cm]}[nb/(GeVSr)^3] \qquad (3.37)
\end{aligned}
$$

Finally, taking the detection efficiencies into account,

$$
\frac{d\sigma}{dK} = \frac{N_{dK}}{dK} \times \frac{2.661A}{N_{FCup}\rho l} \times \frac{1}{\epsilon(\vec{p}_1)\epsilon(\vec{p}_2)\epsilon(\vec{p}_1,\vec{p}_2)}[nb/(GeVSr)^3] \qquad (3.38)
$$

where $\epsilon(\vec{p}_1)$ and $\epsilon(\vec{p}_2)$ are the detection efficiencies for the two detected nucleons, which could be two protons or one neutron and one proton. The close tracks efficiency $\epsilon(\vec{p}_1,\vec{p}_2)$ is appliable only to the pp pairs at forward kinematics (see section 3.7 and 3.4.5). Note that the electron efficiency is assumed to be 100% in the determination of the target thickness (see section 3.6).

3.9 Radiative Corrections

The fact that electrons radiate in the presence of electromagnetic fields makes analysis of electron scattering experiments difficult. Electrons can radiate photons either in the electromagnetic field of other nuclei (external bremsstrahlung) or in the electromagnetic field of the nucleus on which the reaction occurs (internal bremsstrahlung). Corrections also arise from higher order virtual photon effects. Additionally, ionization energy loss in the target and other materials can also alter the energy of the electron and cause shifts in the observed missing energies and missing momenta. In order to compare data to theory, we have to correct our data for radiative effects.

Although the radiative effects of (e,e'NN) are similar to those of (e,e'), additional complications arises in (e,e'NN) measurements due to their exclusive nature. Up to now, nobody has completely worked out the theoretical formulas for three arm coincident experiments. Moreover, the radiative unfolding is so difficult and time consuming that a complete job is almost impossible. However, our data analysis is concentrated on the lowest missing energy region (the first missing energy peak), which considerably simplifies our radiative corrections.

3.9.1 Radiation in the Field of Reaction Nuclei

For electrons radiating in the electromagnetic field of the same nuclei they scatter from, there are several types of radiation processes as shown in Fig. 3-44. If the electron radiates a photon with the energy $k_\gamma > \Delta E$ where ΔE is the interval of the integration for the missing energy peak, we call it hard photon emission. This kind of events will end up outside the peak and create a radiative tail. We must correct the tail back into the peak and the procedure is called Schwinger correction. This type of multiplicative correction is the main form of correction we will apply to our data. Emission of soft photons, $k_\gamma < \Delta E$, only re-distribute the data within the interval of the integration and does not change the cross section.

We will take ^{3}He(e,e'pp) as an example. The missing energy distribution is shown in Fig. 3-45. The first peak position (about 10 MeV) corresponds to the sum of the nuclei bounding energy and the small amount of kinetic energy of the missing neutron. The width of the peak corresponds to the combination of the energy resolutions of the electron and the two protons. We put the cut at 100 MeV above the peak position, so $\Delta E = 100$ MeV.

The Schwinger correction will bring the radiative tail back into the peak (Note the radiative tail shown in Fig. 3-45 does not include all the events to be brought back, because part of the real radiative tail might be out of the detection coverage). We applied the Schwinger correction by multiplying the observed cross section by the Schwinger factor [69] [67].

$$\sigma_{rad} = e^{\delta(\Delta E)}(1+\delta')^{-1}\sigma_{meas} \tag{3.39}$$

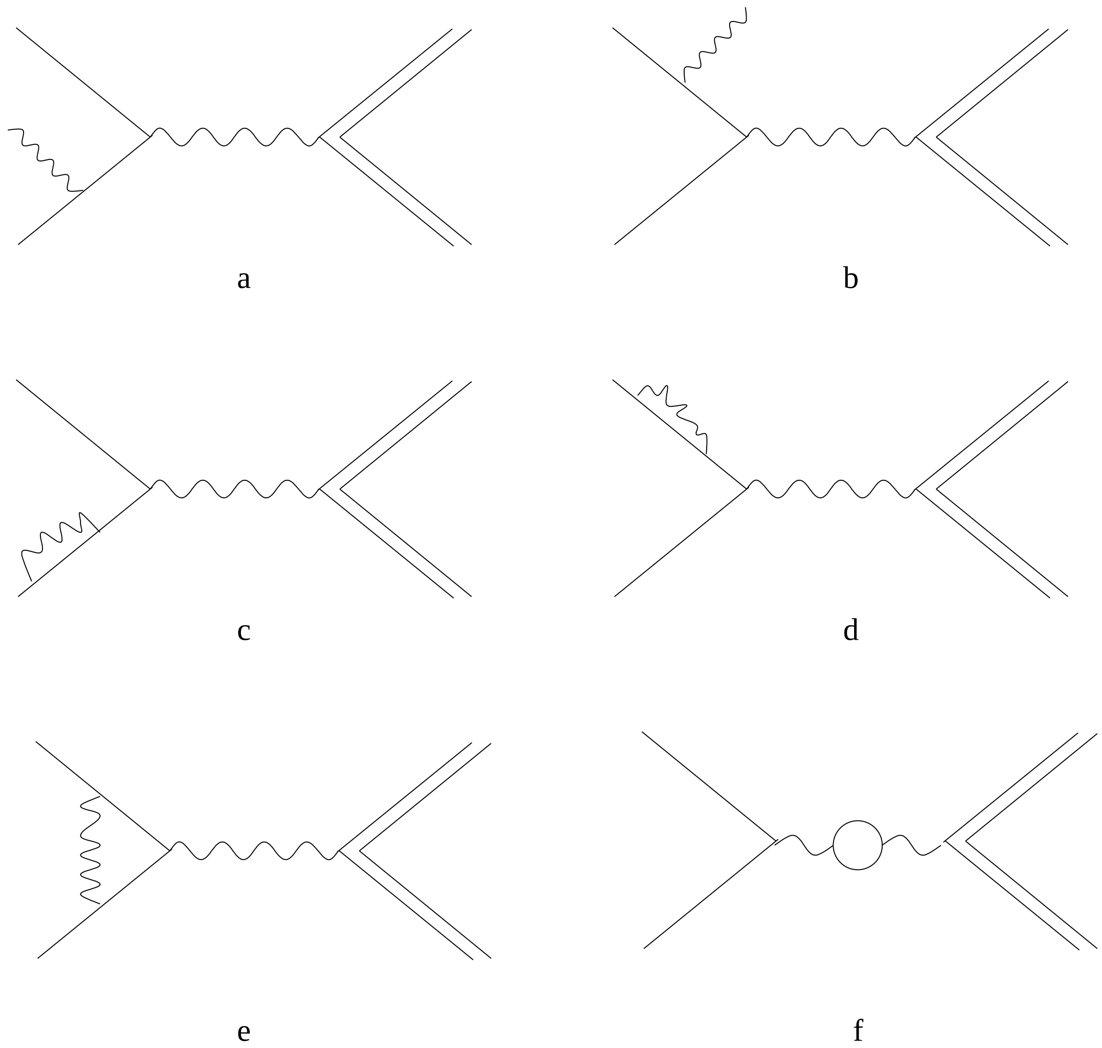

Figure 3-44: Feynman diagrams for internal bremsstrahlung. Diagram a and b correspond to the emission of a real photon from the electron before and after the reaction respectively. Diagram c and d result in the re-normalization of the electron mass. Diagram e amounts to an overall re-normalization of the vertex. Diagram f results in the re-normalization of the virtual photon due to the vacuum polarization.

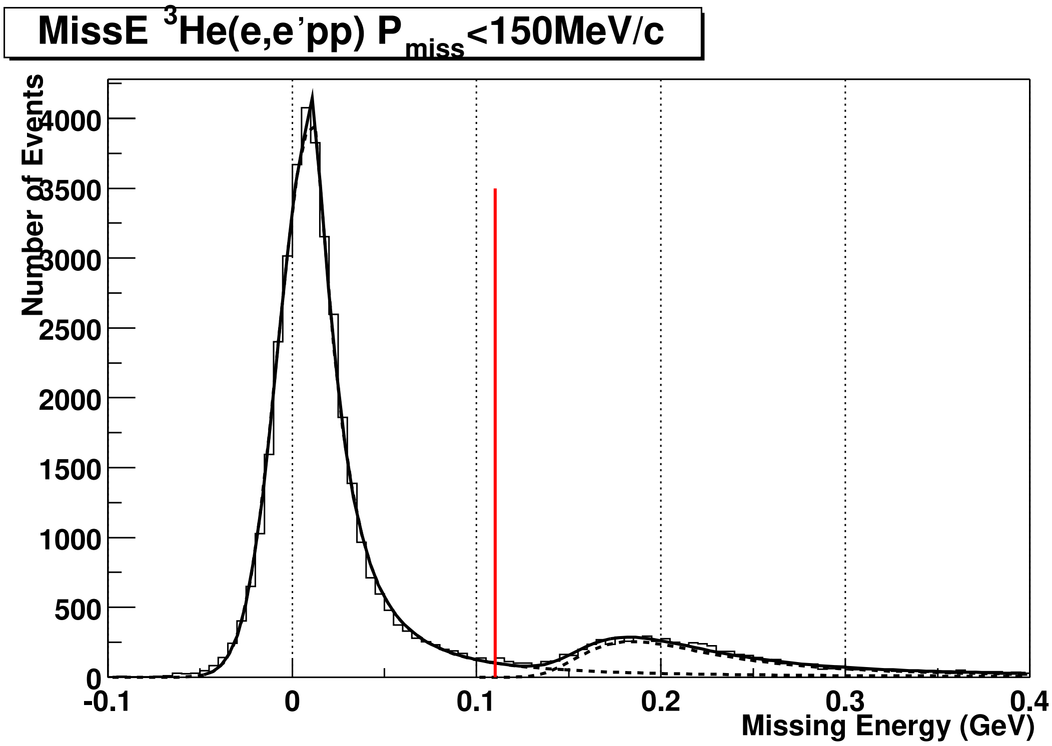

Figure 3-45: Missing energy of ^{3}He(e,e'pp). We put the cut at 100 MeV above the first peak position.

where

$$\delta(\Delta E) = \frac{2\alpha}{\pi} \ln \left(\frac{\sqrt{E_i E_f}}{\Delta E} \right) \left(\ln \frac{Q^2}{m_e^2} - 1 \right) \tag{3.40}$$

and the ΔE independent factor

$$\delta' = \frac{2\alpha}{\pi} \left(-\frac{14}{9} + \frac{13}{12} \ln \frac{Q^2}{m_e^2} \right) - \frac{\alpha}{2\pi} \ln^2 \frac{E_i}{E_f} - \frac{\alpha}{\pi} \left(\frac{\pi^2}{6} - \Phi(\cos^2 \frac{\theta_e}{2}) \right) \tag{3.41}$$

where α is the fine structure constant, m_e is the electron mass, E_i and E_f are the energies of incoming and outgoing electrons respectively, and θ_e is the electron scattering angle. The Spence function $\Phi(x)$ is defined by

$$\Phi(x) = \int_0^x \frac{-\ln(|1-y|)}{y} dy \tag{3.42}$$

Because the correction is kinematics dependent, we made the correction on an event by event base, i.e. we assigned each event with a weight which is equal to the correction factor calculated using the kinematic variables of that particular event.

One thing we should notice is that we present our cross sections as functions of the "initial pair relative momentum per nucleon" instead of the missing energy. Although emission of soft photons will not change the integrated cross section, it could change the relative strength for different relative momentum. One solution to minimize this effect is choosing an appropriate bin width of the relative momentum so that emission of soft photons could not re-distribute events between bins. We define "initial pair relative momentum per nucleon" as

$$\vec{p}_{rel} = \frac{\vec{p}_1 - \vec{q} - \vec{p}_2}{2} \tag{3.43}$$

where $\vec{q}$, $\vec{p}_1$ and $\vec{p}_2$ are the momentum transfer and the two nucleons' momenta respectively. The worst case is that all the three momenta are parallel to each other and

$$\Delta p_{rel} = \Delta q/2 \tag{3.44}$$

where

$$q = \sqrt{E_i^2 + E_f^2 - 2E_iE_f \cos\theta_e} \tag{3.45}$$

therefore

$$\Delta p_{rel} = \frac{\Delta q}{2} = \frac{1}{2q}|E_i - E_f \cos\theta_e|\Delta E_i \tag{3.46}$$

for the case that the photon is emitted by the incoming electron, or

$$\Delta p_{rel} = \frac{1}{2q}|E_f - E_i \cos\theta_e|\Delta E_f \tag{3.47}$$

for the case that the photon is emitted by the outgoing electron. Fig. 3-46 shows the distribution of the values of $|E_i - E_f \cos\theta_e|/q$ and $|E_f - E_i \cos\theta_e|/q$ for ^{3}He(e,e'pp) reaction at two different incident energies with our kinematics selections (those for other reactions are similar). We can see the values are all smaller than 0.5. so if $\Delta E = 100$ MeV,

$$p_{rel} < 0.5 \times 0.5 \Delta E = 25\ MeV/c \tag{3.48}$$

So we choose 25 MeV/c as the bin width of the relative momentum. Emission of soft photons ($k_\gamma < 100$ MeV) can not re-distribute the events between bins.

Fig. 3-47 shows the comparison of the cross sections before and after the radiative corrections for ^{3}He(e,e'pp) and ^{3}He(e,e'np) at different kinematics conditions (the results for others are similar). We can see that the radiative corrections preserve the shapes and the overall correction is about 20%.

To test the consistency of the procedure, we also tried to put the missing energy cut at $\Delta E = 50$ MeV instead of 100 MeV. Of course the cut results in fewer surviving events, but also bigger correction factors. The final corrected cross sections only differ by 1% from the final corrected cross sections using $\Delta E = 100$ MeV.

3.9.2 Other Radiative Effects

Two other radiative effects reduce the cross section of a peak [69]. The first process is external bremsstrahlung, radiation in the field of nuclei other than the one where the reaction took place. The other process involves the energy loss due to ionizing which removes atomic electrons. This is sometimes called Landau straggling. Both processes, since they are caused by external nuclei and atoms, have an effect on the cross sections proportional to the target thickness. The correction formulas for these effects are taken from [1, 68].

The correction factor for cross section loss due to external bremsstrahlung is e^{δ_B}, where

$$\delta_B = \frac{t}{x_0 \ln 2} \ln\left(\frac{\Delta E}{E_i}\right) \tag{3.49}$$

(This equation holds for $\frac{t}{x_0 \ln 2} \ll 1$) where t is the target thickness, E_i is the energy

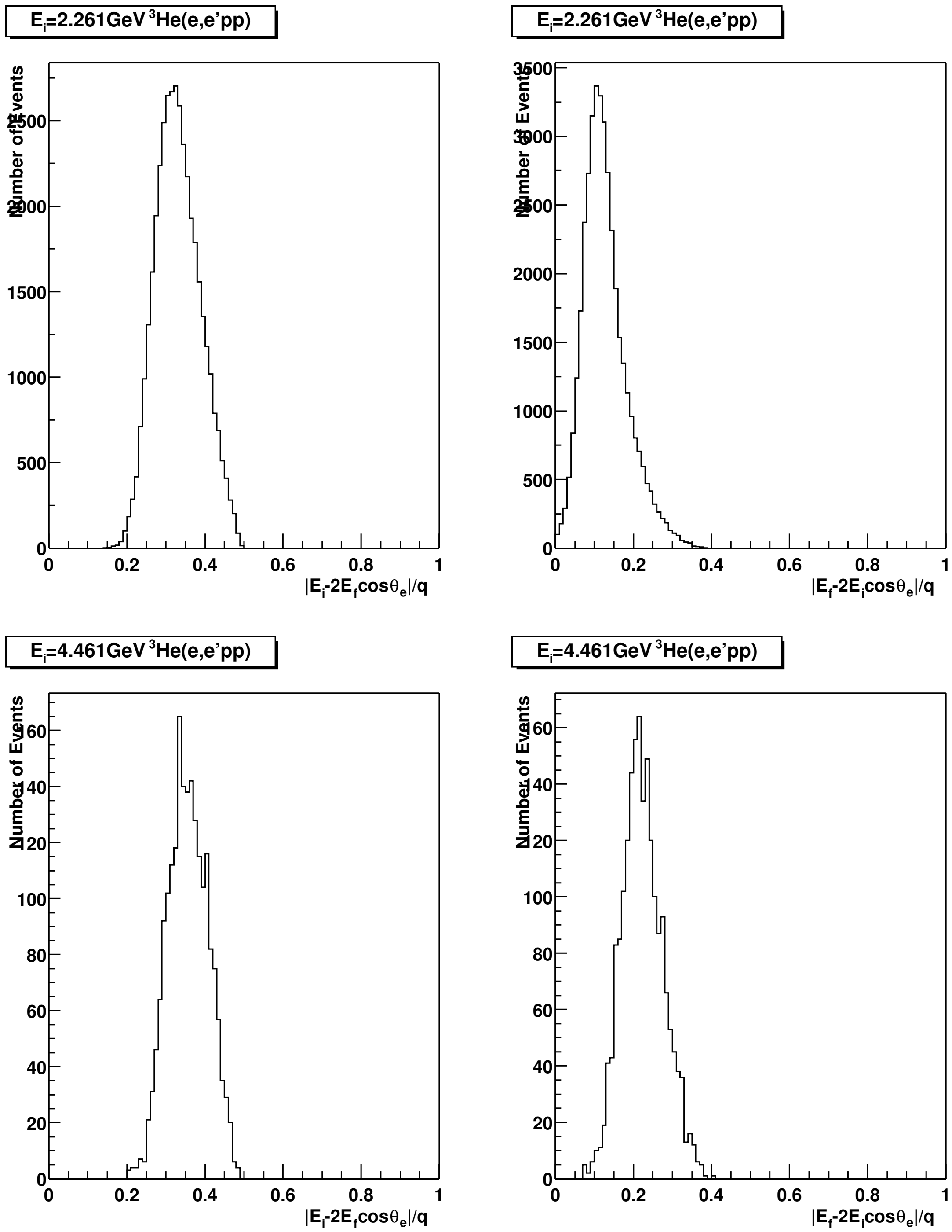

Figure 3-46: Distribution of the values of $|E_i - E_f \cos\theta_e|/q$ and $|E_f - E_i \cos\theta_e|/q$ for ^{3}He(e,e'pp) reaction at two different incident energies with our kinematics selections. These values are used to determine the bin width for the initial relative momentum per nucleon. The left column is for the radiation before the scattering and the right column is for the radiation after the scattering.

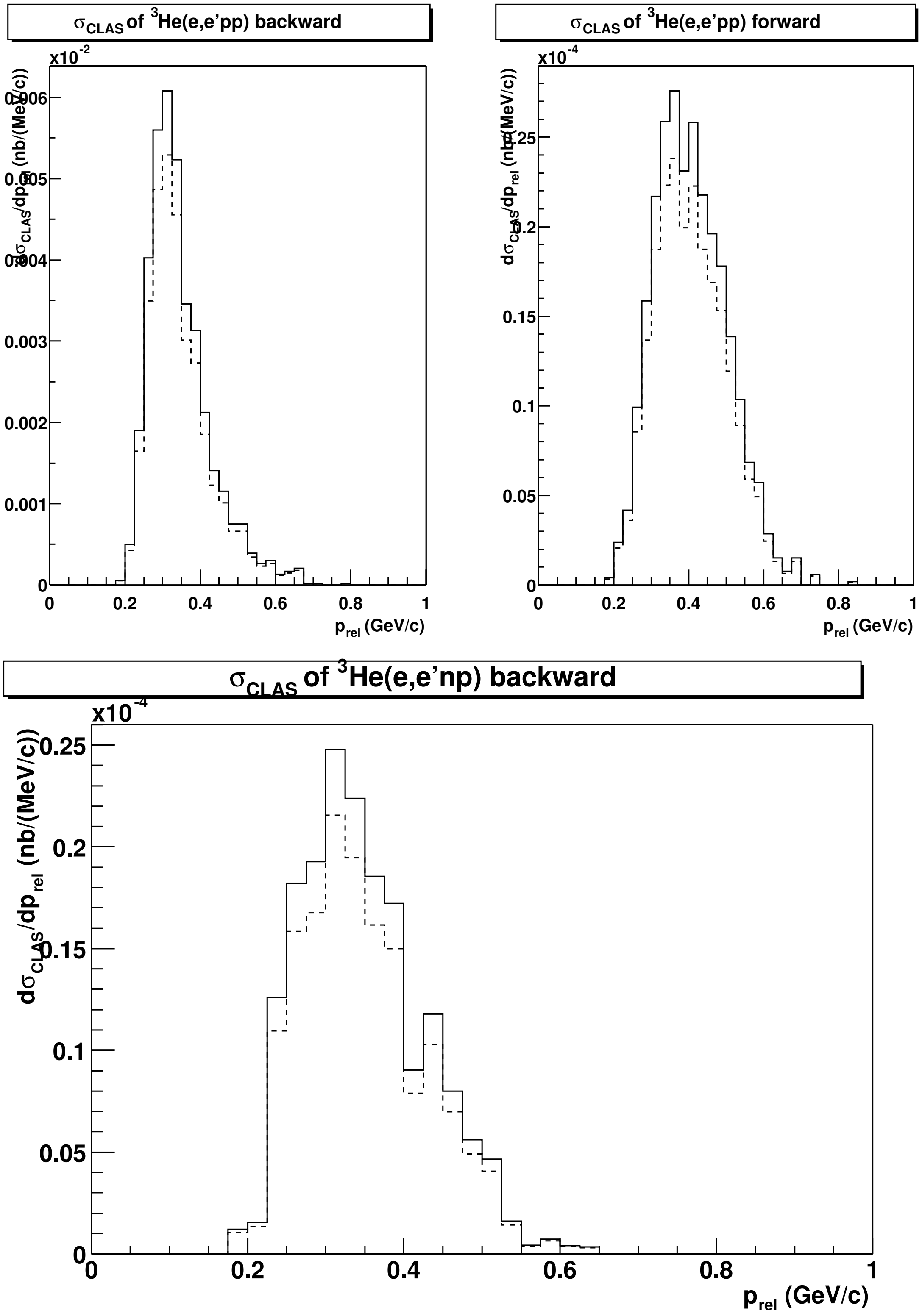

Figure 3-47: Comparison the cross sections integrated over the CLAS phase space volume before and after radiative corrections for ^{3}He(e,e'pp) and ^{3}He(e,e'np) at different kinematics conditions. Dash lines are before radiative corrections and solid lines are after radiative corrections. The incident energy is 2.261 GeV.

$\Delta E = 100$ MeV		e^{δ_B}	$1-\delta_I$
$E_i = 2.261$ GeV	^{3}He	0.9851	0.99996
	^{4}He	0.9741	0.99991
	^{12}C	0.9821	0.99997
$E_i = 4.461$ GeV	^{3}He	0.9819	0.99996
	^{4}He	0.9685	0.99991
	^{12}C	0.9782	0.99997

Table 3.3: External bremmstrahlung and Landau straggling corrections

of the incident electrons, and x_0 is the radiation length of the target nuclei

$$x_0 = \frac{A}{4\alpha N_A Z(Z+1) r_e^2 \ln(183 Z^{-1/3})} \tag{3.50}$$

where Z and A are the charge and the atomic number of the nuclei respectively, $N_A = 6.02 \times 10^{23}$ and the electron radius $r_e = 2.818 \times 10^{-13}$ cm. So $x_0(^3He) = 71.9\ g/cm^2$, $x_0(^4He) = 95.9\ g/cm^2$ and $x_0(^{12}C) = 44.4\ g/cm^2$. Combining everything, when $\Delta E = 100$ MeV, we find the correction factors to be very small (less than 3%, see Table 3.3 for the exact values).

The correction factor for cross section loss due to Landau straggling is $1 - \delta_I$, where

$$\delta_I = \frac{\lambda}{\lambda(\lambda + \ln\lambda + C)}. \tag{3.51}$$

The Euler-Mascheroni constant $C = 0.577$, and

$$\lambda = \frac{\Delta E - e_0}{\xi}, \tag{3.52}$$

where

$$\xi\ [MeV] = 0.0154 \times t\ [g/cm^2]. \tag{3.53}$$

$$e_0 = \xi \left(\ln \frac{\xi}{e'} + 1 - C \right) \tag{3.54}$$

is the most probable energy loss,

$$e' = 2.718\frac{(1-\beta^2)I^2}{2m_e}, \tag{3.55}$$

and

$$I = 13.5 \times 10^{-6} Z \ [MeV] \tag{3.56}$$

is the average atomic ionization potential. The corrections are negligible (See Table 3.3 for the exact values).

3.10 Systematic Error Estimation

We actually estimated the systematic errors at each step of the analysis described above. The total errors are dependent on the actual reactions. Estimations for the total systematic errors and the individual contributions are summarized in Table 3.4 (we took the upper limit for each individual error contributor). Note the uncertainties from the proton detection are counted twice for (e,e'pp) reactions, close tracks efficiency is applied only on (e,e'pp) forward kinematics.The electron detection efficiency is assumed to be 100% and its error is compensated in the error of the target thickness (see Section 3.6).

3.11 Monte Carlo Simulation and Comparing Theory to Data

We only have calculations for ^{3}He reactions which we can compare with our data. Theoretical calculations are mostly given in the form of differential cross sections for specific kinematics. For instance, calculations for $^3He(e,e'p_fp_b)$ are given as the differential cross sections

$$\frac{d^8\sigma}{d\omega d\Omega_e dp_f d\Omega_f d\Omega_b}$$

Error Source	(e,e'pp) backward (%)	(e,e'pp) forward (%)	(e,e'np) backward (%)
electron ID	2	2	2
electron acceptance	4	4	4
proton ID	$3\sqrt{2}$	$3\sqrt{2}$	3
proton acceptance	$5\sqrt{2}$	$5\sqrt{2}$	5
proton efficiency	$2\sqrt{2}$	$2\sqrt{2}$	2
close tracks efficiency	N/A	1	N/A
neutron ID	N/A	N/A	2
neutron acceptance	N/A	N/A	6
neutron efficiency	N/A	N/A	4
beam charge	0.2	0.2	0.2
target thickness	10	10	10
total	14	14	15

Table 3.4: Summary of systematic errors

where the subscriptions f and b denote the forward the backward protons in respect to the momentum transfer direction. Our data are actually the average of the above differential cross sections over the detection volume of CLAS.

$$\langle\frac{d^8\sigma}{d\omega d\Omega_e dp_f d\Omega_f d\Omega_b}\rangle = \frac{\int_{CLAS} \frac{d^8\sigma}{d\omega d\Omega_e dp_f d\Omega_f d\Omega_b} d\omega d\Omega_e dp_f d\Omega_f d\Omega_b}{\int_{CLAS} d\omega d\Omega_e dp_f d\Omega_f d\Omega_b} \tag{3.57}$$

To compare theory with data, we have to average the theoretical cross sections over the CLAS volume.

We use the Monte Carlo method to do the averaging. For example, in the case of $^3He(e,e'p_fp_b)$ reaction, we generate random events with variables of ω, θ_e, ϕ_e, p_f, θ_f, ϕ_f, θ_b and ϕ_b within the desired coordinates and range, then transform them into CLAS coordinates and check if they are within CLAS coverage (if they could passed the fiducial cuts which were discussed in the previous sections). For those events within CLAS coverage, we integrate the theoretical differential cross sections. In the meantime, we also integrate the phase space volume. Each generated event carries a grid of the total phase volume

$$\Delta V = \frac{\Delta\omega\Delta\cos\theta_e\Delta\phi_e\Delta p_f\Delta\cos\theta_f\Delta\phi_f\Delta\cos\theta_b\Delta\phi_b}{N} \tag{3.58}$$

where N is the total number of generated events. For any event that passes the kinematic cuts and the fiducial cuts, we accumulate its grid phase space. The average theoretical cross sections are obtained by dividing the integrated theoretical cross sections by the accumulated phase space volume for each bin of the "initial relative momentum" of the NN pair per nucleon

$$\vec{p}_{rel} = \frac{\vec{p}_f - \vec{q} - \vec{p}_b}{2}. \tag{3.59}$$

Chapter 4

Results and Discussions

4.1 Results for ^{3}He(e,e'pp) and ^{3}He(e,e'pn)

The cross sections within CLAS detection volume are presented as functions of "initial relative momentum per nucleon of the NN pair" as described in Section 1.2.1,

$$\vec{p}_{rel} = \frac{\vec{p}_1 - \vec{q} - \vec{p}_2}{2} \tag{4.1}$$

where $\vec{p}_1$ is the momentum of the detected nucleon which is assumed to be hit by the virtual photon, $\vec{p}_2$ is the momentum of the other detected nucleon, and $\vec{q}$ is the momentum transfer carried by the virtual photon. the nucleon with the larger final momentum is always assumed to be the one the virtual photon hits. In the plane wave picture, p_{rel} is the initial momentum of each nucleon in the center of mass frame of the nucleon-nucleon pair.

Fig. 4-2 shows the cross section for ^{3}He(e,e'pp) backward kinematics at 2.261 GeV incident energy. Fig. 4-3 shows the cross section for ^{3}He(e,e'pp) forward kinematics at 2.261 GeV incident energy. Fig. 4-4 shows the cross section for ^{3}He(e,e'pp) backward kinematics at 4.461 GeV incident energy. Fig. 4-5 shows the cross section for ^{3}He(e,e'pp) forward kinematics at 4.461 GeV incident energy. Fig. 4-1 shows the cross

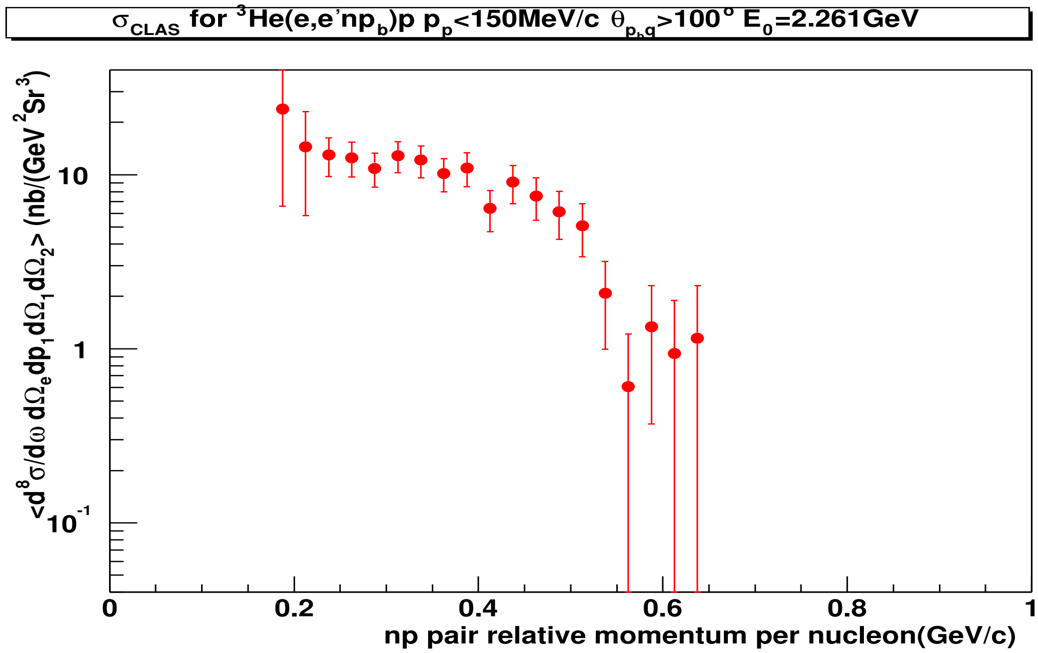

Figure 4-1: ^{3}He(e,e'np) Cross Section in CLAS for Backward Kinematics at 2.261 GeV

section for ^{3}He(e,e'np) backward kinematics at 2.261 GeV incident energy.

In the figures of ^{3}He(e,e'pp) reactions, the theoretical calculations by J.M. Laget, which were discussed in Chapter 1, are also showed. The dotted lines are plane wave inpulse approximation (PWIA) calculations, which only include one-body hadronic currents. The dashed lines are calculations which also include final state interactions (FSI). The solid lines are full calculations which also include meson exchange currents (MEC). The features of short range correlations (SRC) are built into the ground state wave function of ^{3}He, which was taken as the solution to the Faddeev equations [47] with the Paris potential [32] as discussed in Chapter 1. More detailed discussions about the experimental results and the theoretical calculations will be given in Section 4.4.

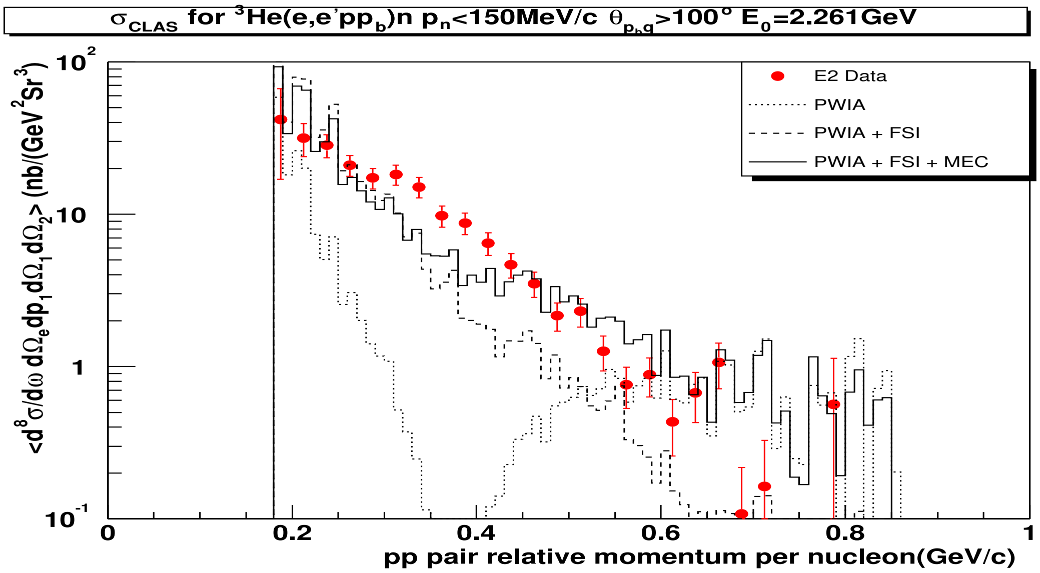

Figure 4-2: ^{3}He(e,e'pp) Cross Section in CLAS for Backward Kinematics at 2.261 GeV. The points are our data. The histograms are J.M. Laget's calculations with PWIA, FSI and MEC effects turned on step by step [51].

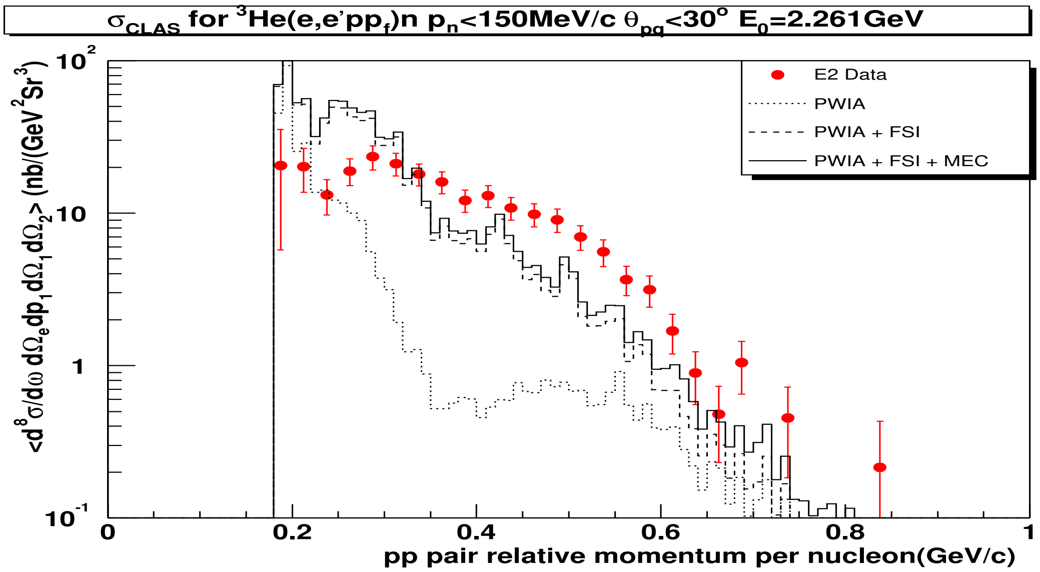

Figure 4-3: ^{3}He(e,e'pp) Cross Section in CLAS for Forward Kinematics at 2.261 GeV. The points are our data. The histograms are J.M. Laget's calculations with PWIA, FSI and MEC effects turned on step by step [51].

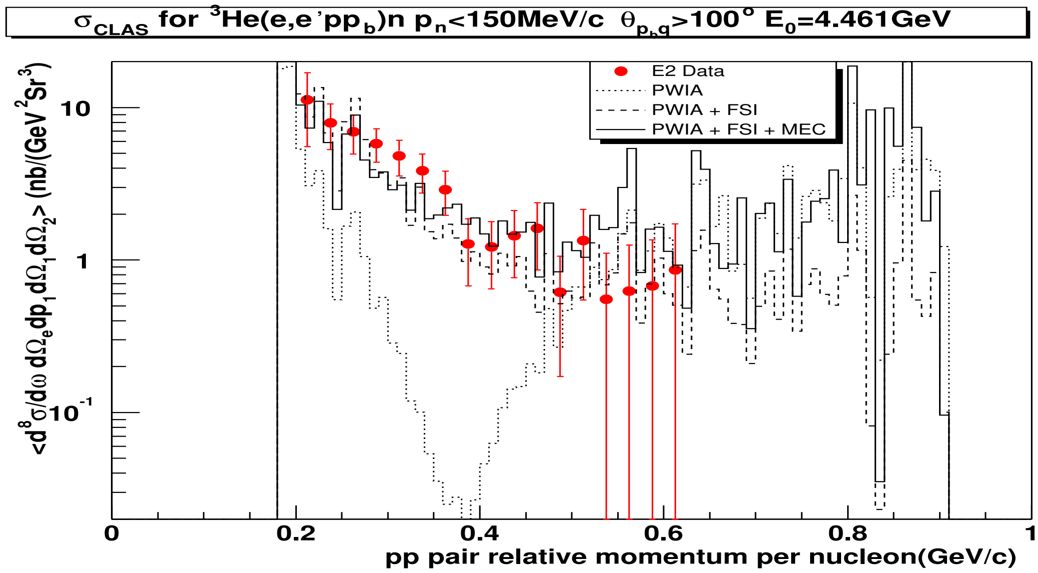

Figure 4-4: ^{3}He(e,e'pp) Cross Section in CLAS for Backward Kinematics at 4.461 GeV. The points are our data. The histograms are J.M. Laget's calculations with PWIA, FSI and MEC effects turned on step by step [51].

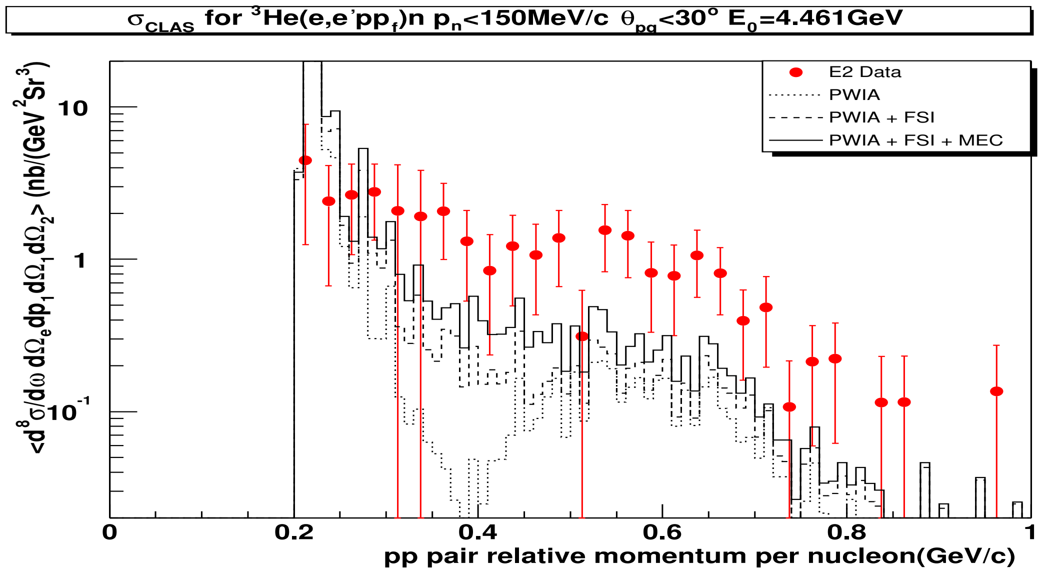

Figure 4-5: ^{3}He(e,e'pp) Cross Section in CLAS for Forward Kinematics at 4.461 GeV. The points are our data. The histograms are J.M. Laget's calculations with PWIA, FSI and MEC effects turned on step by step [51].

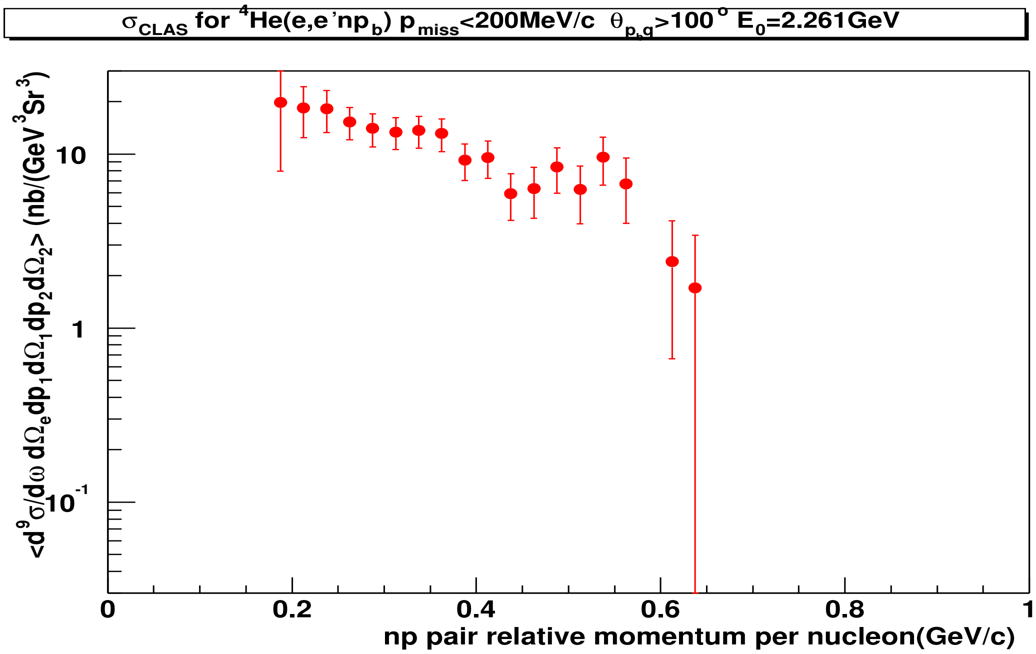

Figure 4-6: ^{4}He(e,e'np) Cross Section in CLAS for Backward Kinematics at 2.261 GeV

4.2 Results for ^{4}He(e,e'pp) and ^{4}He(e,e'np)

Because at this time we do not have theoretical calculations available with which to compare, I only show our data here. The actual numbers are listed in Appendix B. Discussion will be given in Section 4.4. Fig. 4-7 is ^{4}He(e,e'pp) backward kinematics at 2.261 GeV incident energy, Fig. 4-8 is ^{4}He(e,e'pp) forward kinematics at 2.261 GeV incident energy, Fig. 4-9 is ^{4}He(e,e'pp) backward kinematics at 4.461 GeV incident energy, Fig. 4-10 is ^{4}He(e,e'pp) forward kinematics at 4.461 GeV incident energy, and Fig. 4-6 is ^{4}He(e,e'np) backward kinematics at 2.261 GeV incident energy.

4.3 Results for ^{12}C(e,e'pp) and ^{12}C(e,e'np)

Because at this time we do not have theoretical calculations available with which to compare, I only show our data here. The actual numbers are listed in Appendix B. Discussions will be given in Section 4.4. Fig. 4-12 is ^{12}C(e,e'pp) backward kinematics

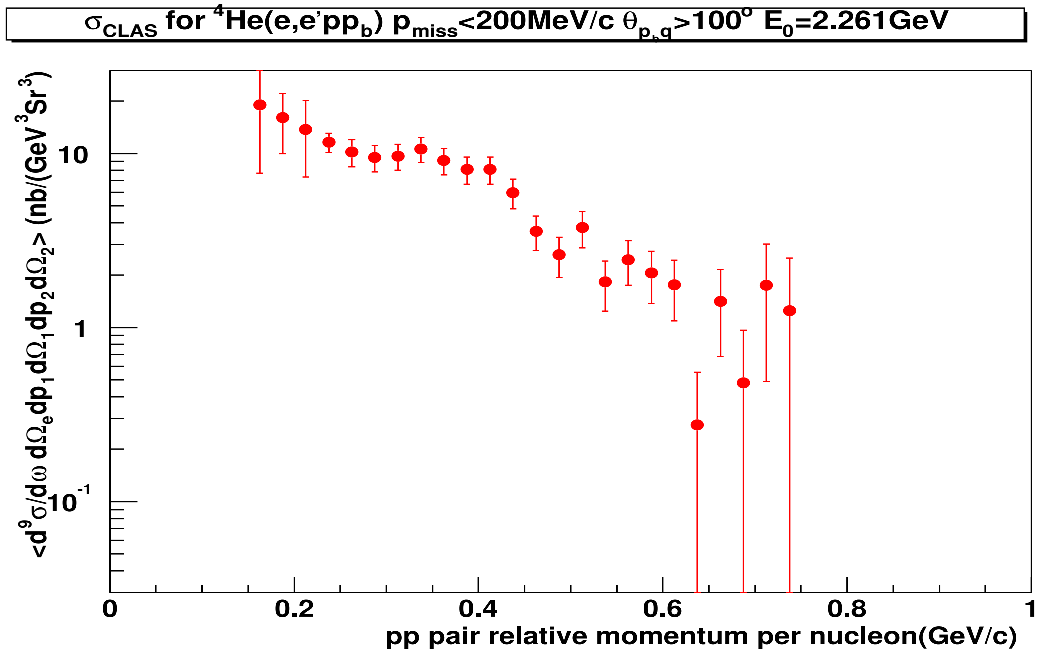

Figure 4-7: ^{4}He(e,e'pp) Cross Section in CLAS for Backward Kinematics at 2.261 GeV

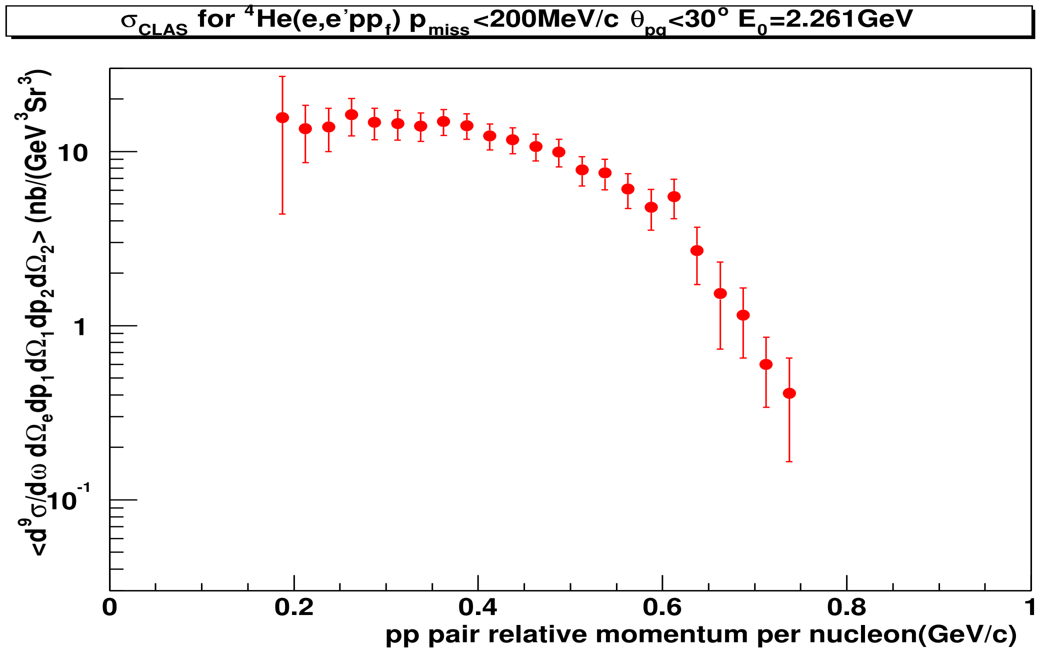

Figure 4-8: ^{4}He(e,e'pp) Cross Section in CLAS for Forward Kinematics at 2.261 GeV

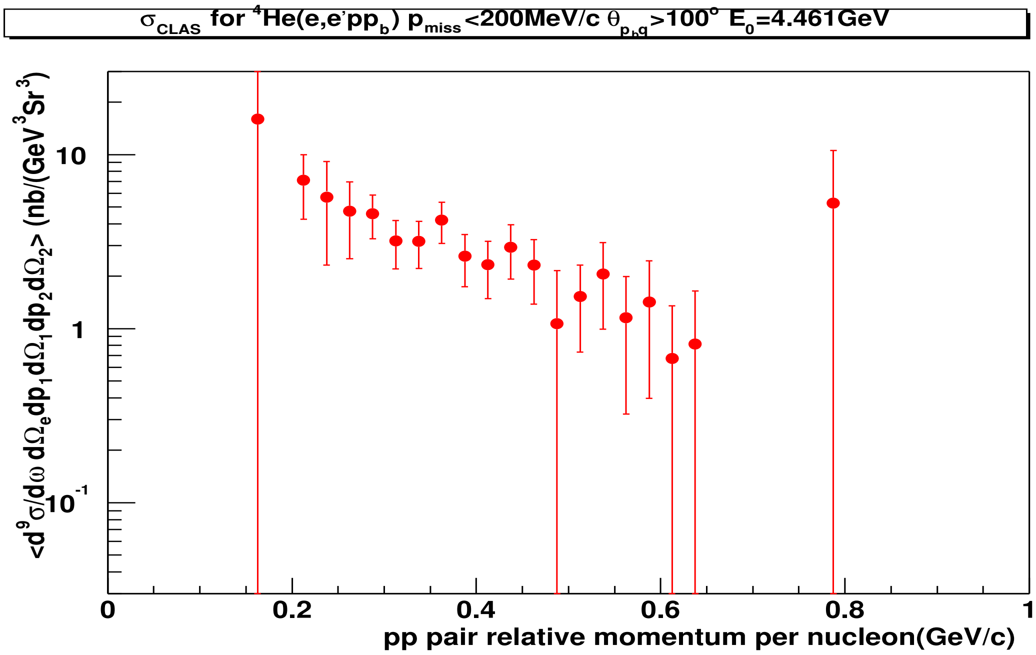

Figure 4-9: ^{4}He(e,e'pp) Cross Section in CLAS for Backward Kinematics at 4.461 GeV

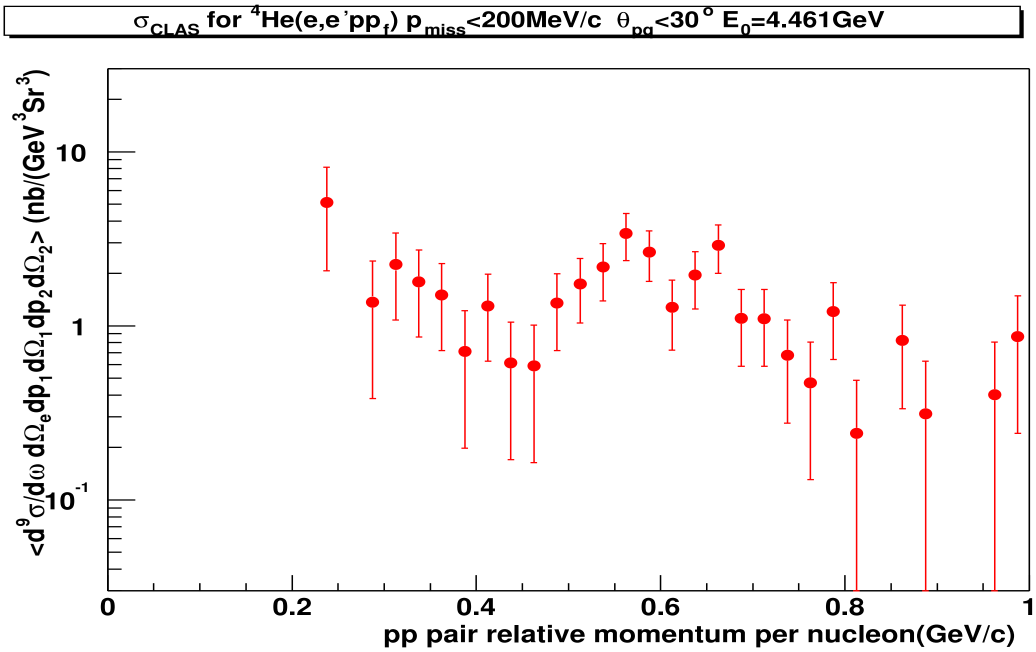

Figure 4-10: ^{4}He(e,e'pp) Cross Section in CLAS for Forward Kinematics at 4.461 GeV

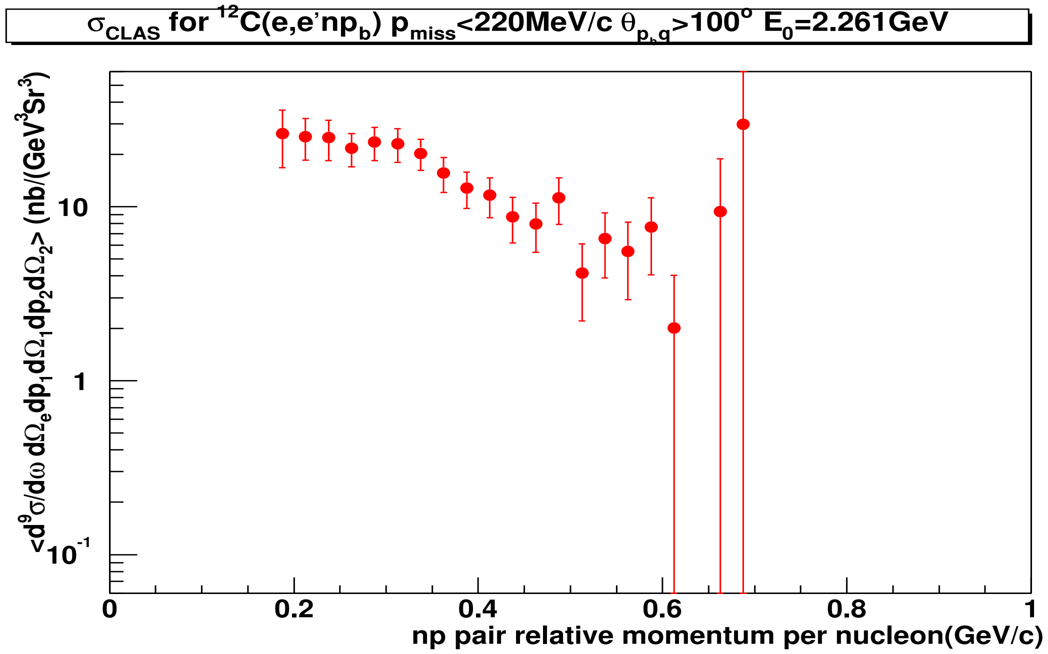

Figure 4-11: ^{12}C(e,e'np) Cross Section in CLAS for Backward Kinematics at 2.261 GeV

at 2.261 GeV incident energy, Fig. 4-13 is ^{12}C(e,e'pp) forward kinematics at 2.261 GeV incident energy, Fig. 4-14 is ^{12}C(e,e'pp) backward kinematics at 4.461 GeV incident energy, Fig. 4-15 is ^{12}C(e,e'pp) forward kinematics at 4.461 GeV incident energy, and Fig. 4-11 is ^{12}C(e,e'np) backward kinematics at 2.261 GeV incident energy.

4.4 Discussion and Conclusions

In the previous section, I presented the experimental cross sections of (e,e'NN) reactions for different energy transfers, different momentum transfers, different nucleon-nucleon pairs and different nucleus. What can we learn from those results? I will base my discussions on the comparisons of those different cases.

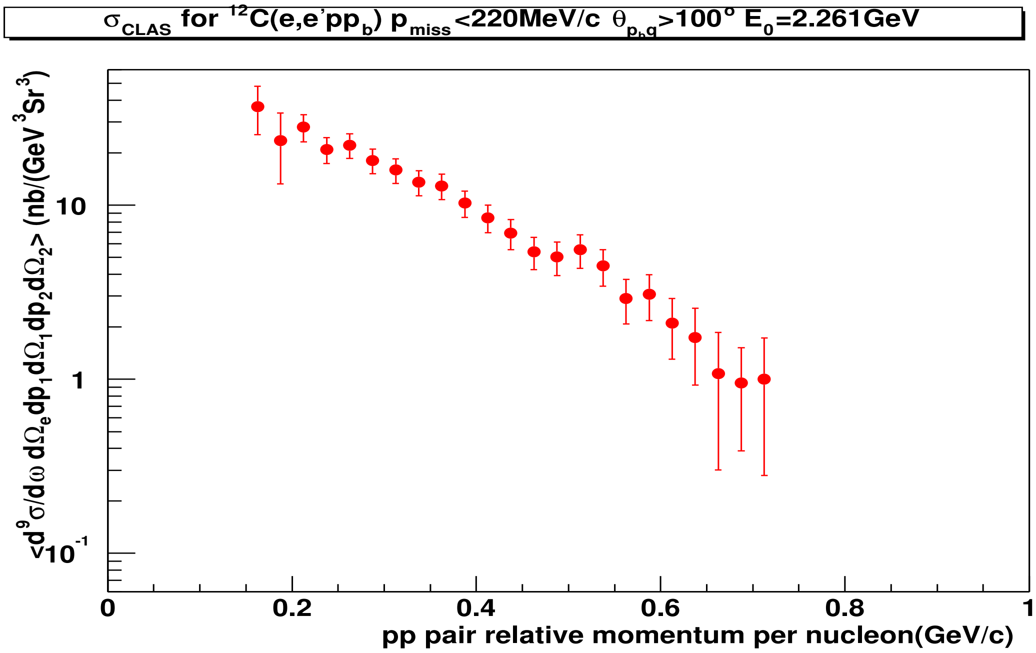

Figure 4-12: ^{12}C(e,e'pp) Cross Section in CLAS for Backward Kinematics at 2.261 GeV

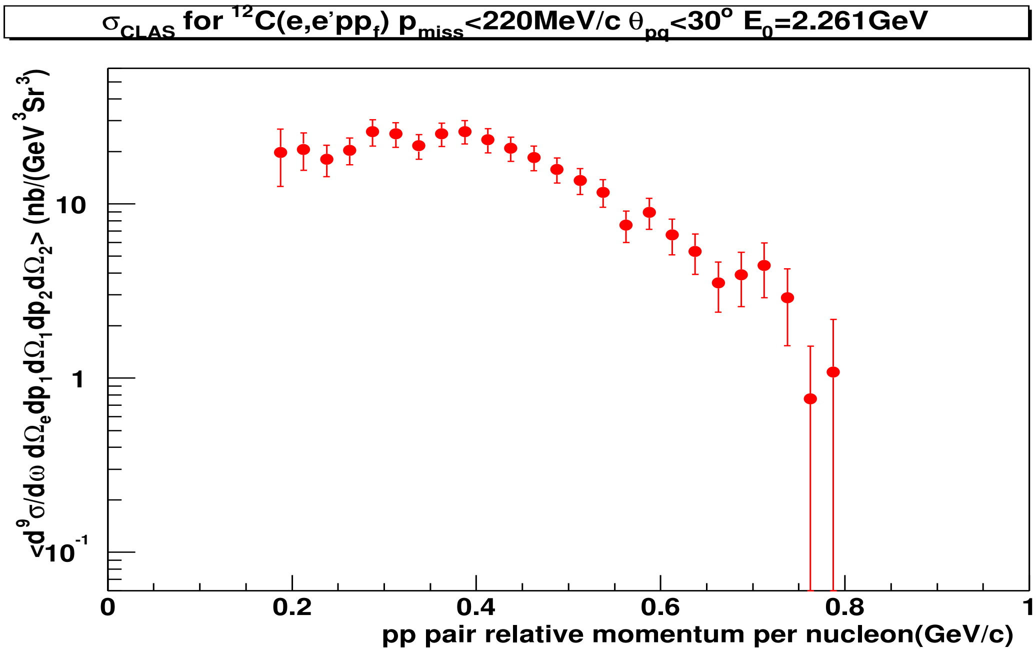

Figure 4-13: ^{12}C(e,e'pp) Cross Section in CLAS for Forward Kinematics at 2.261 GeV

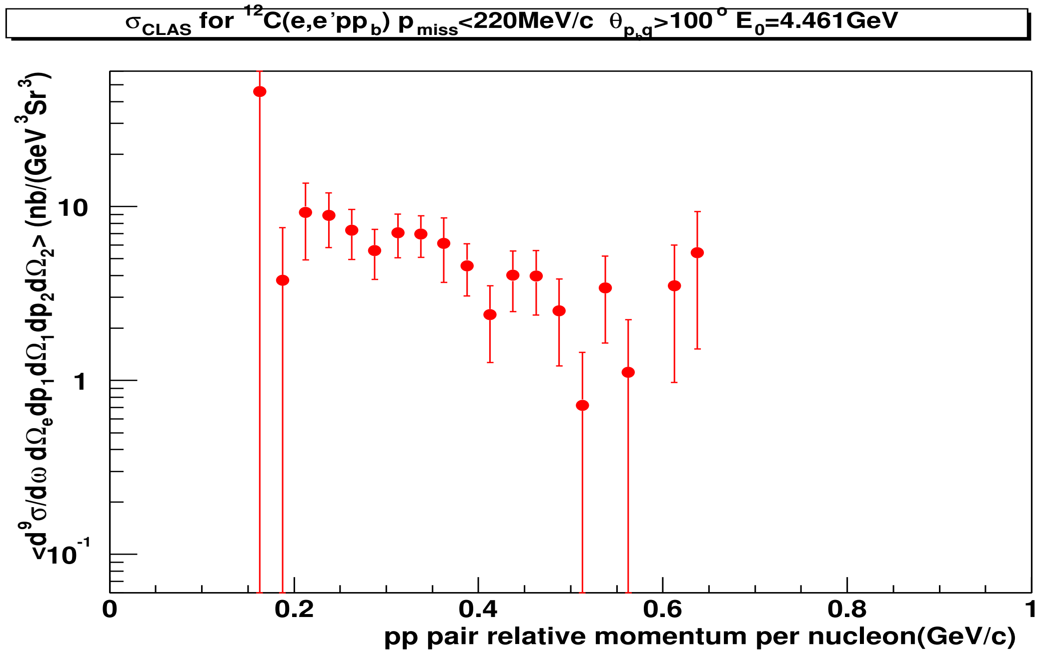

Figure 4-14: ^{12}C(e,e'pp) Cross Section in CLAS for Backward Kinematics at 4.461 GeV

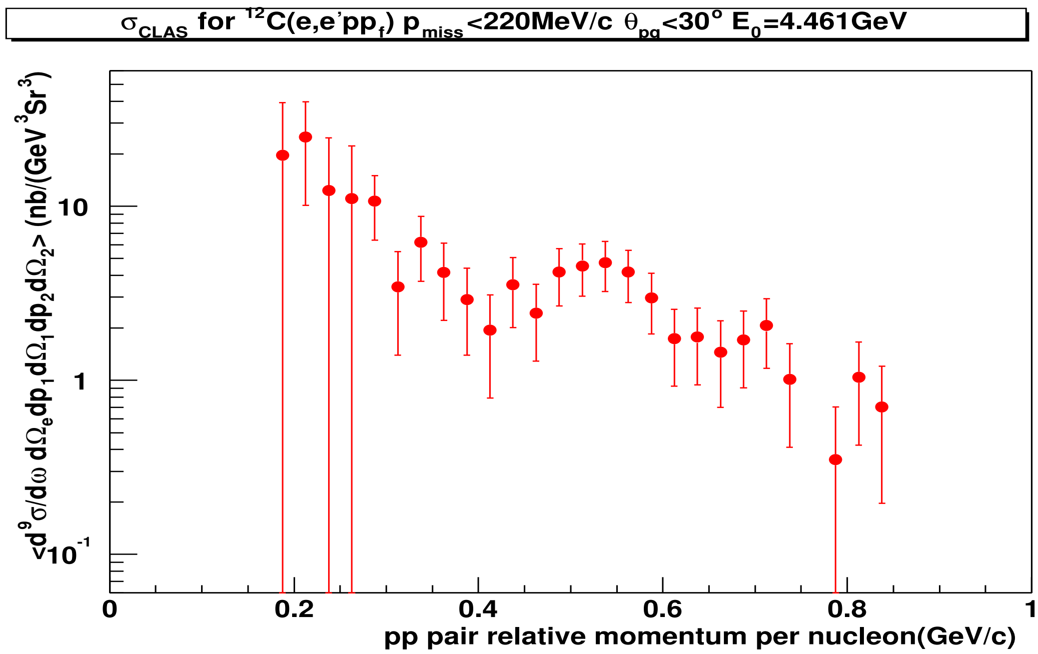

Figure 4-15: ^{12}C(e,e'pp) Cross Section in CLAS for Forward Kinematics at 4.461 GeV

4.4.1 Backward Kinematics vs Forward Kinematics

The backward and the forward kinematics are defined according to the direction, with respect to $\vec{q}$ direction, of the recoiling nucleon of the pair in the final state (see Section 3.7 for details). The backward kinematics means that the virtual photon hits the nucleon initially moving forward with respect to $\vec{q}$ direction and leaves the partner nucleon in the pair recoiling backward ($\theta_{p_b q} > 100^o$). The forward kinematics means that the virtual photon hits the nucleon initially moving backward with respect to $\vec{q}$ direction, turns it around and both nucleons of the pair are moving forward in the final state (both $\theta_{pq} < 30^o$).

The kinematical difference between the two cases manifests itself in the energy transfer ω. In ^{3}He(e,epp)n reactions at 2.261 GeV incident energy (Fig. 4-2 and Fig. 4-3), it is found that in both cases the average values of the momentum transfer q are approximately equal ($q \sim 1.0$ GeV/c). However, in the backward kinematics, more energy transfer is required to put both nucleons on shell compared to the forward kinematics. In fact, the backward kinematics is on the high energy side of the quasi-elastic peak and the average value of $x_{Bj} = Q^2/2M_N\omega$ is 0.6. The forward kinematics is on the lower energy side of the quasi-elastic peak and the average value of x_{Bj} is 1.5. Fig. 4-16 shows the Q^2 vs ω for the two kinematics. The red lines in the plots indicate the central positions of the quasi-elastic peak.

The fact that the two kinematics are on different side of the quasi-elastic peak implies that the meson exchange current (MEC) effects should be smaller in forward kinematics than that in backward kinematics. The reason is that the forward kinematics is farther away from the Δ region and the missing energy is small compared to the pion mass ($E_m = \omega - T_1 - T_2 < 100$ MeV). This is confirmed by the calculations of J.M. Laget in Fig. 4-2 and Fig. 4-3. Remember in Chapter 1 we mentioned that the MEC effects are suppressed in (e,e'pp) reactions because the virtual photon does not couple to neutral exchanged pions to the first order. However, if the kinematics are chosen to be close to the Δ region, the strength of MEC becomes considerable.

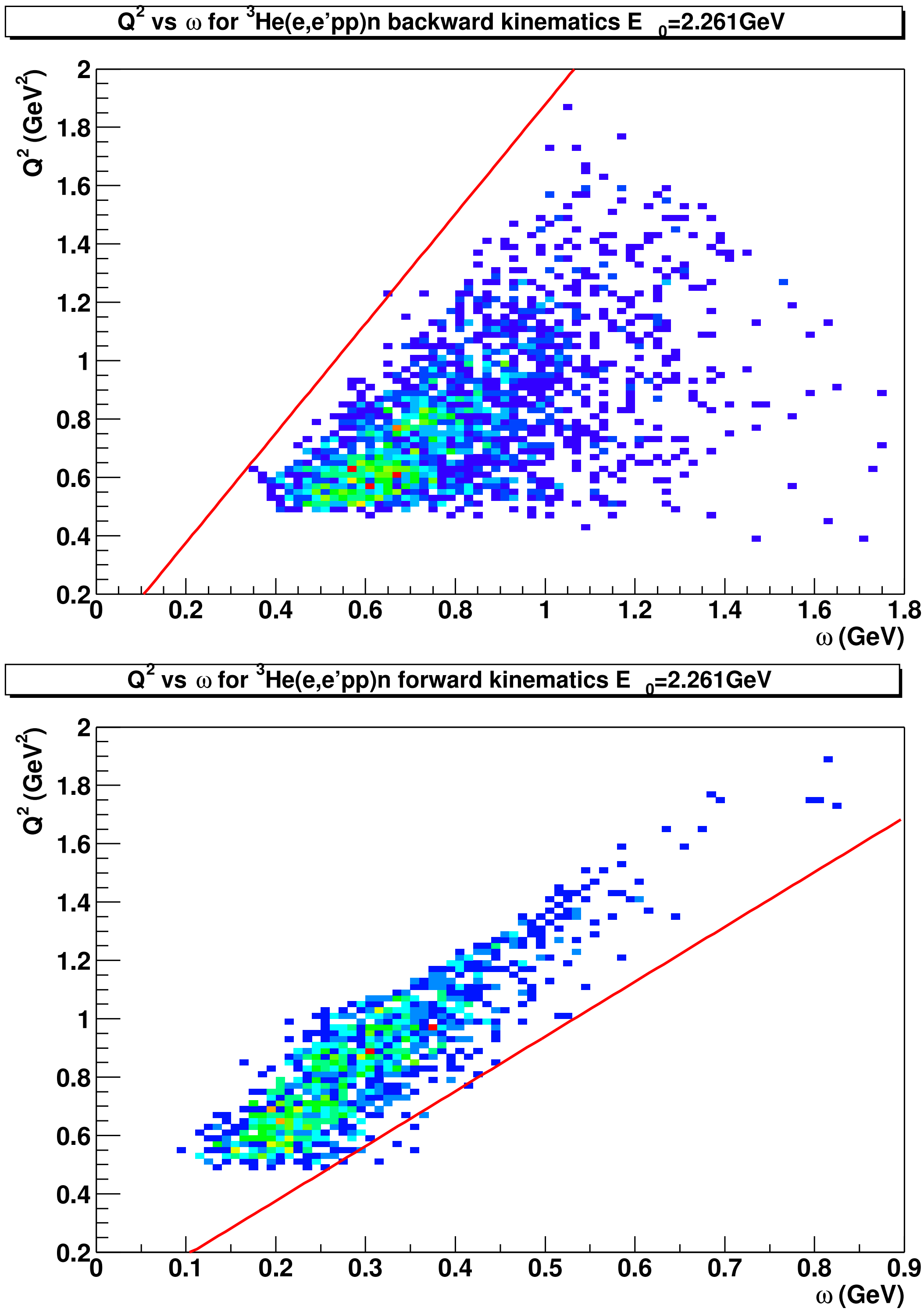

Figure 4-16: Q^2 vs ω for the backward and the forward kinematics for ^{3}He(e,e'pp)n with 2.261 GeV incident energy. The red lines indicate the central positions of the quasi-elastic peak.

This can be seen in Fig. 4-2. The bigger the initial momentum (in the plane wave picture, p_{rel} is the initial momentum of each nucleon in the center of mass frame of the nucleon-nucleon pair) , the larger the energy transfer is required, and the larger the relative strength of MEC becomes.

In both of the kinematics settings, the calculation shows that the final state interaction (FSI) contributions are very large (Fig. 4-2 and Fig. 4-3). FSI effects almost dominate the cross sections. The dips of the PWIA calculation curves in the figures correspond to the fact that the the S-state wave function of the pp pair in the space of their relative momentum per nucleon crosses zero at around 400 MeV/c. This dip is one of the kinematic signatures for the ground state correlations. However, according to the calculations, the FSI effect completely fill up the dip. Generally speaking, the rescattering amplitude of the NN pair becomes smaller if the final momenta of the two nucleons are farther away from each other (vectorially). For example, in the dip region of the forward kinematics, each nucleon has about 500 MeV/c initial momentum. When a momentum of 1 GeV/c is transfered to one nucleon in the opposite direction, the final momenta of the two nucleons are both about 500 MeV/c. In this case the FSI contribution is believed to be large. The FSI contribution is expected to be smaller if we increase the momentum transfer (see next section).

4.4.2 2.261 GeV vs 4.461 GeV in Incident Energy

The average momentum transfer with 4.461 GeV incident energy is about 1.5 GeV/c, while for 2.261 GeV incident energy the average momentum transfer is about 1 GeV/c. Fig. 4-17 shows the Q^2 vs ω for the two kinematics with incident energy of 4.461 GeV. The red lines in the plots indicate the central positions of the quasi-elastic peak.

Presumably the meson exchange current (MEC) contribution for the backward kinematics with 4.461 GeV incident energy is still important, for it is close to the Δ region. The calculation of J.M. Laget (Fig. 4-4) confirms that the MEC contribution is still important especially for higher initial momenta where the events are closer to

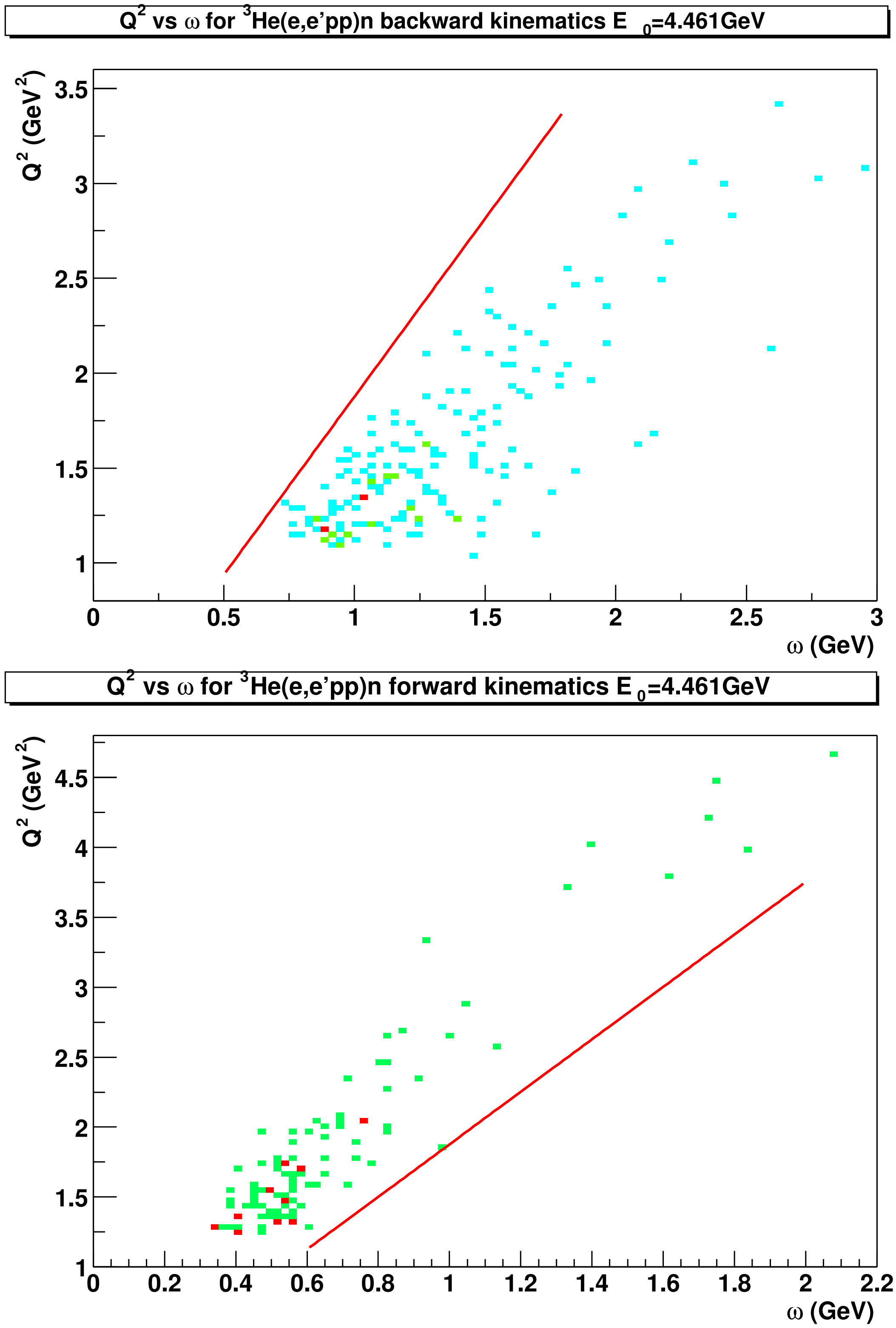

Figure 4-17: Q^2 vs ω for the backward and the forward kinematics for ^{3}He(e,e'pp)n with 4.461 GeV incident energy. The red lines indicate the central positions of the quasi-elastic peak.

the Δ region. The FSI contributions are expected to be smaller than for the 2.261 GeV incident energy case for both kinematic conditions, because the momentum transfer is bigger and the final momenta of the two emitted nucleons are farther apart from each other vectorially. However, the plane wave cross sections of the 4.461 GeV data are also smaller than that of the 2.261 GeV data, because the elementary cross section for knocking out one nucleon decreases when Q^2 increases. This results in that the relative importance of FSI is still considerable for the 4.461 GeV data (see calculations in Fig. 4-4 and Fig. 4-5).

It is interesting to notice that the dip at about 400 MeV/c discussed in Section 4.4.1 is seen in Fig. 4-4 and Fig. 4-5. Effects of FSI and MEC have not completely filled up the dip and the ground state properties of the correlated nucleon pair is more clearly revealed compared to 2.261 GeV data. The dips can be seen not only in ^{3}He data, but also in ^{4}He data (Fig. 4-9 and Fig. 4-10) and ^{12}C data (Fig. 4-14 and Fig. 4-15). The dips are generally more recognizable in the forward kinematics compared to the backward kinematics. One of the reasons probably is, as we discussed in Section 4.4.1, that the MEC contribution is less important in the forward kinematics than that in the backward kinematics.

4.4.3 Proton-Proton Pair vs Neutron-Proton Pair

If we assume that the residual system is a spectator and at rest, for a proton-proton pair, the $^1S_0$ wave is dominant in the (e,e'pp) reaction. However, in the (e,e'np) reaction, for a neutron-proton pair, both S waves ($^1S_0$ and $^3S_1$) and the $^3D_1$ wave contribute. By reference [52], the (e,e'np) cross section is dominated by the $^3D_1$ contribution [52]. As the result, in the plane wave impulsive approximation (PWIA), the cross section for (e,e'np) is bigger than the cross section for (e,e'pp) by at least one order of magnitude [52]. Moreover, the meson exchange current (MEC) contribution should be bigger in (e,e'np) than in (e,e'pp), because the virtual photon interacts more with charged exchanged pions than with neutral exchanged pions.

Fig. 4-18 shows the comparison of the cross sections for ^{3}He(e,e'pp)n and ^{3}He(e,e'np)p at backward kinematics with 2.261 GeV incident energy (Fig. 4-2 and Fig. 4-1 plotted together on the same scale). One can see the cross sections for ^{3}He(e,e'pp)n and ^{3}He(e,e'np)p are of the same order of magnitude. The same is true for ^{4}He and ^{12}C data (Fig. 4-7 vs Fig. 4-6 and Fig. 4-12 vs Fig. 4-11). It is likely due to the fact the final state interaction (FSI) effects are so big that they have completely undermined the PWIA picture and, moreover, the FSI contributions for the two cases are similar in amplitude. Fig. 4-18 also shows that the np pair cross section is smaller than the cross section of pp pair when $p_{rel} < 400$ MeV/c, while the situation is the contrary when $p_{rel} > 400$ MeV/c. This is possibly due to the fact that the MEC contribution is more important at large p_{rel} than at small p_{rel}, which is also shown in Fig. 4-2. It would be interesting to see the same comparison for data with higher momentum transfer, because of the argument we made in Section 4.4.2 that the FSI contribution becomes smaller if we increase the momentum transfer. Unfortunately, we do not have this kind of data because at this time we can not detect high momentum neutrons (> 2 GeV/c) in CLAS.

4.4.4 ^{3}He vs ^{4}He vs ^{12}C

We do not have theoretical calculations available for ^{4}He and ^{12}C data, therefore we can not make a quantitative comparison between the data and the theory at this time. However, we are still able to make a "qualitative" discussion about the different nuclei. The most apparent difference between ^{3}He, ^{4}He and ^{12}C nuclei is the number of nucleons. This results in the different numbers of nucleon-nucleon (NN) pairs that can be formed. Another difference between these nuclei is the density. This results in the different possibilities for a NN pair to be close to each other and the different importances of short range correlations (SRC). The densities of ^{4}He and ^{12}C are more close to each other, while the density of ^{3}He is relatively smaller. If we disregard the density difference, the number of correlated NN pairs of these nuclei

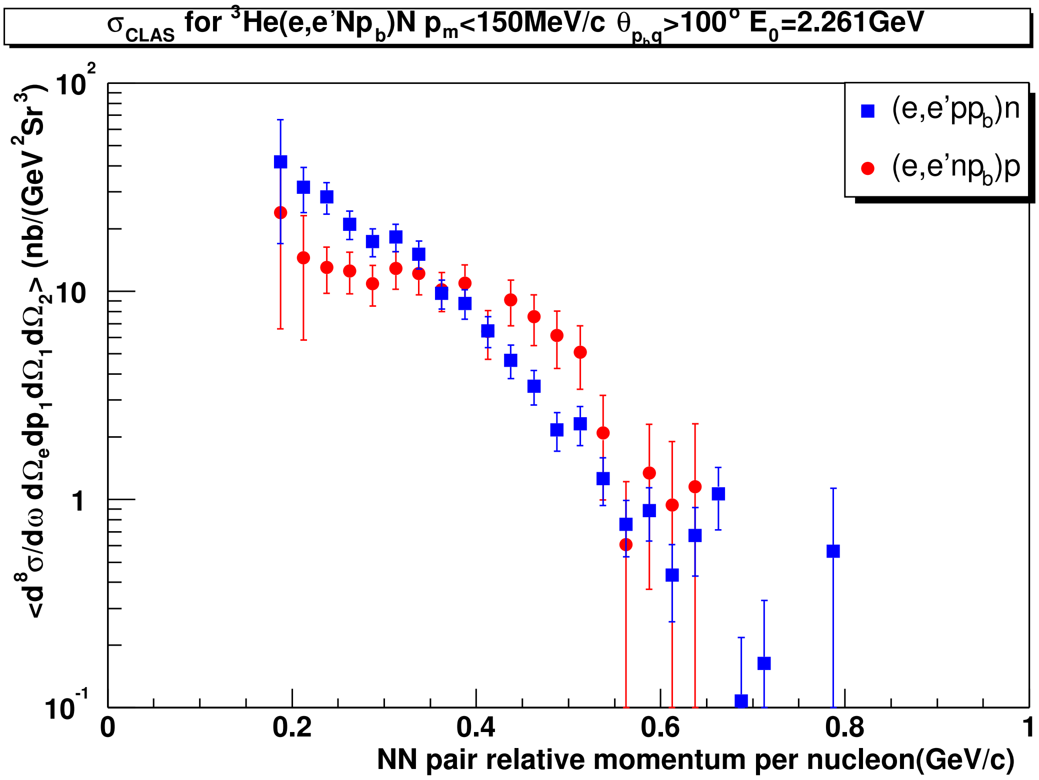

Figure 4-18: Comparison of the cross sections for ^{3}He(e,e'pp)n and ^{3}He(e,e'np)p at backward kinematics with 2.261 GeV incident energy.

should correspond to the number of nucleons that form the pairs.

^{3}He has two protons and one neutron, which can form one proton-proton (pp) pair and one neutron-proton (np) pair. ^{4}He has two protons and two neutrons, which can form one pp pair and two np pair. ^{12}C has six protons and six neutrons, which can form three pp pair and six np pair. As we mentioned, if we disregard the density difference, in a plane wave picture, the ratios of cross sections for knocking out a NN pair should be the same as the ratios of available pairs, i.e.

$$\frac{\sigma_{pp}(^4He)}{\sigma_{pp}(^3He)} = 1, \quad \frac{\sigma_{pp}(^{12}C)}{\sigma_{pp}(^3He)} = 3, \quad \frac{\sigma_{pp}(^{12}C)}{\sigma_{pp}(^4He)} = 3 \tag{4.2}$$

$$\frac{\sigma_{np}(^4He)}{\sigma_{np}(^3He)} = 2, \quad \frac{\sigma_{np}(^{12}C)}{\sigma_{np}(^3He)} = 6, \quad \frac{\sigma_{np}(^{12}C)}{\sigma_{np}(^4He)} = 3 \tag{4.3}$$

Fig. 4-19 shows the ratios of (e,e'pp) and (e,e'np) cross sections for the backward and forward kinematics between ^{3}He, ^{4}He and ^{12}C. The incident energy is 2.261 GeV. It is interesting to see that the ratios in the middle column, which is (e,e'pp) at the forward kinematics, are more or less close the ratios between the number of pp pairs. However, the ratios in the first column ((e,e'pp) at the backward kinematics) and the third column ((e,e'np) at the backward kinematics) are smaller than the ratios of the pp or np pairs by approximately 50%. This, to some extent, implies that the reactions at the forward kinematics are closer to the plane wave picture compared to the backward kinematics. Remember that in the previous discussions, the calculations for ^{3}He data (Fig. 4-3 and Fig. 4-5) show that the meson exchange currents contributions are much smaller at the forward kinematics than at the backward kinematics. However, the final state interaction (FSI) contributions are still considerably important at the forward kinematics. One possible explanation is that the FSI effects are similar at the forward kinematics for different nuclei so the ratios are retained. On the contrary, the FSI and the MEC effects are more important and different at the backward kinematics for different nuclei.

It would be interesting to see the same ratios for 4.461 GeV data, where the FSI and the MEC effects are expected to be smaller compared to 2.261 GeV data. Fig. 4-20 shows the ratios of the cross sections of (e,e'pp) for the 4.461 GeV data. Unfortunately, due to limited statistics, the error bars are so big that one can hardly conclude anything.

4.5 Summary

We performed the measurements for electron induced two nucleon knockout reactions (e,e'pp) and (e,e'np) for ^{3}He, ^{4}He and ^{12}C nuclei with incident energies of 2.261 GeV and 4.461 GeV. We focused on the case where the missing momentum is below the Fermi level and assumed the residual system is a spectator. We studied two different

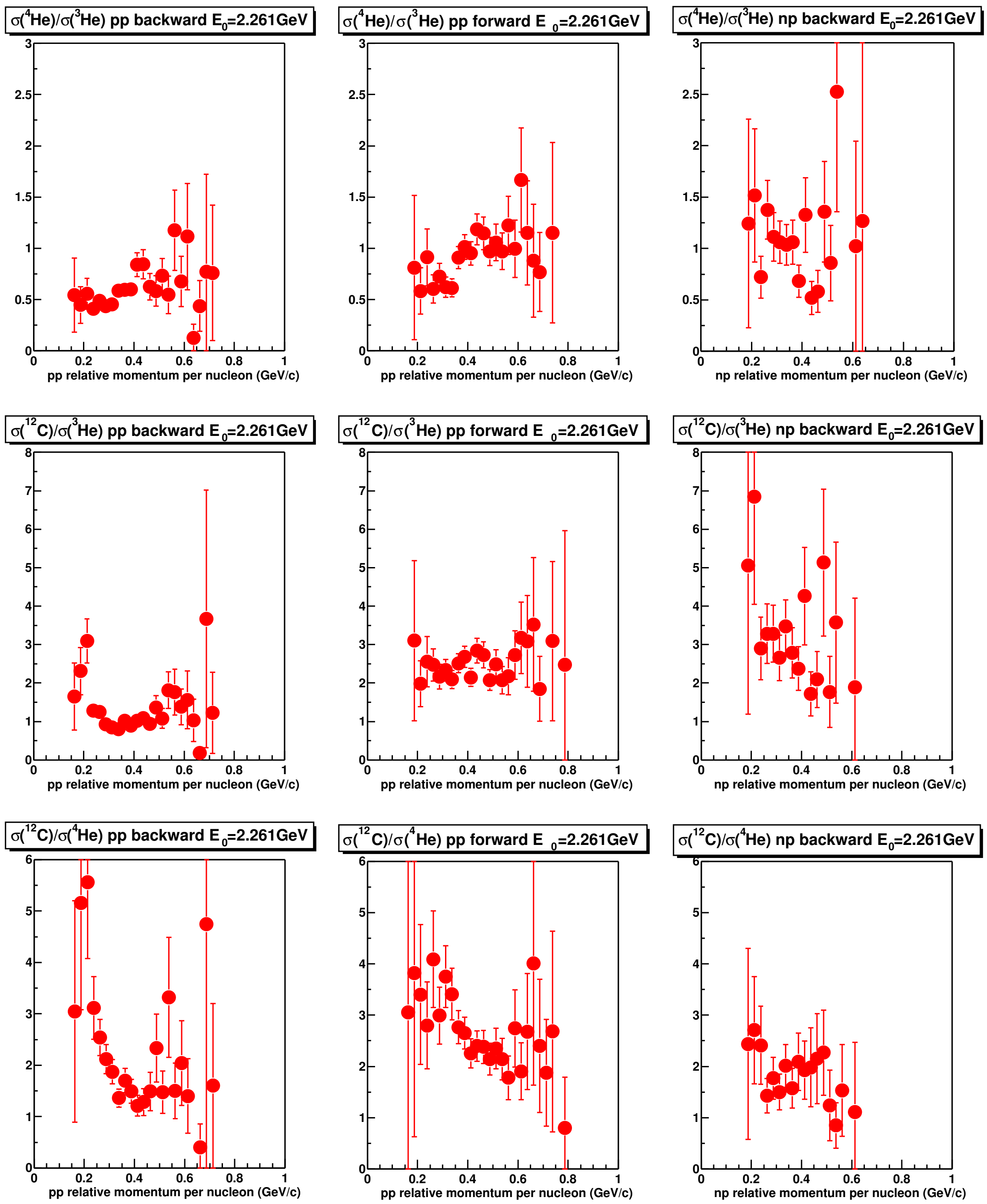

Figure 4-19: The ratios of (e,e'pp) and (e,e'np) cross sections for the backward and forward kinematics between ^{3}He, ^{4}He and ^{12}C nucleus. The incident energy is 2.261 GeV.

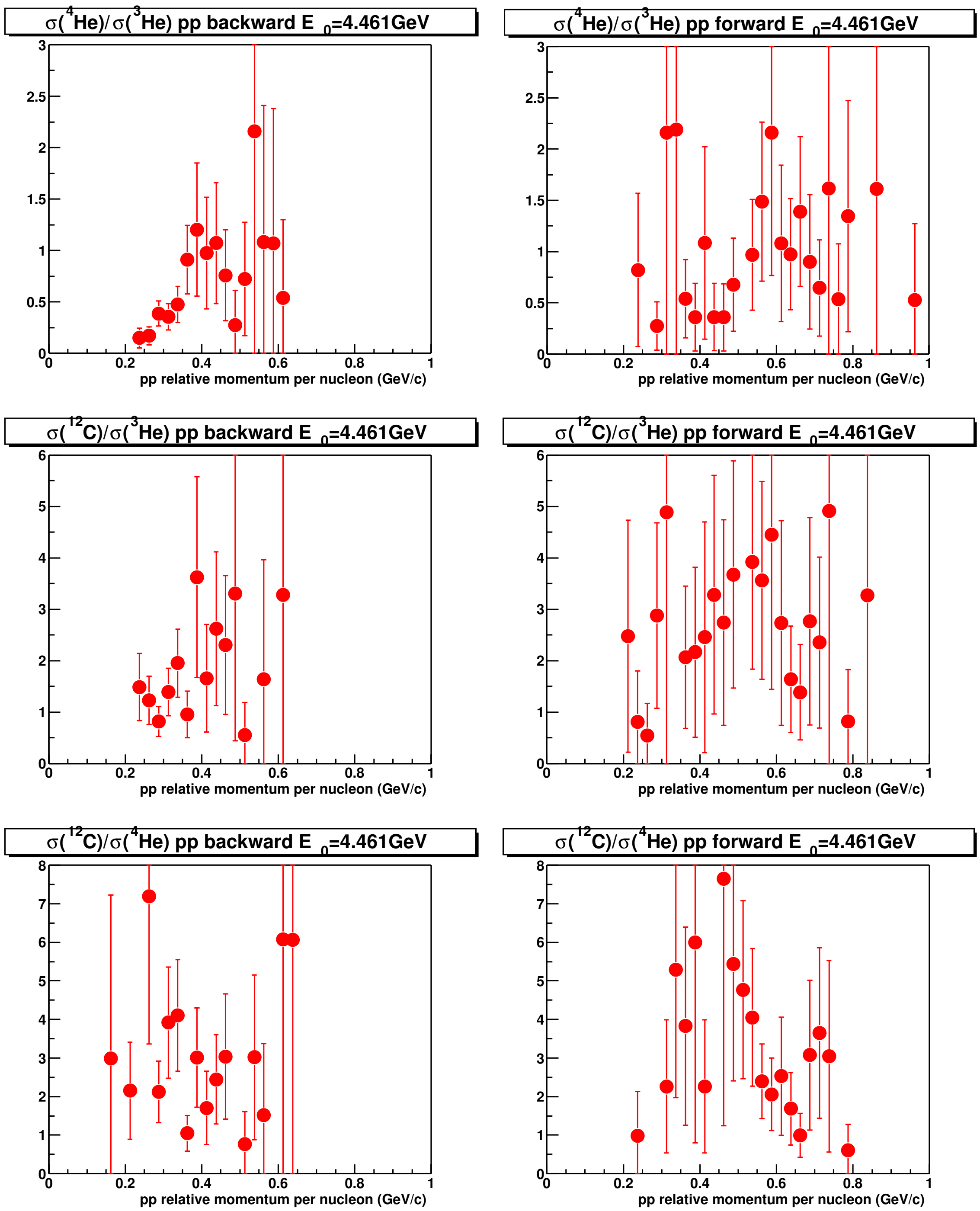

Figure 4-20: The ratios of (e,e'pp) cross sections for the backward and forward kinematics between ^{3}He, ^{4}He and ^{12}C nucleus. The incident energy is 4.461 GeV.

kinematics. The backward kinematics means that the virtual photon hits the nucleon initially moving forward with respect to the $\vec{q}$ direction and leaves the partner nucleon in the pair recoiling backward ($\theta_{p_b q} > 100^o$). The forward kinematics means that the virtual photon hits the nucleon initially moving backward with respect to the $\vec{q}$ direction, turns it around and both nucleons of the pair are moving forward in the final state (both $\theta_{pq} < 30^o$). We present the cross sections as average values within the CLAS phase space volume and as functions of the "initial relative momentum of the NN pair per nucleon".

Our results show that the initial relative momentum of the NN pair per nucleon extends up to 800 MeV/c, which is well above the Fermi level, with considerable strength. In Fig. 4-2–4-5, the PWIA calculations used the ground state wave function of ^{3}He as the Faddeev solution with the Paris potential. The short range correlations are built into the wave function by the Paris potential. If one uses the mean field description of the ground state wave function, for this kind of initial momentum, the cross sections should be much smaller than the PWIA calculations in the figures. This is indicated by Fig. 4-21, in which two proton momentum distributions in ^{3}He are showed. One distribution is using the Salme spectral function, which is the Faddeev solution with SRC builtin. The other distribution is a simple Gaussian parameterization using the Woods-Saxon potential (the parameters were chosen to yield the right rms radius of ^{3}He), which is mean field theory. Both distributions are normalized by $\int_0^\infty 4\pi p^2 n(p) dp = 1$. One can clearly see that the mean field curve drops more rapidly above 300 MeV/c compared to the Salme curve and the difference is in orders of magnitude. Moreover, this difference is considerably magnified when considering the probability of finding two protons simultaneously with high initial momenta.

However, the full calculations also indicate that the final state interactions (FSI) between the two emitted nucleons and the meson exchange currents (MEC) are very important and almost dominate the cross sections. This makes it difficult to single out

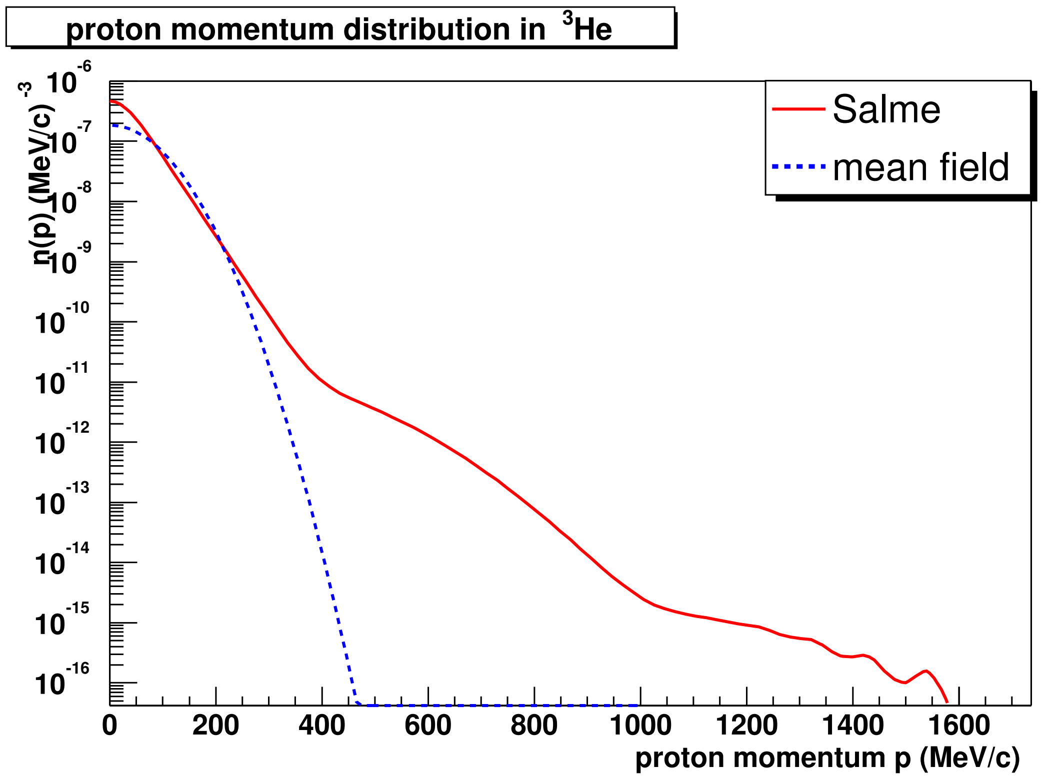

Figure 4-21: Proton momentum distributions in ^{3}He. The solid line is the Salme spectral function. The dashed line is a simple Gaussian parameterization using the Woods-Saxon potential. Both distributions are normalized by $\int_0^\infty 4\pi p^2 n(p) dp = 1$.

the ground state properties and study the influences of the detailed treatments for the SRC of various modern NN potentials. For example, in the plane wave picture, the possibility of np emission should be bigger than pp emission by orders of magnitude. But due to the dominant roles of FSI and MEC, the cross sections of np emission and pp emission are of the same order of magnitude (see Fig. 4-18).

One important observation from our results is that the node around 400 MeV/c for the $^1S_0$ pp pair shows up in 4.461 GeV data, especially at the forward kinematics. This implies that with large momentum transfer and on the lower energy side of the quasi-elastic peak, the FSI and MEC contributions will not completely mask the ground state properties of the nucleon-nucleon pair.

In the future, with accelerators being able to deliver higher energy electron beams (e.g. Jefferson Lab is now hoping to upgrade to 12 GeV), we shall be able to make measurements at higher momentum transfers and include appropriate neutron detection within a wider momentum range. By looking at the forward kinematics (or so-called "super anti-parallel" kinematics), we expect the ground state properties of NN pairs will become more and more important in electron induced two nucleon emission reactions. This, together with quantitative theories with precise treatments of FSI and MEC effects, will provide better opportunities to study the detailed short range behaviors of nucleons in the nucleus.

Appendix A

CLAS Fiducial Acceptance Functions for Electrons, Protons and Neutrons

File "EFid_2GeV_2250A.dat" (Electron Fiducial Cuts Function For 2.2 GeV Data):
62.2935, -92.5133, 87.0360, -38.4696, 6.3177, 0, 0, 0, 0, 78.5134, -58.5975, 3.30928, 77.4749, -64.3984, 14.4860, 0, 0, 0, -140.845, 1381.30, -4499.99, 7557.27, -7140.27, 3828.75, -1086.21, 126.468, 0, 497.951, -1846.42, 2759.58, -1634.71, 345.006, 0, 0, 0, 0, 9.40986, 180.752, -646.771, 1055.14, -909.094, 424.435, -99.8368, 9.02086, 0, 288.485, -1016.03, 1463.72, -859.231, 185.976, 0, 0, 0, 0, 61.1474, -88.768, 82.6446, -36.2780, 5.92310, 0, 0, 0, 0, 78.5134, -58.5975, 3.30928, 77.4749, -64.3984, 14.4860, 0, 0, 0, 21.3087, 138.975, -672.710, 1324.20, -1326.12, 714.866, -197.531, 21.9144, 0, 375.091, -1411.50, 2082.58, -1192.17, 239.685, 0, 0, 0, 0, -121.816, 1182.59, -3800.98, 6319.82, -5937.33, 3179.37, -903.954, 105.764, 0, -4781.96, 43165.9, -159567, 318502, -376469, 271207, -116893, 27698.9, -2775.61, 61.1474, -88.7680, 82.6446, -36.2780, 5.92310, 0, 0, 0, 0, 73.7620, -34.6321, -41.8796, 117.543, -81.2043, 17.1718, 0, 0, 0, 157.046, -765.472, 1735.21, -2053.86, 1371.34, -515.214, 101.081, -8.07402, 0, -608.740, 4827.18, -13239.6, 17742.4, -12420.0, 4369.11, -607.877, 0, 0, -274.278, 2380.63, -7560.19, 12582.3, -

11924.5, 6464.66, -1863.44, 221.134, 0, -1240.72, 8096.04, -19407.0, 23942.9, -16052.3, 5559.32, -776.123, 0, 0, 61.1474, -88.7680, 82.6446, -36.2780, 5.92310, 0, 0, 0, 0, 78.5134, -58.5975, 3.30928, 77.4749, -64.3984, 14.4860, 0, 0, 0, -71.2528, 879.668, -3027.37, 5226.61, -4999.19, 2689.35, -761.206, 88.1242, 0, -1269.89, 9486.25, -26103.8, 35581.2, -25373.0, 9062.87, -1277.60, 0, 0, -186.640, 1811.85, -6032.01, 10283.3, -9808.11, 5285.35, -1501.87, 174.799, 0, -530.826, 4643.56, -13864.2, 20580.2, -15898.0, 6106.69, -916.365, 0, 0, 61.6665, -90.4268, 84.5606, -37.2240, 6.09207, 0, 0, 0, 0, 78.5134, -58.5975, 3.30928, 77.4749, -64.3984, 14.4860, 0, 0, 0, -1.53910, 216.936, -701.057, 1167.26, -1111.92, 615.364, -183.854, 22.8595, 0, -19.7415, 454.317, -1250.51, 1512.52, -762.408, 137.695, 0, 0, 0, -55.9612, 657.449, -2049.73, 3295.30, -2995.85, 1553.68, -427.764, 48.4324, 0, -522.682, 3356.77, -7535.50, 8756.49, -5518.61, 1795.60, -235.144, 0, 0, 61.1474, -88.7680, 82.6446, -36.2780, 5.92310, 0, 0, 0, 0, 73.7620, -34.6321, -41.8796, 117.543, -81.2043, 17.1718, 0, 0, 0, -82.0368, 883.261, -2828.84, 4621.53, -4223.56, 2185.52, -598.218, 67.2908, 0, 608.323, -2743.56, 4942.01, -4045.58, 1558.07, -226.240, 0, 0, 0, 4.07203, 138.882, -321.983, 282.702, -12.9566, -129.159, 74.5884, -12.9994, 0, -866.737, 5984.13, -15129.6, 19134.6, -12757.7, 4276.79, -566.056, 0, 0

74.4893, -158.720, 251.241, -200.000, 52.2984, 25.4188, -18.8692, 3.27217, 90.8413, -226.800, 358.487, -259.260, 30.9359, 68.7248, -38.9760, 6.47933, 117.102, -429.455, 1208.29, -1922.72, 1791.40, -965.135, 277.459, -32.8536, 55.0676, 91.0959, -444.252, 791.284, -717.492, 350.325, -87.3235, 8.68087

77.7940, -192.492, 361.852, -394.127, 246.499, -84.6133, 13.9182, -0.713846, 41.2902, 110.603, -586.690, 1130.70, -1137.27, 633.345, -185.038, 22.1482

-12998.3, 57694.0, -109085, 114102, -71303.6, 26616.9, -5494.45, 483.756, 17842.9, -74659.9, 133869, -133170, 79380.0, -28352.3, 5617.88, -476.314, 65.5364, -99.8689, 88.5645, 24.8299, -121.327, 102.818, -37.8275, 5.28492, 66.4049, -76.4096, -20.8674, 230.072, -318.905, 206.721, -66.3286, 8.48753, 100.262, -358.882, 957.267, -1495.42, 1396.73, -765.881, 226.791, -27.9341, 50.4447, 48.3032, -315.976, 580.141, -525.583, 252.075, -59.9294, 5.34805, 78.5845, -155.728, 320.528, -420.296, 341.899, -164.626, 42.5274, -4.50224, 95.9430, -221.787, 391.495, -350.033, 131.391, 13.2965, -24.0460, 4.92253

```fortran
      subroutine ReadEFidPars
c     read the parameters for electron fiducial cut
c     from the file EFid_2GeV_2250A.dat which must be in current dir

      real par_phi(9,6,6)
      real par_the3(8,4)
      real par_the4(8,2)
      real par_the5(8,8)
      common /EFidPars/par_phi,par_the3,par_the4,par_the5

      open(unit=99,file="EFid_2GeV_2250A.dat",status="old")
      read (99,*) par_phi
      read (99,*) par_the3
      read (99,*) par_the4
      read (99,*) par_the5
      close(99)
      return
      end

      subroutine EFiducialCut_2GeV_2250A(px, py, pz, status)
c     electron fiducial cut for 2.2Gev 2250A
c     subroutine ReadEFidPars must be called once before this
c     subroutine is called for the first time to get the parameters
c     input : real px py pz, three component of electron momentum
c     output: int status, 1 means passing the cut, 0 means not passing

      real par_phi(9,6,6)
      real par_the3(8,4)
      real par_the4(8,2)
      real par_the5(8,8)
      common /EFidPars/par_phi,par_the3,par_the4,par_the5

      real px, py, pz
      integer status, sector, ipar, dpar
      real p, theta, phi, tmptheta
      real con_phi(6)
      real con_the3(4)
      real con_the4(2)
      real con_the5(8)

      status = 1
      phi=atan2(py,px)*180./3.14159265
      if (phi.lt.-30) phi=phi+360
      sector=int((phi+30.)/60.)+1
      if (sector.lt.1) sector=1
      if (sector.gt.6) sector=6
      phi=phi-(sector-1)*60.
      theta=atan2(sqrt(px*px+py*py),pz)*180./3.14159265
      p=sqrt(px*px+py*py+pz*pz)
      do 771 ipar=1,6
         con_phi(ipar) = 0.0
         do 772 dpar=1,9
            con_phi(ipar) = con_phi(ipar)*p
     $           + par_phi(10-dpar,ipar,sector)
 772     continue
 771  continue
      if(phi.lt.0) then
         tmptheta=con_phi(1)-con_phi(4)/con_phi(3)
     $        +con_phi(4)/(con_phi(3)+phi)
         if(theta.gt.tmptheta.and.
     $        tmptheta.ge.con_phi(1).and.
```

```
     $        theta.lt.con_phi(2)) then
                status = 1
             else
                status = 0
             endif
          else
             tmptheta=con_phi(1)-con_phi(6)/con_phi(5)
     $        +con_phi(6)/(con_phi(5)-phi)
             if(theta.gt.tmptheta.and.
     $        tmptheta.ge.con_phi(1).and.
     $        theta.lt.con_phi(2)) then
                status = 1
             else
                status = 0
             endif
          endif

c         knockout bad sc paddles

          if(sector.eq.3) then
             do 661 ipar=1,4
                con_the3(ipar) = 0.0
                do 662 dpar=1,8
                   con_the3(ipar) = con_the3(ipar)*p
     $                  + par_the3(9-dpar,ipar)
 662            continue
 661         continue
             if(theta.gt.con_the3(1).and.
     $        theta.lt.con_the3(2)) status=0
             if(theta.gt.con_the3(3).and.
     $        theta.lt.con_the3(4)) status=0
          elseif(sector.eq.4) then
             do 551 ipar=1,2
                con_the4(ipar) = 0.0
                do 552 dpar=1,8
                   con_the4(ipar) = con_the4(ipar)*p
     $                  + par_the4(9-dpar,ipar)
 552            continue
 551         continue
             if(theta.gt.con_the4(1).and.
     $        theta.lt.con_the4(2)) status=0
          elseif(sector.eq.5) then
             do 441 ipar=1,8
                con_the5(ipar) = 0.0
                do 442 dpar=1,8
                   con_the5(ipar) = con_the5(ipar)*p
     $                  + par_the5(9-dpar,ipar)
 442            continue
 441         continue
             if(theta.gt.con_the5(1).and.
     $        theta.lt.con_the5(2)) status=0
             if(theta.gt.con_the5(3).and.
     $        theta.lt.con_the5(4)) status=0
             if(theta.gt.con_the5(5).and.
     $           theta.lt.con_the5(6)) status=0
             if(theta.gt.con_the5(7).and.
     $        theta.lt.con_the5(8)) status=0
          endif

          return
          end
```

File "PFid_2GeV_2250A.dat" (Proton Fiducial Cuts Function For 2.2 GeV Data):
60.2165, -189.720, 446.990, -523.122, 320.721, -97.8518, 11.5258, -1457.16, 13814.2, -43182.7, 66646.0, -54355.1, 22423.5, -3683.76, 17.1086, 54.2974, -103.464, 111.325, -70.7673, 27.2551, -5.02858, -2547.86, 22143.1, -66326.6, 101105.0, -82187.8, 33959.7, -5607.59, 65.7242, -246.922, 759.745, -1198.32, 1007.05, -428.060, 72.2644, 3384.16, -19353.1, 54083.5, -79843.4, 63870.2, -26079.2, 4250.29, 85.2489, -441.821, 1327.52, -1978.53, 1567.84, -633.530, 102.928, 411.998, -533.572, 599.925, 2099.52, -5061.48, 3701.58, -891.843, 110.022, -558.044, 1512.96, -2098.53, 1579.55, -613.478, 96.3279, 3937.29, -23745.1, 59651.0, -76988.6, 54276.0, -19900.2, 2974.95, 35.8488, -46.9595, 107.492, -93.9141, 10.5845, 26.1910, -9.89460, -326.838, 4634.99, -11155.2, 11811.4, -5405.80, 554.030, 175.526, 38.9338, -62.8663, 118.218, -56.6953, -40.5083, 46.1782, -11.5822, 1864.83, -11735.6, 34175.4, -48928.5, 37315.8, -14496.1, 2254.05, 23.6892, 9.69854, 94.4521, -270.119, 288.132, -140.031, 25.9272, -261.086, 4863.13, -11760.4, 13791.1, -8983.19, 3136.52, -457.183, -11.0252, 348.901, -1172.63, 1980.73, -1759.08, 786.043, -139.299, -2231.41, 23477.1, -78229.3, 129238.0, -111761.0, 48561.4, -8370.65, 104.415, -548.464, 1506.70, -2064.10, 1507.55, -561.677, 83.9247, 1402.87, -9008.78, 25660.0, -37543.3, 29860.8, -12238.4, 2019.03, 20.4577, 66.1373, -205.218, 372.864, -366.625, 177.596, -33.1168, 2059.77, -14468.3, 46492.9, -72168.2, 58275.9, -23615.8, 3800.60, -18.9897, 392.519, -1234.31, 1950.24, -1623.01, 681.260, -113.806, -3478.50, 32840.9, -104381.0, 167656.0, -143070.0, 61909.3, -10690.1

110.007, 121.302, 97.8380, -1679.71, 4022.73, -3973.09, 1422.42, 69.7305, 359.843, -876.383, 649.612, 600.059, -1155.43, 472.866, 13.9334, -236.587, 810.783, -1614.65, 1851.97, -1125.48, 280.069, 10.1644, 51.7943, -527.843, 2071.12, -3480.34, 2663.52, -768.498, 161.555, -263.801, 770.924, -902.814, 503.641, -319.619, 171.147, 154.660, -619.711, 3444.65, -8994.29, 12253.9, -8439.82, 2321.14, 117.461, -1429.96, 6117.79, -13492.3, 16142.2, -9965.40, 2490.47, 7.77411, -17.3501, 279.462, -876.326, 1398.82, -1137.49, 365.383, -31.1460, 1942.49, -9193.97, 21731.0, -26961.3, 16701.7, -4067.85, 154.660, -654.420, 3774.08, -9920.36, 13333.7, -8953.68, 2386.32, 63.2709, -867.859, 4000.97, -9557.57, 12215.1, -7926.91, 2052.90, -28.1127, 484.636, -2665.71, 7484.94, -10740.7, 7561.79, -2076.70, 172.853, -656.312, 3768.76, -10243.0, 14600.3, -10616.3, 3095.27, 270.076, -1938.46, 9276.01, -21861.1, 27363.7, -17479.9, 4490.05, 32.2327, -432.593, 1666.57, -3491.43, 4031.58, -2406.30, 579.944, -44.9153, 638.112, -2971.77, 7223.13, -9328.99, 6080.46, -1576.13, 45.7403, 875.133, -3646.85, 7848.52, -8905.36, 4914.78, -1010.91, 138.000, -449.485, 2806.13, -7725.44, 10777.3, -7482.95, 2056.80, 72.7551, -944.002, 4200.92, -9776.76, 12316.6, -7955.78, 2066.50, -9.59531, 180.519, -795.797, 2124.85, -2978.29, 2040.14, -541.811, 77.5100, 494.571, -1625.99, 2397.48, -1177.99, -574.604, 530.446, 117.869, -56.8761, 330.252, -715.276, 807.257, -497.124, 133.989, 7.66164, -208.001, 996.883, -2772.33, 4100.81, -3008.90, 864.126, -25.3497, 346.501, -1458.46, 3513.62, -4625.70, 3088.01, -818.696

-28.1486, 425.124, -935.693, 1065.39, -608.526, 137.658, -15.2084, 345.466, -697.657, 751.738, -419.288, 95.2206

17.1490, 294.605, -640.590, 707.758, -386.730, 83.2529, 35.9318, 204.580, -404.489, 413.240, -209.580, 41.7819, 47.6825, 274.777, -754.725, 1117.80, -846.816, 255.607, 44.7484, 344.543, -872.200, 1113.89, -694.736, 168.061, -205.978, 828.617, -1199.65, 875.482, -317.846, 45.6938, -240.595, 961.068, -1370.34, 977.625, -345.743, 48.3834, -136.104, 479.276, -593.135, 374.730, -118.350, 14.7923, -196.773, 700.974, -894.540, 577.460, -185.690, 23.6201

81.8115, 139.810, -445.130, 804.212, -821.194, 364.924, 79.5053, 317.287, -1582.80, 3987.05, -4880.55, 2305.63, -137.480, 633.288, -954.383, 721.057, -269.140, 39.4822, -145.605, 697.662, -1088.74, 853.855, -330.883, 50.3421

-29.9426, 370.963, -714.697, 707.343, -348.995, 67.7647, -27.4173, 372.536, -693.341, 652.792, -302.559, 54.7761, -47.1617, 132.967, -104.776, 41.7673, -7.68238, 0.404311, -54.5895, 149.685, -111.590, 41.2556, -6.93943, 0.301087, -79.1386, 275.678, -341.972, 218.907, -69.5520, 8.66381, -97.5794, 352.616, -468.487, 322.829, -111.159, 15.0975, 22.5823, -182.064, 365.317, -294.653, 108.779, -15.2712, -7.59521, 2.91795, 31.6773, -28.3085, 10.5943, -1.57966

```
c     ------------------------------------------------------------------------


      subroutine ReadPFidPars
c     read the parameters for proton fiducial cuts
c     from the file PFid_2GeV_2250A.dat which must be in current dir

      real par_for(7,4,6)
      real par_bak(7,4,6)
      real par_pth2(6,2)
      real par_pth3(6,8)
      real par_pth4(6,4)
      real par_pth5(6,8)
      common /PFidPars/par_for,par_bak,par_pth2,par_pth3,par_pth4,par_pth5

      open(unit=99,file="PFid_2GeV_2250A.dat",status="old")
      read (99,*) par_for
      read (99,*) par_bak
      read (99,*) par_pth2
      read (99,*) par_pth3
      read (99,*) par_pth4
      read (99,*) par_pth5
      close(99)
      return
      end



c     -------------------------------------------------------------------------



      subroutine PFiducialCut_2GeV_2250A(px, py, pz, status)
c     proton fiducial cuts for 2.2GeV 2250A data
c     subroutine ReadPFidPars must be called once before this
c     subroutine is called for the first time to get the parameters
c     input : real px py pz, three components of proton momentum
c     output: int status, 1 means passing the cut, 0 means not

      real par_for(7,4,6)
      real par_bak(7,4,6)
      real par_pth2(6,2)
      real par_pth3(6,8)
      real par_pth4(6,4)
      real par_pth5(6,8)
      common /PFidPars/par_for,par_bak,par_pth2,par_pth3,par_pth4,par_pth5

      real px, py, pz
      integer status, sector, ipar, dpar
      real p, p_for, p_bak, p_pth
      real theta0, theta, tmptheta
      real phi, phi_lower, phi_upper
      real con_for(4)
      real con_bak(4)
      real con_pth2(2)
      real con_pth3(8)
      real con_pth4(4)
      real con_pth5(8)

      status = 1
      phi=atan2(py,px)*180./3.14159265
```

```
      if (phi.lt.-30) phi=phi+360
      sector=int((phi+30.)/60.)+1
      if (sector.lt.1) sector=1
      if (sector.gt.6) sector=6
      phi=phi-(sector-1)*60.
      theta=atan2(sqrt(px*px+py*py),pz)*180./3.14159265
      p=sqrt(px*px+py*py+pz*pz)
      if(p.lt.0.25) then
         status = 0
         return
      endif

c     calculate the momentum after energy loss which is actually measured
      if(p.lt.1.) then
         p = -0.157371 + 1.68142*p -0.968966*p*p + 0.449868*p*p*p
      endif

      p_for = p
      if (p_for.lt.0.3) p_for = 0.3
      if (p_for.gt.1.6) p_for = 1.6
      p_bak = p
      if (p_bak.lt.0.2) p_bak = 0.2
      if (p_bak.gt.1.0) p_bak = 1.0
      theta0 = 8.5
      phi_lower = -24.0
      phi_upper = 24.0

c     calculate the parameters for this momentum

      do ipar=1,4
         con_for(ipar) = 0.0
         con_bak(ipar) = 0.0
         do dpar=1,7
            con_for(ipar) = con_for(ipar)*p_for
     $           + par_for(8-dpar,ipar,sector)
            con_bak(ipar) = con_bak(ipar)*p_bak
     $           + par_bak(8-dpar,ipar,sector)
         enddo
      enddo

c     check forward region

      if(phi.lt.0) then
         tmptheta = theta0 - con_for(2)/con_for(1)
     $        + con_for(2)/(con_for(1)+phi)
         if(theta.gt.tmptheta.and.
     $        tmptheta.ge.theta0.and.
     $        phi.ge.phi_lower) then
            status = 1
         else
            status = 0
            return
         endif
      else
         tmptheta = theta0 - con_for(4)/con_for(3)
     $        + con_for(4)/(con_for(3)-phi)
         if(theta.gt.tmptheta.and.
     $        tmptheta.ge.theta0.and.
     $        phi.le.phi_upper) then
            status = 1
         else
```

```
            status = 0
            return
         endif
      endif

c     check backward region

      if(theta.gt.con_bak(1)) then
         status = 0
         return
      elseif(theta.gt.con_bak(2)) then
         if((phi-phi_lower)/(theta-con_bak(2)).ge.
     $        (con_bak(3)-phi_lower)/(con_bak(1)-con_bak(2))
     $        .and.(phi-phi_upper)/(theta-con_bak(2)).le.
     $        (con_bak(4)-phi_upper)/(con_bak(1)-con_bak(2))) then
            status = 1
         else
            status = 0
            return
         endif
      endif



c     knock out bad sc paddles



      p_pth = p
      if (p_pth.lt.0.2) p_pth = 0.2
      if(sector.eq.2) then
         do ipar=1,2
            con_pth2(ipar) = 0.0
            do dpar=1,6
               con_pth2(ipar) = con_pth2(ipar)*p_pth
     $              + par_pth2(7-dpar,ipar)
            enddo
         enddo
         if(theta.gt.con_pth2(1).and.
     $        theta.lt.con_pth2(2)) status = 0
      elseif(sector.eq.3) then
         do ipar=1,8
            con_pth3(ipar) = 0.0
            do dpar=1,6
               con_pth3(ipar) = con_pth3(ipar)*p_pth
     $              + par_pth3(7-dpar,ipar)
            enddo
         enddo
         if(theta.gt.con_pth3(1).and.
     $        theta.lt.con_pth3(2)) status = 0
         if(theta.gt.con_pth3(3).and.
     $        theta.lt.con_pth3(4)) status = 0
         if(theta.gt.con_pth3(5).and.
     $        theta.lt.con_pth3(6)) status = 0
         if(theta.gt.con_pth3(7).and.
     $        theta.lt.con_pth3(8)) status = 0
      elseif(sector.eq.4) then
         do ipar=1,4
            con_pth4(ipar) = 0.0
            do dpar=1,6
               con_pth4(ipar) = con_pth4(ipar)*p_pth
```

```
$              + par_pth4(7-dpar,ipar)
       enddo
    enddo
    if(theta.gt.con_pth4(1).and.
$        theta.lt.con_pth4(2)) status = 0
    if(theta.gt.con_pth4(3).and.
$        theta.lt.con_pth4(4)) status = 0
 elseif(sector.eq.5) then
    do ipar=1,8
       con_pth5(ipar) = 0.0
       do dpar=1,6
          con_pth5(ipar) = con_pth5(ipar)*p_pth
$              + par_pth5(7-dpar,ipar)
       enddo
    enddo
    if(theta.gt.con_pth5(1).and.
$        theta.lt.con_pth5(2)) status = 0
    if(theta.gt.con_pth5(3).and.
$        theta.lt.con_pth5(4)) status = 0
    if(theta.gt.con_pth5(5).and.
$        theta.lt.con_pth5(6)) status = 0
    if(theta.gt.con_pth5(7).and.
$        theta.lt.con_pth5(8)) status = 0
 endif

 return
 end
```

File "EFid_4Gev_2250A.dat" (Electron Fiducial Cuts Function For 4.4 GeV Data):

0 1 24.0741005 0.395599991 0. 0. 0. 0.

1 1 6.43149996 119.104897 -105.467003 39.4380989 -7.03779984 0.489100009

10 1 35.0825996 -14.0466003 7.74259996 -4.50930023 2.55500007 -0.4463

20 1 -45.5629005 121.894501 -101.024597 38.3568993 -6.92549992 0.486600012

11 1 37.6369019 -16.6257 1.65939999 0.76700002 0.263799995 -0.102300003

21 1 -58.6417007 150.647903 -114.576599 37.2220993 -5.06169987 0.196899995

0 2 23.6692009 0.39199999 0. 0. 0. 0.

1 2 -0.1193 137.083405 -122.393402 46.8152008 -8.5656004 0.610800028

10 2 29.2801991 81.5289993 -148.424103 93.9627991 -24.8906994 2.36430001

20 2 15.5390997 -67.2201004 94.7798004 -53.2652016 13.1357002 -1.18799996

11 2 13.9976997 39.5521011 -51.6329994 30.1618004 -7.51000023 0.643299997

21 2 -11.5064001 67.2117004 -73.0533981 34.0093994 -7.31589985 0.601899981

0 3 23.9736004 0.416099995 0. 0. 0. 0.

1 3 1.94149995 136.523102 -126.626503 49.9534988 -9.3366003 0.673500001

10 3 51.2840996 -63.031601 53.2925987 -20.6212006 4.1111002 -0.338999987

20 3 -41.8026009 109.766701 -87.0271988 30.4908009 -4.7665 0.257400006

11 3 56.5984001 -70.1407013 74.4999008 -40.9314995 11.0177002 -1.1128

21 3 13.8989 -39.9438019 51.9203987 -27.7106991 6.54020023 -0.570299983

0 4 24.0531998 0.4014 0. 0. 0. 0.

1 4 -1.13829994 135.481293 -117.829697 43.6276016 -7.67749977 0.523500025

10 4 -16.5499001 144.855301 -181.921799 99.2256012 -24.1030006 2.14249992

20 4 -14.3964996 40.1487007 -10.1948996 -9.77200031 4.95300007 -0.610400021

11 4 0.133900002 80.5208969 -95.1136017 52.0494995 -12.8950996 1.18519998

21 4 -1.41770005 18.7894993 -11.3976002 1.08940005 0.606400013 -0.1109

0 5 24.3038998 0.409200013 0. 0. 0. 0.

1 5 38.2610016 34.5934982 -20.2551994 -0.817399979 1.93599999 -0.273999989

10 5 42.5320015 -34.9434013 20.1032009 -1.69459999 -1.41789997 0.253600001

20 5 -74.5908966 227.184402 -228.307907 105.768204 -23.0837002 1.92850006

11 5 -2.9526 105.106499 -138.414398 81.1844025 -21.2688999 2.04439998

21 5 -33.3260002 90.8761978 -69.0875015 22.4258003 -3.09369993 0.130999997

0 6 23.7462006 0.390700012 0. 0. 0. 0.

1 6 -6.68760014 148.980499 -129.403793 48.1958008 -8.52499962 0.584900022

10 6 -8.70049953 112.619904 -137.991592 77.8462982 -19.9897995 1.898

20 6 -8.88290024 45.1467018 -39.4914017 14.1594 -2.18050003 0.1131

11 6 116.116699 -225.172195 200.693802 -82.9617004 15.9406996 -1.14129996

21 6 -41.8960991 145.580597 -153.899002 72.8448029 -16.0142994 1.33200002

```
      SUBROUTINE EFID_CUT_4GeV(PX, PY, PZ, STATUS)


c     electron fiducial cuts for 4.461 GeV data
c     input real px, py, pz momentum components of electron
c     output int status 1 means passing, 0 means failure


      REAL T0_P(6,6)
      REAL T1_P(6,6)
      REAL B_P(6,2,6)
      REAL A_P(6,2,6)
      COMMON /EFID_PAR/T0_P, T1_P, B_P, A_P

      REAL PX, PY, PZ
      REAL P, TH,PHI
      REAL EN
      REAL phimin, phimax;
      REAL T0, T1, BP(2), AP(2)
      INTEGER SECTOR, K, I
      INTEGER STATUS

      STATUS = 0
      P = SQRT(PX*PX+PY*PY+PZ*PZ)
      PHI = ATAN2(PY,PX)*180./3.14159265
      IF (PHI.LT.-30) PHI=PHI+360.
      TH = ATAN2(SQRT(PX*PX+PY*PY),PZ)*180./3.14159265
      EN = P

      SECTOR = INT((PHI+30.)/60.)+1;

      IF(SECTOR.LE.0) SECTOR = 1
      IF(SECTOR.GT.6) SECTOR = 6

      T0 =T0_P(SECTOR,1)/(EN**T0_P(SECTOR,2))
      T1 = 0.
      DO I=1,6
         T1 = T1 + T1_P(SECTOR,I)*(EN**(I-1))
      ENDDO

      DO I=1,2
         BP(I) = 0.
         AP(I) = 0.
         DO K = 1,6
            BP(I) = BP(I) + B_P(SECTOR,I,K)*(EN**(K-1))
            AP(I) = AP(I) + A_P(SECTOR,I,K)*(EN**(K-1))
         ENDDO
      ENDDO

      IF(T1.LT.45.)T1 = 45.
      IF(T0.LT.TH.and.TH.LT.T1)THEN
         PHIMIN = 60.*(SECTOR-1) - BP(1)*(1.
     &        - 1./((TH-T0)/(BP(1)/AP(1))+1.))
         PHIMAX = 60.*(SECTOR-1) + BP(2)*(1.
     &        - 1./((TH-T0)/(BP(2)/AP(2))+1.))
      ELSE
         PHIMIN = 60.*(SECTOR - 1)
         PHIMAX = 60.*(SECTOR - 1)
      ENDIF
```

```
      IF(PHIMIN.LT.PHI.and.PHI.LT.PHIMAX.and.TH.GT.15.
     &     .and. EN .gt. 0.9)THEN
         STATUS = 1
      ENDIF
      END



C------------------------------------------------------------
      SUBROUTINE  INIT_FID_PARMS
C------------------------------------------------------------


C-    This Subroutine reads and fills
C-   Arrays with parameters for Fiducial Cuts.
C-   You have to first call this function once then call
C-   Fiducial cut function for every event.
C-



       REAL    T0_P(6,6)
       REAL    T1_P(6,6)
       REAL    B_P(6,2,6)
       REAL    A_P(6,2,6)
       COMMON /EFID_PAR/T0_P, T1_P, B_P, A_P
       INTEGER CI,PTYPE,K,I, ICOUNT

       REAL PARM(6)

       open(unit=99,file='EFid_4Gev_2250A.dat',status='old')

       ICOUNT = 0

 110   CONTINUE

C----DO I=1,6

         READ(99,*,end=111)PTYPE,CI,PARM(1),PARM(2),PARM(3),
     +     PARM(4),PARM(5),PARM(6)
C-----

         IF(PTYPE.EQ.0) THEN
            DO K = 1,6
               T0_P(CI,K) = PARM(K)
            ENDDO
         ENDIF

C-----

         IF(PTYPE.EQ.1) THEN
            DO K = 1,6
               T1_P(CI,K) = PARM(K)
            ENDDO
         ENDIF

C-----

         IF(PTYPE.EQ.10) THEN
            DO K = 1,6
```

```
            B_P(CI,1,K) = PARM(K)
         ENDDO
      ENDIF

C------

      IF(PTYPE.EQ.11) THEN
         DO K = 1,6
            B_P(CI,2,K) = PARM(K)
         ENDDO
      ENDIF

C------

      IF(PTYPE.EQ.20) THEN
         DO K = 1,6
            A_P(CI,1,K) = PARM(K)
         ENDDO
      ENDIF

C------

      IF(PTYPE.EQ.21) THEN
         DO K = 1,6
            A_P(CI,2,K) = PARM(K)
         ENDDO
      ENDIF

C------
      ICOUNT = ICOUNT + 1
      GOTO 110

 111  CLOSE(99)

      WRITE(*,*) ICOUNT,'    parameters were read'


     END
C---------------------------------------------------
```

File "PFid_4Gev_2250A.dat" (Proton Fiducial Cuts Function For 4.4 GeV Data):

26.2564,0.441269,-29.7632,94.5137,7.71903,2.10915
29.7455,-0.826489,4.09596,91.8187,8.38108,1.5016
29.5399,-0.878321,43.1909,64.9772,11.1844,0.825411
28.5857,0.4061,98.6296,95.5022,13.7297,0.415071
31.9803,0.341766,257.124,103.504,14.2357,0.43387
29.2846,-0.257616,51.1709,84.3207,10.2963,1.69991
34.7359,-1.45301,660.653,-79.1375,11.3239,1.05352
30.6992,0.71858,442.087,4.20897,3.62722,3.35155
19.1518,3.71404,-197.134,177.828,9.63173,1.35402
23.9897,1.52101,23.9288,71.4476,8.89464,1.69512
22.6619,2.4697,-54.5174,112.22,11.2561,0.687839
20.9859,3.86504,-56.5229,230.635,13.6587,0.270987
24.683,0.470268,124.501,-9.04329,8.60129,1.66063
26.2736,-0.591497,182.954,-51.059,7.65701,2.29757
24.8681,1.15526,111.322,22.2304,9.46319,1.6834
29.3639,1.307,282.797,89.5863,11.7162,0.376266
36.8099,-0.785452,655.368,46.4935,12.0443,0.500522
25.8401,0.899645,141.723,27.6687,9.62103,1.7379
32.9905,-0.580968,464.263,30.5379,11.7414,0.320415
26.8867,0.748481,150.349,51.4182,8.70942,1.51013
26.0729,0.357197,136.456,24.1839,6.70568,0.820883
25.8339,1.018,149.648,38.7987,6.56928,0.527773
27.997,0.0685368,268.87,-45.3343,5.26386,3.08026
30.3568,1.60206,359.39,197.047,11.1523,0.451219
-24.4118,4.20154,-0.0480933,-0.0800641,0.000311929,0.000511191
-34.5523,8.81812,0.221281,-0.203846,-0.00115322,0.00119883
-29.4962,6.57417,0.0830637,-0.142094,-0.000271087,0.000801481

-29.5177,6.23458,0.183415,-0.160458,-0.00121912,0.0010282
-19.8091,4.37431,-0.046672,-0.124147,-7.21454e-05,0.000931229
-38.1865,10.6462,0.363126,-0.267793,-0.00212252,0.00162732
-15.6987,3.34818,-0.155291,-0.102923,0.000736214,0.000775517
-15.9442,1.75807,-0.196246,-0.0524198,0.00118102,0.000398854
-14.4453,1.65733,-0.269699,-0.0423913,0.00187485,0.000274252
-18.5972,1.41622,-0.144491,-0.0369631,0.000874762,0.000326006
-17.1008,0.577868,-0.173353,-0.021315,0.00108238,0.000189545
2.21904,-3.38706,-0.636698,0.0953525,0.0038789,-0.000559086
-13.7253,-1.53789,-0.296133,0.0648705,0.00269427,-0.000928492
-12.356,-2.62192,-0.366191,0.115155,0.0033624,-0.00137599
-2.52638,-9.6591,-0.743505,0.380195,0.0067055,-0.00369404
-34.5804,15.3815,0.417723,-0.489802,-0.00337546,0.00370894
1.87747,-7.70598,-0.919924,0.376373,0.00776553,-0.00354661
-12.3968,-2.37408,-0.367352,0.114661,0.00352523,-0.00148841
-29.5895,10.9088,0.248994,-0.326966,-0.00154954,0.00202508
-7.20087,-6.19132,-0.568426,0.257971,0.00476513,-0.00236084
-10.0076,-3.66545,-0.468027,0.163446,0.00421363,-0.00175242
-9.03582,-5.14009,-0.515592,0.221044,0.00482855,-0.00237549
-8.55955,-5.27785,-0.504058,0.201472,0.00404296,-0.00175892
-21.122,5.19264,-0.0761427,-0.0826774,0.0018747,-0.000390706
131.839,-6.64199,-22.8623,4.91185,126.5,20
132.055,-5.2283,2.20945,-1.57951,128.429,11.4286
137.945,-7.90553,-12.8716,3.94534,119.857,22.8571
124.743,-3.54503,-22.8263,5.62231,130.429,11.4286
136.455,-7.59559,-18.6847,4.52149,123.5,20
126.556,-4.02284,-22.2328,5.23298,124.857,22.8571
97.3917,2.99764,26.7715,-5.95695,126.5,20

132.154,-6.60261,0.000146616,1.53542,128.429,11.4286

113.746,-1.24667,32.0728,-9.35241,119.857,22.8571

118.596,-2.44983,22.2973,-5.40976,130.429,11.4286

125.129,-3.96273,21.6178,-5.86908,123.5,20

111.201,-0.178015,25.1267,-6.55928,124.857,22.8571

File “PFid_4Gev_2250A.inc”:

```
      real Pfidft1l(6,6)
      real Pfidft1r(6,6)
      real Pfidft2l(6,6)
      real Pfidft2r(6,6)
      real Pfidbt1l(6,6)
      real Pfidbt1r(6,6)
      real Pfidbt2l(6,6)
      real Pfidbt2r(6,6)
      real Pfidbl(6,6)
      real Pfidbr(6,6)
      parameter(pi = 3.141592654)
      common /PFidPars/Pfidft1l Pfidft1r,Pfidft2l,Pfidft2r,
     x Pfidbt1l,Pfidbt1r,Pfidbt2l,Pfidbt2r,Pfidbl,Pfidbr
```

```
      subroutine ReadPFidPars
c     call once before the first call of the fiducial cuts to
c     read the parameters
      include 'PFid_4Gev_2250A.inc'
      open(unit=99,file="PFid_4Gev_2250A.dat",status="old")

      read (99,*) Pfidft1l
      read (99,*) Pfidft1r
      read (99,*) Pfidft2l
      read (99,*) Pfidft2r
      read (99,*) Pfidbt1l
      read (99,*) Pfidbt1r
      read (99,*) Pfidbt2l
      read (99,*) Pfidbt2r
      read (99,*) Pfidbl
      read (99,*) Pfidbr
      close(99)

      return
      end

      subroutine PFiducialCut_4Gev_2250A(px, py, pz, status)
c     input real px py pz components of proton momentum
c     output int status 1 means pass, 0 means failure
      include 'PFid_4Gev_2250A.inc'

      real px,py,pz
      logical*4 forward
      logical*4 s1s4,s5,s6
      real p, theta, phi, tmptheta
      integer status, sector,ipar,jpar

      real parfidl(3)
      real parfidr(3)
      real parfidbl(2)
      real parfidbr(2)
      real cphil,cphir,phi45l,phi45r
      real phi60l,phi60r
      real thetamin,thetamax
      real thetab,pb
      real dl,el,dr,er
      status = 0

      phi=atan2(py,px)*180./pi
      if (phi.lt.-30) phi=phi+360
      sector=int((phi+30.)/60.)+1
      if (sector.lt.1) sector=1
      if (sector.gt.6) sector=6
      phi=phi-(sector-1)*60.
      theta=atan2(sqrt(px*px+py*py),pz)*180./pi
      p=sqrt(px*px+py*py+pz*pz)
      do ipar=1,3
         parfidl(ipar)=0.0
         parfidr(ipar)=0.0
      enddo
      do jpar=1,2
         parfidbl(jpar)=0.0
         parfidbr(jpar)=0.0
      enddo
      forward=.false.
      thateb=45.
```

```
      pb=0.575
      thetamax=140
      if (p.lt.0.2) p=0.2
      if (p.gt.4.4) p=4.4

      if(p.lt.0.6) thetamax=Pfidbl(5,sector)+ Pfidbl(6,sector)*p
      else thetamax=Pfidbl(5,sector)+ Pfidbl(6,sector)*pb
      forward=.true.

      if(p.lt.0.6) then
         do ipar=1,3
            jpar=2*ipar-1
            parfidl(ipar)=Pfidft1l(jpar,sector)+
     $           Pfidft1l(jpar+1,sector)/p;
            parfidr(ipar)=Pfidft1r(jpar,sector)+
     $           Pfidft1r(jpar+1,sector)/p;
        enddo
      else
         do ipar=1,3
            jpar=2*ipar-1
            parfidl(ipar)=Pfidft2l(jpar,sector)+
     $           Pfidft2l(jpar+1,sector)/p;
            parfidr(ipar)=Pfidft2r(jpar,sector)+
     $           Pfidft2r(jpar+1,sector)/p;
         enddo
      endif

      phi45l=parfidl(1)*(parfidl(3)-45.)/(45.-parfidl(3)+
     $     (parfidl(2)/parfidl(1)))
      phi45r=-parfidr(1)*(parfidr(3)-45.)/(45.-parfidr(3)+
     $     (parfidr(2)/parfidr(1)))

      if(theta.gt.thetab) then
         if(theta.gt.140.) theta =140.
         if(p.gt.1)p=1.

         forward=.false.

        if(p.lt.0.6) then
            do ipar=1,3
               jpar=2*ipar-1
               parfidl(ipar)=Pfidbt1l(jpar,sector)+
     $              Pfidbt1l(jpar+1,sector)/p;
               parfidr(ipar)=Pfidbt1r(jpar,sector)+
     $              Pfidbt1r(jpar+1,sector)/p;
            enddo

            do ipar=1,2
               jpar=2*ipar-1
               parfidbl(ipar)=Pfidbl(jpar,sector)+
     $              Pfidbl(jpar+1,sector)/p;
               parfidbr(ipar)=Pfidbr(jpar,sector)+
     $              Pfidbr(jpar+1,sector)/p;
            enddo
         else
            do ipar=1,3
               jpar=2*ipar-1
               parfidl(ipar)=Pfidbt2l(jpar,sector)+
     $              Pfidbt2l(jpar+1,sector)/p;
               parfidr(ipar)=Pfidbt2r(jpar,sector)+
     $              Pfidbt2r(jpar+1,sector)/p;
```

```
          enddo

          do ipar=1,2
             jpar=2*ipar-1
             parfidbl(ipar)=Pfidbl(jpar,sector)+
     $            Pfidbl(jpar+1,sector)/pb;
             parfidbr(ipar)=Pfidbr(jpar,sector)+
     $            Pfidbr(jpar+1,sector)/pb;
          enddo
       endif
      endif

      if (forward) then
         if(p.lt.0.6) then
            thetamin=14
         else thetamin=11;
         endif
         cphil=parfidl(1)*(parfidl(3)-theta)/(theta-parfidl(3)+
     $        (parfidl(2)/parfidl(1)));
         cphir=-parfidr(1)*(parfidr(3)-theta)/(theta-parfidr(3)+
     $        (parfidr(2)/parfidr(1)));

      else
         phi60l=parfidl(1)+ parfidl(2)*60.+ parfidl(3)*3600.
         phi60r=-(parfidr(1)+ parfidr(2)*60.+ parfidr(3)*3600.)
         if(theta.lt.60) then
            cphil=parfidl(1)+ parfidl(2)*theta+parfidl(3)*theta*theta
            cphir=-(parfidr(1)+ parfidr(2)*theta+parfidr(3)*theta*theta)
         endif
         dl=parfidbl(1)
         el=parfidbl(2)
         dr=parfidbr(1)
         er=parfidbr(2)
         if(theta.gt.45.and.theta.lt.60) then
            if(cphil.gt.phi45l) cphil=phi45l
            if(cphir.lt.phi45r) cphir=phi45r
         endif
         if(theta.ge.60.and.theta.le.dl) cphil=phi60l
         if(theta.gt.dl.and.theta.le.thetamax) cphil=
     $        (140-theta)*(phi60l-el)/(140-dl) +el
         if(theta.gt.thetamax) cphil=0

         if(theta.ge.60.and.theta.le.dr) cphir=phi60r
         if(theta.gt.dr.and.theta.le.thetamax) cphir=
     $        (140-theta)*(phi60r-er)/(140-dr) +er
         if(theta.gt.thetamax) cphir=0

      endif

      if(phi.lt.0.and.phi.gt.cphil) status = 1
      if(phi.ge.0.and.phi.lt.cphir) status = 1

      if(theta.lt.thetamin) status=0
      if(forward.and.p<0.6.and.theta.lt.20.6-11.4*p)status=0
      s1s4=(theta.lt.11.7.and.(sector.eq.1.or.sector.eq.4))
      s5=(theta.lt.12.2.and.sector.eq.5)
      s6=(theta.lt.11.4.and.sector.eq.6)
      if(p.ge.0.6.and.p.lt.1.5.and.(s1s4.or.s5.or.s6)) status=0

      return
      end
```

File “NFid.dat” (Neutron Fiducial Cuts Function For Both 2.2 and 4.4 GeV Data)”:

1.006358e+01, -2.073713e-02, 5.380570e-02, -2.098145e-04, -1.016657e-04, 2.813799e-07, 2.246853e-07, 9.801566e+00, -3.208999e-02, 5.890263e-02, 2.254323e-04, -1.105457e-04, -3.952539e-07, 2.403583e-07, 8.700328e+00, 4.066929e-02, 3.810611e-02, -2.125965e-04, -5.804629e-05, 3.169588e-07, 1.656714e-07, 1.115194e+01, 2.895261e-02, 3.870534e-02, 5.845715e-05, -2.106982e-05, 9.819791e-08, 1.198035e-07, 9.572513e+00, -2.508784e-01, 4.524328e-02, 8.727145e-04, -8.233513e-05, -1.452907e-06, 2.072440e-07, 8.304816e+00, 1.607310e-02, 4.548254e-02, -3.566758e-05, -8.701080e-05, 5.323235e-08, 1.974612e-07 4.484192e+01, -4.557507e-03, 5.327638e-03, 4.472945e+01, 6.629484e-03, 5.188613e-03, 4.495271e+01, -9.797151e-04, 3.700512e-03, 4.467528e+01, 7.399025e-03, 4.519021e-03, 4.389896e+01, -6.824078e-03, 4.743576e-03, 4.449698e+01, -2.987475e-03, 4.571902e-03

```
      subroutine ReadNFidPars
c     read parameters for neutron fiducial cuts
c     from the file NFid.dat which must be in current dir

      real par_Nfor(7,6)
      real par_Nbak(3,6)
      common /NFidPars/par_Nfor,par_Nbak

      open(unit=99,file="NFid.dat",status="old")
      read (99,*) par_Nfor
      read (99,*) par_Nbak
      close(99)
      return
      end

      subroutine NFid(px, py, pz, status)
c     neutron fiducial cuts
c     subroutine ReadNFidPars must be called once before this
c     subroutine is called for the first time to get the parameters.
c     input : real px py pz, three components of neutron momentum
c     output: int status, 1 means passing the cut, 0 means not

      real par_Nfor(7,6)
      real par_Nbak(3,6)
      common /NFidPars/par_Nfor,par_Nbak

      real px, py, pz
      integer status, sector, dpar
      real theta, phi, ftheta, btheta

      status = 0
      phi=atan2(py,px)*180./3.14159265
      if (phi.lt.-30) phi=phi+360
      sector=int((phi+30.)/60.)+1
      if (sector.lt.1) sector=1
      if (sector.gt.6) sector=6
      phi=phi-(sector-1)*60.
      theta=atan2(sqrt(px*px+py*py),pz)*180./3.14159265
      p=sqrt(px*px+py*py+pz*pz)
      if(p.lt.0.6.or.p.gt.1.9) then
         status = 0
         return
      endif

c     calculate the two theta limits for given phi
      ftheta = 0.0
      btheta = 0.0
      do dpar=1,7
         ftheta = ftheta*phi + par_Nfor(8-dpar,sector)
      enddo
      do dpar=1,3
         btheta = btheta*phi + par_Nbak(4-dpar,sector)
      enddo

      if(theta.gt.ftheta.and.theta.lt.btheta) then
         status = 1
      endif

      return
      end
```

Appendix B

Data Tables For (e,e'NN)

All cross sections listed here are integrated within CLAS acceptance which is specified in the fiducial cuts functions showed in detail in Appendix A

p_{rel} [GeV/c]	$d\sigma/dp_{rel}$ [nb/(MeV/c)]	StatErr [nb/(MeV/c)]	SysErr [nb/(MeV/c)]
0.1875	5.96766e-07	3.44543e-07	8.35473e-08
0.2125	4.95862e-06	9.91725e-07	6.94207e-07
0.2375	1.89793e-05	1.93706e-06	2.65709e-06
0.2625	4.02272e-05	2.81647e-06	5.63181e-06
0.2875	5.59808e-05	3.31602e-06	7.83732e-06
0.3125	6.08059e-05	3.44799e-06	8.51284e-06
0.3375	5.23173e-05	3.18984e-06	7.32442e-06
0.3625	3.45782e-05	2.58449e-06	4.84095e-06
0.3875	3.13163e-05	2.45288e-06	4.38429e-06
0.4125	2.12218e-05	2.01429e-06	2.97106e-06
0.4375	1.40737e-05	1.63603e-06	1.97032e-06
0.4625	1.15462e-05	1.47834e-06	1.61647e-06
0.4875	7.53428e-06	1.19127e-06	1.05481e-06
0.5125	7.51094e-06	1.18758e-06	1.05153e-06
0.5375	3.93207e-06	8.58048e-07	5.50492e-07
0.5625	2.61903e-06	6.99964e-07	3.66664e-07
0.5875	2.98358e-06	7.45895e-07	4.17701e-07
0.6125	1.30305e-06	4.92508e-07	1.82428e-07
0.6375	1.67214e-06	5.57381e-07	2.34102e-07
0.6625	2.03996e-06	6.15071e-07	2.85594e-07
0.6875	1.85496e-07	1.85496e-07	2.59694e-08
0.7125	1.85733e-07	1.85733e-07	2.60027e-08
0.7875	1.86262e-07	1.86262e-07	2.60767e-08

Table B.1: Cross Sections in CLAS for ^{3}He(e,e'pp) Backward Kinematics at 2.261 GeV

p_{rel} [GeV/c]	$d\sigma/dp_{rel}$ [nb/(MeV/c)]	StatErr [nb/(MeV/c)]	SysErr [nb/(MeV/c)]
0.1875	3.99408e-07	2.82424e-07	5.59171e-08
0.2125	2.38786e-06	6.89317e-07	3.34301e-07
0.2375	4.17768e-06	9.11644e-07	5.84875e-07
0.2625	9.91485e-06	1.40217e-06	1.38808e-06
0.2875	1.58481e-05	1.77186e-06	2.21872e-06
0.3125	2.17014e-05	2.06915e-06	3.03819e-06
0.3375	2.58663e-05	2.25995e-06	3.62128e-06
0.3625	2.75918e-05	2.34031e-06	3.86285e-06
0.3875	2.31088e-05	2.12734e-06	3.23524e-06
0.4125	2.58388e-05	2.26622e-06	3.61744e-06
0.4375	2.17621e-05	2.05631e-06	3.04668e-06
0.4625	1.96046e-05	2.00089e-06	2.74465e-06
0.4875	1.77946e-05	1.86538e-06	2.49124e-06
0.5125	1.38567e-05	1.64449e-06	1.93994e-06
0.5375	1.03555e-05	1.46448e-06	1.44976e-06
0.5625	6.85683e-06	1.14281e-06	9.59957e-07
0.5875	5.71175e-06	1.04282e-06	7.99645e-07
0.6125	2.85151e-06	7.36255e-07	3.99212e-07
0.6375	1.52266e-06	5.38342e-07	2.13172e-07
0.6625	7.60725e-07	3.80362e-07	1.06501e-07
0.6875	1.52104e-06	5.37768e-07	2.12945e-07
0.7375	5.69626e-07	3.28874e-07	7.97477e-08
0.8375	1.89887e-07	1.89887e-07	2.65841e-08

Table B.2: Cross Sections in CLAS for ^{3}He(e,e'pp) Forward Kinematics at 2.261 GeV

p_{rel} [GeV/c]	$d\sigma/dp_{rel}$ [nb/(MeV/c)]	StatErr [nb/(MeV/c)]	SysErr [nb/(MeV/c)]
0.1875	1.20353e-06	8.51022e-07	1.80529e-07
0.2125	1.54543e-06	8.92257e-07	2.31815e-07
0.2375	1.26035e-05	2.52069e-06	1.89053e-06
0.2625	1.82122e-05	3.07843e-06	2.73184e-06
0.2875	1.92712e-05	3.08586e-06	2.89068e-06
0.3125	2.47786e-05	3.43617e-06	3.71679e-06
0.3375	2.23679e-05	3.22853e-06	3.35519e-06
0.3625	1.85469e-05	2.82838e-06	2.78204e-06
0.3875	1.72114e-05	2.79205e-06	2.58171e-06
0.4125	9.04276e-06	1.97329e-06	1.35641e-06
0.4375	1.17799e-05	2.31024e-06	1.76699e-06
0.4625	8.00391e-06	1.83622e-06	1.20059e-06
0.4875	5.61451e-06	1.50054e-06	8.42176e-07
0.5125	4.65046e-06	1.40217e-06	6.97569e-07
0.5375	1.61491e-06	8.07455e-07	2.42237e-07
0.5625	4.34591e-07	4.34591e-07	6.51886e-08
0.5875	7.30033e-07	5.16211e-07	1.09505e-07
0.6125	4.12739e-07	4.12739e-07	6.19109e-08
0.6375	3.40788e-07	3.40788e-07	5.11182e-08

Table B.3: Cross Sections in CLAS for ^{3}He(e,e'np) Backward Kinematics at 2.261 GeV

p_{rel} [GeV/c]	$d\sigma/dp_{rel}$ [nb/(MeV/c)]	StatErr [nb/(MeV/c)]	SysErr [nb/(MeV/c)]
0.2125	3.43251e-07	3.43251e-07	4.80551e-08
0.2375	3.75761e-06	1.13296e-06	5.26064e-07
0.2625	5.46299e-06	1.36575e-06	7.64818e-07
0.2875	8.15451e-06	1.66453e-06	1.14163e-06
0.3125	6.76967e-06	1.51374e-06	9.47754e-07
0.3375	5.39002e-06	1.34751e-06	7.54603e-07
0.3625	4.00179e-06	1.15522e-06	5.60252e-07
0.3875	1.65734e-06	7.41187e-07	2.32028e-07
0.4125	1.65255e-06	7.39041e-07	2.31356e-07
0.4375	1.65959e-06	7.42189e-07	2.32342e-07
0.4625	1.64137e-06	7.34042e-07	2.29792e-07
0.4875	6.46983e-07	4.57486e-07	9.05776e-08
0.5125	9.77733e-07	5.64494e-07	1.36883e-07
0.5375	3.25222e-07	3.25222e-07	4.55311e-08
0.5625	3.23438e-07	3.23438e-07	4.52814e-08
0.5875	3.23803e-07	3.23803e-07	4.53325e-08
0.6125	3.22988e-07	3.22988e-07	4.52183e-08

Table B.4: Cross Sections in CLAS for ^{3}He(e,e'pp) Backward Kinematics at 4.461 GeV

p_{rel} [GeV/c]	$d\sigma/dp_{rel}$ [nb/(MeV/c)]	StatErr [nb/(MeV/c)]	SysErr [nb/(MeV/c)]
0.2125	6.88069e-07	4.86538e-07	9.63296e-08
0.2375	6.89574e-07	4.87602e-07	9.65403e-08
0.2625	1.02816e-06	5.93609e-07	1.43943e-07
0.2875	1.36646e-06	6.83229e-07	1.91304e-07
0.3125	3.43276e-07	3.43276e-07	4.80587e-08
0.3375	3.35278e-07	3.35278e-07	4.69389e-08
0.3625	1.35241e-06	6.76203e-07	1.89337e-07
0.3875	1.00969e-06	5.82947e-07	1.41357e-07
0.4125	6.70462e-07	4.74088e-07	9.38646e-08
0.4375	9.96629e-07	5.75404e-07	1.39528e-07
0.4625	9.91441e-07	5.72408e-07	1.38802e-07
0.4875	1.32151e-06	6.60755e-07	1.85011e-07
0.5125	3.29444e-07	3.29444e-07	4.61222e-08
0.5375	1.64785e-06	7.36942e-07	2.30699e-07
0.5625	1.66416e-06	7.44235e-07	2.32982e-07
0.5875	9.84623e-07	5.68472e-07	1.37847e-07
0.6125	9.84383e-07	5.68334e-07	1.37814e-07
0.6375	1.64077e-06	7.33774e-07	2.29707e-07
0.6625	1.65269e-06	7.39106e-07	2.31377e-07
0.6875	9.84349e-07	5.68314e-07	1.37809e-07
0.7125	1.36908e-06	7.90438e-07	1.91671e-07
0.7375	3.28429e-07	3.28429e-07	4.59801e-08
0.7625	6.57322e-07	4.64797e-07	9.20251e-08
0.7875	6.56698e-07	4.64356e-07	9.19378e-08
0.8375	3.29517e-07	3.29517e-07	4.61323e-08
0.8625	3.29116e-07	3.29116e-07	4.60762e-08
0.9625	3.36132e-07	3.36132e-07	4.70585e-08

Table B.5: Cross Sections in CLAS for ^{3}He(e,e'pp) Forward Kinematics at 4.461 GeV

p_{rel} [GeV/c]	$d\sigma/dp_{rel}$ [nb/(MeV/c)]	StatErr [nb/(MeV/c)]	SysErr [nb/(MeV/c)]
0.1625	9.71906e-07	5.61131e-07	1.36067e-07
0.1875	2.57332e-06	9.09806e-07	3.60265e-07
0.2125	5.72711e-06	1.34989e-06	8.01793e-07
0.2375	1.23803e-05	1.98243e-06	1.73324e-06
0.2625	2.62121e-05	2.87716e-06	3.66971e-06
0.2875	3.08928e-05	3.12065e-06	4.32491e-06
0.3125	3.68364e-05	3.39106e-06	5.15709e-06
0.3375	4.05754e-05	3.54509e-06	5.68055e-06
0.3625	3.02991e-05	3.04517e-06	4.24187e-06
0.3875	2.58045e-05	2.79889e-06	3.61263e-06
0.4125	2.41025e-05	2.69475e-06	3.37436e-06
0.4375	1.60891e-05	2.18943e-06	2.25245e-06
0.4625	9.74343e-06	1.69611e-06	1.36408e-06
0.4875	6.17214e-06	1.34687e-06	8.64102e-07
0.5125	7.83911e-06	1.50864e-06	1.09747e-06
0.5375	3.48293e-06	1.00544e-06	4.87609e-07
0.5625	4.61605e-06	1.15401e-06	6.46247e-07
0.5875	3.15482e-06	9.51214e-07	4.41675e-07
0.6125	2.28666e-06	8.08458e-07	3.20133e-07
0.6375	2.86431e-07	2.86431e-07	4.01004e-08
0.6625	1.13434e-06	5.67168e-07	1.58807e-07
0.6875	2.87629e-07	2.87629e-07	4.02681e-08
0.7125	5.65422e-07	3.99814e-07	7.91591e-08
0.7375	2.84513e-07	2.84513e-07	3.98318e-08

Table B.6: Cross Sections in CLAS for ^{4}He(e,e'pp) Backward Kinematics at 2.261 GeV

p_{rel} [GeV/c]	$d\sigma/dp_{rel}$ [nb/(MeV/c)]	StatErr [nb/(MeV/c)]	SysErr [nb/(MeV/c)]
0.1625	3.23808e-07	3.23808e-07	4.53331e-08
0.1875	6.46992e-07	4.57493e-07	9.05789e-08
0.2125	2.89607e-06	9.65358e-07	4.05451e-07
0.2375	5.43932e-06	1.31923e-06	7.61505e-07
0.2625	8.26065e-06	1.62005e-06	1.15649e-06
0.2875	1.38873e-05	2.09358e-06	1.94422e-06
0.3125	2.20113e-05	2.96648e-06	3.07982e-06
0.3375	3.00145e-05	3.66508e-06	4.20132e-06
0.3625	3.58982e-05	3.36218e-06	5.02575e-06
0.3875	3.70977e-05	3.41512e-06	5.19367e-06
0.4125	3.42145e-05	3.27716e-06	4.79003e-06
0.4375	3.30779e-05	3.18292e-06	4.63091e-06
0.4625	2.82341e-05	2.95974e-06	3.95277e-06
0.4875	2.49189e-05	2.75183e-06	3.48865e-06
0.5125	1.80068e-05	2.36441e-06	2.52096e-06
0.5375	1.46987e-05	2.09981e-06	2.05782e-06
0.5625	1.03181e-05	1.82401e-06	1.44454e-06
0.5875	6.82189e-06	1.52542e-06	9.55065e-07
0.6125	6.64919e-06	1.41761e-06	9.30886e-07
0.6375	2.62837e-06	8.76123e-07	3.67971e-07
0.6625	1.16996e-06	5.84982e-07	1.63795e-07
0.6875	1.75311e-06	7.15704e-07	2.45435e-07
0.7125	1.74995e-06	7.14414e-07	2.44993e-07
0.7375	8.74191e-07	5.04714e-07	1.22387e-07
0.7875	5.85979e-07	4.14352e-07	8.20371e-08
0.8125	5.81288e-07	4.11032e-07	8.13803e-08
0.9125	2.89764e-07	2.89764e-07	4.05669e-08

Table B.7: Cross Sections in CLAS for ^{4}He(e,e'pp) Forward Kinematics at 2.261 GeV

p_{rel} [GeV/c]	$d\sigma/dp_{rel}$ [nb/(MeV/c)]	StatErr [nb/(MeV/c)]	SysErr [nb/(MeV/c)]
0.1875	2.95921e-06	1.70851e-06	4.43882e-07
0.2125	1.11385e-05	3.21542e-06	1.67078e-06
0.2375	1.62037e-05	3.62325e-06	2.43055e-06
0.2625	2.60011e-05	3.83349e-06	3.89002e-06
0.2875	3.30904e-05	5.10596e-06	4.96356e-06
0.3125	3.73616e-05	5.39268e-06	5.60424e-06
0.3375	3.69466e-05	5.22504e-06	5.54201e-06
0.3625	3.21117e-05	4.84103e-06	4.81676e-06
0.3875	2.04943e-05	3.74173e-06	3.07414e-06
0.4125	1.84459e-05	3.54994e-06	2.76689e-06
0.4375	9.76351e-06	2.52093e-06	1.46453e-06
0.4625	8.53275e-06	2.46319e-06	1.27991e-06
0.4875	1.04888e-05	2.62221e-06	1.57332e-06
0.5125	6.28058e-06	2.09353e-06	9.42087e-07
0.5375	8.50706e-06	2.27361e-06	1.27606e-06
0.5625	4.90539e-06	1.85406e-06	7.35808e-07
0.6125	1.14581e-06	8.10207e-07	1.71871e-07
0.6375	5.39572e-07	5.39572e-07	8.09358e-08
0.7375	5.22956e-07	5.22956e-07	7.84434e-08

Table B.8: Cross Sections in CLAS for ^{4}He(e,e'np) Backward Kinematics at 2.261 GeV

p_{rel} [GeV/c]	$d\sigma/dp_{rel}$ [nb/(MeV/c)]	StatErr [nb/(MeV/c)]	SysErr [nb/(MeV/c)]
0.1625	2.05071e-07	2.05071e-07	2.87101e-08
0.2125	1.41537e-06	5.34959e-07	1.98152e-07
0.2375	6.06402e-07	3.50107e-07	8.48963e-08
0.2625	1.01112e-06	4.52186e-07	1.41556e-07
0.2875	3.41436e-06	8.28103e-07	4.78011e-07
0.3125	2.60667e-06	7.22959e-07	3.64934e-07
0.3375	2.77707e-06	7.42203e-07	3.88789e-07
0.3625	3.94801e-06	8.82802e-07	5.52722e-07
0.3875	2.16121e-06	6.51629e-07	3.02569e-07
0.4125	1.74436e-06	5.81454e-07	2.44211e-07
0.4375	1.92876e-06	6.09928e-07	2.70027e-07
0.4625	1.35022e-06	5.10334e-07	1.89031e-07
0.4875	1.92885e-07	1.92885e-07	2.70039e-08
0.5125	7.64776e-07	3.82388e-07	1.07069e-07
0.5375	7.61603e-07	3.80801e-07	1.06624e-07
0.5625	3.79795e-07	2.68556e-07	5.31713e-08
0.5875	3.75894e-07	2.65797e-07	5.26251e-08
0.6125	1.88628e-07	1.88628e-07	2.64079e-08
0.6375	1.88415e-07	1.88415e-07	2.63779e-08
0.7875	1.87011e-07	1.87011e-07	2.61816e-08

Table B.9: Cross Sections in CLAS for ^{4}He(e,e'pp) Backward Kinematics at 4.461 GeV

p_{rel} [GeV/c]	$d\sigma/dp_{rel}$ [nb/(MeV/c)]	StatErr [nb/(MeV/c)]	SysErr [nb/(MeV/c)]
0.2375	6.13044e-07	3.53941e-07	8.58261e-08
0.2875	4.04273e-07	2.85865e-07	5.65983e-08
0.3125	8.04288e-07	4.02144e-07	1.12598e-07
0.3375	7.96141e-07	3.98071e-07	1.11461e-07
0.3625	7.90533e-07	3.95266e-07	1.10675e-07
0.3875	3.95413e-07	2.79599e-07	5.53578e-08
0.4125	7.88749e-07	3.94375e-07	1.10425e-07
0.4375	3.90368e-07	2.76032e-07	5.46515e-08
0.4625	3.85001e-07	2.72237e-07	5.39002e-08
0.4875	9.68466e-07	4.33111e-07	1.35585e-07
0.5125	1.34931e-06	5.09991e-07	1.88903e-07
0.5375	1.73057e-06	5.76858e-07	2.42279e-07
0.5625	2.68353e-06	7.17203e-07	3.75694e-07
0.5875	2.30781e-06	6.66204e-07	3.23092e-07
0.6125	1.15313e-06	4.70763e-07	1.61438e-07
0.6375	1.73083e-06	5.76943e-07	2.42316e-07
0.6625	2.49013e-06	6.90637e-07	3.48618e-07
0.6875	9.59721e-07	4.29199e-07	1.34361e-07
0.7125	9.57143e-07	4.28047e-07	1.34101e-07
0.7375	5.74909e-07	3.31924e-07	8.04873e-08
0.7625	3.82824e-07	2.70697e-07	5.35953e-08
0.7875	9.59303e-07	4.29013e-07	1.34302e-07
0.8125	1.91279e-07	1.91279e-07	2.67791e-08
0.8625	5.75412e-07	3.32214e-07	8.05577e-08
0.8875	2.04003e-07	2.04003e-07	2.85605e-08
0.9625	1.91939e-07	1.91939e-07	2.68714e-08
0.9875	3.83495e-07	2.71172e-07	5.36893e-08

Table B.10: Cross Sections in CLAS for ^{4}He(e,e'pp) Forward Kinematics at 4.461 GeV

p_{rel} [GeV/c]	$d\sigma/dp_{rel}$ [nb/(MeV/c)]	StatErr [nb/(MeV/c)]	SysErr [nb/(MeV/c)]
0.1625	6.40015e-06	1.77508e-06	8.96021e-07
0.1875	1.76776e-05	2.94627e-06	2.47486e-06
0.2125	4.01142e-05	4.42987e-06	5.61599e-06
0.2375	5.17151e-05	5.02302e-06	7.24012e-06
0.2625	7.72761e-05	6.12839e-06	1.08187e-05
0.2875	7.79869e-05	6.14623e-06	1.09182e-05
0.3125	7.62384e-05	6.06521e-06	1.06734e-05
0.3375	6.82401e-05	5.72658e-06	9.55362e-06
0.3625	6.10871e-05	5.39938e-06	8.55218e-06
0.3875	4.64947e-05	4.69668e-06	6.50926e-06
0.4125	3.53979e-05	4.08739e-06	4.95571e-06
0.4375	2.49251e-05	3.42371e-06	3.48949e-06
0.4625	1.96484e-05	3.03181e-06	2.75077e-06
0.4875	1.71985e-05	2.82741e-06	2.40779e-06
0.5125	1.62071e-05	2.73948e-06	2.26898e-06
0.5375	1.24904e-05	2.40378e-06	1.74866e-06
0.5625	7.39128e-06	1.84782e-06	1.03478e-06
0.5875	6.90049e-06	1.78171e-06	9.66068e-07
0.6125	3.65589e-06	1.29256e-06	5.11827e-07
0.6375	2.29597e-06	1.02679e-06	3.21436e-07
0.6625	9.18078e-07	6.49179e-07	1.28531e-07
0.6875	1.36384e-06	7.87415e-07	1.90938e-07
0.7125	9.05977e-07	6.40622e-07	1.26837e-07

Table B.11: Cross Sections in CLAS for ^{12}C(e,e'pp) Backward Kinematics at 2.261 GeV

p_{rel} [GeV/c]	$d\sigma/dp_{rel}$ [nb/(MeV/c)]	StatErr [nb/(MeV/c)]	SysErr [nb/(MeV/c)]
0.1375	4.95225e-07	4.95225e-07	6.93315e-08
0.1625	3.45091e-06	1.30432e-06	4.83126e-07
0.1875	4.44022e-06	1.48007e-06	6.21629e-07
0.2125	1.27792e-05	2.50621e-06	1.78909e-06
0.2375	2.20644e-05	3.28917e-06	3.08902e-06
0.2625	4.15396e-05	4.50561e-06	5.81554e-06
0.2875	4.97744e-05	4.92839e-06	6.96842e-06
0.3125	7.40111e-05	6.00308e-06	1.03615e-05
0.3375	9.50011e-05	7.37343e-06	1.32995e-05
0.3625	1.17981e-04	7.63147e-06	1.65172e-05
0.3875	1.23256e-04	7.82679e-06	1.72559e-05
0.4125	1.10010e-04	8.00132e-06	1.53901e-05
0.4375	9.41973e-05	6.74561e-06	1.31876e-05
0.4625	7.89216e-05	6.23931e-06	1.10489e-05
0.4875	6.29662e-05	5.52251e-06	8.81527e-06
0.5125	5.08248e-05	4.91342e-06	7.11547e-06
0.5375	3.85965e-05	4.31522e-06	5.40351e-06
0.5625	2.20895e-05	3.22208e-06	3.09252e-06
0.5875	2.25842e-05	3.29425e-06	3.16179e-06
0.6125	1.46027e-05	2.66608e-06	2.04438e-06
0.6375	9.85089e-06	2.14964e-06	1.37913e-06
0.6625	5.62608e-06	1.62411e-06	7.87651e-07
0.6875	5.14729e-06	1.62772e-06	7.20623e-07
0.7125	4.68402e-06	1.48122e-06	6.55763e-07
0.7375	2.34429e-06	1.04841e-06	3.28201e-07
0.7625	4.67548e-07	4.67548e-07	6.54567e-08
0.7875	4.71393e-07	4.71393e-07	6.59949e-08
0.9375	4.70563e-07	4.70563e-07	6.58788e-08

Table B.12: Cross Sections in CLAS for ^{12}C(e,e'pp) Forward Kinematics at 2.261 GeV

p_{rel} [GeV/c]	$d\sigma/dp_{rel}$ [nb/(MeV/c)]	StatErr [nb/(MeV/c)]	SysErr [nb/(MeV/c)]
0.1625	8.22831e-06	3.67981e-06	1.23425e-06
0.1875	1.37758e-05	4.59194e-06	2.06637e-06
0.2125	2.83283e-05	6.33441e-06	4.24925e-06
0.2375	2.81205e-05	5.99529e-06	4.21807e-06
0.2625	5.39437e-05	8.42458e-06	8.09155e-06
0.2875	7.10012e-05	1.10883e-05	1.06499e-05
0.3125	7.50101e-05	1.20096e-05	1.12498e-05
0.3375	6.28396e-05	8.47329e-06	9.42594e-06
0.3625	4.40026e-05	7.54638e-06	6.60039e-06
0.3875	3.28517e-05	5.99787e-06	4.92776e-06
0.4125	2.66421e-05	5.55523e-06	3.99629e-06
0.4375	1.69382e-05	4.23456e-06	2.54074e-06
0.4625	1.31012e-05	3.63361e-06	1.96518e-06
0.4875	1.68681e-05	4.35529e-06	2.53019e-06
0.5125	5.17724e-06	2.31533e-06	7.76586e-07
0.5375	7.17358e-06	2.71136e-06	1.07604e-06
0.5625	5.00465e-06	2.23815e-06	7.50697e-07
0.5875	5.02224e-06	2.24601e-06	7.53335e-07
0.6125	8.47185e-07	8.47185e-07	1.27078e-07
0.6625	9.85255e-07	9.85255e-07	1.47788e-07
0.6875	9.55977e-07	9.55977e-07	1.43397e-07

Table B.13: Cross Sections in CLAS for ^{12}C(e,e'np) Backward Kinematics at 2.261 GeV

p_{rel} [GeV/c]	$d\sigma/dp_{rel}$ [nb/(MeV/c)]	StatErr [nb/(MeV/c)]	SysErr [nb/(MeV/c)]
0.1625	6.13852e-07	6.13852e-07	8.59393e-08
0.1875	6.13144e-07	6.13144e-07	8.58401e-08
0.2125	3.04454e-06	1.36156e-06	4.26236e-07
0.2375	6.06282e-06	1.91723e-06	8.48795e-07
0.2625	7.2674e-06	2.09792e-06	1.01744e-06
0.2875	7.23694e-06	2.08913e-06	1.01317e-06
0.3125	1.02119e-05	2.47675e-06	1.42967e-06
0.3375	1.14035e-05	2.61615e-06	1.59649e-06
0.3625	9e-06	3.40168e-06	1.26e-06
0.3875	6.5073e-06	1.96202e-06	9.11022e-07
0.4125	2.97224e-06	1.32923e-06	4.16114e-07
0.4375	4.71854e-06	1.66826e-06	6.60595e-07
0.4625	4.10239e-06	1.55056e-06	5.74335e-07
0.4875	2.3166e-06	1.1583e-06	3.24324e-07
0.5125	5.8178e-07	5.8178e-07	8.14492e-08
0.5375	2.29855e-06	1.14927e-06	3.21797e-07
0.5625	5.7556e-07	5.7556e-07	8.05783e-08
0.6125	1.14708e-06	8.11111e-07	1.60592e-07
0.6375	1.14227e-06	8.07705e-07	1.59917e-07

Table B.14: Cross Sections in CLAS for ^{12}C(e,e'pp) Backward Kinematics at 4.461 GeV

p_{rel} [GeV/c]	$d\sigma/dp_{rel}$ [nb/(MeV/c)]	StatErr [nb/(MeV/c)]	SysErr [nb/(MeV/c)]
0.1875	6.14429e-07	6.14429e-07	8.60192e-08
0.2125	1.84447e-06	1.06491e-06	2.58225e-07
0.2375	6.05683e-07	6.05683e-07	8.47957e-08
0.2625	6.06111e-07	6.06111e-07	8.48555e-08
0.2875	4.25952e-06	1.60995e-06	5.96333e-07
0.3125	1.81808e-06	1.04967e-06	2.54531e-07
0.3375	4.20958e-06	1.59107e-06	5.89341e-07
0.3625	3.02761e-06	1.35398e-06	4.23864e-07
0.3875	2.37099e-06	1.18551e-06	3.31939e-07
0.4125	1.78487e-06	1.03049e-06	2.49881e-07
0.4375	3.54678e-06	1.44797e-06	4.96551e-07
0.4625	2.94454e-06	1.31684e-06	4.12236e-07
0.4875	5.26681e-06	1.75559e-06	7.37353e-07
0.5125	6.43799e-06	1.94113e-06	9.01319e-07
0.5375	7.01062e-06	2.02379e-06	9.81487e-07
0.5625	6.42534e-06	1.93731e-06	8.99547e-07
0.5875	4.75059e-06	1.67959e-06	6.65082e-07
0.6125	2.91383e-06	1.30309e-06	4.07936e-07
0.6375	2.91592e-06	1.30404e-06	4.08229e-07
0.6625	2.47915e-06	1.23958e-06	3.47081e-07
0.6875	2.95068e-06	1.31958e-06	4.13095e-07
0.7125	3.49391e-06	1.42638e-06	4.89148e-07
0.7375	1.74942e-06	1.01003e-06	2.44919e-07
0.7875	5.83588e-07	5.83588e-07	8.17024e-08
0.8125	1.75081e-06	1.01083e-06	2.45113e-07
0.8375	1.16812e-06	8.25986e-07	1.63537e-07

Table B.15: Cross Sections in CLAS for ^{12}C(e,e'pp) Forward Kinematics at 4.461 GeV

Bibliography

[1] J. Bergstrom. Line shapes and the radiative tail near the elastic peak. *Medium Energy Nuclear Physics with Electron Lenear Accelerator*, page 251, 1967.

[2] H. Bethe. *Phys. Rev.*, 103:1353, 1956.

[3] DeForest. *Nuclear Physics*, A(392), 1983.

[4] C. Ciofi degli Atti. *Nuclear Theory*, v1, 2002.

[5] T.W. Donnelly (edited by R.P. Whitney et al.). Summer workshop at continuous electron beam accelerator facility, 1984, p254.

[6] A. Tang et al. *arXiv Preprint nucl-ex/0206003*, 2002.

[7] B. Kotlinski et al. *Eur. Phys. J.*, A9:537, 2000.

[8] C. Giusti et al. *Nuclear Physics*, A(535):573, 1991.

[9] C. Giusti et al. *Phys. Rev. C*, 57:1691, 1998.

[10] C. Mahaux et al. *Adv. Nucl. Phys.*, 20:61, 1991.

[11] D. Groep et al. *Phys. Rev. Lett.*, 83(26):5443, 1999.

[12] D. Lawrence et al. Clas drift chamber calibration: Software and procedures. CLAS Notes 018, 1999.

[13] D.E. Brown et al. *Nuclear Theory*, v1, 2001.

[14] E. Dumonteil et al. Neutron detection efficiency in clas. CLAS Notes 006, 2001.

[15] E. Hackett et al. Neutron detection in the clas calorimeter. CLAS Notes 014, 1998.

[16] E. S. Smith et al. The time-of-flight system for clas. *Nucl. Instr. and Meth.*, A(432):265, 1999.

[17] E. Smith et al. Calibration of the clas tof system. CLAS Notes 011, 1999.

[18] G. Adams et al. The clas cherenkov detector. *Nucl. Instr. and Meth.*, A(465):414, 2001.

[19] G. Rosner et al. *Prog. Part. Nucl. Phys.*, 44:99, 2000.

[20] H. Bagdasaryan et al. Implementation of e2 targets into gsim and proton energy loss corrections. CLAS Notes 006, 2001.

[21] H. Heisenberg et al. *Nuclear Theory*, v5, 1998.

[22] H. Muther et al. *Phys. Rev. C*, 49:17, 1994.

[23] H. Muther et al. *Phys. Rev. C*, 61:14304, 1999.

[24] J. Goff et al. *Phys. Rev. C*, 55:1600, 1997.

[25] J. Golak et al. *Phys. Rev. C*, 51:1638, 1995.

[26] K. Blomqvist et al. *Elsevier Preprint*, 1997.

[27] K. Brueckner et al. *Phys. Rev.*, 95:217, 1954.

[28] K. Egiyan et al. Study of nucleon short range correlation in (e,e') reaction at $x_b > 1$. CLAS Analysis Notes 011, 2001.

[29] K. Mikhailov et al. Methods for close-track efficiency study and its application for clas. CLAS Notes 011, 2001.

[30] M. Amarian et al. The clas forward electromagnetic calorimeter. *Nucl. Instr. and Meth.*, A(460):460, 2001.

[31] M. D. Mestayer et al. The clas drift chamber system. *Nucl. Instr. and Meth.*, A(449):81, 2000.

[32] M. Lacombe et al. *Phys. Lett.*, B(101):139, 1981.

[33] R. Florizone et al. *Phys. Rev. Lett.*, 83:2308, 1999.

[34] R. Machleidt et al. *Phys. Rev. C*, 53:1483, 1996.

[35] R. Wiringa et al. *Phys. Rev. C*, 51:38, 1995.

[36] R. Wiringa et al. *Nuclear Theory*, v1, 2002.

[37] S. Pieper et al. *Phys. Rev. C*, 46:1741, 1992.

[38] T. Ohmura et al. *Prog. Theo. Phys.*, 15:222, 1956.

[39] V. Stoks et al. *Phys. Rev. C*, 49:2950, 1994.

[40] E. Fermi. *Nuclear Physics.* The Univ. of Chicago Press, 1948.

[41] A. Fetter and J. Walecka. *Quantum Theory of Many-Particle Syserms.* McGraw-Hill, New York, 1971.

[42] C. Gearhart. PhD thesis, Washington University, 1994.

[43] J. Golak. PhD thesis, Jagellonian University Cracow, 1995.

[44] J. Goldstone. *Proc. Roy. Soc. (London)*, A(239):267, 1957.

[45] K. Gottfried. *Nuclear Physics*, 5:577, 1958.

[46] D. Groep. PhD thesis, NIKHEF, Netherland, 2000.

[47] C. Hajduk and P. Sauer. *Nucl. Phys.*, A(369):321, 1981.

[48] J. Kelly. PhD thesis, Massachusetts Institute of Technology, 1981.

[49] A. Klimenko. http://www.physics.odu.edu/ klim/checkelectron.html.

[50] Jefferson Lab. *The Science Driving the 12 GeV Upgrade of CEBAF.* Jefferson Lab, 2001.

[51] J.M. Laget. private communication.

[52] J.M. Laget. *Phys. Rev. C*, 35:832, 1987.

[53] J. Leeuwe. PhD thesis, Universiteit Utrecht, 1996.

[54] L. Lepikas. *Nuclear Physics*, A(553):297, 1993.

[55] K. Loukachine. PhD thesis, Virginia Polytechnic Institute, 2000.

[56] R. Niyazov. PhD thesis, Old Dominion University, 2002.

[57] D. Protopopescu. PhD thesis, University of New Hampshire, 2002.

[58] D. Rowntree. PhD thesis, Massachusetts Institute of Technology, 1995.

[59] M. Rvachev. private communication.

[60] J. Rychebusch. *Phys. Lett.*, B(383):1, 1996.

[61] J. Ryckebusch. Contribution to the workshop on electron-nucleus scattering, italy, 1998.

[62] M. Sargsian. Computer code for inclusive electroproduction reactions and radiative corrections. CLAS Notes 007, 1990.

[63] A. Skabelin. PhD thesis, Massachusetts Institute of Technology, 2001.

[64] R. Starink. PhD thesis, Vrije Universiteit, 1999.

[65] S. Stepanya. private communication.

[66] S. Stepanya. Simple event builder (seb) in the framework of recsis.

[67] Y. Tsai. Radiative corrections to electron scattering. *SLAC-PUB*, (848), 1971.

[68] H. Uberall. *Electron Scattering from Complex Nuclei.* Academic Press, 1971.

[69] L. Weinstein. PhD thesis, Massachusetts Institute of Technology, 1988.

Acknowledgments

Without the help of many people, this thesis would not have been finished. I would like to take this opportunity to express my gratitude to all individuals who helped me and contributed to this project. The names listed here are definitely not complete, but any possible omission is unintentional.

First of all, I would like to thank my advisor, Professor William Bertozzi, for his guidance and support throughout my graduate career. Bill has an incredible physics intuition as well as generous attention, patience and encouragement to young physicists. I feel fortunate to have done my thesis research under his supervision. During the past five years, he educated me by his unique enlightenments and guided me all the way from a new college graduate to the accomplishment of a Ph.D. in experimental nuclear physics.

I would like to thank my thesis committee members: Dr. Bill Donnelly and Prof. Robert Redwine for their comments, suggestions and corrections to this thesis. Their contributions made this thesis more clear and readable.

I would like to thank Dr. Jean-Marc Laget for his theorectical support. We had many productive discussions in the stage of analyzing the data and presenting the data. His calculations for ^{3}He data are essential in terms of understanding the features of the results.

I would like to thank Dr. Shalev Gilad for many fruitful discussions and important suggestions during the data analysis. I would also like to thank the post-docs in our group who helped me a lot during this research project. They are: David Rowntree, Jianguo Zhao, Zilu Zhou, Kevin Fissum, Riad Suleiman and Douglas Higinbotham.

I would like to thank Professor Larry Weistein at ODU for his leading role in the multihadron physics program at Jefferson Lab and for his many suggestions and comments on my data analysis. Special thanks to Dr. Stepan Stepanyan, who dedicated a lot of efforts to the data taking and the calibrations. He was a big help when I tried to get familiar with the CLAS softwares. I would also like to thank Dr. Will Brooks for his help when I calibrated the CLAS calorimeter.

I would like to thank all other members of the E2 physics working group for their participation in the experiment and cooperation during the analysis. Some of them are: Dr. Kim egiyan, Prof. Maurik Holtrop, Prof. Bill Hersman, Dr. Alex Stavinsky, Dr. Nikolai Pivnyuk, Rustam Niyazov, Gagik Gavalian, Dan Protopopescu, Steven McLauchlan, Westley Ingram and Hovannes Bagdasaryan. I would also like to thank all collaborators of CLAS for taking shifts and making the experiment successful.

I would like to thank all my fellow graduate students both at MIT and at Jefferson Lab. The friendship with them made my life as a graduate student more enjoyable. They are: Juncai Gao, Nilanga Liyanage, Alex Skabelin, Zhengwei Chai, Marat Rvachev, Xiaochao Zheng, Peter Monaghan, Yuan Xiao, Chi Zhang, Feng Xiong, Wang Xu, Lingyan Zhu, Ji Li, Xiaofeng Zhu, Lulin Yuan, Lei Guo and Joe Santoro. Special memories to Jindong Zhou, who passed away several months after he started his thesis research at Jefferson Lab. He was my college classmate and also joined our group at MIT for his Ph.D. education.

I would like to thank my parents for their support and providing me opportunities to receive better education. They have been helping me by any means within their capabilities. I would thank them for the rest of my life.

At last, but definitely not least, I owe special gratitude to my wife, Mei Li, for her love, patience and support during all these years. We have been so happy together no matter how many difficult times we have to face. I am so fortunate to have her. Without her, finishing this work would not be possible.